

High-Spin States in Neutron-Rich Tantalum Isotopes

Nyaladzi Palalani

**A thesis submitted for the degree of
Doctor of Philosophy in Physics at
The Australian National University**

February, 2016

Preface

This thesis describes an investigation of the structure of neutron-rich ^{182}Ta and ^{183}Ta . The research was undertaken between February 2011 and September 2015 at the Department of Nuclear Physics, The Australian National University (ANU), Canberra, Australia.

The data used in this work was collected at Argonne National Laboratory (Chicago, USA) by Dr Greg Lane and Professor George Dracoulis from ANU as the project leaders, in collaboration with other researchers from Argonne National Laboratory and University of Massachusetts Lowell. The initial offline data sorting into a database was carried out by Dr Greg Lane. Subsequent sorting, data analysis and interpretation was performed by the author under the guidance of my supervisors Dr Greg Lane and Professor George Dracoulis, together with research team members Professor Andrew Stuchbery, Dr Tibor Kibedi, Dr Matt Reed, Dr Sankha Hota and Dr Alan John Mitchell. The majority of the computer analysis codes used in the present work are from the ANU, while the Radware suite from David Radford was also used.

Preliminary results for ^{183}Ta have been published in the proceedings of the Heavy Ion Accelerator Symposium held in April 2012 at the ANU [Pal12]. No other part of this thesis has been submitted in whole or in part for a degree at any other university.



Nyaladzi Palalani

February, 2016

Acknowledgements

First I would like to thank my supervisor Dr Greg Lane for all of his advice, encouragement and support throughout my PhD. Also, my sincere thanks to Professor Andrew Stuchbery and Dr Tibor Kibedi for their support when I first commenced my studies, as well as reviewing my thesis. Thanks to the late Professor George Dracoulis for his advice and contribution to my work. I would also like to express my gratitude to the following members of our research group, Dr Matt Reed, Dr Sankha Hota and Dr Alan John Mitchell for the time they spent helping on various aspects of my research and for having open doors whenever I had a random question.

I would also like to thank all members of the Nuclear Physics department for the wonderful environment, regular birthday cakes and Friday afternoon drinks.

I'm thankful to the University of Botswana for their financial support throughout my study. Nothing would have been possible for me without their support.

To my family in Botswana, thank you for your support and understanding throughout. I know I missed a lot of events, wedding ceremonies, graduation parties etc, but you never got angry with me for being absent. To my mum and dad, this is for you, thanks for the encouragement, love and support throughout my entire life. To my brothers and sisters, thank you so much for your endless phone calls and keeping me updated. I never missed home. To my friends Chaxman Raphaka, Makhonyela Aroon, Mpaphi Tsholofelo, Mochizo, Buyani, Kb-Lotshwao, Bernard Baituti, Super-T Nthula, thank you for all the support and encouragement.

Finally, I would like to thank God for giving me the opportunity to come across and work with all these wonderful people who willingly and tirelessly transformed my life to something I will forever be proud of.

Abstract

Deep-inelastic reactions between \sim 6.2 MeV/A ^{136}Xe ions and a thick ^{186}W target have been used to investigate excited states in neutron-rich tantalum isotopes, establishing new structures in ^{182}Ta and ^{183}Ta . Spins and parities were determined from angular correlations, internal conversion coefficients deduced from intensity balances, and consideration of transition strengths. The structure and configuration assignments have been established from the measured magnetic properties and aligned angular momenta of the observed rotational bands, as well as comparison with multi-quasiparticle calculations. Multi-quasiparticle calculations using adjusted Nilsson energies and a Lipkin-Nogami pairing model were performed for the series of tantalum nuclei between A=181 and A=185.

The previously known 1300 ns isomer in ^{183}Ta was fully characterised with its energy deduced as 1332 keV, a new lifetime of 1200(140) ns, and a $K^\pi = 19/2^+$ assignment. Several new multi-quasiparticle states, including two isomers with $\tau = 41(5)$ ns, $K^\pi = 29/2^-$ and $\tau = 70(4)$ ns, $K^\pi = 41/2^-$, have been further identified and found to be feeding the 1200 ns isomer. From the multi-quasiparticle calculations, a three-quasiparticle configuration was assigned to both the $K^\pi = 19/2^+$ and $29/2^-$ isomers, while the upper-most isomer at $41/2^-$ was established to have a five-quasiparticle nature.

The out-of-beam γ ray coincidence data revealed a new level structure in coincidence with tantalum X-rays. Measurements of the magnetic properties of this structure from branching ratios, together with the yields from various data sets using ^{186}W , ^{185}Re , ^{187}Re and ^{192}Os targets, enabled an isotopic assignment of this structure to ^{182}Ta . Three isomeric states were found to be feeding the known 10^- isomer in ^{182}Ta . A rotational band built on the 10^- isomer has been observed and is found to be fed by a new 14^+ , 356 ns isomer at 1950 keV. Several intrinsic states above this

isomer are also identified. Firm spins and parities have been established up to the 14^+ isomeric state. Due to limited spectroscopic information, the spins and parities for the levels above this isomer are tentative.

The structure of ^{182}Ta and ^{183}Ta has also been investigated by comparing the measured transition strengths with similar transitions in the mass region. Most of the transition strengths are in good agreement with expectations in the region, except for a few cases of $E1$ decays that are anomalous. Possible explanations for some of these anomalous transition strengths have been discussed.

There are few cases where the predicted yrast states are not observed experimentally in both ^{182}Ta and ^{183}Ta and possible explanations are given.

Both the calculations and experimental results suggest a high density of intrinsic states occurs along the yrast line at high excitation energy in both nuclei. This pattern seems to emerge in the more neutron-rich tantalum isotopes, resulting in a more complex level scheme that is difficult to interpret.

Contents

Preface	i
Acknowledgements	iii
Abstract	v
1 Introduction	1
1.1 Scope of the current work	2
2 Theory	5
2.1 Nuclear structure models	5
2.1.1 Spherical shell model	5
2.1.2 Nuclear deformation	7
2.1.3 Nilsson model/deformed shell model	8
2.1.4 Pairing correlations	14
2.1.5 Residual interactions	17
2.2 Nuclear decay modes	18
2.2.1 Gamma decay	19
2.2.2 Internal conversion and internal pair formation	20
2.3 Collective nuclear motion	21
2.3.1 Nuclear vibrations	21
2.3.2 Nuclear rotation	22
2.4 Aligned angular momenta	27
2.5 Transition strengths	29
2.6 Properties of rotational bands	32
2.7 Effects of nuclear rotations	34
2.8 Isomeric states	35
2.8.1 Spin traps	35

2.8.2	K-isomers	36
3	Experimental methods	39
3.1	Accessing neutron-rich nuclei	39
3.1.1	Heavy-ion fusion-evaporation reactions	40
3.1.2	Incomplete-fusion reactions	40
3.1.3	Fission reactions	41
3.1.4	Fragmentation reactions	41
3.1.5	Deep-inelastic reactions	41
3.2	Detection of γ radiation	43
3.2.1	γ -ray detectors	43
3.2.2	Interaction of γ rays with matter	43
3.2.3	Compton suppression	45
3.2.4	Multi-detector arrays	46
3.2.5	GAMMASPHERE	47
3.3	Coincidence spectroscopy	48
3.3.1	Coincidence histograms	48
3.3.2	Prompt and delayed coincidence	50
3.3.3	Elemental and isotopic assignments	52
3.4	Lifetime analysis methods	53
3.5	Spin and parity assignment methods	57
3.5.1	Derived internal conversion coefficients	57
3.5.2	Angular correlations	59
3.6	Experimental details	65
3.6.1	Data with ^{186}W target	65
3.6.2	Offline data sorts	65
4	Results and level scheme for ^{183}Ta	67
4.1	Previous studies on ^{183}Ta	67
4.2	Current analysis and results for ^{183}Ta	68
4.2.1	New states in ^{183}Ta	68
4.2.2	Lifetime measurements in ^{183}Ta	75

4.2.3	Spin and parity assignments	78
5	Results and level scheme for ^{182}Ta	87
5.1	Previous studies on ^{182}Ta	87
5.2	Current analysis and results for ^{182}Ta	88
5.2.1	New states in ^{182}Ta	89
5.2.2	Isotopic assignment from yields	94
5.2.3	Placement above the 10^- state in ^{182}Ta	96
5.2.4	Lifetime measurements	97
5.2.5	Spin and parity assignments	99
6	Multi-quasiparticle calculations	107
6.1	Low-lying states in tantalum isotopes	107
6.1.1	Odd-even isotopes	107
6.1.2	Odd-odd isotopes	109
6.2	Multi-quasiparticle calculations	109
6.2.1	Testing the results and summary of the calculations	112
7	Configuration assignments	125
7.1	Magnetic properties	125
7.2	Alignments	126
7.2.1	Harris parameters	128
7.3	Configuration assignments in ^{183}Ta	130
7.3.1	Single-quasiparticle states	130
7.3.2	Multi-quasiparticle states	131
7.4	Configuration assignments in ^{182}Ta	137
7.4.1	Two-quasiparticle states	137
7.4.2	Four and six-quasiparticle states	139
8	Discussion	145
8.1	Transition strengths in ^{183}Ta	145
8.1.1	$9/2^-$, 157 ns isomer	145
8.1.2	$19/2^+$, 1200 ns isomer	145

8.1.3	$29/2^-$, 40 ns isomer	146
8.1.4	$41/2^-$, 70 ns isomer	146
8.1.5	Transitions from states with lifetime limits of $\tau < 5$ ns	146
8.2	Transition strengths in ^{182}Ta	150
8.2.1	10^- , 1380 s isomer	150
8.2.2	14^+ , 356 ns isomer	150
8.2.3	(18^-) , 106 ns isomer	150
8.2.4	Transitions from states with lifetime limits $\tau < 5$ ns	151
8.3	Comments on transition strengths	154
8.3.1	Enhanced $E1$ strengths for the 110 and 145 keV transitions in ^{183}Ta	154
8.3.2	$B(E1) \sim 10^{-9}$ W.u for the 638 keV transition in ^{182}Ta	154
8.3.3	468 and 496 keV transitions competing with in-band decays in ^{182}Ta	155
8.4	Comments on overall state configurations and changes between them.	155
8.4.1	Commonality of base configurations in ^{183}Ta	155
8.4.2	Missing 15^- and 16^- states in ^{182}Ta	156
8.4.3	Missing $21/2^+$ state in ^{183}Ta	158
8.4.4	Structural changes and systematics	158
9	Conclusions	163
9.1	New findings	163
9.2	Physics summary	164
9.3	Future work	165
Appendices		167
A	Appendix A	169
A.1	Properties of all γ rays in ^{183}Ta and ^{182}Ta	169
A.2	Single and two-quasiparticle states in tungsten isotopes.	169
B	Appendix B	175
B.1	Published results on ^{183}Ta	175

Bibliography	181
---------------------	------------

List of Figures

1.1	Coupling of single particle angular momenta in an axially deformed nucleus for one and three particles	2
2.1	Two-proton separation energies for isotonic series and two-neutron separation energies for isotopic series	6
2.2	Quantum numbers for motion of a single nucleon within an axially deformed potential with symmetry axis Z'	10
2.3	Nilsson diagram for proton numbers $50 \leq Z \leq 82$	12
2.4	Nilsson diagram for neutron numbers $82 \leq N \leq 126$	13
2.5	Coupling of the single-particle angular momentum j to the collective angular momentum R in axially symmetric nuclei.	23
2.6	Strong coupling and weak-coupling/rotational alignment of the single-particle angular momentum j to the collective rotation R	26
2.7	The aligned angular momentum of the single particle due to the Coriolis force.	29
2.8	Strongly-coupled band, illustrating how the configuration may be reflected in the measured branching ratio of the $E2$ and $M1/E2$ transitions.	32
3.1	Schematic representation of a deep-inelastic reaction.	42
3.2	Interaction cross-sections for gamma rays in Ge crystal as a function of energy.	44
3.3	Schematic representation of the Compton-suppressed HPGe detectors in GAMMASPHERE.	45
3.4	Photo of the GAMMASPHERE array.	48

3.5 Schematic representation of a symmetric γ - γ -matrix used in construction of nuclear level schemes and illustration of the corresponding level scheme.	49
3.6 Level scheme that will exhibit prompt and delayed coincidence events and schematic timing of the related γ rays.	51
3.7 Illustration of a centroid shift measurement of a nuclear state lifetime. .	54
3.8 Schematic representation of the time distribution for γ rays emitted from an isomeric state.	55
3.9 Representation of beam pulsing conditions as applied in the present work to investigate the isomeric states.	56
3.10 A decay scheme to illustrate the use of intensity balances and deduced conversion coefficients to assign spins and parities.	59
3.11 Schematic view of a γ -ray cascade from nuclear excited states and the related $\gamma - \gamma$ angular correlation.	61
3.12 Expected angular correlation, $W(\theta)$, for various combinations of un-stretched ($\lambda > \Delta I$) and stretched ($\lambda = \Delta I$) $E1$ and $E2$ transitions. .	63
3.13 Expected angular correlation, $W(\theta)$, for combinations of stretched ($\lambda = \Delta I$) $M1/E2$ and $E2$ transitions showing various positive mixing ratios.	63
3.14 Expected angular correlations, $W(\theta)$, for combinations of stretched ($\lambda = \Delta I$) $M1/E2$ and $E2$ transitions showing various negative mixing ratios.	64
4.1 Partial level scheme for ^{183}Ta established by Shizuma <i>et al.</i> [Shi09]. .	67
4.2 New level scheme for ^{183}Ta deduced in the current work.	69
4.3 Out-of-beam, double-gated coincidence spectra for low-lying transitions in ^{183}Ta	70
4.4 (a) New γ rays obtained by double-gating on the transitions below the 1332 keV isomer in ^{183}Ta and projecting the preceding transitions in the out-of beam data. (b) Known γ rays obtained by double-gating on the new transitions and projecting transitions that arrive later in time.	71

4.5	Double-gated spectra from the out-of-beam cube demonstrating co-incidence relationships for the new transitions in ^{183}Ta	72
4.6	Double-gated spectra from the out-of-beam cube demonstrating co-incidence relationships for the new transitions in ^{183}Ta	73
4.7	In-beam, double-gated spectra for ^{183}Ta showing prompt feeding γ rays at 319, 337, 383, 395 and 629 keV.	74
4.8	Summed spectrum of time differences between the 73 keV γ ray (stop) and the 832, 893 and 871 keV γ rays (start), yielding the lifetime of the 73 keV isomer in ^{183}Ta	75
4.9	Representative decay curve for the 1332 keV isomer in ^{183}Ta	76
4.10	Time difference spectra for γ -ray pairs in the region between (a) the 1332 and 2475 keV levels and (b) the 2475 and 3870 keV levels in ^{183}Ta , compared to the spectrum from a known prompt γ -ray pair.	76
4.11	Time-difference spectra between γ -ray pairs across the 2475 keV state in ^{183}Ta , confirming it is an isomer.	77
4.12	Lifetime curve for the 2475 keV isomer in ^{183}Ta , produced from a sum of time difference spectra, and giving a lifetime of $\tau = 41(4)$ ns.	77
4.13	Decay curve for the 3870 keV isomer in ^{183}Ta , giving a lifetime of $\tau = 70(5)$ ns.	78
4.14	Total conversion coefficients deduced from intensity balances for some of the transitions depopulating states in ^{183}Ta	82
4.15	Angular correlations and deduced mixing ratios for selected transition pairs between the 1332 and 2953 keV states in ^{183}Ta	83
4.16	Angular correlations and deduced mixing ratios for selected transition pairs between the 2304 and 3870 keV levels in ^{183}Ta	85
5.1	Summary of the known structures of ^{182}Ta from previous studies.	88
5.2	Single-gated spectra from the 4 s chopped beam data for the known 147, 172 and 185 keV transitions in ^{182}Ta	90
5.3	Level scheme for ^{182}Ta deduced in the current work.	91
5.4	Various gated spectra for ^{182}Ta proving the existence of new isomers.	92

5.5	Sums of double-gated spectra from the out-of-beam cube demonstrating coincidence relations of the new transitions in ^{182}Ta	93
5.6	Double-gated spectra in ^{182}Ta from the out-of-beam cube proving the ordering of transitions between the 1950 keV and 3399 keV states. . . .	94
5.7	Yields of different tantalum isotopes from various targets, normalised by the target flux and compared to yields from the ^{186}W target.	96
5.8	Section of the nuclear chart showing the proximity of the targets, ^{185}Re , ^{187}Re , ^{186}W and ^{192}Os , to the neutron-rich tantalum isotopes and used to illustrate expected tantalum yields.	96
5.9	Time spectrum to illustrate the $\tau=356(16)$ ns isomer in ^{182}Ta	98
5.10	Time difference spectra between the depopulating 293 keV transition and the two feeding transitions at 709 and 1098 keV, giving a lifetime of $\tau=1.7(5)$ ns for the 2243 keV state in ^{182}Ta	98
5.11	Representative decay curve for the 3399 keV isomer in ^{182}Ta , giving a lifetime of $\tau=106(4)$ ns.	99
5.12	Angular correlations for selected transition pairs between the 519 and 1950 keV isomeric states in ^{182}Ta	101
5.13	Angular correlations for selected transitions between the 1950 keV and 3399 keV isomeric states in ^{182}Ta	104
5.14	Total conversion coefficients deduced from intensity balances for transitions in ^{182}Ta compared to theoretical expectations.	104
6.1	Nilsson single-particle energies for orbitals close to the neutron and proton Fermi surfaces in neutron-rich tantalum isotopes and adjustments applied for the multi-quasiparticle calculations.	111
6.2	Predicted multi-quasiparticle states in ^{181}Ta , excluding the effects of residual interactions.	115
6.3	Predicted multi-quasiparticle states in ^{183}Ta , excluding the effects of residual interactions.	116
6.4	Predicted multi-quasiparticle states in ^{185}Ta , excluding the effects of residual interactions.	117

6.5	Systematics of selected yrast and near-yrast multi-quasiparticle states in odd-mass, neutron-rich tantalum isotopes as predicted by multi-quasiparticle calculations with Lipkin-Nogami pairing.	118
6.6	Calculated yrast and near-yrast states compared to the experimental single-and multi-quasiparticles states known in ^{181}Ta , ^{183}Ta and ^{185}Ta	119
6.7	Predicted multi-quasiparticle states in ^{182}Ta , excluding the effects of residual interactions.	121
6.8	Predicted multi-quasiparticle states in ^{184}Ta , excluding the effects of residual interactions.	122
6.9	Calculated yrast and near-yrast states compared to the experimental states known in ^{182}Ta and ^{184}Ta	123
7.1	Aligned angular momenta for selected single-quasineutron bands in ^{181}W and ^{183}W , as well as some of the single-quasiproton bands in ^{181}Ta and ^{183}Ta	127
7.2	Alignments for some of the known multi-quasiparticle bands in ^{180}Ta and ^{182}W , used to illustrate the additivity of alignment in multi-quasiparticle states.	128
7.3	Aligned angular momenta for the $\pi 9/2^-[514]$ band in ^{183}Ta compared to the same band in ^{181}Ta [Dra98a, Sai98] and the $\pi 7/2^+[404]$ band in ^{183}Ta [Shi09]. See table 7.1 for the reference parameters used for each nucleus. Open and filled symbols are used for the different signatures in each band.	131
7.4	Calculated yrast and near-yrast states in ^{183}Ta compared with experimental energies from the present work.	132
7.5	Aligned angular momenta for the 5^+ , 10^- and 15^+ bands in ^{182}Ta compared to single-particle rotational bands in the nearby odd-mass nucleus ^{183}W and the 10^+ band in ^{182}W	139
7.6	Calculated yrast and near-yrast states in ^{182}Ta , compared with the experimental energies from the present work.	140

8.1	Partial level scheme of ^{182}Ta above the 356 ns isomer as deduced in the present work.	157
8.2	Known level scheme for $^{176,177}\text{Ta}$ showing many intrinsic states with rotational structures.	159
8.3	Intrinsic state energies for ^{184}W from multi-quasiparticle calculations compared to the collective bands known experimentally.	160
8.4	Intrinsic state energies for ^{183}Ta from multi-quasiparticle calculations performed in the present work, compared to the collective bands known experimentally.	161

List of Tables

3.1	Angles of the 110 detector positions in GAMMASPHERE.	48
4.1	Transition strengths and corresponding reduced hindrances for the 465 and 23 keV transitions, assuming different spins and parities for the 1200 ns isomeric state.	80
5.1	Transition strengths and corresponding reduced hindrances for the 245 and 570 keV transitions, assuming alternative possibilities of $K^\pi = 14^+$ and $K^\pi = 14^-$ for the 356(13) ns isomeric state.	102
6.1	Known low-lying two-neutron states in ^{184}W that are likely to contribute to multi-quasiparticle states observed in ^{183}Ta	108
6.2	Deformation parameters, ε_2 and ε_4 , for tantalum isotopes between A=181-185 as predicted by Möller <i>et al.</i> [Mol95]	110
7.1	Reference parameters, \mathfrak{S}_0 and \mathfrak{S}_1 , used in the present work to deduce the aligned angular momenta for rotational structures in the tantalum, tungsten and hafnium isotopes.	129
7.2	Measured in-band branching ratios for the $9/2^-$ [514] band in ^{183}Ta , together with inferred gyromagnetic ratios.	130
7.3	Predicted multi-quasiparticle states in ^{183}Ta compared with experimentally observed states.	134
7.4	Measured in-band branching ratios for the 5^+ , 10^- and 15^+ bands in ^{182}Ta , together with inferred gyromagnetic ratios.	138
7.5	Predicted multi-quasiparticle states in ^{182}Ta compared with experimentally observed states.	141
8.1	Transition strengths observed in ^{183}Ta	147

8.2 Known transition strengths for $9/2^- \rightarrow 7/2^+$, $E1$ decays in $^{179,181,183,185}\text{Ta}$	149
8.3 Transition strengths observed in ^{182}Ta	152
A.1 Properties of transitions in ^{183}Ta	170
A.2 Properties of transitions in ^{182}Ta	172
A.3 Low-lying, two-neutron states known in ^{182}W , ^{184}W and ^{186}W that are likely to contribute to the multi-quasiparticle states in ^{181}Ta , ^{183}Ta and ^{185}Ta , respectively.	173
A.4 Known single-neutron states in odd-tungsten isotopes that are likely to contribute to the multi-quasiparticle states in odd-odd tantalum isotopes between $A = 180$ and $A = 186$	173

Introduction

The atomic nucleus is a microscopic system comprised of protons and neutrons, collectively known as nucleons, that interact primarily via the long-range Coulomb and the short-range strong nuclear forces. The nucleons exist inside the nucleus in certain allowed energy levels within an average potential created by the other nucleons, known as the mean field. These energy levels show large gaps that correspond to filled major shells for both proton and neutrons. For the nuclei with closed shells, the number of protons (Z) and neutrons (N) are equal to 2, 8, 20, 28, 50, 82 or 126; where their sum $N + Z$ gives the mass number, A , of the nucleus. These nucleon numbers are known as magic numbers. Although all these magic numbers have been confirmed for neutron shell gaps, the next shell gap for protons above $Z=82$ is still a matter of debate. Nuclei can take a variety of shapes depending on the total number of protons and neutrons. Those in the region of Z and N equivalent to magic numbers usually take spherical equilibrium shapes, but further away from these numbers where shells are partially filled, the nuclei acquire permanent deformation; the latter case will be discussed in more detail in chapter 2.1. The present research is focused on the rare-earth elements around mass-180, known to be prolate deformed and generally axially symmetric in shape.

Different energy states are found within the nucleus that depend upon the arrangement of nucleons within the mean field. The orbitals that the nucleons occupy are defined by specific quantum numbers. In spherical nuclei, the single-particle angular momentum j is a good quantum number, while for axially deformed nuclei the projection $j_z = \Omega$ along the symmetry axis, z , can be defined (see Chapter 2). Figure 1.1(a) illustrates the single-particle angular momentum j and its projection Ω for the unpaired nucleon in an odd- A prolate nucleus. For several unpaired nu-

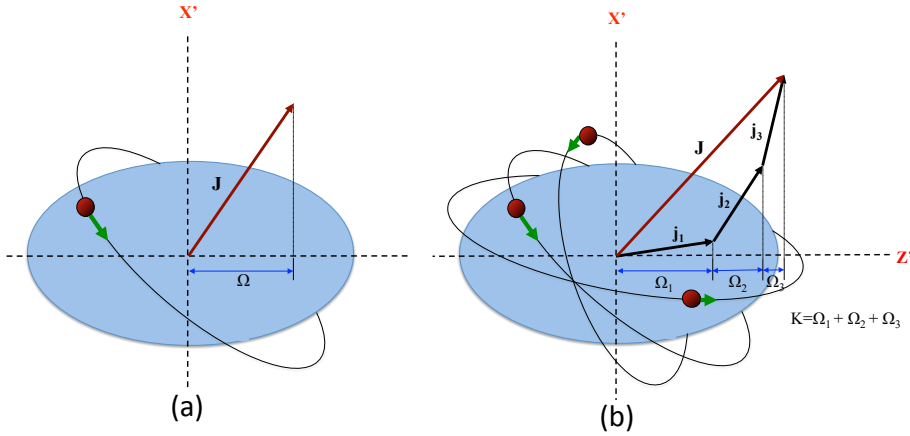


Figure 1.1: Total angular momentum projection along the symmetry axis in the case of (a) a single particle and (b) the coupling of three particles, illustrating $K = \sum \Omega_i$.

cleons, the coupled total angular momentum has a spin projection that is denoted by a quantum number, K , where $K = \Omega_1 + \Omega_2 + \Omega_3 + \dots + \Omega_i$, see figure 1.1(b). Excited states in nuclei can originate from excitation of individual valence nucleons between energy levels or through the collective behaviour of nucleons such as rotational or vibrational motion [Kra88]. For each arrangement of nucleons in deformed nuclei (the particle configuration), collective motions can occur in the form of surface vibrations or collective rotation (the latter usually around the axis perpendicular to the symmetry axis). Collective modes within the nucleus (be it rotational or vibrational) can be coupled to single/multi-quasiparticle states (see section 2.1.4) and are manifest as a band structure built upon the non-collective level known as a band head [Boh75]. The de-excitation of collective motion is characterised by a cascade of internal transitions through excited states to the band head. By measuring the properties of these transitions such as γ ray energies, angular momenta, transition strengths and emission sequences, information such as magnetic g-factors for intrinsic states, electric quadrupole moments and the shapes of the atomic nuclei can be obtained.

1.1 Scope of the current work

The single particle orbitals for nuclei in the region of $A \approx 180$ include high- Ω orbitals that lies close to both the proton and neutron Fermi surfaces. The high- K

states that result from coupling these high- Ω orbitals can undergo decays via transitions that involve a change in K quantum number between the initial and the final states, ΔK , that is greater than the transition multipolarity, λ , i.e. $\Delta K > \lambda$. Such transitions are, in principle, forbidden. However, in practice they provide a large degree of hindrance to the decay probability of the transition that is characterised by the forbiddenness, $\nu = \Delta K - \lambda$. With the decreasing transition rate for every extra unit of ν for such hindered transitions [Löb68], long lifetimes ranging from a few nanoseconds to years can be observed for the decaying K -states [Wal99, Wal01]. These metastable states are known as K -isomers.

The identification and characterisation of these isomers together with other, non-isomeric, multi-quasiparticle states can reveal important information on nuclear structure, including shapes, since the behaviour of the K quantum number in the region from $A \sim 180$ to $A \sim 190$ will change as the nuclear shapes are expected to change from prolate to triaxial shapes [Ste05, Rob09, Nom11]. Despite the long-standing theoretical predictions for the existence of K -isomers around the neutron-rich mass-180 region [Åbe78], experimental information has been mainly limited to neutron-deficient nuclei due to their easy accessibility from fusion-evaporation reactions.

Experimental access to the neutron-rich nuclei has been restricted mainly by lack of stable beams and targets for these reactions, as well as the preference for neutron over proton evaporation in this region of the nuclear chart. Such limitations have resulted in a lack of experimental information on high- K isomers and the competing collective degrees of freedom expected in this mass region. Recently, studies using deep-inelastic [Bro06] and fragmentation reactions [Pfüt98] with heavy-ion projectiles, in conjunction with large γ -ray detector arrays, have proven to be successful in populating higher spins and high- K isomers in neutron-rich isotopes. The majority of these structures have been observed in isotopes of erbium, lutetium, hafnium, tantalum, rhenium as well as osmium isotopes (see, for example, Refs. [Dra96, Dra09, Dra06a, Kon09, Dra04, Dra10a, Whe01, D'Al99,

Lan09, Lan10, Dra12] and references therein).

The research performed for this thesis had the goal of revealing new information on high-spin states, isomerism and shape changes in the neutron-rich tantalum nuclei. The heaviest stable tantalum nucleus is ^{181}Ta and little is known concerning high-spin states in isotopes heavier than ^{182}Ta , with the exception of a $\tau=1300$ ns isomer in ^{183}Ta [Shi09], the $K^\pi = 21/2^-$ isomer in ^{185}Ta [Lan09] and $\tau = 32$ s and $\tau > 7.2$ min isomers (but no γ -ray transitions) in ^{187}Ta [Ree10]. No excited state information is known for ^{184}Ta and ^{186}Ta .

Deep-inelastic reactions and the GAMMASPHERE array [Nol94, Jan96] were used to discover new structures in ^{182}Ta and ^{183}Ta . The current work is part of an ongoing program by the ANU spectroscopy group and its international collaborators with the aim of exploring the structures of the poorly studied, neutron-rich nuclei in this region using deep-inelastic reactions. One of the major goals is to map how the nuclear structure evolves with deformation or with increasing Z and N numbers in this region, as well as better understand the nature of the K -quantum number.

Chapter 2 describes various theoretical models relevant to the current studies. Detailed experimental methods used in this work are presented in Chapter 3. Chapters 4 and 5 covers the results and analysis for ^{182}Ta and ^{183}Ta , respectively. This is followed by details of multi-quasiparticle calculations and configuration assignments in Chapters 6 and 7, respectively. Discussion of these results in Chapter 8, precedes the summary and conclusions that are presented in Chapter 9.

Theory

Most of the theories used to explain nuclear structure are based on knowledge concerning the nature of the forces between nuclear constituents and on techniques for applying the laws governing these forces in many-body systems. This chapter gives a brief account of some of these theories, focussing on nuclear models that are applicable to deformed nuclei. These include the Nilsson, particle-rotor and nuclear-pairing models, although brief mention is also made concerning spherical nuclei.

2.1 Nuclear structure models

2.1.1 Spherical shell model

One of the key pieces of experimental evidence for the existence of nuclear shells was the observed gradual increase in neutron and proton separation energies, except for sudden drops at Z and N values of 2, 8, 20, 28, 50, 80 and 126, now known as the magic numbers. Figure 2.1 shows two-proton separation energies for isotonic series and two-neutron separation energies for isotopic series [Kra88, Wap77]. The discontinuities at the magic numbers were linked to the filling of nuclear shells and this led to the development of the shell model. This model best describes the independent motions of nucleons in nuclei consisting of closed shells with a few extra nucleons outside (particles) and/or a few nucleons short of (holes) closed shells. This model is analogous to the atomic shell model that describes the arrangement of electrons in an atom.

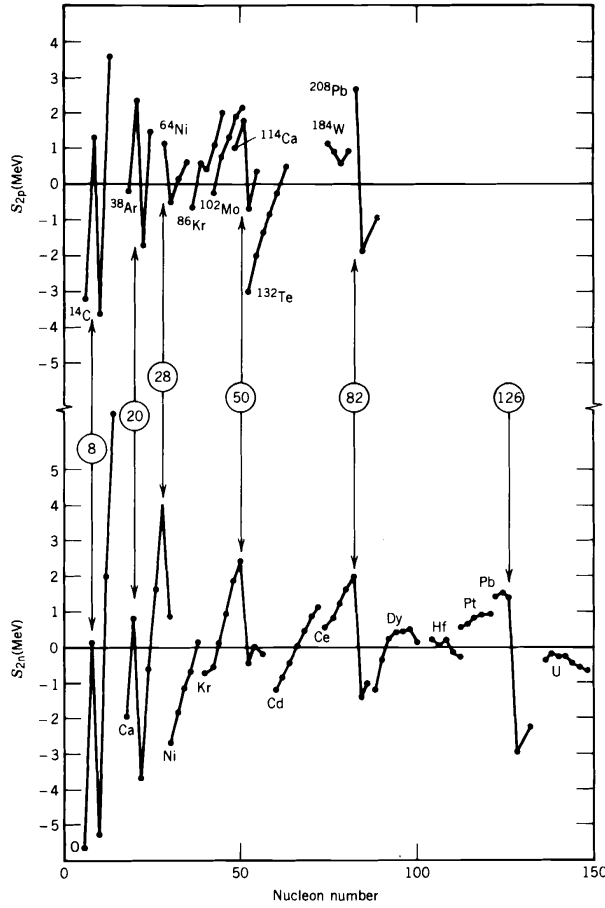


Figure 2.1:

Two-proton separation energies for isotonic series (top) and two-neutron separation energies for isotopic series (bottom). The sharp discontinuities corresponding to the filling of major shells are clearly visible. The figure is adapted from Ref. [Kra88], with the data originally from Ref. [Wap77].

In the nuclear shell model, the particles are assumed to be moving inside an average spherical potential created by the nucleons themselves and their mutual interaction [Rin80]. The potential adopted to represent the nuclear mean field can be based upon a particular geometric model, such as a harmonic oscillator, or can be derived self consistently from an effective interaction. Whatever potential is chosen needs to be able to reproduce all the nucleon shells from the three dimensional solution of the Schrödinger equation. Approximations from harmonic oscillator or infinite well potentials can only reproduce experimental observations for low magic numbers, with major discrepancies at high energy levels. Also, the choice of any of the above mentioned potentials implies an infinite separation energy for the nucle-

ons, which is unphysical. The Woods-Saxon potential [Woo54] with an additional spin-orbit term as proposed by Haxel [Hax49] and Mayer [May50a, May50b] gives a good approximation of the spherical nuclear potential. The spin-orbit term that arises from the coupling of the nucleon orbital angular momentum \vec{l} and its intrinsic spin \vec{s} , results in the splitting of each of the l levels into two levels with $j = l + s$ and $j = l - s$, each with degeneracy of $2j + 1$. The spin-orbit term also lowers the energies of each of the $j = l + s$ orbits sufficiently so that, at least in the higher shells, it is brought down amongst the levels of the next lower shell. It is this feature that correctly reproduces an energy level spectrum having gaps at the seven known magic numbers. The shell model explains well the features of nuclei in the vicinity of closed shells, but fails for nuclei far from magic numbers.

2.1.2 Nuclear deformation

Nuclei in the regions far from filled neutron and proton shells are known to have substantial distortions from spherical shape as a result of large numbers of nucleons occupying the partially filled shells. The shapes of these deformed nuclei can generally be described in terms of their radius being an expansion in terms of the spherical harmonics, $Y_{\lambda\mu}(\theta, \phi)$

$$R(\theta, \phi) = R_{av}[1 + \alpha_{00} + \sum_{\lambda=1}^{\infty} \sum_{\mu=-\lambda}^{\lambda} \alpha_{\lambda\mu} Y_{\lambda\mu}(\theta, \phi)], \quad (2.1)$$

where $\alpha_{\lambda\mu}$ are the expansion coefficients, R_{av} represents the radius of a spherical nucleus with the same volume, and θ and ϕ are angular coordinates of a point on the nuclear surface. The two quantities $\lambda = 0, 1, 2, \dots, \infty$ and $\mu = -\lambda, \dots, +\lambda$ define the deformation shape. The α_{00} term corresponds to changes in the nuclear volume, while $\lambda=1$ terms describe a translation of the centre-of-mass of the nucleus. Due to incompressibility of the nucleus, the volume of the nucleus must be constant, hence $\alpha_{00} = 0$, while the $\alpha_{1\mu}$ terms can be omitted when describing the shape of a deformed nucleus. Most deformed nuclei are known to be dominated by permanent quadrupole deformation corresponding to $\lambda=2$ so that the radii for these nuclei can be written as

$$R(\theta, \phi) = R_{av} [1 + \sum_{\mu} \alpha_{2\mu} Y_{2\mu}(\theta, \phi)]. \quad (2.2)$$

The five possible deformation parameters $\alpha_{2\mu}$ can be reduced to just α_{20} and α_{22} by taking $\alpha_{2-2}=\alpha_{22}$ and $\alpha_{2-1} = \alpha_{21}=0$ [Rin80]. It is therefore convenient, to represent the two deformation parameters α_{20} and α_{22} in terms of two new shape parameters (β_2, γ) using

$$\alpha_{20} = \beta_2 \cos \gamma, \quad (2.3)$$

$$\alpha_{22} = \frac{1}{\sqrt{2}} \beta_2 \sin \gamma, \quad (2.4)$$

where β_2 corresponds to the magnitude of the nuclear quadrupole deformation, while γ corresponds to the degree of axial asymmetry. The parameter γ ranges from 0° to 360° , with γ -values equivalent to the multiples of 60° representing the axially symmetric nuclei (prolate or oblate), while γ between these values denotes triaxial shapes. Prolate deformed nuclei are characterised by $\gamma = 0^\circ, 120^\circ$ and 240° , while $\gamma = 60^\circ, 180^\circ$ and 300° correspond to oblate deformation [Eji89, Rin80]. The full range of shapes are described by the $\gamma = 0^\circ$ to 60° range. Other regions are rotations of these shapes with different choices of symmetry axis.

Other deformation parameters related to β_2 are often encountered, these include the ε, δ or $\varepsilon_2/\varepsilon_4$ parameters used in various forms of the Nilsson model, see section 2.1.3.

2.1.3 Nilsson model/deformed shell model

Independent motion of nucleons still occurs in the deformed system. The model based description of single-particle motion in deformed nuclei first requires the choice of an appropriate deformed potential and an effective interaction. The first successful shell model calculations for a deformed nucleus were performed by Nilsson [Nil55]. He assumed the nuclear potential was a deformed (spheroidal) harmonic oscillator defined by [Nil69]

$$V_{osc} = \frac{M}{2} [\omega_{\perp}^2 (x^2 + y^2) + \omega_z^2 z^2], \quad (2.5)$$

where ω_{\perp} and ω_z are oscillator frequencies, with $\omega_{\perp} = \omega_x = \omega_y \neq \omega_z$. In the case of an axially symmetric potential, it is convenient to introduce the deformation parameter ε_2 [Nil69, Nil95], related to the oscillator frequencies by

$$\omega_z = \omega_o(\varepsilon_2)(1 - \frac{2}{3}\varepsilon_2), \quad (2.6)$$

$$\omega_{\perp} = \omega_o(\varepsilon_2)(1 + \frac{1}{3}\varepsilon_2). \quad (2.7)$$

The deformation parameter is defined such that $\varepsilon_2 > 0$ corresponds to prolate shape and $\varepsilon_2 < 0$ to oblate deformation, and its magnitude is related to the coordinate β referred to above via $\varepsilon_2 \simeq 0.95\beta_2$ [Nil55]. In order to obtain good agreement with experimental observations, Nilsson added two terms $C\hat{l} \cdot \hat{s}$ and $D(\hat{l}^2 - \langle \hat{l}^2 \rangle_N)$ to the potential, leading to the following single-particle Hamiltonian for axially symmetric nuclei

$$\hat{H}_{sp} = -\frac{\hbar^2}{2m} \Delta + \frac{m}{2} (\omega_x^2 + \omega_y^2 + \omega_z^2) - C\hat{l} \cdot \hat{s} - D(\hat{l}^2 - \langle \hat{l}^2 \rangle_N). \quad (2.8)$$

Two constants, κ and μ , together with $\hbar\omega_0$, define the values of $C = -2\hbar\omega_0\kappa$ and $D = -\hbar\omega_0\kappa\mu$. The C term is the familiar spin-orbit force similar to the spherical shell model, while the D term shifts the levels with high l -values downwards so as to partially mimic the effect of a finite depth potential. For large deformations, the $\hat{l} \cdot \hat{s}$ and \hat{l}^2 terms can be neglected and the quantum numbers, N , n_z , Λ , Σ of the anisotropic harmonic oscillator are well defined and can be used to characterise the single-particle states in deformed nuclei [Rin80]. Each of these so-called ‘‘Nilsson’’ states are labelled by $[Nn_z\Lambda\Sigma]$ or equivalently, $\Omega^\pi[Nn_z\Lambda]$. Figure 2.2 shows the relationship between some of these quantum numbers. The $\Omega = \Lambda + \Sigma$ denotes the projection of the single-particle angular momentum (j) along the Z' axis; by convention this is the symmetry axis for axially symmetric nuclei. Λ and Σ are the projections of the orbital angular momentum \hat{l} and the intrinsic spin \hat{s} , respectively,

along the symmetry axis (note that $\Sigma = \pm 1/2$). N is the principle quantum number that denotes the major shell, with n_z being the number of nodes in the wavefunction along the Z' axis. The quantum number π denotes the parity of each level, and is given by $(-1)^l$.

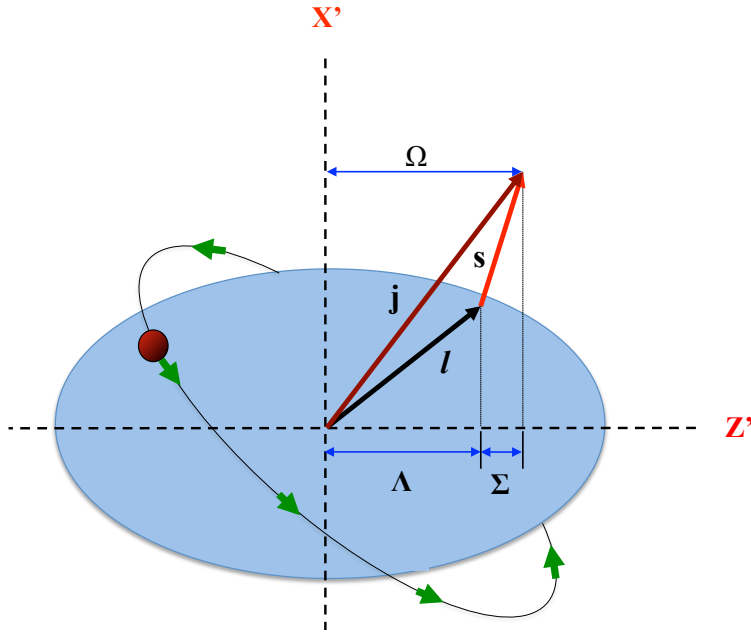


Figure 2.2: Quantum numbers for motion of a single nucleon within an axially deformed potential with symmetry axis Z' .

Figure 2.3 and 2.4 illustrate the deformed single-particle energies plotted as a function of the deformation parameter ε_2 for protons and neutrons, respectively. In each of these Nilsson diagrams, the levels are labelled by $\Omega^\pi[Nn_z\Lambda]$ as described above. It can be noticed that the single-particle levels that are determined by the angular momentum j in the spherical shell model at zero deformation, split into $(2j+1)/2$ states with eigenvalues $\pm\Omega$, in deformed nuclei. Due to reflection symmetry in the deformed nucleus, levels with $+\Omega$ and $-\Omega$ will have the same energy, giving the levels a maximum occupancy (degeneracy) of 2. Another important feature of Nilsson states is that with increasing values of ε , the levels can change their slopes. This is due to interactions between any two levels with the same Ω and π values so that, as a rule, the two orbitals never cross, but rather repel each other. See, for example, the $5/2^+[402]$ and $5/2^+[642]$ orbitals at $\varepsilon \sim 0.4$ in Fig. 2.3.

In the vicinity of the crossing, the experimental levels are a mixture of the two component wavefunctions.

For most configurations in the region around mass-180, the equilibrium deformed shapes possess axially symmetry, which enables the Nilsson model to be effective for investigation of the nuclear structure in this region.

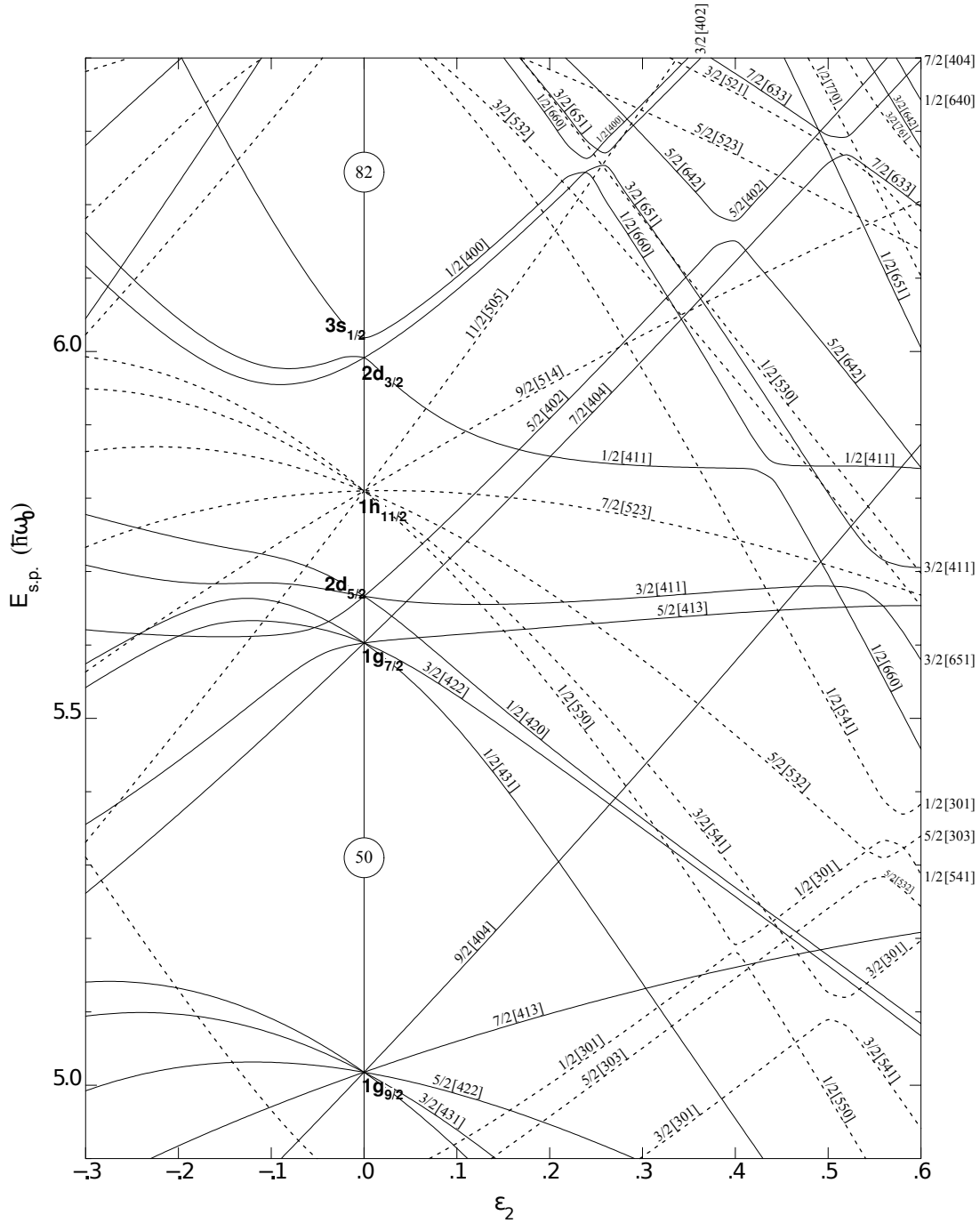


Figure 2.3: Nilsson diagram for proton numbers $50 \leq Z \leq 82$. The solid lines correspond to orbitals with positive parity, with dashed lines indicating negative parity. Figure taken from Ref. [Fir99].

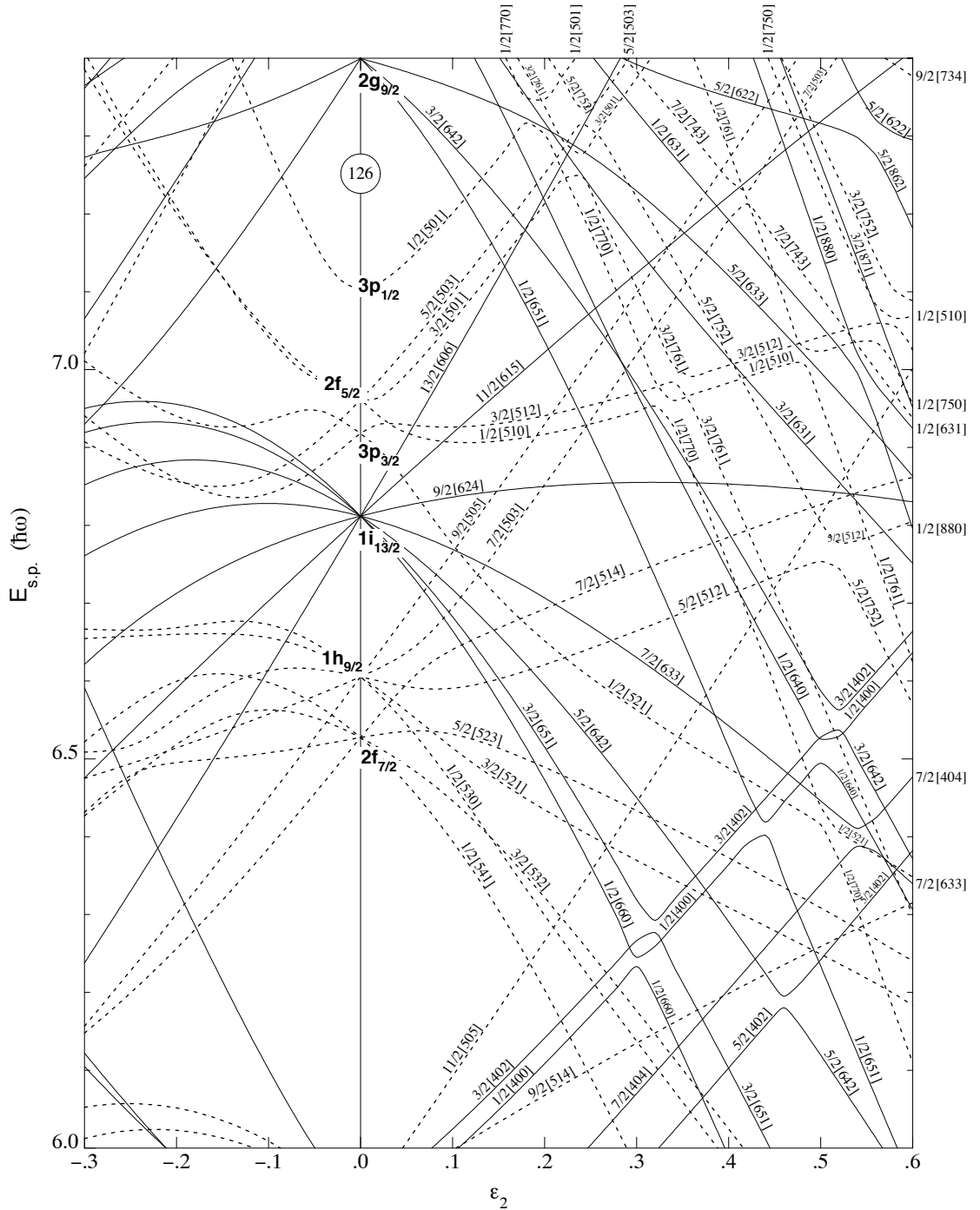


Figure 2.4: Nilsson diagram for neutron numbers $82 \leq N \leq 126$. The solid lines correspond to orbitals with positive parity, with dashed lines indicating negative parity. Figure taken from Ref. [Fir99].

2.1.4 Pairing correlations

The pairing force is another important interaction that affects the structure in all nuclei. The pairing interaction is a short range force that favours the anti-parallel coupling of two particles in the same j state, to form a $J^\pi = 0^+$ state. The existence of the pairing interaction has been linked to numerous experimental observations such as the fact that all even-even nuclei have a $J^\pi = 0^+$ ground state, there is an energy gap between the nuclear ground state and the multi-quasiparticle states in even-even nuclei (pair-gap), and the disappearance of this gap in odd- A or odd-odd nuclei. The tendency of even-even nuclei to have greater binding energy than their neighbouring odd-even nuclei is also linked to nuclear pairing. Furthermore, the fact that the nuclear moments of inertia are reduced compared to the rigid-body estimate is also a consequence of pairing interactions [Cas00, Fén02].

The pairing interaction scatters pairs of particles to nearby orbitals, keeping them coupled in a time-reversed pair. In the absence of pairing, the lowest energy state will have all the nucleon orbitals filled up to the so-called Fermi energy, with all higher levels being empty. This particle-pair scattering has the effect of smearing out the level occupancy such that a sharply defined Fermi surface is no longer applicable. Moreover, the presence of a single particle in a given orbit blocks the scattering of pairs into it and prevents these levels from participating in the scattering process; this is referred to as "pair blocking" [Sol61].

The pairing correlation has to be taken into account in order to make meaningful comparisons to experimental observations. In the theoretical treatment of pairing correlations in, for example, a neutron-neutron or proton-proton paired system, the total Hamiltonian can be expressed in terms of the single particle term \hat{H}_{sp} and the pairing interaction term, \hat{H}_{pair} [Zen83, Bur96]

$$\hat{H} = \hat{H}_{sp} + \hat{H}_{pair} = \sum_{i>0} \epsilon_i (a_i^\dagger a_i + a_{\bar{i}}^\dagger a_{\bar{i}}) - \sum_{i,x>0} G_{xi} a_x^\dagger a_{\bar{x}}^\dagger a_{\bar{i}} a_i, \quad (2.9)$$

where ϵ_i are the single-particle energies, the index \bar{i} denotes the time-reversed

state of i , with i representing all the quantum numbers that specify a given single-particle orbital (e.g. $\Omega^\pi[Nn_z\Lambda]$ in Nilsson states). a_i^\dagger and a_i are the pair creation and annihilation operators, respectively, while G is the average strength of the nuclear pairing interaction.

Following the approximations by Bohr, Mottelson, and Pines [Boh58] that the observed effects of nucleon pairing are similar to those of electron pairing in superconductors, the Bardeen-Cooper-Schrieffer (BCS) theory of superconductivity [Bar57] was first applied by Belyaev [Bel59] to investigate the effect of pairing correlations on various properties of nuclei. Within the BCS approach, the ground state of an even-even nucleus can be represented by the BCS wavefunction [Rin80]

$$|BCS\rangle \equiv \prod_{i>0} (u_i + v_i a_i^\dagger a_i^\dagger) |0\rangle, \quad (2.10)$$

where the parameters u_i and v_i have to satisfy the normalization condition $u_i^2 + v_i^2 = 1$. These parameters are determined by variation (minimisation) of the energy, with the restriction that the expectation value of the particle number operator \hat{N} is equal to the actual particle number, N . When dealing with the nuclear system, one major drawback with the above assumption is that the BCS wavefunction does not conserve the number of particles under investigation, hence errors in deducing quantities such as excitation energies and the pairing gap inevitably occur. One possible way of addressing this problem is to modify the original Hamiltonian in equation 2.9 by introducing a Lagrange multiplier λ and the particle (nucleon) number operator \hat{N} to obtain a new form for the BCS Hamiltonian

$$H' \equiv \hat{H} - \lambda \hat{N} = \sum_{i>0} (\epsilon_i - \lambda)(a_i^\dagger a_i + a_i^\dagger a_i^\dagger) - \sum_{i,x>0} G_{xi} a_x^\dagger a_x^\dagger a_i a_i. \quad (2.11)$$

Using the Lagrange multiplier variational method, the BCS ground state can be evaluated from the minimization of the expectation value of equation 2.11, thus giving the occupation (v_i) and non-occupation (u_i) probabilities as

$$v_i^2 = \frac{1}{2} \left\{ 1 - \frac{\epsilon_i - \lambda}{\sqrt{(\epsilon_i - \lambda)^2 + \Delta^2}} \right\}, \quad (2.12)$$

$$u_i^2 = \frac{1}{2} \left\{ 1 + \frac{\epsilon_i - \lambda}{\sqrt{(\epsilon_i - \lambda)^2 + \Delta^2}} \right\}, \quad (2.13)$$

where λ denotes the Fermi energy that lies in the region between the previously occupied and unoccupied energy levels. Δ is the pair gap energy related to the pairing strength G and the occupation probabilities through

$$\Delta = G \sum_{i \neq i_j} u_i v_i, \quad (2.14)$$

with i_j referring to singly occupied (blocked) orbitals. Values of G are different for neutrons and protons and tend to decrease with mass. They can be estimated by

$$G_p = \frac{17}{A} \text{ (MeV)}, \quad G_n = \frac{23}{A} \text{ (MeV)} \quad (2.15)$$

for proton and neutron pairs, respectively [Cas00]. The lower values of G_p are due to Coulomb repulsion. The value of Δ is typically given by ($\Delta \approx 12/A^{1/2}$) [Sie87]. With the BCS treatment of nuclear pairing, the excitation energy ϵ_i of a single-particle (Nilsson-like) state is now replaced by the energy of quasi-particle given by

$$E_{qp} = \sqrt{(\epsilon_i - \lambda)^2 + \Delta^2}. \quad (2.16)$$

The BCS approach to the nuclear system initially turned out to be insufficient to accurately describe the influence of pairing correlations on nuclear properties. It was found to be satisfactory only if the interaction is very strong, or the number of particles is very large. To account for limitations in the BCS theory, an extension to this method for the treatment of pairing in nuclei was first suggested by Lipkin [Lip60], and later developed by Nogami [Nog64, Nog65, Pra73]. This model, known as the Lipkin-Nogami (LN) technique, suggested the use of a modified Hamiltonian of the form $H - \lambda \hat{N} - \lambda_2 \hat{N}^2$, rather than the conventional $\hat{H} - \hat{N}\lambda$, to account for the nucleon number fluctuations. \hat{H} is the original pairing Hamiltonian, \hat{N} denotes the nucleon number operator, while λ_i are both Lagrange multipliers. The LN pairing model has been used for multi-quasiparticle calculations for nuclei

around the mass-180 region [Kon96, Dra98a, Dra10, Hug12] and a similar approach is used in the present work (see Chapter 6).

An excited state can be comprised of several nucleons from broken pairs, coupled together giving a higher angular momentum. These so-called multi-quasiparticle (MQP) states have, to a first-approximation, a energy E_{mqp} equivalent to the sum of the energies of each of the single-quasiparticles involved, that is

$$E_{mqp} = \sum_i^n (E_{qp})_i \quad (2.17)$$

where $i=1,\dots,n$ are the single-particle states occupied by unpaired nucleons [Jai95].

The process of performing pairing (BCS or Lipkin Nogami) calculations when evaluating MQP energies from equation 2.17, involves evaluation of Δ for each nucleon arrangement, simplified by ignoring states that are far away from the Fermi surface.

Other than blocking, the pairing correlations are also sensitive to nuclear rotations [Mot60], especially at very large rotational frequencies where Coriolis forces start to dominate and reduce the gap parameter Δ , see section 2.7.

2.1.5 Residual interactions

Just like the nucleon pairing forces, the residual interactions between the unpaired nucleons significantly affect the excitation energies of the multi-quasiparticle states. Jain *et al.* [Jai94, Jai95] have shown that residual interactions play a significant role in determining the energetically favoured angular momentum (K) coupling of a given multi-quasiparticle configuration.

Generally, multi-quasiparticle states are generated by breaking nucleon pairs and exciting the unpaired particles above the energy gap. Each n -quasiparticle configuration gives rise to a multiplet of 2^{n-1} states that split in energy due to the residual interactions. For a state with n -quasiparticles, the residual interactions

can be taken as the sum of all possible two-body interactions from each two-quasiparticle coupling that make up the multi-quasiparticle state. Note that the Gallagher-Moszkowski (GM) [Gal58] rules serves as a guide for parallel and anti-parallel coupling for any two-quasiparticle configuration. This is such that for $\pi - \pi$ or $\nu - \nu$ couplings, anti-parallel coupling is energetically favoured while for $\pi - \nu$ couplings, parallel coupling is favourable, where π and ν denote protons and neutrons, respectively. From Jain *et al.* [Jai94, Jai95], the residual interaction for a n -quasiparticle state is given by

$$E_{res} = \sum_{i_1 \neq i_2} [E_{i_1 i_2}^{(GM)} (\frac{1}{2} - \delta_{\sum_{i_1 i_2}, 0}) - \delta_{K_{i_1 i_2}, 0} E_{i_1 i_2}^{(N)} \Pi_{i_1 i_2}], \quad (2.18)$$

where $E_{i_1 i_2}^{(GM)}$ is the Gallagher-Moszkowski (GM) [Gal58] splitting energy between parallel and anti-parallel coupling of two-quasiparticle states, $E_{i_1 i_2}^{(N)}$ is the odd-even Newby shift [New62], $\sum_{i_1 i_2}$ is the intrinsic-spin projection on the symmetry axis and $\Pi_{i_1 i_2}$ is the parity. The splitting energy $E^{(GM)}$ can be derived from experimental data, for example see Ref. [Jai95] for the $E^{(GM)}$ values for various proton-proton, neutron-neutron and proton-neutron configurations. For any two-quasiparticle combination, the signs of the $\pi\pi$ or $\nu\nu$ interactions are opposite to those of $\pi\nu$ interactions [Jai94], implying that the total residual interaction for a given configuration can take positive or negative values.

Hence the excitation energy of each member of a multiplet can be considered to be the sum of the excitation energies of odd-nucleons, E_{part} , with the energy due to pairing incorporated, plus a residual interaction term, E_{res} . That is

$$E_{mfp} = \sum_i^n (E_{qp})_i + E_{res}. \quad (2.19)$$

2.2 Nuclear decay modes

There are several mechanisms by which an excited/unstable nucleus can emit excess energy in the form of radiation, for example α , β^+ , β^- or γ -ray emission, internal conversion and electron capture. Two decay mechanisms relevant to the current

work, γ -ray emission and internal conversion, are discussed below.

2.2.1 Gamma decay

An excited nucleus can lose energy by emitting a γ -ray photon with an energy E_γ that is equivalent to the energy difference between the initial and final nuclear states. Gamma-ray energies cover a wide range from kilo-electronvolts (keV) up to tens of MeV. The electromagnetic radiation emitted from γ -decays can be characterised into electric (E) and magnetic (M) transitions. The E and M transitions are the result of a change in the charge distribution and current densities, respectively. In addition to energy, the γ -ray photons also carry angular momentum (L) with integer values greater than zero. If I_i and I_f are the angular momenta of the initial and final states, respectively, the decay can only proceed if the angular momentum of the emitted photon falls within the limit [Lil01]

$$|I_i - I_f| \leq L \leq I_i + I_f. \quad (2.20)$$

Both the electric and magnetic γ -ray transitions can be classified by their multipolarity, which is dependent on the orbital angular momentum L carried by the photon. For $L=0, 1, 2, 3$, the transitions show monopole, dipole, quadrupole and octupole character respectively. Since the intrinsic spin of the γ rays is $1\hbar$, $L = 0$ photons cannot occur and hence transitions between two spin-zero states are forbidden to proceed via γ -emission (see 2.20). Instead, they decay by internal conversion or, if the transition energy is above 1.022 MeV, internal pair formation (see section 2.2.2). The parity π of electric and magnetic transitions of multipole order L are given by,

$$\pi(EL) = (-1)^L, \quad (2.21)$$

$$\pi(ML) = (-1)^{L+1}, \quad (2.22)$$

respectively. It is possible for γ -ray transitions to be a mixture of two multipolarity transitions characterised by a mixing ratio δ . Since these two competing transitions need to conserve parity, this will require one transition to be electric and the other

to be magnetic, for example an $M1 + E2$ or $E1 + M2$ mixture. The gamma-ray transition rates will be discussed later in section 2.5.

2.2.2 Internal conversion and internal pair formation

Internal conversion is a result of the overlap of the electron and nuclear wavefunctions, giving rise to an electromagnetic interaction of the nucleons and the orbiting atomic electron. In this process, the transition energy (E_γ) is transferred directly to a bound atomic electron (without prior emission of a photon), that is then ejected from the atom with an energy (E_{el}) given by

$$E_{el} = E_\gamma - B_{el}, \quad (2.23)$$

where B_{el} denotes the binding energy of the electron in the atom. Internal conversion is usually accompanied by emission of characteristic X-rays that are produced when electrons from the outer shells fill the vacancy left by the emitted electron.¹ The relative intensity between γ -ray decay and internal conversion processes is quantified by the internal conversion coefficient α_i , defined as the intensity ratio between the intensity of conversion electrons (I_{ie}) and emitted γ rays I_γ [Pau75, Lil01];

$$\alpha_i = \frac{I_{ie}}{I_\gamma}, \quad (2.24)$$

where i represents conversion in a major electron shell, e.g. $i = K, L, M, \dots$. The total internal conversion coefficient α_T is the sum of the individual coefficients for each atomic shell, hence $\alpha_T = \alpha_K + \alpha_L + \alpha_M + \dots$. In the present work we only deal with total conversion coefficients inferred from intensity balances (see Sect 3.5.1).

The rate of internal conversion depends on the transition energy, multipolarity of the transition and the proton number (Z). It tends to dominate over γ -ray emission for transitions of lower energy ($E_\gamma \leq 200$ keV) and/or high angular

¹Auger electrons can be an alternative to X-ray emission. In this case, the energy of the de-exciting electron, rather than being emitted as X-rays, is transferred to less bound electrons that are ejected from the atom.

momentum transitions ($L \geq 2$), giving rise to a rapid increase in α_T values with decreasing transition energy and increasing multipolarity. Also, the electron conversion is generally higher for magnetic transitions than for electric transitions. The strong dependence on multipolarity means that experimental measurements of the conversion coefficient can be used to assign multipolarities (see Sect 3.5.1).

When the transition energy is > 1.022 MeV, it is possible for spontaneous emission of e^-/e^+ pairs to take away the transition energy. This is not a significant process in the present work since few high-energy γ rays were observed experimentally.

2.3 Collective nuclear motion

Earlier chapters described single-particle motion in spherical and deformed systems. However, nuclear excitation can also arise from collective motion such as rotation and vibration. This section describe these two collective motions and their contribution/effects to the observed spectra in deformed nuclei.

2.3.1 Nuclear vibrations

It is well known from both the shell model and the Nilsson model that nucleons exist and move inside a static average field/potential generated collectively by all the particles. Such a system of particles can also perform collective oscillations that resemble the degrees of freedom possessed by the matter in bulk. Therefore, the collective oscillations associated with the nucleus are best understood as the surface vibration of this potential. Such collective vibrational motion is known to be present in both spherical and deformed nuclei.

Different modes of nuclear vibrations are characterised by their multipole order (λ) when describing the nuclear shape as an expansion of the radius in terms of spherical harmonics like in equation 2.2, with coefficients $\alpha\lambda$.

The monopole vibrational mode ($\lambda = 0$) requires the expansion and the contraction

of the nucleus as a whole. However, due to incompressibility of the nucleus, this mode is essentially forbidden as it would occur only at very high energy. A dipole ($\lambda=1$) vibrational mode corresponds to the net displacement of the whole system instead of deformation of the nucleus. Such vibrations result from external rather than internal nuclear forces and cannot contribute to nuclear excitations [Gre96]. Hence, the $\lambda=2$ (quadrupole) vibration is the lowest mode of nuclear vibrations and is of great importance to nuclear spectroscopy.

Quadrupole vibrations are common in the $A=180$ region and are known to occur at much lower energy than monopole and dipole vibrations. The nuclear vibrational energies are quantized and a unit/quantum of such vibrational energy is referred to as a phonon, with the parity of each phonon given by $(-1)^\lambda$. A quadrupole phonon carries 2 units of angular momentum, $\lambda = 2$.

In quadrupole deformed nuclei, there are two types of normal vibrations associated with the $\lambda = 2$ vibrational mode. These are β vibrations in which the oscillations are directed along the symmetry axis, thus the nucleus preserves its axial symmetry, and γ vibrations that correspond to deviations from axial symmetry [Cas00]. Other higher multipole oscillations such as octupole ($\lambda=3$) and hexadecapole ($\lambda=4$) can occur in the nucleus. These vibrations can couple to both particle excitation and collective rotational motion (in deformed nuclei) to give the total angular momentum of the nucleus. Since prolate deformed nuclei are prevalent in the mass-180 region, quadrupole vibrations are expected in the tantalum isotopes. For example, a γ -vibrational state has been observed in ^{183}Ta [Shi09].

2.3.2 Nuclear rotation

Unlike vibrational motion, this mode of excitation can only be observed in deformed nuclei. Deformed nuclei can undergo collective rotation to generate high angular momentum excited states. Collective rotational motion is much slower than the internal motion of the individual nucleons inside the deformed nuclear potential. Hence, rotations preserve the shape and internal structure of the nucleus and each

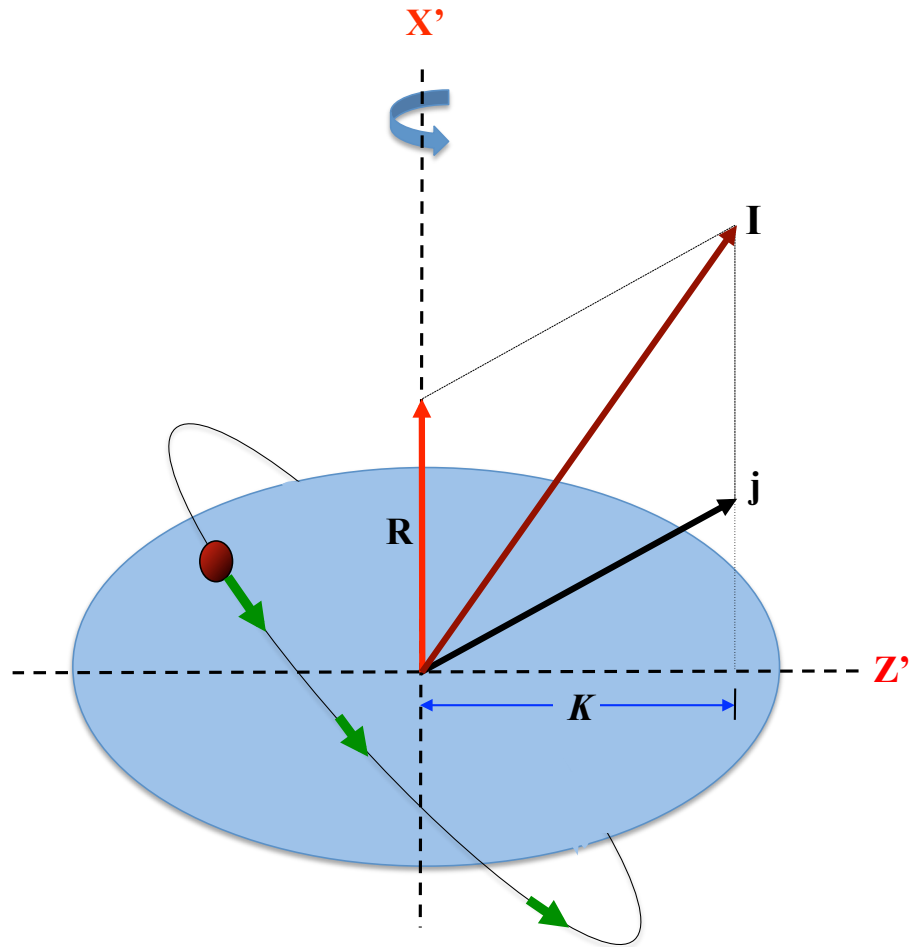


Figure 2.5: Coupling of the single-particle angular momentum j to the collective angular momentum R in axially symmetric nuclei. The rotational axis X' is perpendicular to the symmetry axis Z' . The projection of j along the symmetry axis is denoted by $K=\Omega$.

distinct arrangement of the constituent nucleons can separately undergo rotation.

The elementary understanding of collective excitations is often achieved from macroscopic models. A general frame-work for the description of rotational states in nuclei was introduced by Bohr and Mottelson [Boh75]. For axially symmetric deformed nuclei, rotation can only take place about an axis perpendicular to the symmetry axis (X') as shown in Figure 2.5.

The wavefunction that describes a rotating nucleus can be described by two components, one that describes the independent motion of individual particles in the deformed potential and another that corresponds to the collective rotational or vibra-

tional motion of the entire nucleus [Cas00]. Similarly, the total angular momentum I of the nucleus results from the coupling of the collective angular momentum R of the nuclear core to the single-particle angular momentum j such that $\bar{R} = \bar{I} - \bar{j}$. The nuclear core is built from all the paired nucleons. The total Hamiltonian of the rotating nuclear system can therefore be approximated by

$$\hat{H} = \hat{H}_p + \hat{H}_{rot}, \quad (2.25)$$

where \hat{H}_p is the single-particle Hamiltonian in the absence of rotation and \hat{H}_{rot} is the rotational Hamiltonian. It is possible to then define the moment of inertia \mathfrak{J} for collective rotation such that

$$\hat{H}_{rot} = \frac{\hbar^2}{2\mathfrak{J}}\bar{R}^2 = \frac{\hbar^2}{2\mathfrak{J}}(\bar{I} - \bar{j})^2 = \frac{\hbar^2}{2\mathfrak{J}}[\bar{I}^2 + \bar{j}^2 - 2\bar{I} \cdot \bar{j}]. \quad (2.26)$$

By introducing the angular momentum lowering and raising operators

$$I_{\pm} = I_x \pm iI_y \quad \text{and} \quad j_{\pm} = j_x \pm ij_y, \quad (2.27)$$

the Hamiltonian in equation 2.26 can be expressed as

$$\hat{H}_{rot} = \frac{\hbar^2}{2\mathfrak{J}}[I^2 + j^2 - 2I_zj_z - (I_+j_- + I_-j_+)]. \quad (2.28)$$

The term $\frac{\hbar^2}{2\mathfrak{J}}(I_+j_- + I_-j_+) \equiv \hat{H}_{cor}$ describes the coupling between the motion of the particle in its deformed potential and the collective rotation. It reflects the effects of Coriolis and centrifugal forces acting on the particle in the rotating system. This term is negligible if the rotations are slow but increases with higher rotational frequency ω of the nucleus. For two intrinsic states with j projections Ω and $\Omega \pm 1$ (ie, that differ by $\Delta\Omega = 1$), the Coriolis term H_{cor} gives a non-zero matrix element of the form [Ste75]

$$\langle \Omega \pm 1 | \hat{H}_{cor} | \Omega \rangle = -\frac{\hbar^2}{2\mathfrak{J}}\sqrt{[(I \mp K)(I \pm K + 1)]}\langle \Omega \pm 1 | j_{\pm} | \Omega \rangle \quad (2.29)$$

causing mixing between any states that differ by $\Delta\Omega = 1$. Due to the symmetry

of the total wavefunction of an axially symmetry nucleus against reflection about the axis X' , the wavefunction for an $\Omega = 1/2$ state contains components with both signs of $\pm\Omega$ such that at $\Omega = -1/2$, the quantity $\Omega + 1$ is equal to $+1/2$. These two components therefore behave like two states with $\Delta\Omega = 1$, hence the Coriolis term H_{cor} gives a non-zero diagonal matrix element of the form

$$\langle \Omega_{1/2} | \hat{H}_{cor} | \Omega_{1/2} \rangle = \frac{\hbar^2}{2\Im} [a(-1)^{I+1/2}(I + 1/2)], \quad (2.30)$$

where $a = \sum_j (C_{jl}^{\Omega=1/2})^2 (-1)^{j-1/2}(j + 1/2)$ is the decoupling parameter that describes the degree to which j is coupled to the deformation axis, while $C_{jl}^{\Omega=1/2}$ are the configuration mixing coefficients used in defining the Nilsson energy level wavefunctions.²

The relative effect of the different terms in equations 2.25 and 2.28 depend on the physical situation; for example, the magnitude of the core deformation, the Nilsson orbits are involved in the particle-core angular momentum coupling, as well as the rotational frequency ω of the core. It is therefore useful to consider three limits in which each one of the terms becomes dominant and hence defines varied rotational level structures. By replacing the energy operators with their eigenvalues or expectation values, different expressions for the rotational energies are obtained.

In the case of strongly deformed nuclei with unpaired single-particles of low- j and high- Ω , $K = \sum \Omega$ and the single particles are considered to be strongly coupled to the rotation of the deformed core, see figure 2.6(a). The particle motion is considered to be following that of the rotating potential, with the intrinsic structure unperturbed, since Coriolis effects are negligible. From a quantum mechanical perspective, the value of R in equation 2.26 can then be expressed as $R^2 = [I(I + 1) - K^2]\hbar^2$ and the rotational energy levels are given by

$$E_{rot} = \frac{\hbar^2}{2\Im} [I(I + 1) - K^2]. \quad (2.31)$$

²The wavefunctions for the Nilsson states in Fig 2.3 and 2.4 can be described by a linear combination of the spherical wavefunctions, $|\psi_\Omega\rangle = \sum C_{jl}^\Omega |Njl\Omega\rangle$.

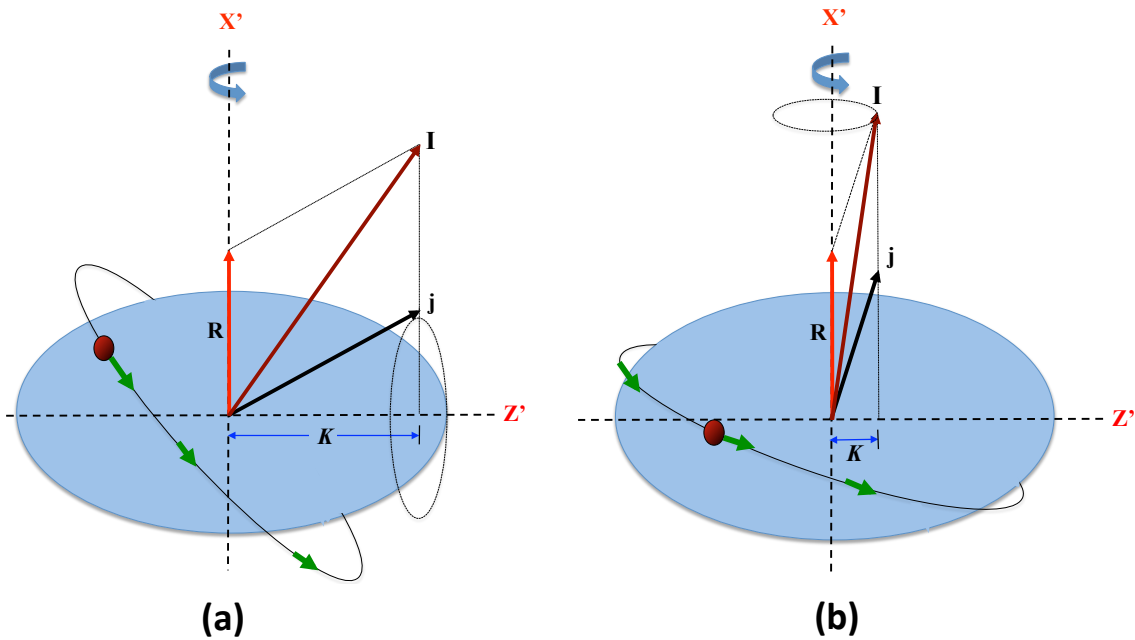


Figure 2.6: (a) Strong coupling of the single-particle angular momentum j to the nuclear deformation. (b) Weak-coupling/rotational alignment, where j is aligned along the axis of rotation of the core. Figure adapted from [Eji89].

The corresponding band has a spin sequence $I = K, K + 1, K + 2, K + 3, K + 4 \dots$, all states having the same parity as the bandhead that is characterised by the single particle structure. Note that a single-particle state with $\Omega = 1/2$ is a special case described below. With each state in the band having the same parity, $M1$ and $E2$ decays occur between the rotational states.

For a rotating even-even nucleus in its ground state, where $I^\pi = 0^+$ and $K = 0$, the corresponding ground-state band has states with energy spacing given by equation 2.31, where $K = 0$ and hence $R^2 = I(I + 1)$. The spins and parities take the following sequence

$$I^\pi = 0^+, 2^+, 4^+, 6^+, 8^+ \dots \quad (2.32)$$

The restriction to even values of I is due to the symmetry of the nucleus that requires the associated wavefunctions to be invariant under a rotation of 180° about an axis perpendicular to the symmetry axis [Sie55, Eji89].

For orbitals with $\Omega = 1/2$, the effects of rotational motion (Coriolis forces) on the

nuclear structure is significantly large, even at lower rotational frequencies [Ste75] due to the diagonal term in equation 2.30. Coriolis forces tend to align the single-particle angular momentum vector j along the axis of rotation, see Figure 2.6(b). So, for an odd- A nucleus, with $\Omega = 1/2$, the single-particle spin is said to be decoupled or weakly coupled to the deformed core. The rotational states due to this weakly coupled motion have energy spacing given by [Boh75]

$$E_{rot} = \frac{\hbar^2}{2\Im}[I(I+1) + a(-1)^{I+1/2}(I+1/2)], \quad (2.33)$$

where a is the decoupling parameter defined in 2.30.

In the case of a weakly deformed nucleus, the motion of the single particles, particularly those with high- j and low- Ω , is highly affected by the Coriolis force [Rin80]. In such cases, the Coriolis force favours the alignment of j with that of the rotating core and the nucleon becomes totally decoupled from the rotating core, see figure 2.6(b). These particles are said to be *rotation-aligned*. The rotational bands built on such rotation-aligned orbits have spin sequences given by $I = j, j+2, j+4, \dots$ and the rotational energies are given by

$$E_{rot} = \frac{\hbar^2}{2\Im}(I - j_x)(I - j_x + 1). \quad (2.34)$$

The other spin sequence does exist but occurs at higher energy and may not be observed. Generally, one can note that at low rotational frequencies, the largest Coriolis effects occur in high- j and low- Ω orbitals, while there is less effect on lower- j and high- Ω orbits [Ste75].

2.4 Aligned angular momenta

For an odd- A rotating nucleus, or a nucleus with a broken pair or pairs, the component of the angular momentum of the unpaired quasi-particle(s) along the rotational

axis is known as the aligned angular momentum and is denoted by i_x (see Fig. 2.7). It can also be approximated as the difference between I_x , the component of the total angular momentum along the axis of rotation, and the rotational angular momentum R . That is

$$i_x = I_x - R. \quad (2.35)$$

The variation of i_x with increasing rotational frequency ω is often a good source of information regarding configuration assignments. For a given rotational band, the experimental rotational frequency at each of the intermediate spin values say $I = K + 1, K + 2, \dots$ can be extracted from the observed energy difference between the two neighbouring states with spins $I + 1$ and $I - 1$, and their projections I_x along the axis of rotation using the relation [Ben79, Ben86]

$$\omega = \frac{dE(I)}{dI_x(I)} \approx \frac{E(I+1) - E(I-1)}{I_x(I+1) - I_x(I-1)}, \quad (2.36)$$

where $E(I+1) - E(I-1)$ is the observed energy difference between the two adjacent members in a rotational band. I_x can be approximated using the Pythagoras theorem to obtain the expression

$$I_x(I) = \sqrt{(I + 1/2)^2 - K^2}, \quad (2.37)$$

where the projection K of the angular momentum on the symmetry axis can be obtained from the bandhead spin.

For a quasiparticle state, the aligned angular momentum i_x can be expressed as a function of rotational frequency ω using the relation

$$i_x = I_x(\omega) - I_{ref}(\omega), \quad (2.38)$$

where $I_{ref}(\omega)$ is the angular momentum of the collective core described by the Harris parameterisation of the effective moment of inertia of the core, $I_{ref} = (\mathfrak{J}^{(0)} + \omega^2 \mathfrak{J}^{(1)})\omega$ [Har65, Ben79]. In the case of states comprised of two or more quasiparticles, the aligned angular momentum of the band is the sum of the alignments of each of the one-quasiparticle constituents, implying the additivity of i_x [Fra81]. Significant values of aligned angular momentum are common in high- j

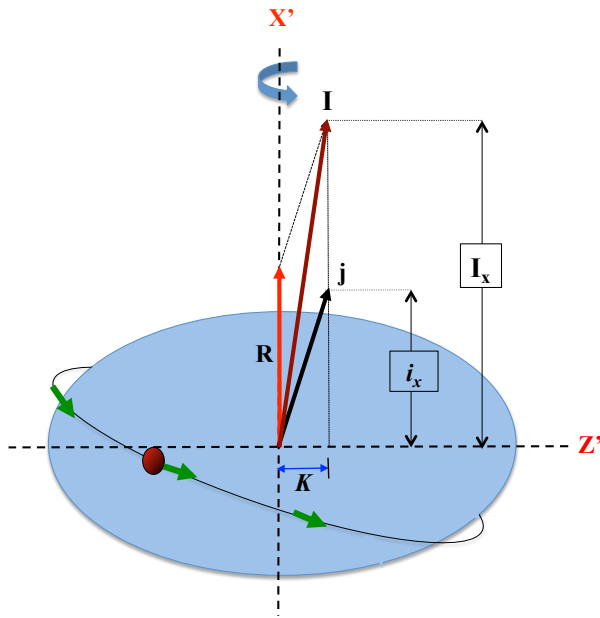


Figure 2.7: The aligned angular momentum of the total single-particle angular momentum j is a result of the Coriolis force acting on the single particles.

cases such as for the $i_{13/2}$ neutron and $h_{9/2}$ proton orbitals in the $A = 180$ region that undergo Coriolis effects [Ste75]. As a result, the presence of one or more of these orbitals in a given configuration is often reflected in the measured alignments.

The procedure that is usually followed is that the aligned angular momentum i_x is plotted as a function of rotational frequency for each band. These curves are then compared to alignments of known bands in the neighbouring isotope/isotones to elucidate the particle configuration. For the current work, especially significant alignments are expected for those configurations containing $11/2^+[615]$ and $9/2^+[624]$ neutron orbitals from the $i_{13/2}$ spherical shell that are near the Fermi-surface in neutron-rich tantalum isotopes.

2.5 Transition strengths

Comparison of experimental γ -ray transition probabilities with theoretical predictions from nuclear models is another essential tool for the analysis of nuclear

structure. Generally, transition probabilities are different for collective and non-collective nuclear motion [Pau75]. Lifetimes of states within a rotational band are typically of the order of picoseconds and are usually faster than single-particle transitions. To make comparisons between transitions of different types, we define the reduced transition probabilities as described below.

The transition strengths for single-particle transitions can be characterised by the ‘reduced transition probability’, $B(XL : I_i \rightarrow I_f)$, given by [Wei51, Boh75]

$$B(XL : I_i \rightarrow I_f) = \frac{1}{2I_i} |\langle I_f | \mathcal{M}(L) | I_i \rangle|^2. \quad (2.39)$$

Here, \mathcal{M} is the electric/magnetic multipole operator. $B(XL : I_i \rightarrow I_f)$ values for single-particle and collective transitions can be estimated theoretically or deduced experimentally for a given multipole transition. Under the assumption that the transition is due to a single particle moving between orbitals, Weisskopf [Wei51] derived the following estimates of reduced transition probabilities for electric and magnetic transitions respectively, such that

$$B_W(EL : I_i \rightarrow I_f) = \frac{1}{4\pi} \left(\frac{3}{L+3}\right)^2 (1.2)^{2L} A^{2L/3} e^2 fm^2, \quad (2.40)$$

$$B_W(ML : I_i \rightarrow I_f) = \frac{10}{\pi} \left(\frac{3}{L+2}\right)^2 (1.2)^{2L-2} A^{(2L-2)/3} \mu_N^2 (fm)^{2L-2}. \quad (2.41)$$

The Weisskopf estimates for single-particle transitions for each multipolarity act as a useful unit with which γ -ray transition probabilities can be compared to one another, irrespective of transition energy, multipolarity or whether the transitions are in different nuclei.

Deduction of the experimental values of reduced transition probabilities $B(XL)$ for each depopulating γ -ray transition out of an excited state requires knowledge of the total transition probability of the level, $P(level)$, and the partial γ -ray probabilities $P_\gamma(XL)$. The total transition probability is the sum of transition probabilities over all depopulating transitions (whether electromagnetic or particle). Its experimental

value is deduced from the meanlife of the state

$$P(level) = \frac{1}{\tau_{level}}. \quad (2.42)$$

The partial γ -ray transition probabilities, $P_\gamma(XL)$, are obtained from the total transition probability by

$$P_\gamma(XL) = P(level) \frac{I_\gamma(XL)}{\sum_d I_d} \quad (2.43)$$

where $I_\gamma(XL)$ is the intensity of one of the depopulating γ -ray transitions and $\sum_d I_d$ is the sum of the intensities of all depopulating transitions including internal conversion. These expressions are valid for pure transitions only. For mixed transitions one needs to take the proportion of each multipolarity component using the mixing ratio and treat each one separately. Details can be found in Chapter 5 of Ref. [Pau75]. The reduced transition probabilities for depopulating γ -ray transitions from a single-particle state are therefore given by;

$$B(XL) = \frac{L[(2L+1)!!]^2 \hbar}{8\pi(L+1)} \left(\frac{\hbar c}{E_\gamma} \right)^{2L+1} P_\gamma(XL), \quad (2.44)$$

where $(2L+1)!! = 1 \times 3 \times 5 \times \dots \times (2L+1)$ and E_γ is the transition energy in MeV. Comparison between experimental values of reduced transition probabilities $B(XL)$ is often facilitated by defining hindrance factors, F , relative to the Weisskopf estimates

$$F = \frac{B_w(XL)}{B(XL)}. \quad (2.45)$$

The reciprocal value gives $B(XL)$ in Weisskopf units (W.u). Simplified numerical expressions to deduce $B_w(XL)$ and $B(XL)$ for different multipolarities can be found on pages 148-149 in Ref. [Pau75].

2.6 Properties of rotational bands

Information concerning the nature of the intrinsic and rotational states in a given rotational band can be determined from the electromagnetic decay properties. Measurable properties include the decay strengths, transition energies and multipolarities, as well as the intensity branching ratios between the $E2$ crossover transitions and the mixed $M1/E2$ cascade transitions (see Figure 2.8). This information can be used to deduce properties of the band such as its moment of inertia, quadrupole moment Q , gyromagnetic factor g and the particle configuration.

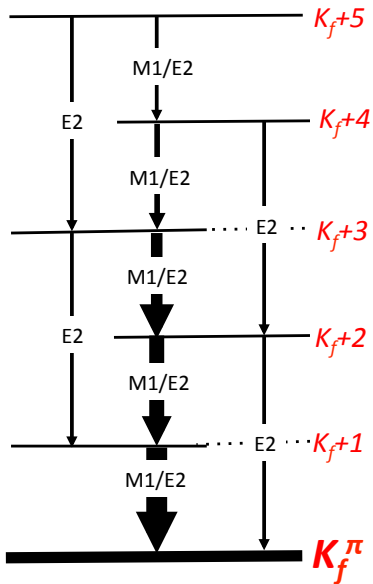


Figure 2.8: For a strongly-coupled band, the particle configuration is reflected in the competition between $E2$ and $M1/E2$ transition intensities.

The transition probabilities of collective transitions are often expressed in terms of collective parameters such as intrinsic quadrupole moments. For an axially symmetric quadrupole deformed nucleus, the reduced transition probability for any in-band $E2$ transition can be expressed as

$$B(E2; K, I_i \rightarrow K, I_f) = \frac{5}{16\pi} Q_0^2 \langle I_i K 20 | I_f K \rangle^2, \quad (2.46)$$

where Q_0 is the intrinsic quadrupole moment of the nucleus in units of eb and the Clebsch-Gordon coefficients describe the coupling between the angular momentum

of the photon and the initial and final state angular momenta. Changes of the $B(E2)$ values in a given band with increasing spin can be a reflection of changes in the internal structure.

The reduced transition probability for $M1$ transitions can be expressed in terms of the gyromagnetic-ratios g_K and g_R , where g_K denotes the g -factor associated with the intrinsic magnetic moment due to the particle configuration, while g_R is the g -factor for the magnetic moment generated by the collective rotation of the nucleus. For elements in the rare-earth region, $g_R \approx 0.35$ [Eji89]. The value of g_K may be calculated from a microscopic model of the particle motion, e.g. the Nilsson model.

For a rotational band with $K > 1/2$ or $K \neq 0$, the reduced transition probability, $B(M1)$, for the in-band $M1$ transition is given by;

$$B(M1; K, I \rightarrow K, I - 1) = \frac{3}{4\pi} (g_K - g_R)^2 \mu_N^2 K^2 \langle IK10 | I - 1K \rangle^2, \quad (2.47)$$

where $\mu_N = \frac{e\hbar}{2M_\pi}$ is the nuclear magneton. The magnetic dipole transition probabilities are sensitive to the single-particle motion.

Branching ratios and g -factors

Information concerning the configurations of the intrinsic states upon which bands are built can often be obtained from the γ -ray intensity branching ratio

$$\lambda_b = \frac{I_\gamma(\Delta I = 2)}{I_\gamma(\Delta I = 1)} \quad (2.48)$$

of the observed crossover $I \rightarrow I - 2$ and cascade $I \rightarrow I - 1$ transitions [Eji89, Boh75]. From the rotational model [Boh75], this experimental ratio can be used to deduce model-dependent values of the mixing ratio δ and $(g_K - g_R)/Q_0$ using the following relations;

$$\frac{1}{\delta^2} = \frac{1}{\lambda_b} \left[\frac{E_\gamma(I \rightarrow I - 2)}{E_\gamma(I \rightarrow I - 1)} \right]^5 \frac{\langle IK20 | I - 2K \rangle^2}{\langle IK20 | I - 1K \rangle^2} - 1 \quad (2.49)$$

$$\frac{g_K - g_R}{Q_0} = 0.933 \times \frac{E_\gamma(I \rightarrow I-1)}{(\sqrt{I^2 - 1})\delta}. \quad (2.50)$$

Here, $E_\gamma(I \rightarrow I-1)$ and $E_\gamma(I \rightarrow I-2)$ are the transition energies in MeV and I is the spin of the parent level at which λ_b is measured. Note that only the magnitudes of δ and $(g_K - g_R)/Q_0$ are determined. If the sign of the mixing ratio δ can be deduced from other methods such as angular correlation measurements, then, since $\text{sign}(\delta) = \text{sign}((g_K - g_R)/Q_0)$, the sign of $(g_K - g_R)/Q_0$ may also be determined. The value of $(g_K - g_R)/Q_0$ should typically be constant within a given rotational band.

In cases where rotational bands are built on multi-quasiparticle states, the value of g_K is the weighted sum of the g_Ω -values of the each of the single quasiparticles that make up the configuration, thus

$$Kg_K = \sum_i \Omega_i g_{\Omega_i}. \quad (2.51)$$

The experimental values for the g -factors obtained for a given band may be compared with either theoretical or known experimental values to determine the configuration of the bandhead.

Note that if the configuration of the quasiparticle state involves levels from high- j intruder shells such as the $h_{9/2}$ protons and $i_{13/2}$ neutrons in the A=180 region [Don87], then configuration mixing from Coriolis forces means that Nilsson model estimates of the (nominal) single-particle configurations could differ markedly from experimental values. Such examples have been observed and studied extensively in tungsten [Sai00] and tantalum [Kon96, Das00] isotopes where strongly Coriolis-mixed orbitals such as $11/2^+[615]$ and $9/2^+[624]$ are prevalent.

2.7 Effects of nuclear rotations

It has been shown earlier that rotational motion in deformed nuclei can have significant effects on the structures of the Nilsson states, especially at high rotational

frequencies, and mainly due to Coriolis forces [Mot60, Ste75].

While the pairing force couples two particles in time-reversed single-particle states, rotation has the opposite effect on the particles forming pairs, with the Coriolis force tending to decouple particles and hence reduce the pairing correlations. With increasing ω , the Coriolis force also increases such that at certain angular momentum it becomes comparable to the pairing force and can break pairs. As a result, the energy gap parameter Δ gradually decreases with increasing rotational frequency ω and there can be an increase in the effective moment of inertia \mathfrak{J} . Some detailed studies on the pairing reduction due to nuclear rotation can be found in Refs. [Mut84, Shi89, Dra98b]

2.8 Isomeric states

Some excited nuclear states have substantial lifetimes. A wide range of isomeric half-lives are observed, ranging from nanoseconds to years [Wal99]. Particularly long-lived examples are known in ^{178}Hf [Hel68, Van80, Mul97] and ^{180}Ta [Cum85, Dra96], having $T_{1/2} = 31$ years and $\tau > 10^{15}$ years, respectively. These metastable states can have excitation energies ranging from a few eV up to several MeV above the ground state. For example, the well known 31 year isomer in ^{178}Hf appears 2.4 MeV above the ground state, while the $\tau > 10^{15}$ years isomer in ^{180}Ta lies just 75 keV [Dra96, Dra98, Whe00] above the ground state, in fact it is the abundant form of ^{180}Ta that is observed naturally. The following sections describe some of the types of isomers that are of relevance to the current work.

2.8.1 Spin traps

Spin traps are metastable states in which the only available decay paths require a large change in nuclear spin, usually at least $\Delta I \geq 2$. The long half life that can result from the fact that high multipolarity radiation has low transition probability may be further enhanced if the decay transition has a low energy. This type of

isomer is more common in the spherical or near-spherical nuclei [Wal99, de V83, Wal01]. However, some cases exist in deformed nuclei, e.g. the $\tau = 192 \mu\text{s}$ isomer in ^{177}Ta [Das00] that decays via an 86 keV $E2$ transition, and the $\tau > 10^{15}$ year isomer in ^{180}Ta that, if it were to decay via γ -ray transition, would have to undergo an $L = 8$ photon emission.

2.8.2 K-isomers

In deformed nuclei, where the K quantum number is used to characterise the intrinsic states (see section 2.1.3), the selection rule for decays involving a change in the K -value requires the multipolarity (λ) of the transition to satisfy the condition [Wal99]

$$\lambda \geq \Delta K. \quad (2.52)$$

It is possible for the change in K -value to be greater than the multipolarity of the radiation, violating the K -selection rule, however, these “ K -forbidden transitions” are often strongly hindered and thus may proceed at very low rates. This hindrance can sometimes result in long half-lives, whereupon the states may be called K -isomers.

The degree of forbiddenness for such transitions is denoted by $\nu = \Delta K - \lambda$. For each extra unit of ΔK that exceeds the multipolarity λ , it has been found empirically that the transition rate is reduced by a factor of about 100 [Löb68]. The value of ν can be used to extract the so-called reduced hindrance, f_ν

$$f_\nu = F_W^{1/\nu}, \quad (2.53)$$

where F_W is the hindrance factor relating the measured transition strength to the Weisskopf estimate, as shown in equation 2.45. For K -isomers with pure K -values (i.e no K -mixing), the empirical values of f_ν for K -hindered transitions typically range between 30 and 300 [Löb68].

Lower values of reduced hindrances outside this range are sometimes observed

and this is usually a result of K -mixing [Dra05a, Dra13]. K -mixing can arise from a number of factors. One interesting case is when there is a chance degeneracy between a K -state and a collective state from a lower- K configuration that has the same spin and parity. Mixing between the states may provide an opportunity to extract the interaction strength between the two energy levels. This scenario has in the $A = 180$ region been observed recently in isotopes of rhenium [Kon99], tungsten [Wal91, Wal94, Lan10], tantalum [Kon04], as well as in lutetium [Dra06, McG00, Dra10b].

In cases where the K -state/isomer lies well above the yrast line and hence in a region of relatively high level density, statistical mixing with states of different K is possible, leading to low values of reduced hindrance for the (nominally) K -hindered transitions. Examples may be found in Refs. [Wal97, Dra05]. Another form of K -mixing results from Coriolis effects that explicitly mix the K -values, especially if the configuration of the isomer involves high- j particles such as $i_{13/2}$ neutrons. Since Coriolis forces give a calculable (predictable) mixture of K -values, it is sometimes possible to recover the underlying value of the reduced hindrance [Dra06].

The existence of K isomers is necessarily limited to axially symmetric deformed nuclei, for which the majority of known cases have been observed around the mass-180 region. Note that in deformed nuclei, isomerism can arise from a simultaneous contribution of both violation of the K -selection rule and a large change in angular momentum for the decay transition. In such a case, the isomer is both a spin trap and a K -isomer. An example of such an isomer is the well known $T_{1/2}=31$ -year, $K^\pi = 16^+$ state in ^{178}Hf .

Experimental methods

This chapter focuses on experimental techniques used in γ -ray spectroscopy. This includes the reaction mechanisms useful in populating high-spin states, with the main focus on deep-inelastic reactions, as well as the γ -ray detection mechanism and systems, in particular the Gammasphere array. Also covered are techniques for identifying the nuclei of interest in the complex deep-inelastic datasets, together with the methods for measuring nuclear lifetimes. This chapter is finalised with spin and parity assignment methods relevant to the current work, together with the experimental details.

3.1 Accessing neutron-rich nuclei

In order to study high-spin states, a reaction that can impart large values of angular momentum into the nucleus of interest is required. Several methods have been developed over the years to study the structures of different nuclei [Bro06, Pfü98, Ahm95] as described in the section below. Early studies using fusion evaporation reaction (3.1.1 and 3.1.2) were limited to neutron-deficient nuclei and only more recent developments have allowed access to neutron-rich nuclei (3.1.4 and 3.1.5). In the current work, deep-inelastic reactions were used as they were the only tool that could reach the neutron-rich nuclei under investigation. As will be discussed below, these reactions are able to populate up to relatively high spins, but not as high as conventional fusion-evaporation reactions.

3.1.1 Heavy-ion fusion-evaporation reactions

One of the most common historical methods known to produce highly excited nuclei is the heavy-ion, fusion-evaporation reaction. In this method, a heavy ion ($A > 4$) is accelerated towards a target nucleus with energies above the Coulomb barrier, resulting in fusion of the two nuclei to form a very hot compound nucleus. The compound nucleus may then undergo spontaneous fission, if its excitation energy is above the fission barrier or particle evaporation of protons, neutrons and α particles, with the emitted number of particles depending on the excitation energy and the particle separation energies. The tendency for spontaneous fission increases with both mass of the compound system and the projectile energy. However, charged-particle emissions are usually hindered by the Coulomb barrier, especially in heavy nuclei, and, as a result, neutron evaporation can often be the favoured emission process. Neutron evaporation leads preferentially to population of neutron-deficient species, thus limiting the production of neutron-rich nuclei from fusion-evaporation reactions.

3.1.2 Incomplete-fusion reactions

Incomplete fusion is another method that has been applied to populate high-spin states in nuclei [Dra97]. The method usually utilises a beam of weakly bound nuclei, such as ^9Be , incident on a heavy target. The incoming ion can break apart in the Coulomb field before reaching the target nucleus, resulting in one fragment flying off and only partial fusion with the target, then following the processes in 3.1.1 above. Since the breakup process can result in the absorption of moderately neutron-rich species such as ^5He , this technique has been found to allow access to nuclei up to one or two neutrons beyond the limits available from fusion-evaporation reactions [Dra97]. Due to these limitations, neutron-rich nuclei in the heavy-mass region remained inaccessible for many years using stable beams and targets.

3.1.3 Fission reactions

A detailed review of fission techniques to access neutron-rich nuclei can be found in [Ahm95]. Since fission results in two light-mass nuclei, it is not possible to access heavy, neutron-rich nuclei using fission.

3.1.4 Fragmentation reactions

Projectile fragmentation has shown to be effective in population of neutron-rich nuclei [Pf  98]. This reaction involves the use of heavy beams at relativistic energies (~ 1 GeV per nucleon). With these high velocities, the nuclear collisions are extremely violent, leading to a vast range of fragments being produced at high excitation energies that then undergo particle evaporation processes and γ -ray decays. Since the reaction is not selective in terms of the products, the nuclei of interest are usually selected and identified using fragment separators. These reactions have not been used in the present work. Recent applications of fragmentation reactions to study neutron-rich nuclei can be found in Refs. [Ree10, Ste11].

3.1.5 Deep-inelastic reactions

Recently, deep-inelastic reaction have been developed [Bro06] as a tool to populate high-spin states in neutron-rich, heavy nuclei using stable beams and targets; this method was used in the current project. This reaction mechanism will be discussed in more detail in this section.

Deep inelastic collisions between two nuclei take place at all intermediate impact parameters between surface and central collisions [Bro06]. In this process, the two nuclei come into contact and strongly interact without fusing. The contact is usually long enough such that significant nucleon/mass transfer between the beam and the target nuclei can take place, resulting in a significant amount of energy transfer through the contact region. The direction of the transfer of the nucleons tends to equalise the N/Z ratio of the system. This implies that during contact there is an overall flow of neutrons into the low N/Z nucleus (usually the lighter

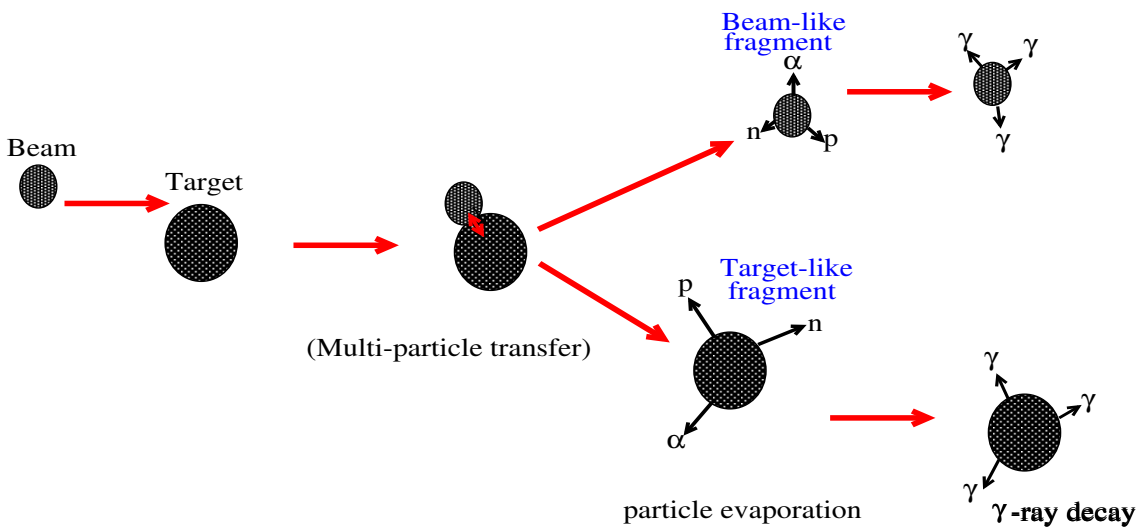


Figure 3.1: Schematic representation of a deep-inelastic reaction. After coming into contact, particle transfer between beam and target occurs. The residual target-like and beam-like nuclei then undergo particle evaporation (proton, neutron or α) followed by γ -ray decay.

binary partner), and, similarly, for protons to high N/Z nuclei [Bro06]. Two hot binary fragments (beam-like and target-like) are produced, which then undergo light-particle evaporation (mainly uncharged particles such as neutrons) and subsequent γ -ray emission. Through a sensible choice of the projectile and target, the yield of reaction products with masses around that of the target can be maximised, thus enabling population of neutron-rich nuclei that could not be accessed from standard fusion-evaporation reactions. The yield distribution for target-like products in deep-inelastic reactions has been discussed by Królas [Kró11]. In order to reach as far as possible into the unknown neutron-rich region, stable neutron-rich nuclei can be selected for both the target and beam, as illustrated by Broda *et al* [Bro06]. Often, a thick target is used to ensure that all reaction products are stopped in the target material [Kró11, Dra05, Dra12, Lan09, Lan10, Whe99, Coc99].

An aspect of deep-inelastic reactions that is different to fusion-evaporation is that during collision, not all of the angular momentum available from the reaction goes into the intrinsic angular momentum of the final products. Instead, some of the angular momentum goes into the relative rotation of the two primary fragments.

3.2 Detection of γ radiation

3.2.1 γ -ray detectors

Scintillator or semiconductor detectors are usually used for γ -ray detection. They work by detecting the energetic electrons and positrons produced when gamma rays interact with the detector material. Different materials may be chosen to give particular characteristics. For example, high efficiency for better statistics or high resolution to enable better distinction between γ rays that are closer in energy. An example of a semiconductor detector is a High-Purity Germanium (HPGe) detector; these have a very high energy resolution of ~ 1.8 keV at a γ -ray energy of 1.332 MeV. Typical scintillation detectors include crystals of sodium iodide (NaI), bismuth germanate ($\text{Bi}_4\text{Ge}_3\text{O}_{12}$) (BGO) and barium fluoride (BaF_2), which have much poorer energy resolutions at 1.332 MeV, ranging from 60 to 150 keV. However, due to their construction from higher-Z materials than germanium detectors, the scintillators generally have considerably higher efficiency for the detection of gamma rays, up to an order of magnitude better. Nevertheless, HPGe detectors were used in the current work since the number of different gamma rays emitted is expected to be high and the need to resolve close-lying energies is the most important detection criterion.

3.2.2 Interaction of γ rays with matter

Gamma-rays are detected via interactions between the photons and the detector crystal that result in all, or part of, the energy of the photon being absorbed by the material. Such interactions can proceed through one or more of the following processes, photoelectric effect, Compton scattering and pair production [Kno89].

Photoelectric effect

In this process, all the energy of the photon is transferred to an atomic electron, resulting in the release of the electron from the atom of the crystal. No secondary photons are produced, implying that the full-energy of the γ -ray photon is directly

transferred to the crystal around the position of interaction. The photoelectric effect is dominant for lower energy γ rays (see figure 3.2) and contributes to full-energy peak events.

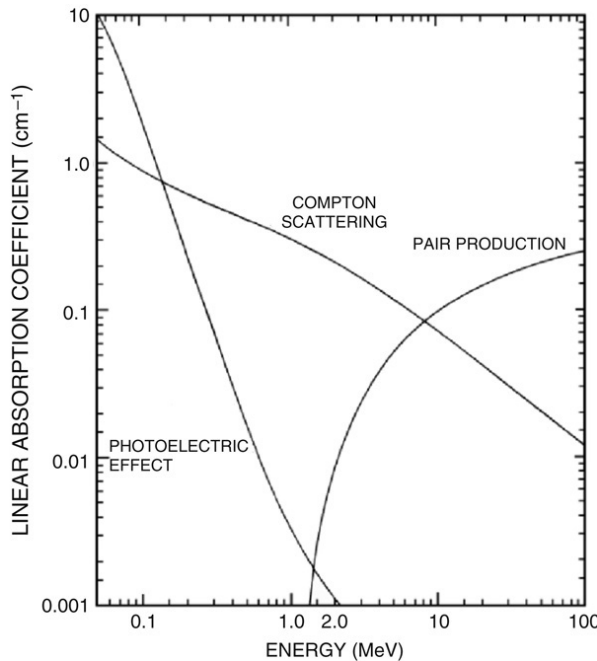


Figure 3.2: Absorption cross-sections for gamma rays in Ge crystal as a function of energy. Figure taken from Ref. [Ebe08]

Compton scattering

A γ -ray photon may scatter from an electron within the crystal, resulting in a lower energy photon and a free electron. The lower energy scattered photon may undergo further Compton scattering inside the material, always lowering in energy until it becomes so low that photoelectric absorption finally occurs. These Compton events contribute to the full energy peak, provided all these Compton events are detected. However, in some cases, a scattered photon may escape to the outside of the detector material, giving a continuous spectrum of low energy events, the so-called Compton continuum. Compton scattering is the dominant process for higher energy photons (~ 1 MeV) compared to the photoelectric effect (see figure 3.2).

Pair Production

Pair production can only take place if $E_\gamma \geq 1.022$ MeV. In this process, part of the original γ -ray photon energy is converted into mass in the form of a positron and electron pair, with the remainder forming their kinetic energy. The positron eventually comes to rest, often inside the detector material. Annihilation with a nearby electron results in the emission of two γ rays each with an energy of 511 keV. The two γ rays are emitted in opposite directions and in turn interact with the detector material via photoelectric effect or Compton scattering. They may deposit all their energy inside the crystal and contribute to the full energy peak. However, in some cases, one or both the photons can escape the detector and produce peaks at 511 or 1022 keV below the full energy peak. Pair production is the dominant process for high-energy gamma-rays as shown in Fig. 3.2 .

3.2.3 Compton suppression

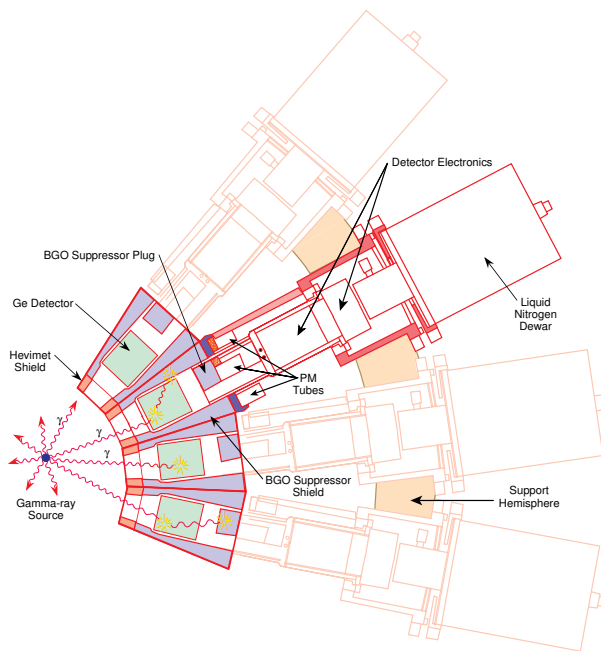


Figure 3.3: Schematic representation of the Compton-suppressed HPGe detectors in GAMMASPHERE. From the online booklet for GAMMASPHERE [Www1].

As discussed earlier, a large continuous background can occur in the γ -ray spec-

trum when large numbers of Compton-scattered γ -ray photons escape the detector crystal. Such large backgrounds can obscure weak γ rays. In most modern detector arrays, this effect is reduced by the Compton-suppression technique, where the primary (HPGe) detector is surrounded by another detector, typically BGO scintillator. The secondary detector is usually shielded from the direct flux of γ rays such that it can only detect Compton-scattered γ rays from the primary detector. For all the events in which the BGO receives signals from Compton-scattered photons, no count is registered in the spectrum. The GAMMASPHERE detector array used in the current work consists of high-purity germanium detectors as primary detectors and bismuth germanate (BGO) as secondary detectors for Compton suppression.

3.2.4 Multi-detector arrays

Over the last few decades a number of gamma-ray detector arrays have been developed that utilise large numbers of high-efficiency, Compton-suppressed HPGe detectors. Such arrays include early designs like TESSA, HERA, OSIRIS and NORDBALL that covered large fractions of solid angle [Ebe08], and the latest arrays with 4π coverage such as GASP, EUROGAM, EUROBALL and GAMMASPHERE [Nol94, Lee90]. Since most of them are Compton-suppressed, the experimental measurements from these arrays have shown a significant improvement in the signal to background ratios of the spectra, as compared to the previous spectrometers. They have also demonstrated better efficiency and hence higher statistics, which enables the observation of weak γ -ray transitions in the presence of many strong lines.

The correlations between cascades of γ rays depopulating high-spin states have been measured successfully using these arrays. Their design and performance have been discussed in detail by many authors including Sharpey-Schafer [Sha88] and Beausang [Bea96]. The evolution of γ -ray spectroscopy has seen the number of detectors included in these arrays rising from as low as six detectors in TESSA [Twin84] to more than 100 in GAMMASPHERE and EUROBALL. The continuous significant improvements in the efficiency of these arrays has enabled the observation of

ever more weakly populated structures in modern nuclear structure experiments. The next generation germanium detector arrays such as AGATA [Akk12] and GRETA/GRETINA [Del99] are also starting to be used in experimental campaigns. These arrays utilise the principle of γ -ray tracking [Lee99] and give greatly improved angular resolution due to their ability to localise the position of the first gamma-ray interaction, while their ability to measure the full energy of the gamma ray even in the case of Compton scattering interactions between different detector crystals, means that they have much higher efficiency compared to the previous generation of arrays such as GAMMASPHERE and EUROBALL. These arrays are currently being dedicated primarily to the study of rare reaction channels produced in experiment with weak beam intensities, for example, radioactive beam measurements [Baz04].

3.2.5 GAMMASPHERE

The GAMMASPHERE array was used for the current work. It is presently located at the ATLAS (Argonne Tandem Linac Accelerator System) facility in Argonne National Laboratory, Chicago, USA. GAMMASPHERE consists of up to 110 large volume, high-purity germanium detectors, each surrounded by bismuth-germanate (BGO) Compton-suppression shields, see Figure 3.3. The detectors are positioned at various angles in a spherical structure around the target with a forward-backward symmetry with respect to the beam axis [Nol94], see Figure 3.4. The corresponding angles for all the detector, relative to the beam direction are shown in Table 3.1. In the current work, 99 Compton-suppressed HPGe detectors were in operation.



Figure 3.4: GAMMASPHERE array comprising up to 110 Compton-suppressed High-Purity Germanium (HPGe) detectors.

Table 3.1: Angles of the 110 detectors in GAMMASPHERE with respect to the beam direction. The detectors are positioned at these angles with a forward-backward symmetry to form a spherical shape around the target, see figure 3.4.

Number of detectors	Angle (θ)
10	17.3
10	31.7
10	37.4
20	50.1
10	58.3
20	69.8
10	79.2
10	80.7
10	90.3

3.3 Coincidence spectroscopy

3.3.1 Coincidence histograms

In many experiments, very complicated spectra are produced as a result of the many bands populated in a large variety of nuclei. Widely used $\gamma - \gamma$ or triple- γ

coincidence techniques make it possible to isolate the individual decay transitions and assign them to the nucleus of origin. For the purpose of nuclear structure studies, the γ -ray events from the residual nuclei can be registered in coincidence, that is, within a short time interval (Δt), when using an array of two or more detectors. The coincidence data is comprised of two parts, the true coincidence events and random coincidences. True coincidences are those events registered that correspond to two or more γ rays from the same nucleus/source, while random events are a result of γ rays from different nuclei happening to arrive by accident within the coincidence overlap time.

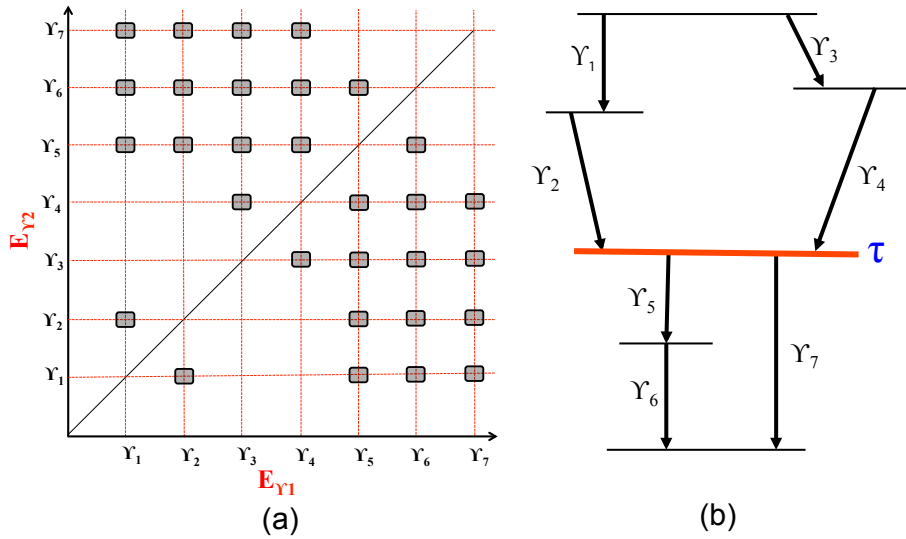


Figure 3.5: (a) Schematic representation of a symmetric γ - γ matrix used in construction of nuclear level schemes. (b) An illustration of the corresponding level scheme.

In order to extract useful information from coincidence data, it is usual to transform or sort it into various n -dimensional histograms. Note that the number of γ rays observed in an event, known as the fold, does not have to equal the dimensions of the histogram. For example, two-dimensional histograms are $\gamma - \gamma$ matrices that result from double-coincidence events or higher-fold events that have been unfolded into double coincidences [Ada97]. Each axis of a histogram might correspond to either the channel number, or the energy (for a calibrated matrix), of the detected γ rays, see figure 3.5(a). Analysis of higher-fold coincidence data is also possible, including $\gamma - \gamma - \gamma$ -cubes, a three dimensional object of

triple-coincidences, or even 4-fold coincidence objects (hypercubes).

Analysis of these high-fold coincidence data leads to the construction of nuclear decay schemes such as the schematic one in figure 3.5(b). The process of building a level scheme from matrices and cubes involves setting narrow windows (gates) on all but one axis of the histogram and projecting a one dimensional γ -ray spectrum of the selected coincidence events on the other axis, hence showing all the transitions that are in coincidence with the gate(s). For example, if a gate is set on the γ_1 transition on the $E_{\gamma 1}$ axis in figure 3.5, the projected spectrum will reflect the coincident γ -rays γ_2 , γ_5 , γ_6 and γ_7 in the $E_{\gamma 2}$ axis. The same applies to a $\gamma - \gamma - \gamma$ cube except that two gates from say $E_{\gamma 1}$ and $E_{\gamma 2}$ axis are now needed to project a third coincident transition in the third axis, $E_{\gamma 3}$. Generally, for an n -fold histogram, $n - 1$ gates are needed to extract coincidence spectra.

The continuous background from Compton scattering of γ -ray transitions, as well as from weak unresolved γ rays, can obstruct the observation of weak transitions. Such background events need to be subtracted from the spectra. Appropriate methods for background subtraction in two and higher-fold γ -ray coincidence data have been discussed by Palameta *et al.* [Pal85], Crowell *et al.* [Cro95] and Radford [Rad95a]. Analysis of these high-fold data requires the use of sophisticated computer programs such as ESCL8R and LEVIT8R [Rad95], for the inspection of $\gamma - \gamma$ matrices and cubes, respectively. These two interactive graphical analysis programs are part of RADWARE, a γ -ray analysis software package developed by David Radford [Rad00]. The programs automatically subtract the background from each gate using algorithms from Ref. [Rad95].

3.3.2 Prompt and delayed coincidence

Two or more γ rays are considered to be in prompt coincidence if they are detected close enough in time such that they appear to have arrived at the same time. As illustrated in figure 3.6(a) and (b), the $\gamma_1 - \gamma_2$, $\gamma_3 - \gamma_4$ and $\gamma_5 - \gamma_6$ pairs of transitions, are considered prompt due to a negligible detection time difference between them.

However, the presence of a measurable lifetime τ means the γ_5 , γ_6 and γ_7 set of transitions will be detected later in time (delayed) relative to γ_1 , γ_2 , γ_3 and γ_4 . These detection time differences may be used to determine state lifetimes (see section 3.4), while prompt transitions can be related to a situation where the states have negligible lifetimes ($\tau < 1$ ns in the present study). The three γ rays below the isomer (γ_5 , γ_6 and γ_7) are said to be delayed relative to those feeding the isomer, termed early γ rays. By examining the time correlations, it is possible to separate the early and delayed coincidence γ rays and increment them into different axes of coincidence histograms so that early/delayed spectra can be created through appropriate gating.

The ability to generate coincidence histograms and gated spectra is the key to level scheme construction and also aids in nuclear and isotopic assignment, as will be seen in Chapters 4 and 5.

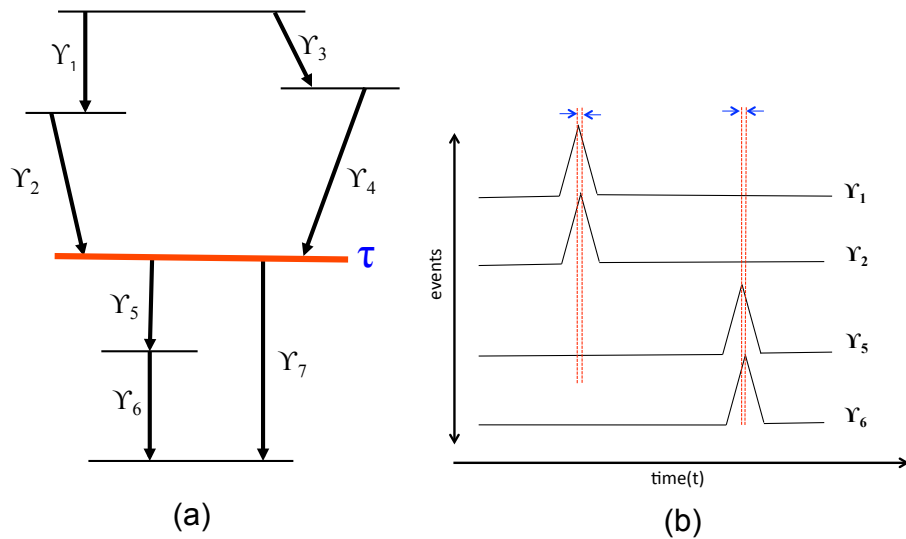


Figure 3.6: (a) Level scheme that will exhibit prompt and early-delayed coincidence events. Prompt events are characterised by a negligible detection time between them, e.g. γ_1 and γ_2 , or γ_3 and γ_4 where there is no intervening lifetime. γ_1 and γ_5 or γ_1 and γ_6 illustrate early-delayed events due to measurable lifetime τ . (b) The arrival times of the γ -ray events compared to the vertical red lines showing a time overlap window, illustrating the different types of coincidence.

3.3.3 Elemental and isotopic assignments

Studies on the distribution of yields from deep-inelastic reactions have been carried out by a number of authors [Bro06, Kró11], with the results showing that many nuclei with N and Z near that of the target-like and beam-like-nuclei are produced. With the latest generation of γ -ray detector arrays, the collected data can be so complex that several nuclear and isotopic assignments methods might be necessary to firmly assign each γ -ray transition to the correct nucleus. The present section focuses on the methodology that was used to identify new tantalum structures, as well as make isotopic assignments to these structures.

Characteristic X-rays

A gated spectrum can show coincident characteristic X-rays that follow from internal conversion. In the present mass region, the K_α and K_β X-ray components are often seen and are unique for a given element. The two prominent characteristic X-ray components in tantalum nuclei lie at 57.53 and 65.22 keV, corresponding to $K_{\alpha 1}$ and $K_{\beta 1}$ transitions, respectively. The presence of these characteristic X-rays in any gated spectrum means that the gating transition belongs to a tantalum nucleus. Note that the neighbouring Z nuclei have $K_{\alpha 1}$ X-rays separated in energy by approximately 1.7 keV, easily resolvable by the HPGe detectors in Gammasphere, and enabling clear elemental assignments (see, for example, the gamma-ray spectra in Chapter 4).

For new transitions coincident with tantalum X-rays, it is not always possible to immediately identify the tantalum isotope from which these γ rays originate. Additional information from previous studies on that particular nucleus can be helpful. In the present case, where possible, projection of early and delayed transitions relative to the new γ rays to establish connections with known γ rays were used to assign the isotopes, refer to Chapter 4 and 5. Sometimes, however, a firm isotopic assignment for a given set of γ rays requires additional information.

Target yields

The production cross section for a given nucleus from deep-inelastic reactions is understood to vary systematically based on the proximity of the residual nucleus to the beam or target nucleus [Das94]. Therefore, comparison of the yield intensities of an unknown structure in different datasets from different targets can be useful to make isotopic assignments. Detailed explanation and analysis of the yields for isotopic assignment is covered in Chapter 5, for the case of ^{182}Ta .

3.4 Lifetime analysis methods

Some nuclear states have long enough lifetimes that the mean lifetime can easily be measured directly through observed time differences. The mean lifetime τ denotes the average time for the nuclei in a given excited state to decay. Measurement of the meanlife provides information required to determine parameters such as the reduced transition probabilities of the depopulating transitions that can then be used to reveal more detailed information on the structure of the nucleus. Beyond lifetime measurements, the systematic time shifts are also useful in ordering γ rays within a decay scheme.

Due to the wide range of nuclear lifetimes observed, from femto-seconds to years, different methods for measuring these quantities have been developed and applied [Ols66, Löb75, Mac89]. The present work is mainly focused on lifetimes in the range of a few nanoseconds and longer where direct electronic observation is possible .

The general principle of the lifetime measurement techniques applicable to the present data involves the measurement and analysis of time differences between transitions feeding and depopulating a state. The presence of a measurable lifetime with $\tau > 5$ ns is usually characterised by the presence of a slope on one side of a distribution of the measured time differences. Alternatively, in the case of shorter lifetimes ($\tau \sim 1\text{-}5$ ns), the observable is a shift of the time distribution centroid,

relative to the position of the centroid for a prompt time distribution. As a result, the common lifetime analysis methods such as the centroid shift [M  r10, R  g09], convolution and slope methods become applicable.

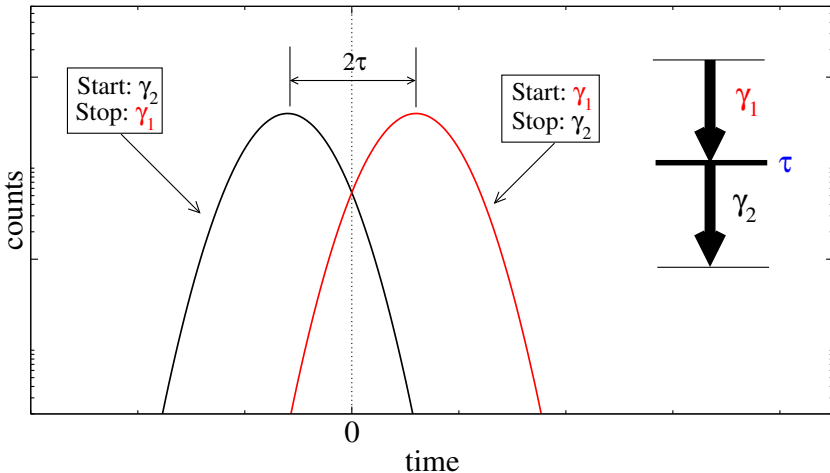


Figure 3.7: Illustration of a delayed coincidence time distribution as a result of the measured time difference between the populating (γ_1) and the depopulating transition (γ_2). The presence of a short lifetime causes a shift in the centroid compared to the spectrum from prompt events (time-zero). The time separation between the two centroids is twice the lifetime of the level.

For the centroid shift method, first the prompt position is derived from a known prompt state in the same level scheme under investigation or from another level scheme from the same data set [Mac89]. In the present work, the known experimental prompt spectra used are from the neighbouring (strongly populated) tungsten nuclei. The presence of a lifetime can then be determined by a shift in the position of the centroid, with the magnitude of the lifetime defined by the difference between the two centroids.

Another approach to the centroid shift method involves the interchange of gates, that is, the order of the start and stop γ rays from which two time spectra are generated, see Figure 3.7. The outcome is that one spectra shifts to the right and the other to the left of the prompt position at $t \approx 0$. In Figure 3.7, starting with γ_1 and stopping with γ_2 results in a spectrum shifted to the right (red) while the reverse causes a shift to the left (black). As a result, the separation between the two

centroids is twice the meanlife of the decaying state. Beyond lifetime measurements, the systematic time shifts are also useful in ordering γ rays within a decay scheme.

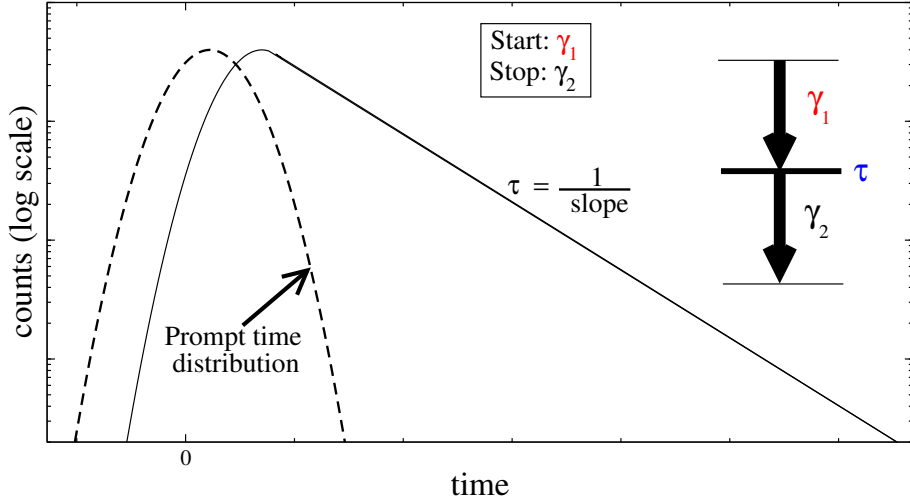


Figure 3.8: Schematic representation of a time distribution in which the lifetime clearly appears as a slope in the delayed part of the time spectrum. The slope gives the lifetime of the decaying state.

For a longer lifetime that can manifest itself as a slope, see Figure 3.8, the experimentally determined delayed time spectrum, with the random coincidences subtracted, can be considered as a convolution of the prompt time distribution $P(t)$ with an exponential decay curve $f(t)$ [Ols66, Löb75]. With the prompt time distribution approximated by a Gaussian function, the experimental delayed time distribution can be expressed analytically as [Mac89]

$$F(t_j) = \gamma \int_A^{+\infty} e^{-\delta(t_j-t)^2} e^{-\lambda(t-A)} dt, \quad (3.1)$$

where γ denotes the normalization constant, A is the centroid of the Gaussian prompt distribution, δ is a parameter determining the width of the Gaussian prompt distribution, and t and t_j denote time. The corresponding decay constant λ , which is related to the meanlife by $\tau = 1/\lambda$, can be estimated from the exponential component (if the lifetime is sufficiently long), or by fitting the convoluted form if the slope is not sufficiently clear. This is known as the convolution method [Bos66, Ols66].

Unlike the convolution and centroid shift methods, analysis of the long lifetimes using the slope method does not require knowing the time distribution of the prompt spectrum. The three methods are best suited for intermediate states in a decay scheme, where both the feeding and depopulating transitions are observed.

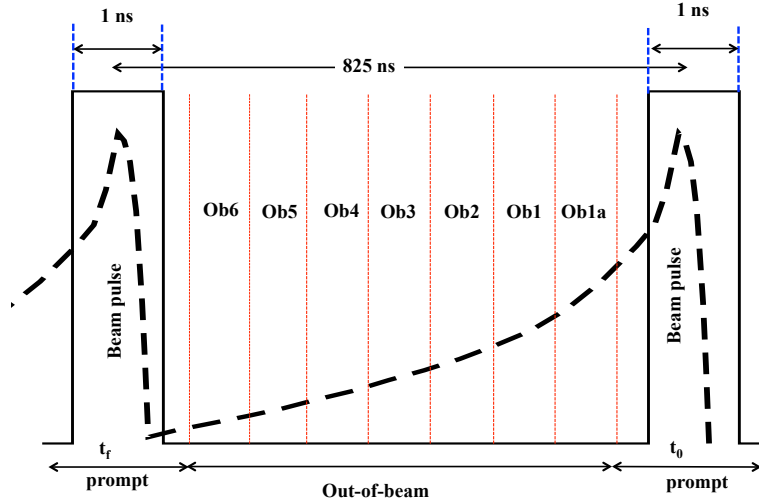


Figure 3.9: Representation of beam pulsing conditions as applied in the present work to investigate the isomeric states. The seven segments Ob1a-Ob6 denotes the $\gamma - \gamma - \gamma$ cubes used to measure the isomeric lifetimes. Note that the time reads from right to left.

In cases where an experiment utilises a pulsed or chopped beam, decays of longer-lived isomeric states can be clearly isolated from the prompt decays by considering only the data recorded between the beam pulses. The intensities of the depopulating transitions from isomers across this beam-off region will decrease with increasing time as shown figure 3.9. The rate of decrease depends on the lifetime of the isomer. A plot of intensity variations for these transitions as a function of time reveals the lifetimes of such isomers. The upper limit that can be measured with this method depends on the time interval between the beam pulses [Löb75]. This method is best suited for the measurement of the highest populated isomer rather than lower isomeric states. For the lower states, the deduced lifetime from this method contains lifetime components from all of the higher-lying isomeric states.

The analysis of the time difference spectra requires the data to be sorted into $\gamma - \gamma - t$ -cubes, where t is the time difference between γ rays. For the other

method using chopped-beam and pulsed-beam measurements, the data is sorted into $\gamma - \gamma - \gamma$ -cubes with specific time cuts to enable intensity measurements in different time regions. Details of all the data sorts are explained in section 3.6.

Examples of actual time spectra, both prompt and showing lifetimes, as well as details of the lifetime analysis and fitting, are found in Sects. 4.2.2 and 5.2.4 for ^{183}Ta and ^{182}Ta , respectively.

3.5 Spin and parity assignment methods

Relative spins and parities of states in level schemes can be derived from the multipolarities of the observed transitions. Many methods have been developed over the years to effectively deduce these multipolarities. For a given decay scheme, one or a combination of such methods can be applied depending on the available information. This section describes the two methods; $\gamma - \gamma$ angular correlations and determining internal conversion coefficients, that were used in the present work. The two methods are based on the common practice of comparing the experimental observations to theoretical predictions in order to derive the spins and parities.

3.5.1 Derived internal conversion coefficients

Experimental values of conversion coefficients compared with corresponding theoretical values, can be used to deduce the multipolarities of γ -ray transitions [Sie66]. Theoretical values of the conversion coefficient can be obtained from the online conversion coefficient calculator (BRICC) by Kibédi *et al.* [Kib08]. For experimental conversion coefficients, the most direct method would be to measure the emitted electrons directly. The ratio of the measured intensity of conversion electrons to that of emitted γ rays gives the experimental α_T values. However, the conversion electrons were not measured in this experiment so a different approach is needed.

Intensity balances

In the present work, the experimental α_T values are deduced indirectly from γ -ray intensity balances between transitions that feed and depopulate a nuclear state. The approach works well if the level scheme is fed by an isomer and the out-of-beam coincidences are considered, since the isomeric decay gives a well-defined pathway for the intensity flow. In such a case, it is appropriate to assume that, across each intermediate state, the incoming total transition intensity, I_T , is equivalent to the total outgoing transition intensity. The total intensity I_T is the sum of the intensity due to γ -ray decay and the intensity due to internal conversion. The total transition intensity I_T is related to α_T from the competing internal conversion process by

$$I_T = I_\gamma(1 + \alpha_T), \quad (3.2)$$

where I_γ denotes the intensity of the emitted γ ray. The quantity I_γ depends on the efficiency ϵ_γ of the γ -ray detector in use. The efficiency of detectors normally depends on the energies E_γ of the transitions. For a given γ -ray transition, its intensity I_γ can be measured from the total counts in the peak and the corresponding efficiency by

$$I_\gamma = \frac{I_{counts}}{\epsilon_\gamma}. \quad (3.3)$$

Using figure 3.10 to illustrate this method, suppose the spin and parity of the τ_1 isomer and the multipolarity for γ_1 are unknown. By setting a double gate on γ_5 and γ_6 in the out-of-beam γ^3 -cube, or a single gate in a γ^2 -matrix, it is possible to measure I_γ for both γ_2 and γ_1 . If the multipolarity of γ_2 is known, one can deduce the internal conversion coefficient of γ_1 from the total intensity balance I_T between γ_1 and γ_2 . The deduced $\alpha_T(\gamma_1)$ can then be compared to theoretical values [Kib08] to deduce the corresponding multipolarity of γ_1 and hence the spin and parity for the isomer.

Note that low-energy transitions are highly converted and α_T can be easily measured, whereas for high-energy transitions (~ 0.4 MeV or more), the internal conversion becomes weak, making this method less accurate. In such a scenario, the $\gamma - \gamma$ -angular correlation measurements tend to offer a much better solution, especially in

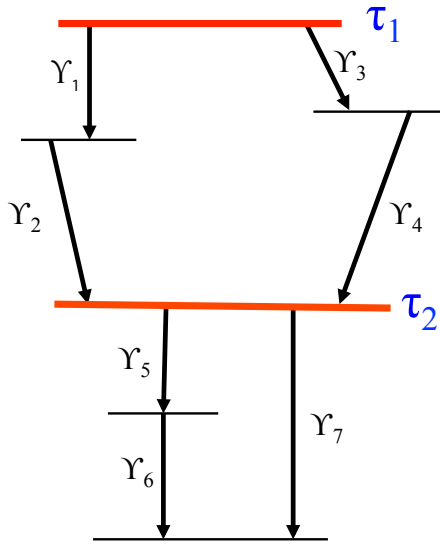


Figure 3.10: A decay scheme to illustrate the use of intensity balances and conversion coefficients to assign spins and parities. The spin and parity for the τ_1 isomer can be derived from γ_1 and γ_2 intensity balances, see text.

modern experiments where highly efficient multi-detector spectrometers are used.

3.5.2 Angular correlations

Theoretical investigations have shown that for two successive transitions, say γ_1 and γ_2 , there exists a correlation between the directions of propagation of the two transitions [Ham40, Ros53]. Such a correlation can be described by the function $W(\theta)$ which gives the probability that the second transition, γ_2 , is emitted at an angle θ relative to the first transition γ_1 (see figure 3.11). This also represents the intensity of either of the transitions in a given direction, and is related to the angular momenta of the states I_1, I_2, I_3 , and the multipolarities λ_1 and λ_2 of the transitions (see page 997 in Ref. [Sie66]). The function $W(\theta)$ is defined as

$$W(\theta) = 1 + A_{22}P_2\cos(\theta) + \dots + A_{k_{max}k_{max}}P_{k_{max}k_{max}}\cos(\theta), \quad (3.4)$$

where $P_k(\cos(\theta))$ are the Legendre polynomials while A_{kk} are the angular correlation coefficients. The highest term in equation 3.4 is determined by the selection rule $k_{max}=\text{Min}(2I_2, 2\lambda_1, 2\lambda_2)$. The experimental result of $\gamma - \gamma$ -angular correlations usually yields only A_{22} and A_{44} . Since higher A_{kk} values have not been observed,

this suggests $k_{max}=4$ for the theoretical equation 3.4. They are related to the spins, transition multipolarities, and the mixing ratios δ_1 and δ_2 of the transitions by

$$A_{kk} = A_k(\lambda_1 \lambda'_1 I_1 I_2) A_k(\lambda_2 \lambda'_2 I_3 I_2), \quad (3.5)$$

where

$$A_k(\lambda_1 \lambda'_1 I_1 I_2) = \frac{F_k(\lambda_1 \lambda_1 I_1 I_2) + 2\delta_1(\gamma_1) F_k(\lambda_1 \lambda'_1 I_1 I_2) + \delta_1^2(\gamma_1) F_k(\lambda'_1 \lambda'_1 I_1 I_2)}{1 + \delta_1^2(\gamma_1)}, \quad (3.6)$$

for the first transition with mixing ratio δ_1 , and with a similar expression for $A_k(\lambda_2 \lambda'_2 I_3 I_2)$ involving δ_2 and where $\lambda'_i = \lambda_i + 1$ corresponds to the second lowest multipolarity for transition i . The coefficient $F_k(\lambda \lambda' I_1 I)$ is defined by

$$F_k(\lambda \lambda' I_i I) = (-1)^{I_i+I-1} [(2\lambda+1)(2\lambda'+1)(2I+1)(2k+1)]^{\frac{1}{2}} \begin{pmatrix} \lambda & \lambda' & k \\ 1 & -1 & 0 \end{pmatrix} \left\{ \begin{array}{ccc} \lambda & \lambda' & k \\ I & I & I_i \end{array} \right\}. \quad (3.7)$$

The arrays in { } and () brackets are the Wigner 3-j and 6-j symbols respectively [Rot59].

Both early and recent publications have already demonstrated how valuable $\gamma - \gamma$ -angular correlations can be for determining the transition multipolarities. Their application with large γ -ray detector arrays such as EUROGAM and NORDBALL has been reported by Ekström [Eks92] and Paul [Pau95]. Previous results from deep inelastic reactions using the GAMMASPHERE array have been published by Dracoulis *et al.* [Dra05] and Wanatabe *et al.* [Wan09], as well as in a report by Lee [Lee06].

In order to evaluate correlation data, the coincident γ rays were sorted into ten γ - γ -matrices corresponding to sets of detector pairs that had different angles of detection between them, θ . Setting gates in these matrices led to the projection of spectra and the measurements of coincidence intensities for each angle difference

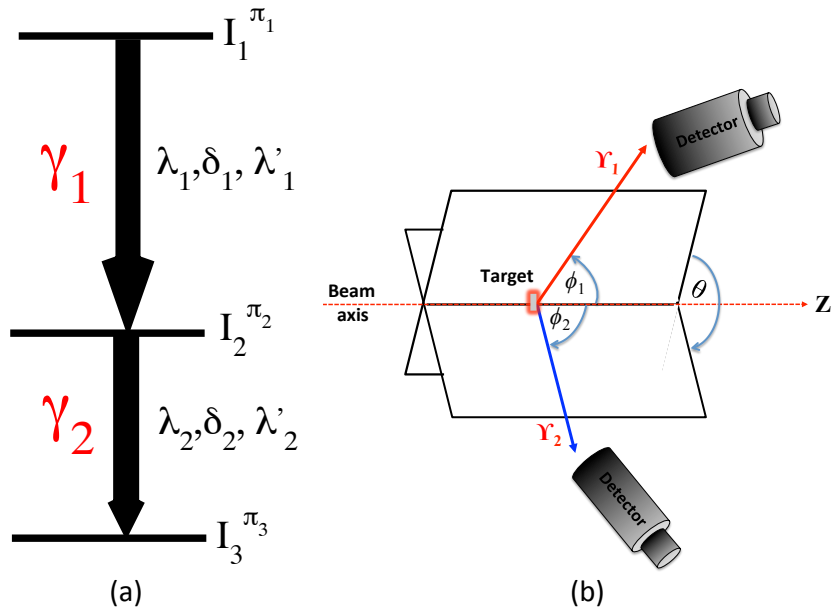


Figure 3.11: (a) Schematic view of a γ -ray cascade from nuclear excited states. (b) Angles in a directional correlation of two successive transitions γ_1 and γ_2 . The intensities detected in each detector depends on the angle θ between the planes. Figures adapted from [Kra73].

θ . The efficiency corrected γ -ray intensities from the projected spectra can be plotted as a function of either the angle θ or $\cos^2(\theta)$. These data can then be fitted with equation 3.4 to deduce experimental values of A_{22}/A_{44} and the corresponding angular correlation curves. There is always a possibility that for any chosen pair of transitions in cascade γ_1 and γ_2 , either one or both of the γ -rays are mixed. Only two types of mixed γ -ray transitions have been observed in the present work, that is a mixed $M1 + E2$ transition and the more rare $E1 + M2$ mixture. The corresponding mixing ratio δ can take a positive or a negative sign, and the angular correlation analysis is the only method used in the present work that is sensitive to the sign of δ (see section 2.6). In the present work, experimental δ values were determined by a χ^2 -analysis of the angular correlation data using the Delta program [Eks84]. The input parameters to this program are the experimental values of A_{22} and A_{44} that are determined from fits of the angular correlation function.

In order to deduce the mixing ratios, several plausible spin combinations were first suggested for a given $\gamma - \gamma$ -correlation. Based on the lifetimes expected for certain multipolarities, the spin combinations corresponding to either dipoles or

quadrupole transitions were preferred. Higher-order multipole transitions such as octupoles are usually unlikely in the absence of long lifetimes. For the different spin combinations suggested, and across the full range of possible mixing ratios, the degree of agreement between the calculated angular correlation and the measured values is used to deduce χ^2 as a function of δ . From these plots, the best-fit value of the mixing ratio for a transition is deduced from the location of χ^2_{min} . All those spin combinations with χ^2_{min} that appear above the 99% confidence limit are highly unlikely and can be excluded. Where a non-zero mixing ratio was observed for a suggested spin change of $\Delta I = 1$, an $E2/M1$ mixed dipole can usually be distinguished from the less common $M2/E1$ on the basis of the expected lifetime for the (slow) $M2$ component. For zero mixing ratio, either a pure $E1$ or pure $M1$ can be suggested depending on other additional experimental observations such as conversion coefficients. For pure quadrupole transitions, a pure $E2$ can be adopted unless there is a long lifetime that might suggest $M2$. Where possible, angular correlation curves for known transitions were measured as a test for the method.

Figures 3.12, 3.13 and 3.14 illustrate the expected angular correlation curves and A_{22} and A_{44} values for various combinations of unstretched ($\lambda > \Delta I$) and stretched ($\lambda = \Delta I$) dipole and quadrupole transitions. The curves were produced by Dr Greg Lane using the DCOPLOT program developed by Professor Andrew Stuchbery, both at the ANU Nuclear Physics Department.

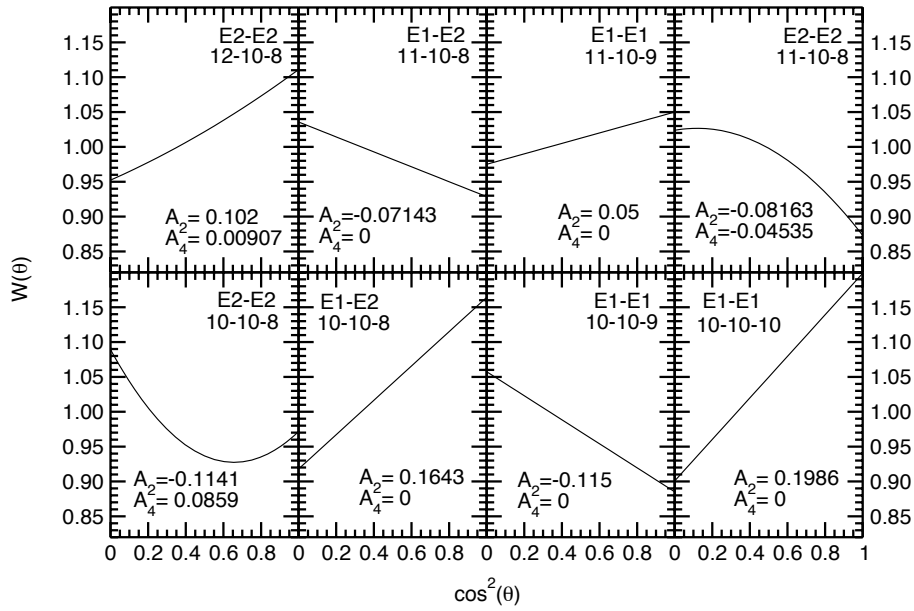


Figure 3.12: Expected angular correlation, $W(\theta)$, for various combinations of unstretched ($\lambda > \Delta I$) and stretched ($\lambda = \Delta I$) $E1$ and $E2$ transitions. The values shown for A_2 and A_4 denote the angular correlation coefficients, A_{22} and A_{44} , that are defined in the text. The spin sequences used for each correlation are denoted by numbers such as 12-10-8 etc.

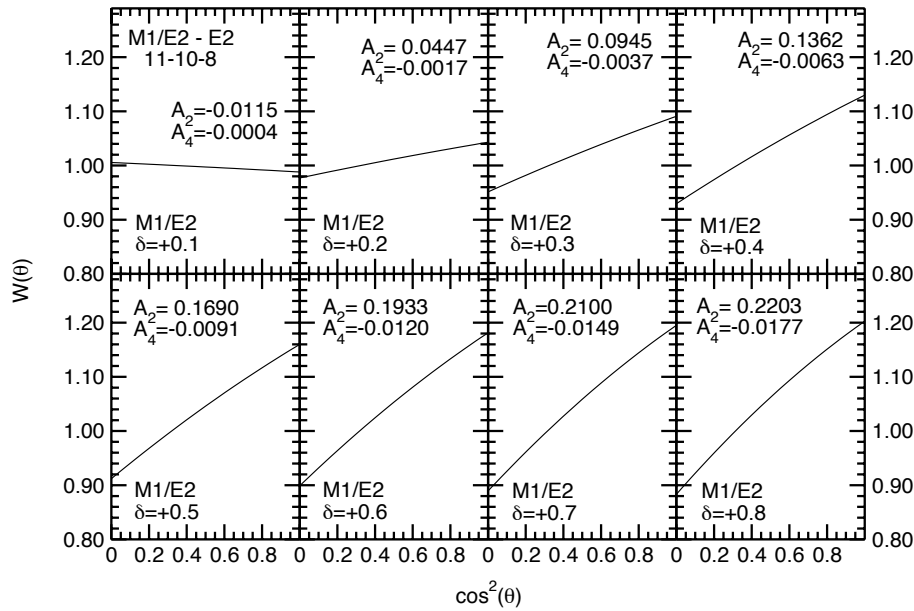


Figure 3.13: Expected angular correlation, $W(\theta)$, for combinations of stretched ($\lambda = \Delta I$) $M1/E2$ and $E2$ transitions showing various positive mixing ratios (δ). The values shown for A_2 and A_4 denote the angular correlation coefficients, A_{22} and A_{44} , that are defined in the text. The spin sequences used for each correlation are denoted by numbers such as 11-10-8 etc.

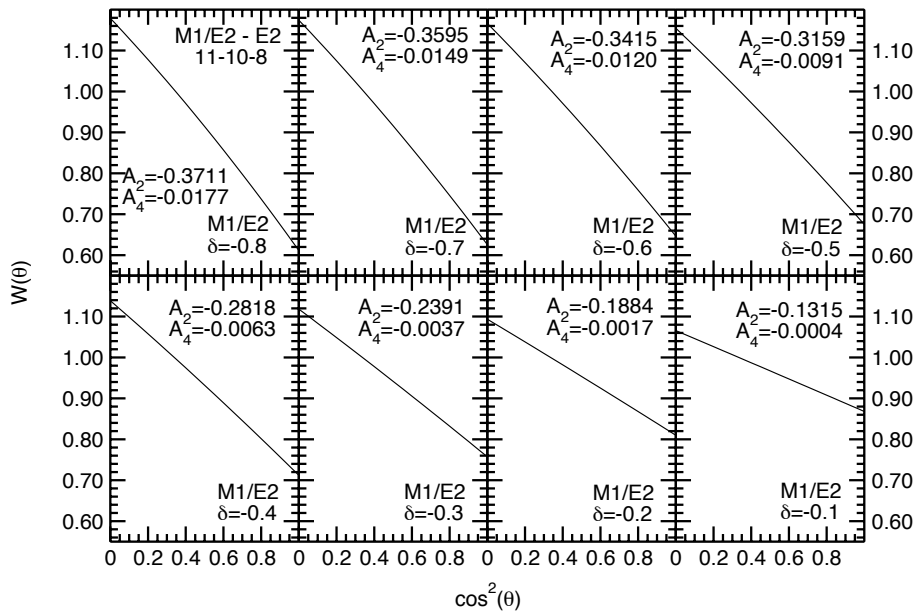


Figure 3.14: Expected angular correlations, $W(\theta)$, for combinations of stretched ($\lambda = \Delta I$) $M1/E2$ and $E2$ transitions showing various negative mixing ratios (δ). The values shown for A_2 and A_4 denote the angular correlation coefficients, A_{22} and A_{44} , that are defined in the text. The spin sequences used for each correlation are denoted by numbers such as 11-10-8 etc.

3.6 Experimental details

The current work is part of an ongoing research program within the Department of Nuclear Physics, ANU, to investigate the structure of nuclei in and around the $A=180$ region. As a result, a series of experiments were carried out using different targets and experimental conditions to populate as many isotopes as possible in this region, particularly the unexplored neutron-rich nuclei. The experiments were performed at Argonne National Laboratory (USA) using the GAMMASPHERE array. Results reported in this thesis are mainly from deep-inelastic reactions between a ^{136}Xe beam and a thick ^{186}W target. Additional data from the ^{136}Xe beam incident on ^{185}Re , ^{187}Re and ^{192}Os targets were also used for isotopic assignments.

3.6.1 Data with ^{186}W target

In this measurement, a beam of 840 MeV ^{136}Xe ions from the ATLAS accelerator was incident on a 99.8% enriched, 6 mg/cm^2 ^{186}W target, with a 25 mg/cm^2 ^{197}Au backing. GAMMASPHERE was used with 99 Compton-suppressed HPGe detectors operational. In this experiment, the coincidence overlap between any two or more γ rays was set to approximately ± 800 ns and just over 1 billion coincidence events with three or more γ rays were collected. Two sets of beam conditions were used to isolate states with different lifetimes:

- **Pulsed beam:** 1 ns beam pulses at 825 ns intervals.
- **Chopped beam:** longer time intervals for studying longer lifetimes ($\sim 5\mu\text{s}$ or more)

3.6.2 Offline data sorts

Most of the initial offline data sorts were carried out by Dr Greg Lane for both the chopped-and pulsed-beam data using methods described in Ref. [Cro01]. From

the pulsed-beam data, those events between 102-720 ns after the beam-pulsed were classified as delayed and correspond to decays from isomers. The prompt data as defined in the present work corresponds to the beam-on events and includes γ rays observed from 30 ns before up to 100 ns after the beam-pulse. The following histograms were generated for data analysis:

- $\gamma - \gamma - \gamma$ **coincidence cube**: (Out-of-beam)
- $\gamma - \gamma - \gamma$ **coincidence cube**: (In-beam)
- $\gamma - \gamma - t$ **coincidence cube**: (For intermediate analysis looking at time difference lifetimes)
- **seven separate $\gamma - \gamma - \gamma$ coincidence cubes**: (Out-of-beam), Gated on different out-of-beam regions for lifetime measurements (see section 3.4).

Data from ^{185}Re , ^{187}Re and ^{192}Os targets were also available under essentially identical conditions. All the above are used for general initial analysis and level scheme construction. In addition, a very large variety of more complex specialised sorts were performed to isolate specific structures in specific nuclei. These were performed by the author using codes developed by Dr Greg Lane. Details of these specialised sorts are given as appropriate in Chapters 4 and 5.

Results and level scheme for ^{183}Ta

This chapter focuses on previous information known for ^{183}Ta as well as the current experimental findings.

4.1 Previous studies on ^{183}Ta

Excited states in ^{183}Ta were previously studied by Shizuma *et al.* [Shi09] using the two-neutron transfer reaction $^{181}\text{Ta}(\text{¹⁸O}, \text{¹⁶O})$. Figure 4.1 shows the level scheme they obtained. The rotational bands built on the $7/2^+[404]$, $9/2^-[514]$ and $5/2^+[402]$ proton states were reported up to moderate spins and an isomeric state with $\tau = 1300(400)$ ns that feeds towards the $9/2^-[514]$ structure via a possible γ -vibrational band was also reported. No discrete γ -ray transitions were observed to depopulate the isomer and so its excitation energy remains unknown. The tentative spin, parity and configuration assignments for the isomer were based on assumptions made concerning the unobserved transition depopulating it, as well as the analysis of the $(13/2^-)$ band.

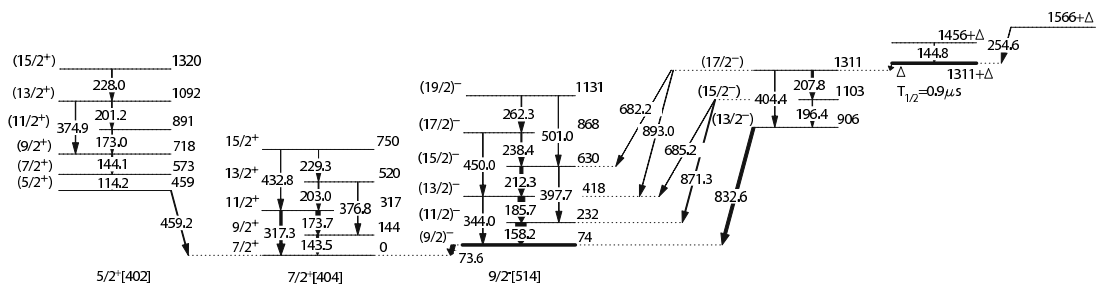


Figure 4.1: Partial level scheme for ^{183}Ta established by Shizuma *et al.* [Shi09] showing rotational bands built upon the low-lying proton states and the $\tau = 1300$ ns isomer.

4.2 Current analysis and results for ^{183}Ta

4.2.1 New states in ^{183}Ta

The $5/2^+[402]$ band previously reported by Shizuma *et al.* [Shi09] is not observed in either the prompt or delayed data in the current work, presumably because it is not fed by a higher-lying isomer and is also sufficiently non-yrast to not be populated strongly in the deep-inelastic reaction. However, several new γ rays have been placed below and above the 1300 ns isomer and a new complete level scheme feeding via this isomer has been constructed as shown in Figure 4.2; note that lifetimes are given in this figure, not halflives. Also, note that the 1300(400) ns isomer lifetime from Ref. [Shi09] has been remeasured in this work (see Sect. 4.2.2) and the new value of 1200 ns is shown in Fig 4.2 and used to describe the isomer from now on. The properties of all the γ rays in this level scheme are summarised in Table A.1. This section is focused on the new in-beam and out-of-beam transitions, and their coincidence relationships, that establish the level scheme. In the initial analysis, several gate combinations were first set in the out-of-beam region using the known γ rays below the 1300 ns isomer. All the known γ rays fed by the isomer were observed, confirming the population of ^{183}Ta in the $^{136}\text{Xe} + ^{186}\text{W}$ deep-inelastic reaction.

Figure 4.3(a) shows a sum of several spectra from the out-of-beam data, double-gated on known transitions in the $9/2^-[514]$ band. New transitions are observed at 443, 465 and 674 keV while the known 73 keV transition clearly confirms the population of the $7/2^+[404]$ ground state. A representative coincidence spectrum double gated on the known transitions of 158 and 238 keV in the $9/2^-[514]$ band is shown in Figure 4.3(b). The absence of the 262 keV γ ray (see Figure 4.1) implies that the two new transitions at 443 and 465 keV directly feed the 867 keV level depopulated by the 238 keV transition.

The absence of the 443 keV γ ray in Figure 4.3(c) implies that the 443 and the 465 keV transitions are parallel. The sum across the 158, 186, 212, 238 and

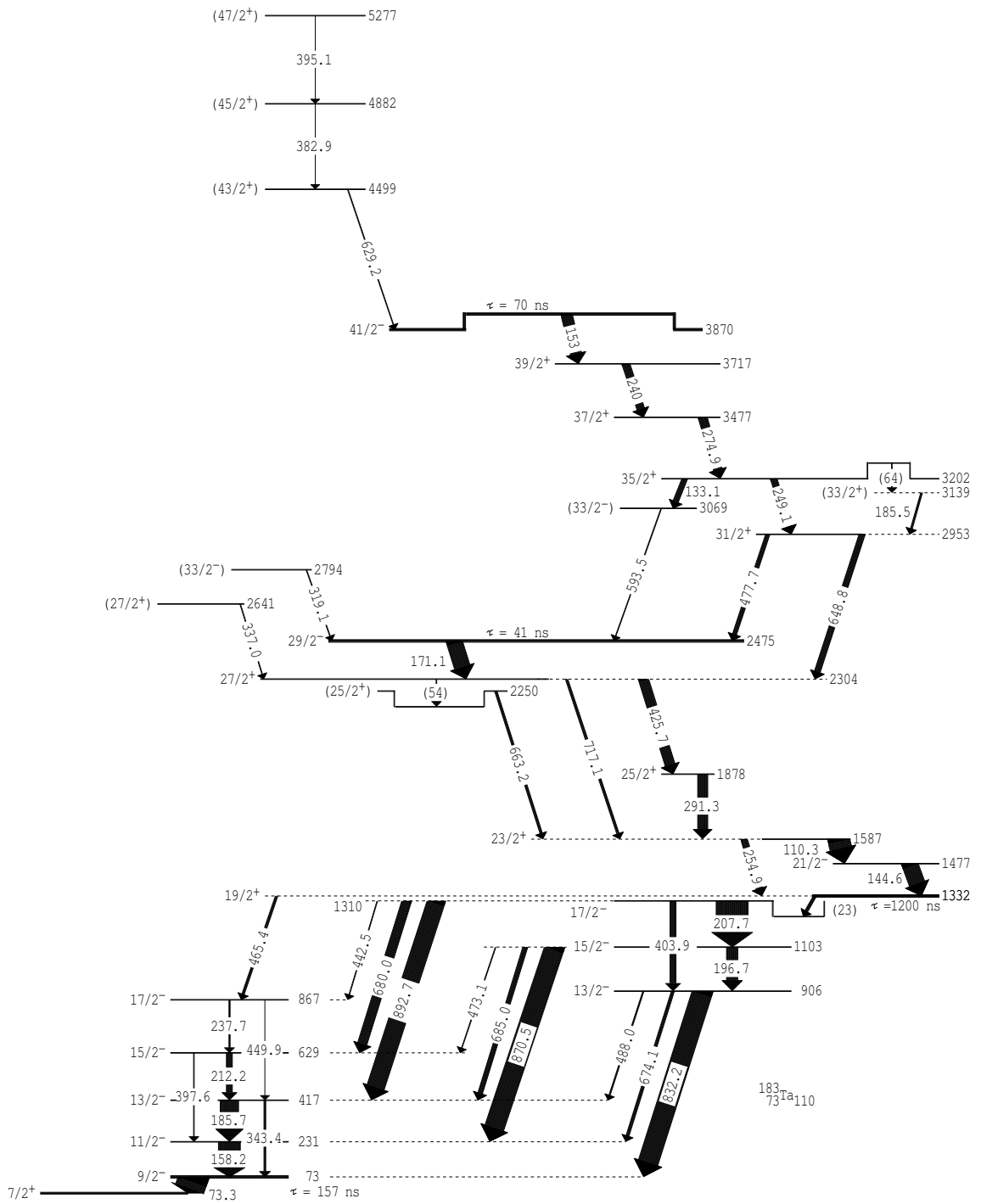


Figure 4.2: New level scheme for ^{183}Ta deduced in the current work. New γ rays of 443 and 465 keV established the unobserved 23 keV transition from the previously known isomer with a lifetime now measured as 1200 ns. Extensive new structures feeding the isomer are now observed.

443 keV cascade is equal to that across the 833, 404 keV cascade, implying that the 443 and 404 keV transitions directly depopulate the same (1310 keV) level.

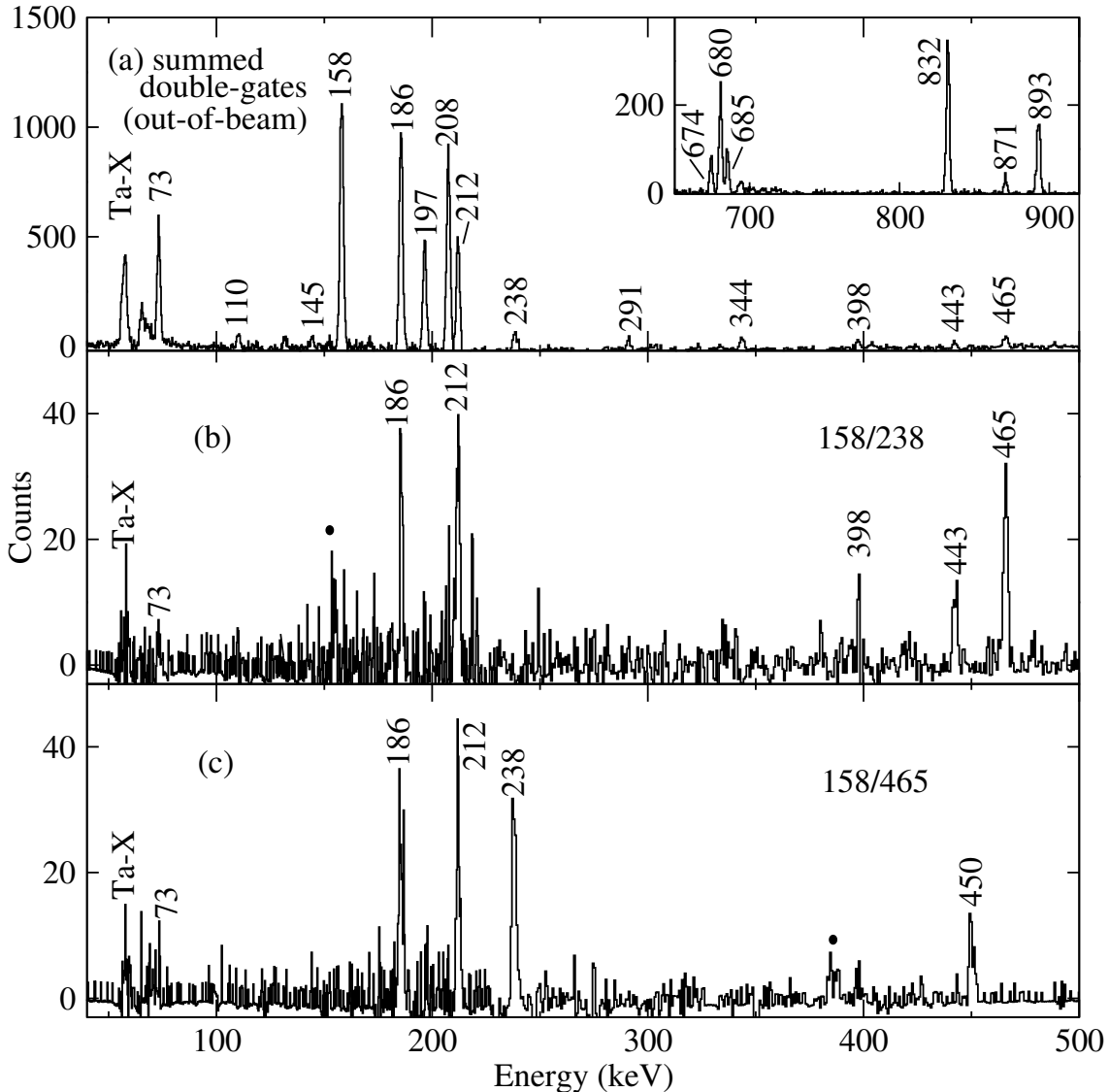


Figure 4.3: Out-of-beam, double-gated coincidence spectra with dots representing unknown contaminants. (a) Summed spectra from double gates on the known γ rays from Ref. [Shi09], (b) The 158/238 coincidence spectrum shows new 465 and 443 keV γ rays in ^{183}Ta . (c) The 158/465 coincidence spectrum shows that the 443 keV transition is parallel to that at 465 keV.

While Shizuma *et al.* [Shi09] did not discover the 443 and 465 keV transitions they suggested the energy of the unobserved isomeric transition to be less than 50 keV for $E1$ or 100 keV for $M1$ and $E2$ alternatives. Two conclusions can be drawn from these observations, (a) the 465 keV γ ray directly depopulates the isomer, and (b) 23 keV is the energy of the unobserved transition that also depopulates the 1332 keV isomer and takes the majority of the intensity.

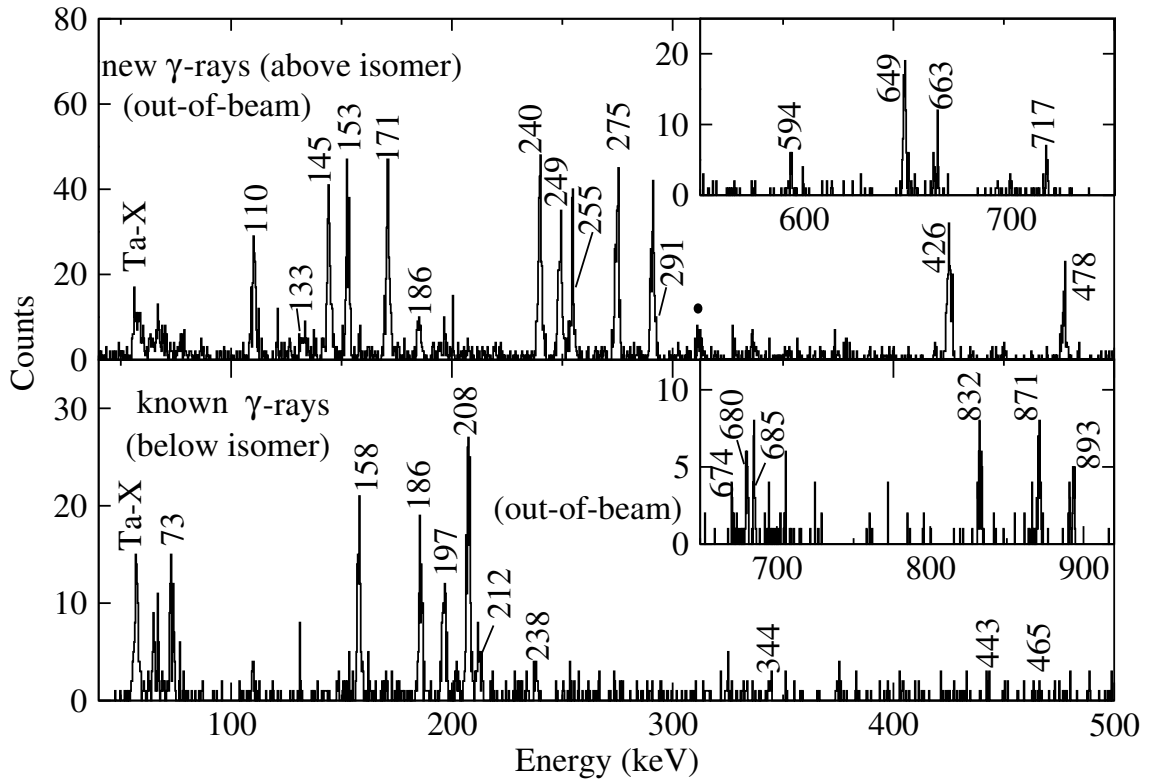


Figure 4.4: (a) New γ rays obtained by double-gating on the transitions below the 1332 keV isomer and projecting the preceding transitions in the out-of beam data. (b) Known γ rays obtained by double-gating on the new transitions and projecting transitions that arrive later in time. These results suggest the presence of a new isomer feeding the known one at 1332 keV.

By selecting pairs of transitions below the 1332 keV isomer that exhibit clean double-gates and projecting γ rays arriving earlier in time by 30-800 ns, but still out-of-beam, a total of 15 new γ rays were observed that must decay from a higher-lying isomer. The projected early γ rays are shown in Figure 4.4(a). Of these, the 145 and 255 keV transitions were previously observed by Shizuma *et al.*, but only in the prompt data, suggesting they directly feed the isomer. By selecting pairs of clean double gates from this new set of transitions and projecting γ rays arriving later in time by 30-800 ns, all known γ rays below the 1332 keV isomer were observed (see Figure 4.4(b)). These observations suggest that at least one other isomer lies above the 1332 keV state. Slight variations on this general procedure have been applied to search across all isomers found.

Figure 4.5(a) shows a double gate on the 145 and 426 keV transitions. The 255, 663 and 717 keV γ rays are not observed in the spectrum. The sum of 110 and

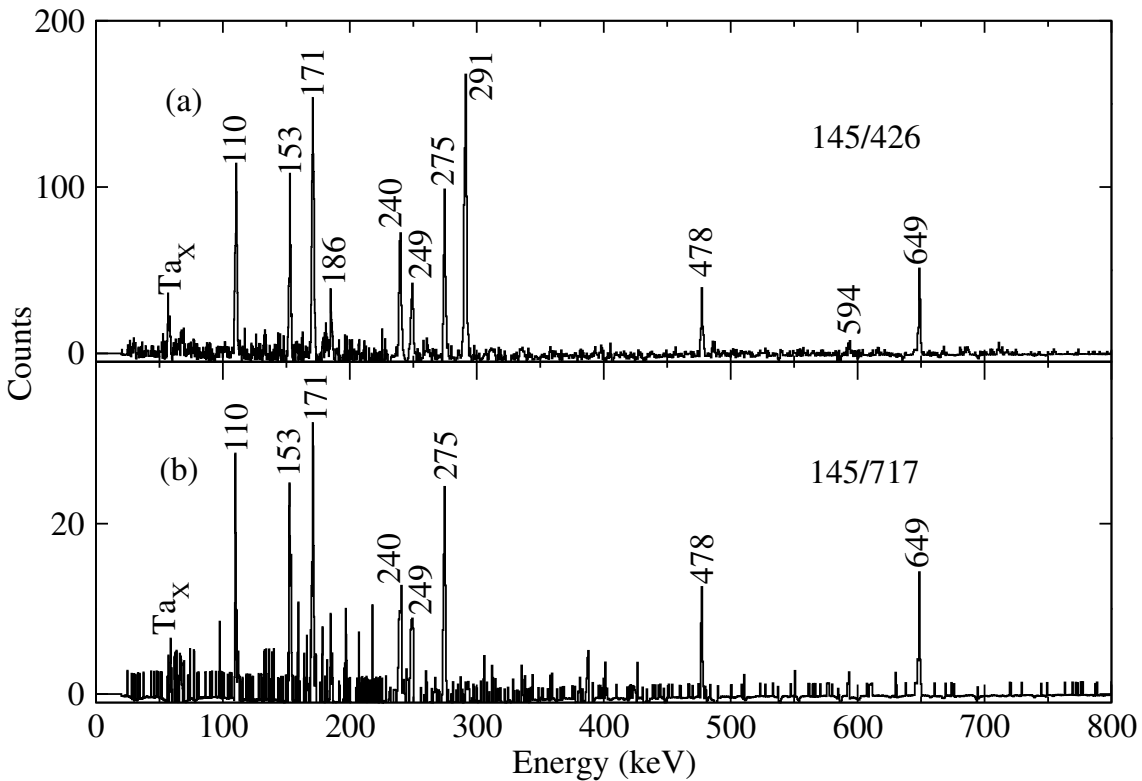


Figure 4.5: (a) and (b) show double-gated spectra from the out-of-beam cube demonstrating coincidence relationships for the new transitions. Gated spectra such as these enabled the ordering of all the γ -ray transitions between the 1332 and 2475 keV levels as shown in the level scheme.

145 is 255 keV, implying that the 110 and 145 keV transitions are parallel to the 255 keV γ -ray, which is confirmed by coincidence relationships. A double gate on 145 and 717 keV as shown in figure 4.5(b) reveals the absence of 291 and 426 keV γ rays whose sum is equivalent to 717 keV. As a result, the 291 and 426 keV transitions were placed parallel to both those at 663 and 717 keV. The unobserved 54 keV transition was inferred from the difference between parallel 717 and 663 keV transitions. Positive identification of a γ ray at this energy is problematic because of the proximity to the tantalum and tungsten (target) X-rays, and the high expected level of internal conversion at such a low energy. The ordering of the 145/110 and 291/426 keV cascades was based on their measured intensities in the prompt data, while that for the 54/663 keV cascade was based on the predicted states from model calculations, as will be discussed later in Chapter 7.

The double gate 649/249 keV shows the absence of 133, 171, 186, 478 and 594 keV

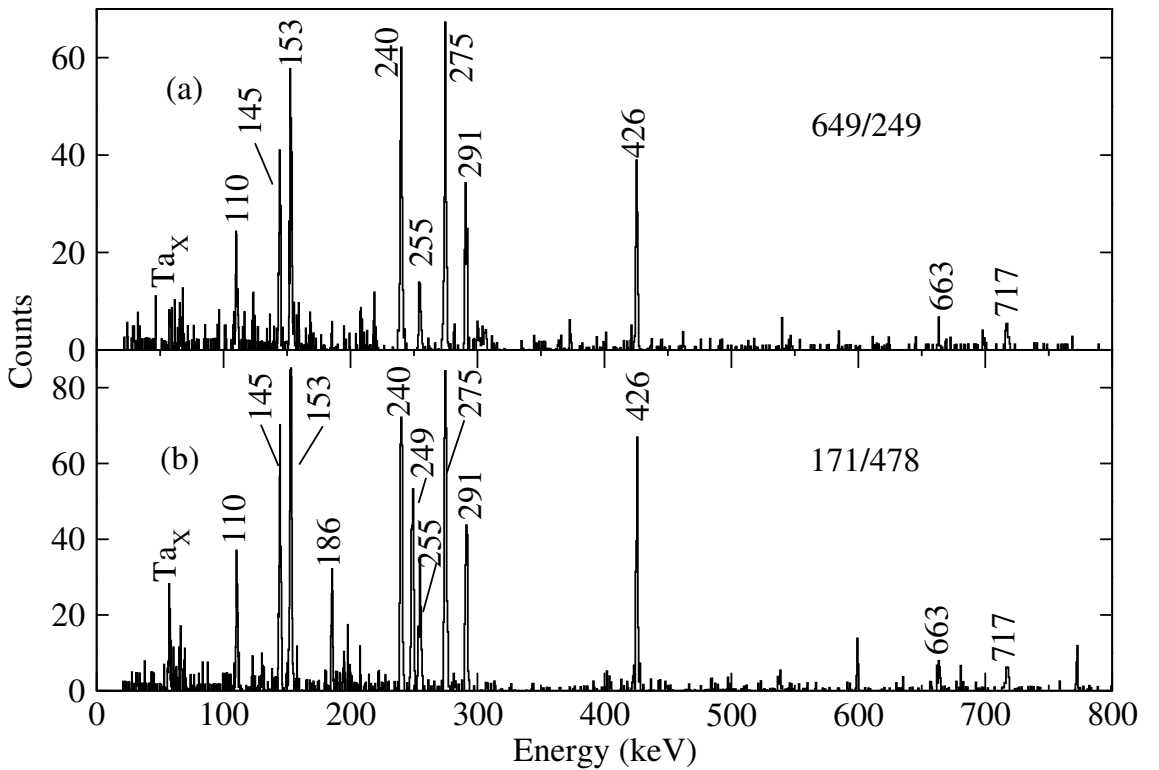


Figure 4.6: (a) and (b) show double-gated spectra from the out-of-beam cube demonstrating coincidence relationships for the new transitions. Gated spectra such as these enabled the ordering of all the γ -ray transitions between the 2304 and 3202 keV levels as shown in the level scheme.

transitions, while the 171/478 keV double gate shows the absence of 133, 594 and 649 keV γ rays, see Figure 4.6. These coincidence relations enabled the ordering of γ -rays between the 2304 and 3202 keV levels as shown in Figure 4.2. The unobserved 64 keV transition is inferred from the energy difference between the parallel 186 and 249 keV γ rays. Similar to the 54 keV transition, its identification is problematic because of its proximity to the tantalum and tungsten X-rays. The order of the 64 and 186 keV transitions remains unclear.

The observed time differences measured between these γ rays, as shown in section 4.2.2 below, further confirms the ordering in the level scheme. For example, the fact that the 478 keV transition feeds an isomer above the 145, 171, 291 and 426 keV γ rays can be clearly seen in the measured time differences. Similarly, the ordering of the 153, 240 and 275 keV cascade relative to the rest of the transitions between the 3202 and the 1332 keV levels is based on the measured time differences

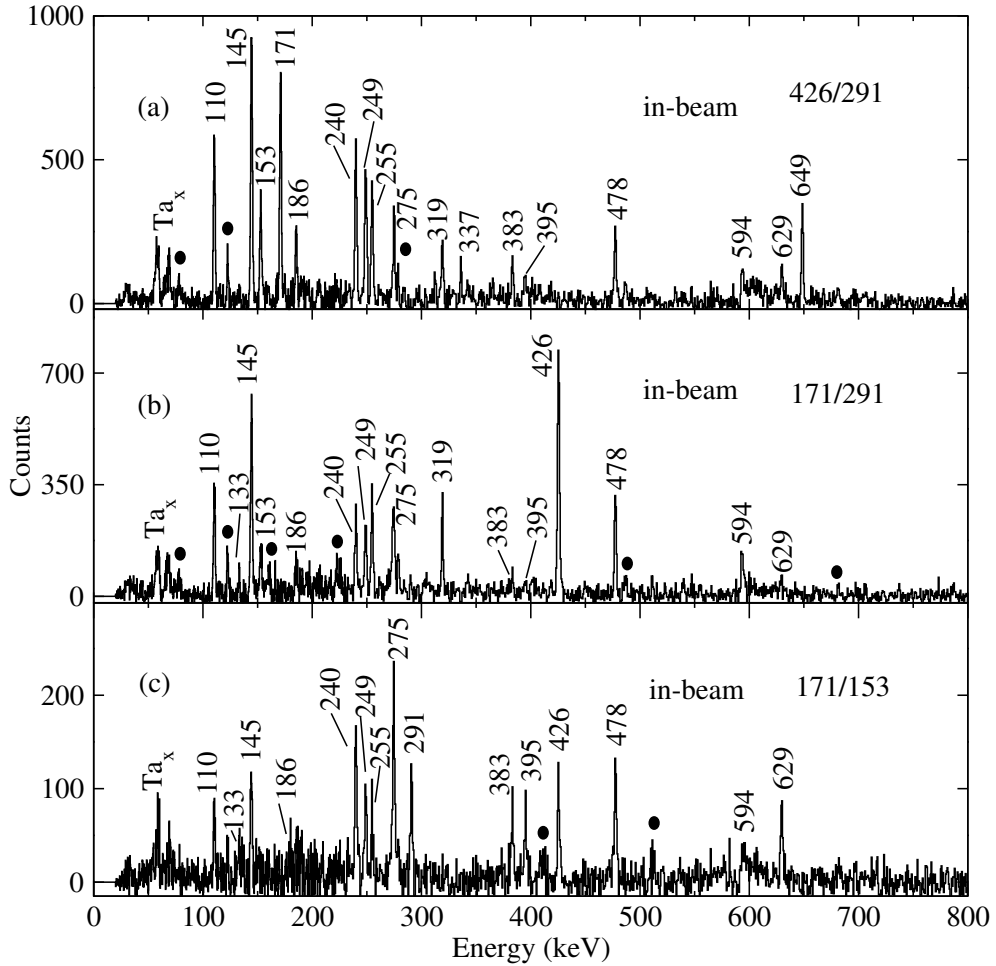


Figure 4.7: (a)-(c) In-beam, double-gated spectra obtained from in-beam cube, showing prompt feeding γ rays at 319, 337, 383, 395 and 629 keV.

(see Figure 4.11 (f)-(h)), while the ordering of these three transitions within the cascade is based on the measured in-beam intensities, with the highest in-beam intensity measured for the 275 keV γ ray, thus placing it at the bottom of the cascade. The 153 keV transition, having the lowest in-beam intensity, is placed directly below the 3870 keV level.

Figure 4.7 shows in-beam spectra, double-gated on some of the new transitions above the 1332 keV level. Five additional transitions at 319, 337, 383, 395 and 629 keV, are observed. The absence of the 337 keV γ ray in Fig 4.7(b) and (c) places it parallel to the 171 keV transition, while the absence of 319 and 337 keV lines in Figure 4.7(c) suggests that the two γ rays are parallel to all transitions above the

2475 keV level. The placement of the 383, 395 and 629 keV transitions above the 3870 keV level is confirmed from Figure 4.7(c), as well as by projecting early γ rays that feed this level.

4.2.2 Lifetime measurements in ^{183}Ta

The lifetime for the 73 keV state in ^{183}Ta has been measured twice previously, yielding $\tau=146(28)$ ns [Shi09] and $\tau=154(16)$ ns [Fir92]. In the current work, a value of $\tau=157(4)$ ns was deduced from time differences between the 73 keV isomeric transition and the 832, 871, 893 keV feeding transitions, in good agreement with the previous measurements, but with a higher precision (see Figure 4.8).

A lifetime of $\tau=1300(400)$ ns for the 1332 keV isomer was previously reported by Shizuma *et al.* [Shi09] following from particle- γ time-difference measurements. The long lifetime of this state yielded insufficient statistics between the populating and the depopulating transitions in the present work, and hence a time-difference measurement was not possible. Instead, the lifetime of this state was measured from the intensity yields of the depopulating transitions in seven γ - γ - γ cubes gated on contiguous regions between the beam bursts. Figure 4.9 shows the lifetime of $\tau=1200(140)$ ns deduced for the isomer, consistent with the previously reported

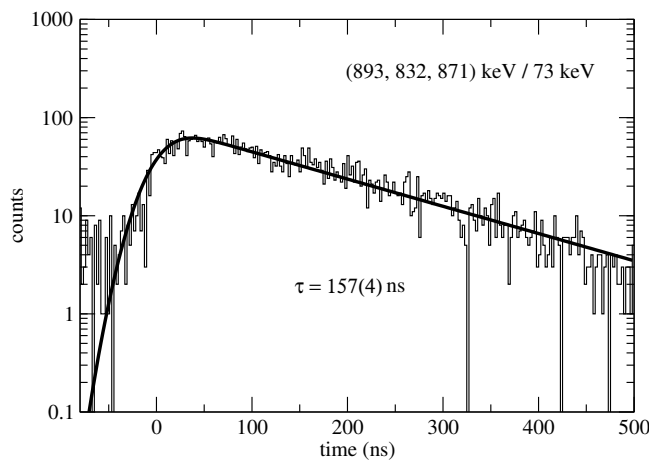


Figure 4.8: Summed spectrum of time differences between the 73 keV γ ray (stop) and the 832, 893 and 871 keV γ rays (start), yielding the lifetime of the 73 keV isomer in ^{183}Ta as $\tau=157(4)$ ns.

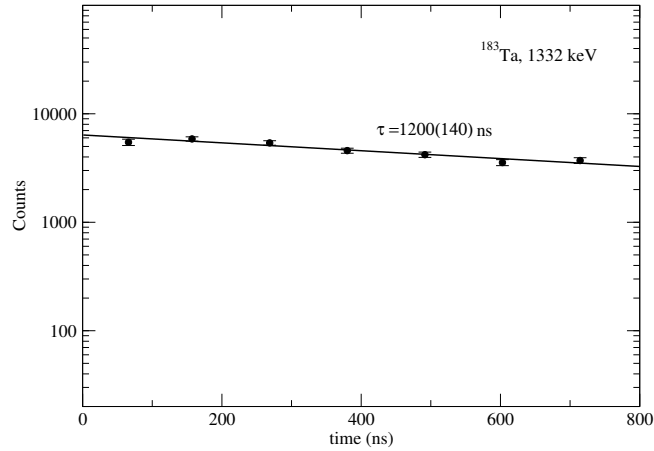


Figure 4.9: Representative decay curve for the 1332 keV isomer in ^{183}Ta , derived from the intensity variation of the depopulating transitions across seven γ - γ - γ -cubes in the out-of-beam region. A lifetime of $\tau=1200(140)$ ns was deduced for this state.

value. The lifetime of most states above the 1332 keV level were directly probed from time-difference spectra between the feeding and the depopulating transitions.

Figures 4.10 and 4.11 show time difference spectra from several γ -ray pairs between

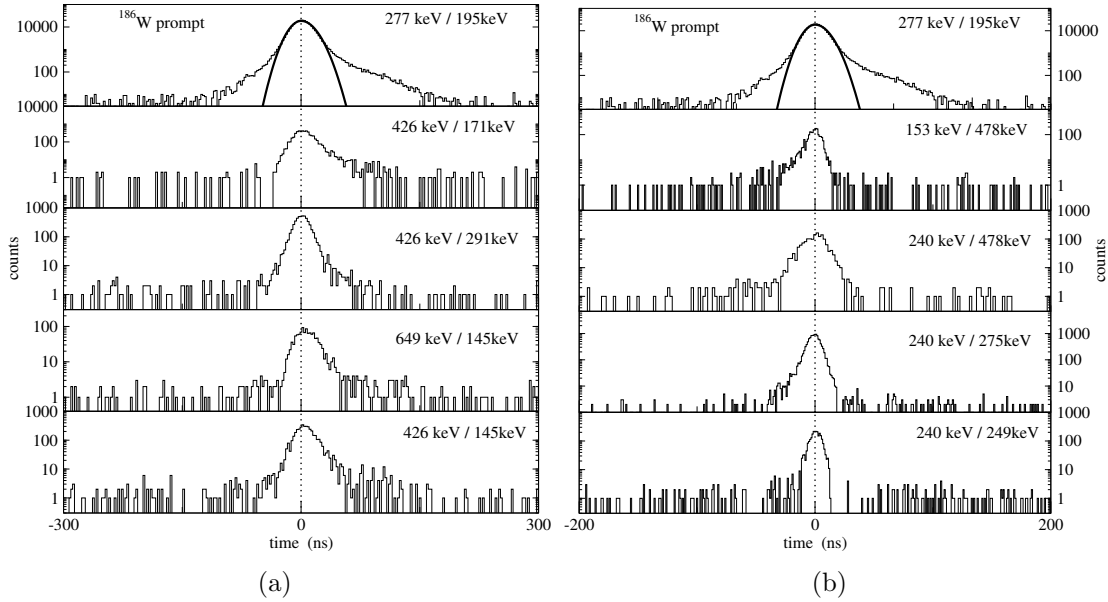


Figure 4.10: Time difference spectra for γ -ray pairs in the region between (a) the 1332 and 2475 keV levels and (b) the 2475 and 3870 keV levels. The spectra are compared to the spectrum from a known prompt γ -ray pair in the strongly populated target nucleus ^{186}W . The absence of significant centroid shifts suggests none of the levels involved are isomeric.

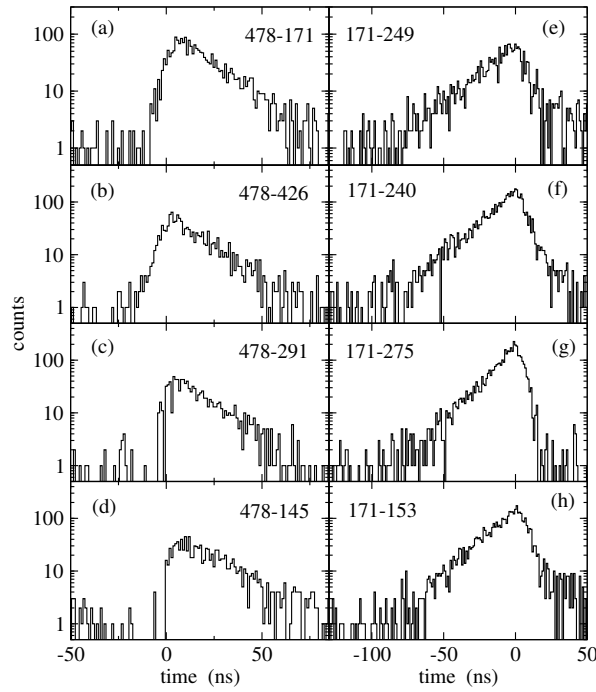


Figure 4.11: (a)-(h). Time-difference spectra between γ -ray pairs across the 2475 keV state. The first energy is the starting transition, while the second is the stopping transition. The time spectra confirm that the 2475 keV state is isomeric and also establish the separation of the feeding and depopulating transitions on each side of the isomer.

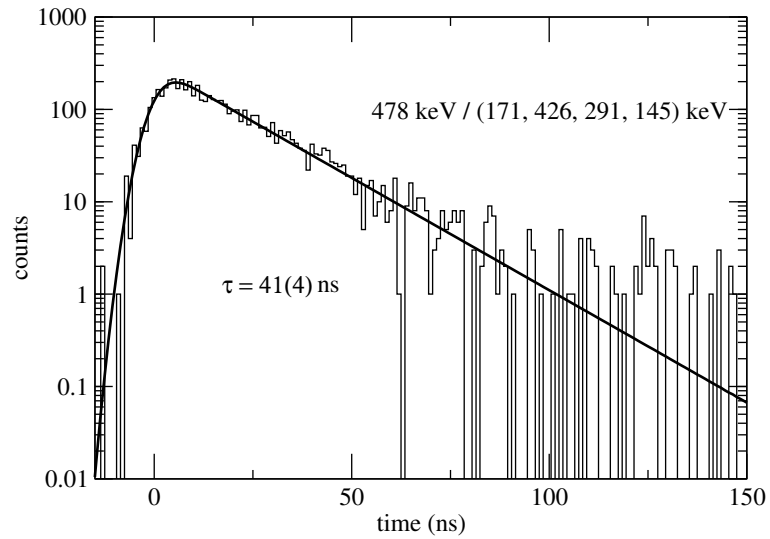


Figure 4.12: Lifetime curve for the 2475 keV isomer in ^{183}Ta , produced from a sum of time difference spectra starting on 478 keV and stopping on 171, 426, 291 and 145 keV transitions. A lifetime of $\tau = 41(4)$ ns can be deduced.

the 1332 and 3870 keV levels. From both centroid shift and slope measurements, no measurable lifetimes are observed for the intermediate states between these two

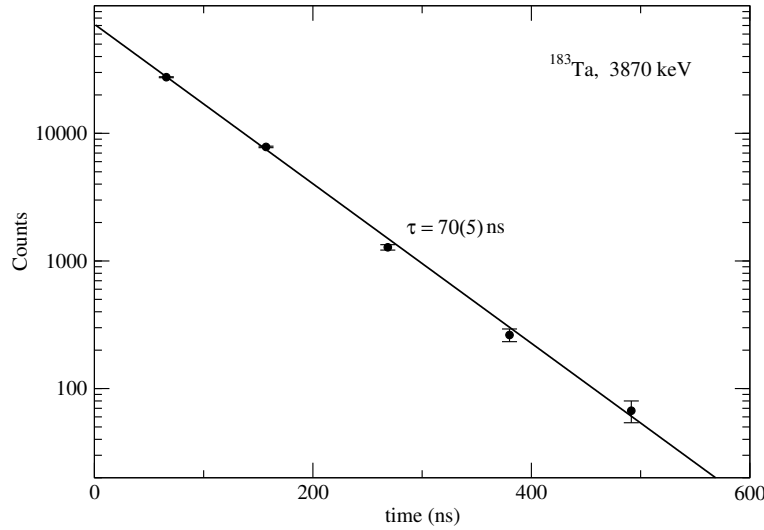


Figure 4.13: Decay curve for the 3870 keV isomer in ^{183}Ta , derived from the coincidence intensity variation of the depopulating transitions in the out-of-beam region. A lifetime of $\tau=70(5)$ ns was deduced.

levels except for the 2475 keV level as shown in Figure 4.11. A value of $\tau = 41(4)$ ns was deduced from time differences between the 478 keV γ ray and the 171, 426, 291 and 145 keV transitions (see the summed spectrum in Figure 4.12). The time-difference spectra also confirm the ordering of all the transitions above the 1332 keV level. From the coincidence intensity variation between the beam bursts, the mean lifetime of the uppermost isomer at 3870 keV was found to be 70(5) ns (see Figure 4.13).

4.2.3 Spin and parity assignments

7/2⁺[404], ground state

The rotational states built on this level that were reported by Shizuma *et al.* [Shi09] are not observed in the present work which is more sensitive to states fed by isomers. The presence of the known 73 keV transition confirms the population of the ground state in the current data. From the intensity balance between the 73 keV transition and the 158 keV transition, the total conversion coefficient (see Figure 4.14) for the 73 keV γ ray was deduced. The calculation accounts for the $\delta=0.196(7)$ mixing

ratio for the 158 keV transition as deduced from the in-band branching ratios (see Chapter 7). Although the expected value falls outside the measured uncertainty, $E1$ multipolarity is clearly preferred for this transition, consistent with Ref. [Shi09].

9/2⁻[514] isomer at 73 keV

Shizuma *et al.* [Shi09] previously assigned the 9/2⁻[514] configuration to the band built upon this isomer based on the in-band decay properties. In the present work, the 9/2⁻ band-head assignment is confirmed from the $E1$ assignment to the 73 keV transition.

19/2⁺ isomer at 1332 keV

Shizuma *et al.* [Shi09] made a tentative $K^\pi=19/2^+$ assignment for the 1200 ns isomer based on K -hindrance considerations and did not observe the depopulating transition. Although the direct depopulating transition at 465 keV has now been observed, the poor statistics for this weak branch meant that no angular correlation or conversion coefficient measurements were possible. To determine the multipolarity of the 23 keV and 465 keV transitions, several possible spins and parities of $K^\pi = 19/2^\pm$ or $K^\pi = 21/2^\pm$ were assumed for the 1332 keV isomeric state and the ambiguity eliminated by inspection of the implied transition strengths of the depopulating decays.

The procedure followed for each K^π case is that the implied multipolarities of the 23 and 465 keV transitions were deduced, and the γ -ray intensities were determined based on the measured γ -ray intensity for the 465 keV transition, whereas intensity balances across the 1310 keV level and theoretical conversion coefficients were used to deduce the γ -ray intensity for the 23 keV transition. These intensities are derived from the 200-800 ns delayed γ -ray spectrum, projected relative to the 1332 keV isomer.

The transition strengths and the reduced hindrances thus obtained for the 23 and 465 keV transitions are shown in table 4.1. Since $E1$ transitions are already

Table 4.1: Transition strengths and corresponding reduced hindrances for the 465 and 23 keV transitions, assuming different spins and parities for the 1200 ns isomeric state. The intensity of the unobserved 23 keV transition is inferred from the intensity balance across the 1310 keV state and implied conversion coefficients. An intensity limit of <30 counts was assumed for both the unobserved 230 and 703 keV transitions.

I^π	E_γ (keV)	XL	I_γ	α_T	$B(XL)$ (W.u)	F_W	ν	f_ν
$19/2^-$	22.7 ^b	<i>M1</i>	2.29(15) ^b	57.46	$3.68(54) \times 10^{-5}$	$2.7(4) \times 10^4$	2	165(10)
	465.4	<i>M1</i>	4.1(8)	0.0628	$7.7(19) \times 10^{-9}$	$1.3(3) \times 10^8$	4	115(8)
	230 ^b	<i>E2</i>	< 0.93 ^b	0.1876	$< 1.8 \times 10^{-4}$	$> 5.6 \times 10^3$	1	> 5600
	703 ^b	<i>E2</i>	< 1.56 ^b	0.0090	$< 1.1 \times 10^{-6}$	$> 9.1 \times 10^5$	3	> 97
$19/2^+$	22.7 ^b	<i>E1</i>	27.01(178) ^a	3.95	$4.1(6) \times 10^{-6}$	$2.44(37) \times 10^5$	2	494(37); 5.0(4) ^a
	465.4	<i>E1</i>	4.14(83)	0.00799	$7.3(18) \times 10^{-11}$	$1.4(3) \times 10^{10}$	4	342(21); 34(2) ^a
	230 ^b	<i>M2</i>	< 0.93 ^b	1.98	$< 1.4 \times 10^{-2}$	> 71	1	> 71
	703 ^b	<i>M2</i>	< 1.56 ^b	0.0592	$< 8.4 \times 10^{-5}$	$> 1.2 \times 10^4$	3	> 22
$21/2^+$	22.7 ^b	<i>M2</i>	0.015(1) ^b	8904	$2.1(3) \times 10^1$	$4.8(7) \times 10^{-2}$	2	0.2
	465.4	<i>M2</i>	4.14(83)	0.2004	$1.5(4) \times 10^{-3}$	$6.7(18) \times 10^2$	4	5.0(3)
$21/2^-$	22.7 ^b	<i>E2</i>	0.036(25) ^b	3790	$4.7(7) \times 10^{-1}$	2.1(3)	2	1.5(1)
	465.4	<i>E2</i>	4.14(83)	0.0242	$1.5(4) \times 10^{-5}$	$6.7(18) \times 10^4$	4	16(1)

(a): Italic values are reduced hindrances with a 10^4 normalisation factor included for the hindered $E1$ transitions.

(b): Energies and intensities of unobserved 23, 230 and 703 keV transitions.

hindered by large factors, the reduced hindrances for $E1$ transitions were calculated both with (in italics) and without (normal font) an additional factor of 10^4 in the nominal single particle hindrance. Reasonable values for the reduced hindrances (expected range 30-300) are only obtained for a $19/2^+$ assignment to the isomeric state. Further discussion on the possibilities and this deduction are given below.

For $K^\pi=19/2^-$, there are potential $E2$ transitions of 703 and 230 keV that should directly depopulate the isomer and feed the 629 and 1103 keV states, respectively. Such transitions were not observed in any of the (various) out-of-beam, double-gated spectra or in the delayed spectrum measured across the isomer. Hence, upper intensity limits were deduced, giving limits on the reduced hindrances for the possible 703 and 230 keV transitions of $f_\nu > 97$ and $f_\nu > 5600$ respectively. The latter limit effectively rules out the $19/2^-$ assignment.

The $21/2^+$ possibility can be ruled out on the basis of the very low values of the reduced hindrances for the 465 and 23 keV transitions, both of which fall outside the expected range.

For the $21/2^-$ alternative, both notional $E2$ decays of 23 and 465 keV are fast, however, they could have been enhanced by mixing between the isomer and the $21/2^-$ state in the $9/2^-$ band, resulting in the low reduced hindrances. If the entire strength of the 465 keV transition were due to a collective admixture of the $K^\pi = 9/2^-$ wavefunction into the isomeric state wavefunction, a mixing matrix element of 23 eV would be implied, as deduced using the method described in [Dra06, Kon04]; this is a reasonable value. However, in this scenario, there should also be a 203 keV $M1/E2$ transition from the isomer to the known $19/2^-$ band member at 1131 keV, with a branching ratio relative to the 465 keV transition that is consistent with the collective properties expected (and observed) in the $9/2^-$ -[514] band.

For the decays from the isomer to reproduce the average $|g_K - g_R|$ for the in-band decays, the intensity ratio $\lambda = I_\gamma(\Delta I = 2; 465)/I_\gamma(\Delta I = 1; 203)$ would have to be 1.07(13), but the observed limit is $\lambda > 2.57$, suggesting $K^\pi = 21/2^-$ is unlikely. It should be noted however, that across the light, odd-mass tantalum isotopes, including neighbouring ^{185}Ta [Lan09], $21/2^-$ isomers are systematically observed, implying that this spin and parity assignment might still be a candidate.

The remaining possibility for the spin assignment is $19/2^+$. The measured reduced hindrances for the 23 and the 465 keV transitions are within acceptable limits, as are the limits for the possible 703 and 230 keV $M2$ transitions of $f_\nu > 22$ and $f_\nu > 71$, respectively. The multi-quasiparticle calculations in Chapter 6 will further demonstrate that the $19/2^+$ assignment is favoured for the 1332 keV isomer.

States at 1477, 1587 1878, 2250 and 2304 keV

For most decays from these states, the statistics were sufficient for effective angular correlations and for conversion coefficient measurements via intensity balances. Figure 4.14 shows those conversion coefficients that could be evaluated from intensity balances, while Figures 4.15 and 4.16 show the angular correlations measured for many of the transitions above the 1332 keV isomer. The conversion coefficients for both the 145 and 110 keV transitions suggest $E1$ character, implying $21/2^-$ and $23/2^+$ for the 1477 and 1587 keV levels, respectively. This observation is also consistent with the $\gamma\gamma$ -correlation results from which a pure stretched dipole for the 110 keV transition is implied, assuming a pure stretched dipole for 145 keV. The apparent absence of a lifetime for the states decaying by these low-energy $E1$ transitions is unusual and difficult to understand and will be explored further in section 8.3.

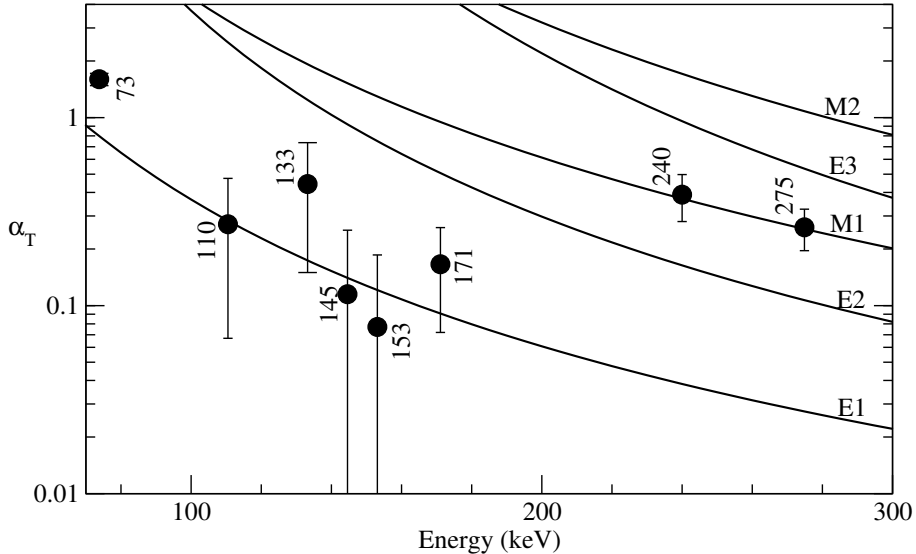


Figure 4.14: Total conversion coefficients deduced from intensity balances for some of the transitions depopulating states in ^{183}Ta . The plot compares the experimental observations (data points with error bars) to theoretical expectations from Ref. [Kib08]

With the suggested pure $E1$ (or at least pure dipole) nature of the 110 keV transition, the 291-110 keV correlation implies a non-zero mixing ratio of $\delta = 0.24(7)$ for the 291 keV transition and hence either an $E2/M1$ or $M2/E1$ multipolarity. Due to the absence of a measurable lifetime, the $M2/E1$ possibility seems unlikely, so the

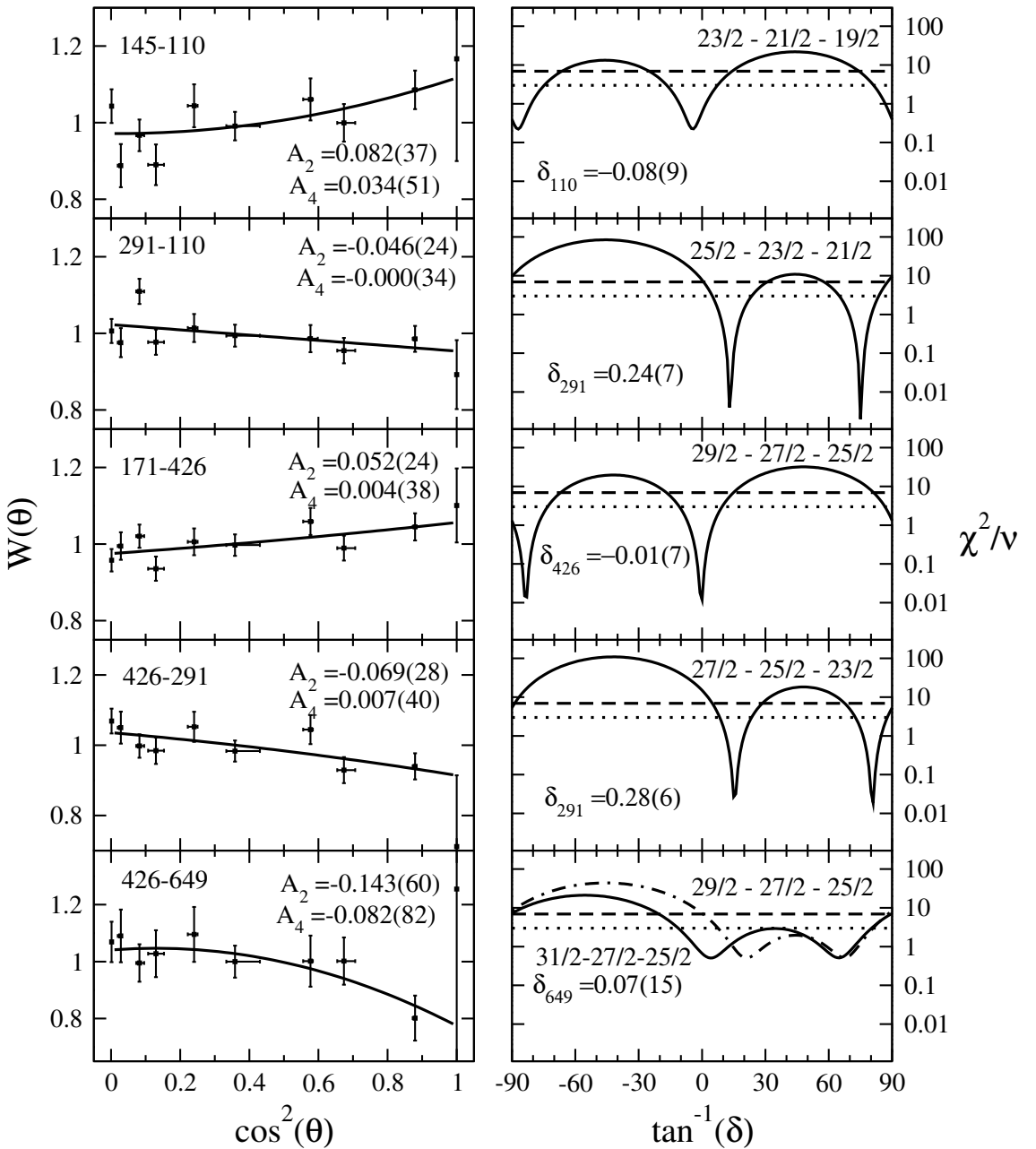


Figure 4.15: Angular correlations and deduced mixing ratios for selected transition pairs between the 1332 and 2953 keV states in ^{183}Ta . The non-zero mixing ratio for the 291 keV $\Delta I = 1$ transition suggests a possible collective state at 1878 keV.

1878 keV level is suggested to have $I^\pi = 25/2^+$ and be a collective state rather than an intrinsic state. With the total conversion coefficient measurement suggesting an $E1$ multipolarity for the 171 keV transition, the 171-426 angular correlation supports a pure stretched dipole assignment for the 426 keV γ ray. Thus the 426 keV could be a pure $M1$ or $E1$, with the latter implying that the 2304 keV level would be

$27/2^-$ and hence the 717 keV would be $M2$. This is highly unlikely considering the short lifetime limit ($\tau < 5$ ns) measured for the 2304 keV level (see Figure 4.10) and hence $I^\pi = 27/2^+$ is preferred.

29/2⁻ isomer at 2475 keV

The isomer decays via the 171 keV, $E1$ transition to a $27/2^+$ state, leading to a $29/2^-$ spin and parity assignment.

States at 2953, 3069, 3139, 3202, 3477 and 3717 keV

A dipole-dipole correlation between the 426 and 649 keV γ rays shows mixing for the 649 keV transition. Since an $E2/M1$ mixture is more favoured as compared to $M2/E1$, only $E2/M1$ character need be considered. This would imply that there should be $E2$ crossover transitions of 703 and 1075 keV to the 2250 and 1878 keV levels, but such transitions are not observed. On that basis, the $E2/M1$, mixed dipole character is unlikely, although it cannot be ruled out completely. A quadrupole assignment for the 649 keV transition gives a zero mixing ratio for this transition from the angular correlation, consistent with either pure $E2$ or $M2$ character. An $M2$ assignment would require a much longer lifetime for the 2953 keV level, hence an $E2$ multipolarity is assigned and implies $I^\pi = 31/2^+$ for the 2953 keV state. The $31/2^+$ assignment is also supported by the information from the 240-478 keV correlation.

The 3202 keV state decays via three branches of 133, 249 and (unobserved) 64 keV. The deduced conversion coefficient for the 133 keV line is consistent with an $E1$ assignment for this transition. The 649-249 angular correlation with 649 keV as a pure quadrupole shows a non-zero mixing ratio for a 249 keV dipole (see Fig. 4.16), suggesting an $E2/M1$ character, since $M2/E1$ is ruled out by the absence of a lifetime. In such a scenario, an $E2$ crossover to the 2953 keV state is anticipated, however no such transition is observed. In addition, a mixed dipole 249 keV transition would require one of either the 185 keV or (unobserved) 64 keV γ ray to be unstretched. The correlation shows no mixing for a 249 keV γ ray having

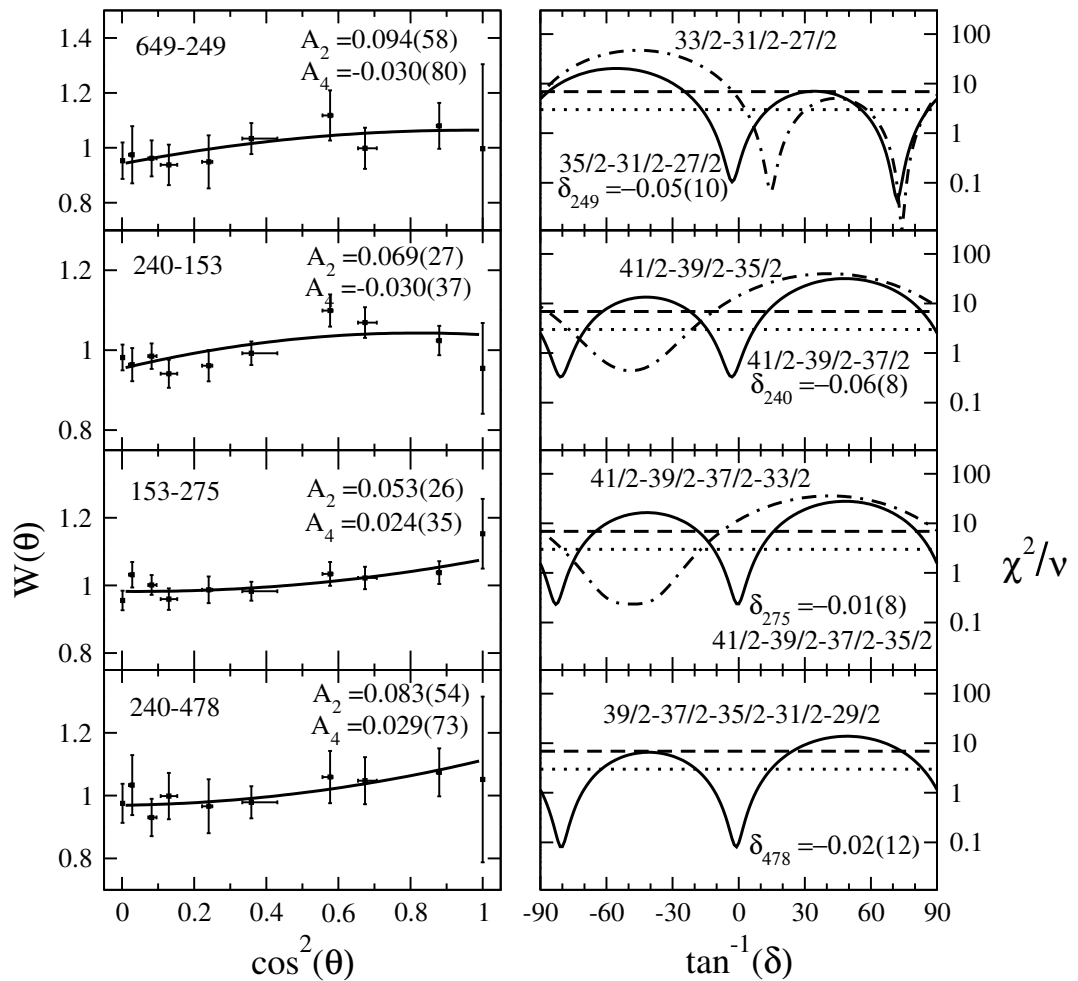


Figure 4.16: Angular correlations and deduced mixing ratios for selected transition pairs between the 2304 and 3870 keV levels in ^{183}Ta .

quadrupole character, consistent with an $E2$ multipolarity, since the $35/2^+$ level has no observed lifetime. The 133 keV $E1$ transition defines $I^\pi=(33/2^-)$ for the 3069 keV level.

Intensity balances across the 3477 and 3717 keV states give deduced conversion coefficients for the 153, 240 and the 275 keV transitions, suggesting $M1$ character for both 240 and 275 keV while the 153 keV γ ray is predicted to be $E1$ (see Figure 4.14). The angular correlations suggest pure stretched dipole character for both the 240 and 275 keV transitions (see Figure 4.16), consistent with $M1$ multipolarities. This gives $37/2^+$ and $39/2^+$ for the 3477 and 3717 keV levels, respectively.

41/2⁻ isomer at 3870 keV

The isomer decays via a single $E1$ transition of 153 keV to the 39/2⁺, 3717 keV state. Hence, $I^\pi = 41/2^-$ is proposed for the 70 ns isomeric state.

Results and level scheme for ^{182}Ta

This chapter discusses the published level scheme for ^{182}Ta as well as the current findings.

5.1 Previous studies on ^{182}Ta

Several previous studies of ^{182}Ta have been carried out, including β -decay of ^{182}Hf [Hel71], as well as $^{181}\text{Ta}(\text{n},\gamma)^{182}\text{Ta}$ [Sun61, Cla68, Biz66, Hel71] and $^{181}\text{Ta}(\text{d},\text{p})^{182}\text{Ta}$ [Ers64] reactions. Early work on this nucleus was carried out by Sunyar *et al.* [Sun61] from neutron activation of ^{181}Ta . Three states with excitation energies of 147, 319 and 503 keV were first reported. The 503 keV level was identified as a $T_{1/2}=16$ minute isomeric state that depopulated via 185 keV, $E3$ and 356 keV, $M4$ transitions, respectively, to rotational states at 319 and 147 keV in the ground state band. The energy levels in this nucleus were also studied by Erskine *et al.* [Ers64] using $^{181}\text{Ta}(\text{d},\text{p})$, identifying several energy levels below 1 MeV. Meanwhile, Clark *et al.* [Cla68] discovered a $\tau=0.283$ seconds isomer in ^{182}Ta that was found to be fed by the 16 min isomeric state and then decayed directly to the ground state. Their work also suggested that the rotational band sequence previously reported by Sunyar *et al.* is actually built on this isomer rather than the ground state. While its energy was not determined in that work, the 0.283 s isomer was proposed to be a $K^\pi = 5^+$ state formed from a $9/2^-[514]$ proton coupled to a $1/2^-[510]$ neutron.

The latest studies on the level structure of ^{182}Ta were carried out by Helmer *et al.* [Hel71] from the β -decay of ^{182}Hf following the $^{180}\text{Hf}(2\text{n},\gamma)$ reaction, as well as

from the decay of ^{182m}Ta and the prompt γ rays emitted following the $^{181}\text{Ta}(\text{n}, \gamma)$ reaction; see figure 5.1(a)-(c) for a summary. $K^\pi = 3^-$ was assigned to the ground state, with the $K^\pi = 5^+$ state confirmed as the 0.283 seconds isomer and measured at 16.5 keV. The 16 min isomer is a 10^- state formed from a $9/2^-$ [514] proton coupled to a $11/2^+$ [615] neutron.

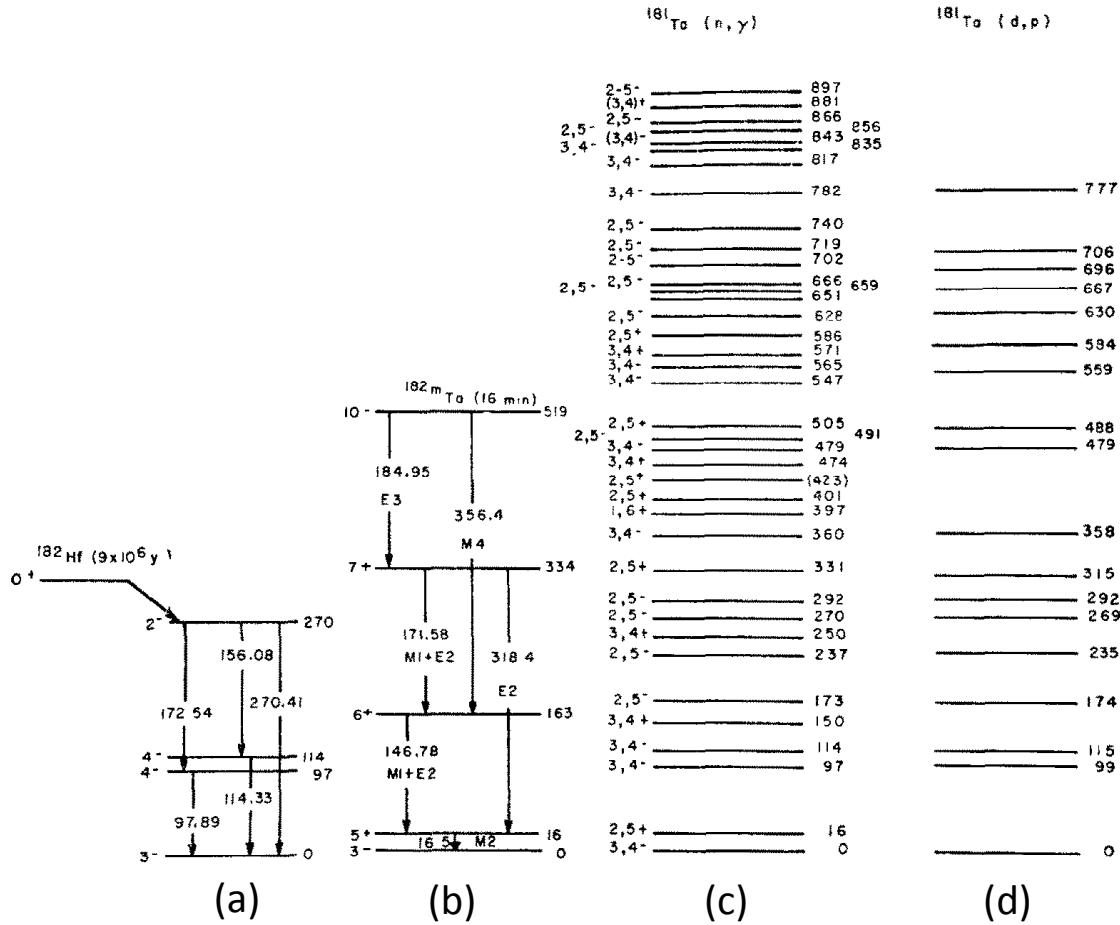


Figure 5.1: A summary of the known structures of ^{182}Ta from previous studies; the figure is adapted from Ref. [Hel71]. (a)-(b) shows the latest studies by Helmer *et al.* [Hel71] from ^{182}Hf and ^{182m}Ta decays, respectively, while (c) is from prompt γ -ray analysis following the $^{181}\text{Ta}(\text{n}, \gamma)$ reaction [Hel71]. The (d, p) data shown in (d) is originally from Erskine *et al.* [Ers64].

5.2 Current analysis and results for ^{182}Ta

The known structure following isomeric decay in ^{182m}Ta as reported by Helmer *et al.* [Hel71] is observed in the current data. Figures 5.2(a)-(c) are three single-gated

spectra taken from the 4 seconds chopped data with a $\gamma - \gamma$ trigger, with gates on the prior known 147, 172 and 185 keV transitions in ^{182}Ta , respectively. The low energy 16 keV transition is not observed in the current work; the energy is too low to be detected by the HPGe detectors used in the array and in any case most of the decay will be via internal conversion; it is also below a $\tau=0.283$ seconds isomer and will not be in coincidence with anything. The current data involving various pulsed and chopped beam conditions for isomeric measurements, allows observation of the decay from the very long lived 16 minute isomer, although its halflife is so long that it is impossible to directly project the feeding/early γ rays. The expected 356 keV interband transition is not observed in the current data. However, the observed limit on the decay branching ratio is consistent with the previous measurements from Refs. [Biz66, Hel71].

5.2.1 New states in ^{182}Ta

Setting double gates and other coincidence conditions in the out-of-beam data revealed a new set of γ rays in coincidence with tantalum X-rays. Analysis of the yields of this sequence from various targets led to this structure being assigned to ^{182}Ta . Its location feeding the 16 minute isomer corresponded with the expected magnetic properties of the associated states, as will be discussed further below. Figure 5.3 shows the deduced level scheme for ^{182}Ta , including the new structure built on the known $K^\pi = 10^-$ state. The properties of all the γ rays in this level scheme are summarised in table A.2. The present section is focused on the coincidence relationships between these newly observed transitions that lead to the established level scheme, as well as the isotopic assignment.

Figure 5.3 shows a rotational sequence above the 10^- state fed by the 245 and 570 keV transition from a new isomer. Figure 5.4(a) shows a sum of clean double gate combinations, including 267/287, 267/632, 287/570, 307/570 and 554/632, that demonstrates clear coincidences with tantalum X-rays and that these γ rays are in mutual coincidence.

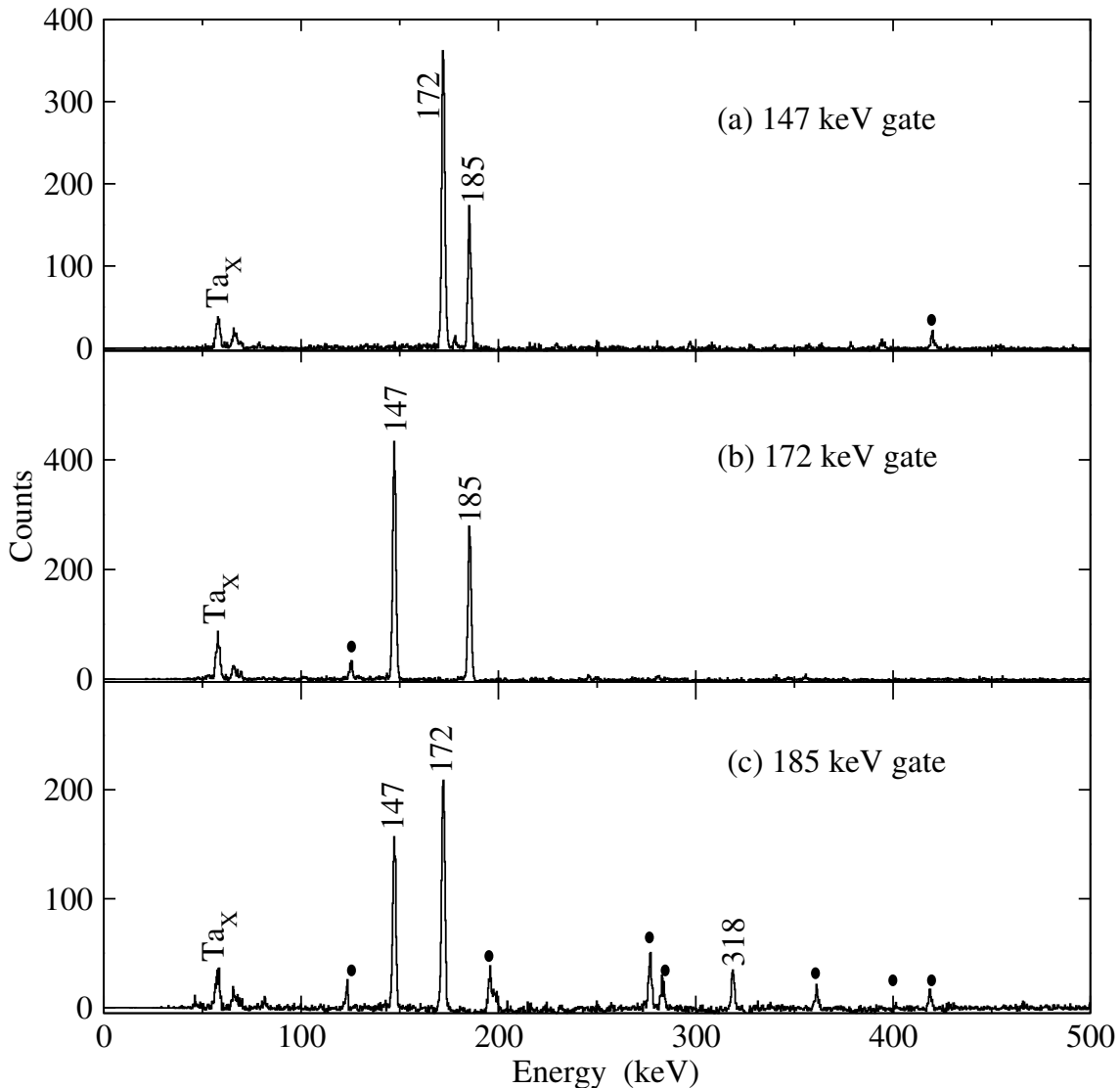


Figure 5.2: (a)-(c) Single-gated spectra from the 4 s chopped beam data for the known 147, 172 and 185 keV transitions in ^{182}Ta with dots representing unknown contaminants. These γ rays are also clearly observed when double gating in the out-of-beam data with 825 ns pulsing.

By using these same double gates and projecting the γ rays that precede them in time by 30-800 ns, a new set of transitions, including 132, 143, 278, 293, 346, 363, 391, 448, 468, 496, 638 and 709 keV, were identified (see figure 5.4(b)). Note that the incremented γ rays in this spectrum are from the out-of-beam region and the spectra imply (a) the γ rays in 5.4(a) are below an isomer, and (b) the γ rays in 5.4(b) are below a higher-lying isomer. Now, gating on these new γ rays and projecting a matrix of 30-800 ns delayed out-of-beam coincidence pairs gives the original 267, 287, 307, 554, 570, 594 and 632 keV set of γ rays, as expected.

The coincidence spectrum in figure 5.5(a) is a sum of double-gated spectra on the 570/287 and 570/307 combinations and shows the absence of 245, 594 and 632 keV transitions. The summation of 267 and 287 keV equals 554 keV, while 287 plus

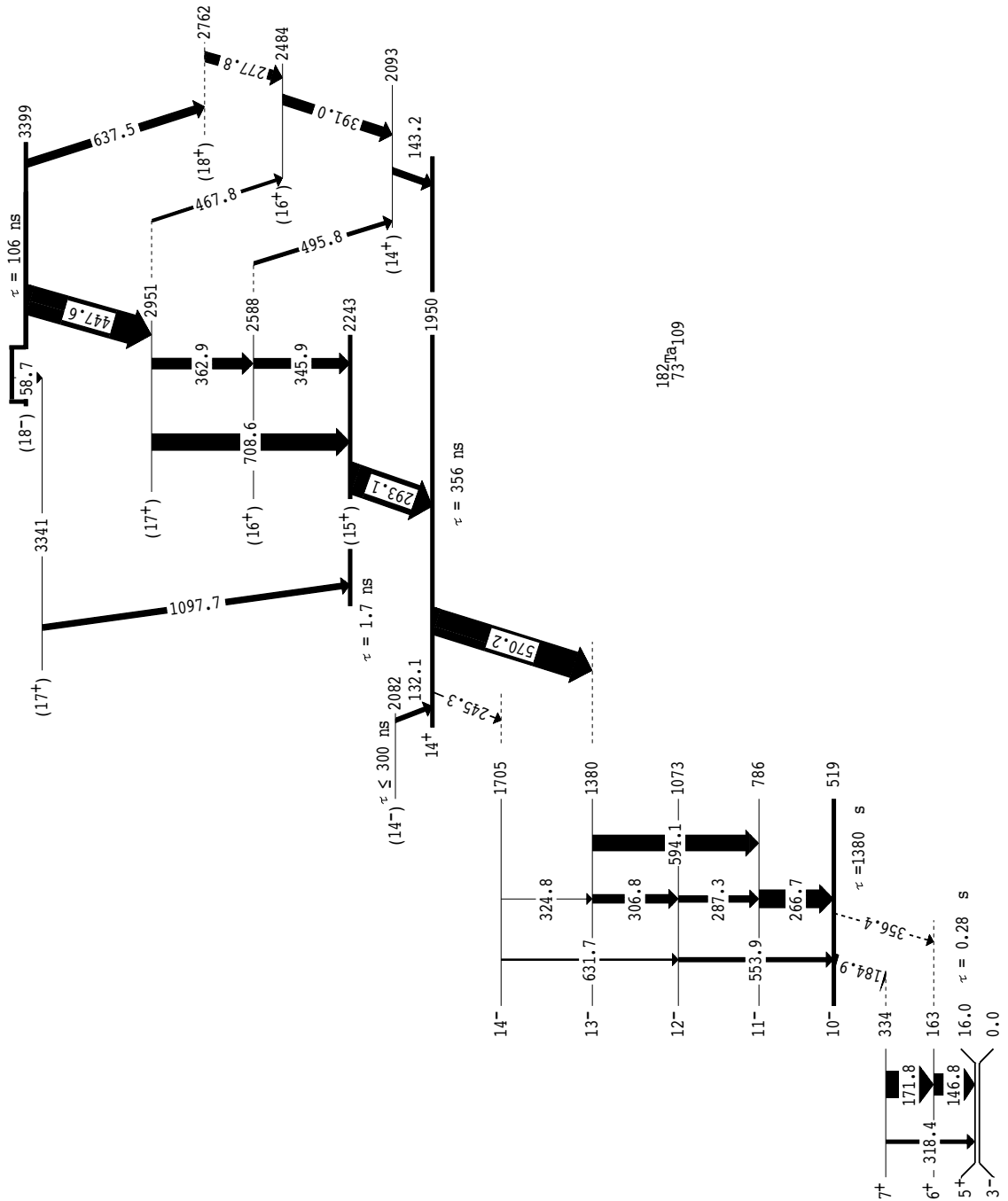


Figure 5.3: Level scheme for ^{182}Ta deduced in the current work. The new structure is assigned to feed the known [Hel71] 10^- isomeric state at 519 keV.

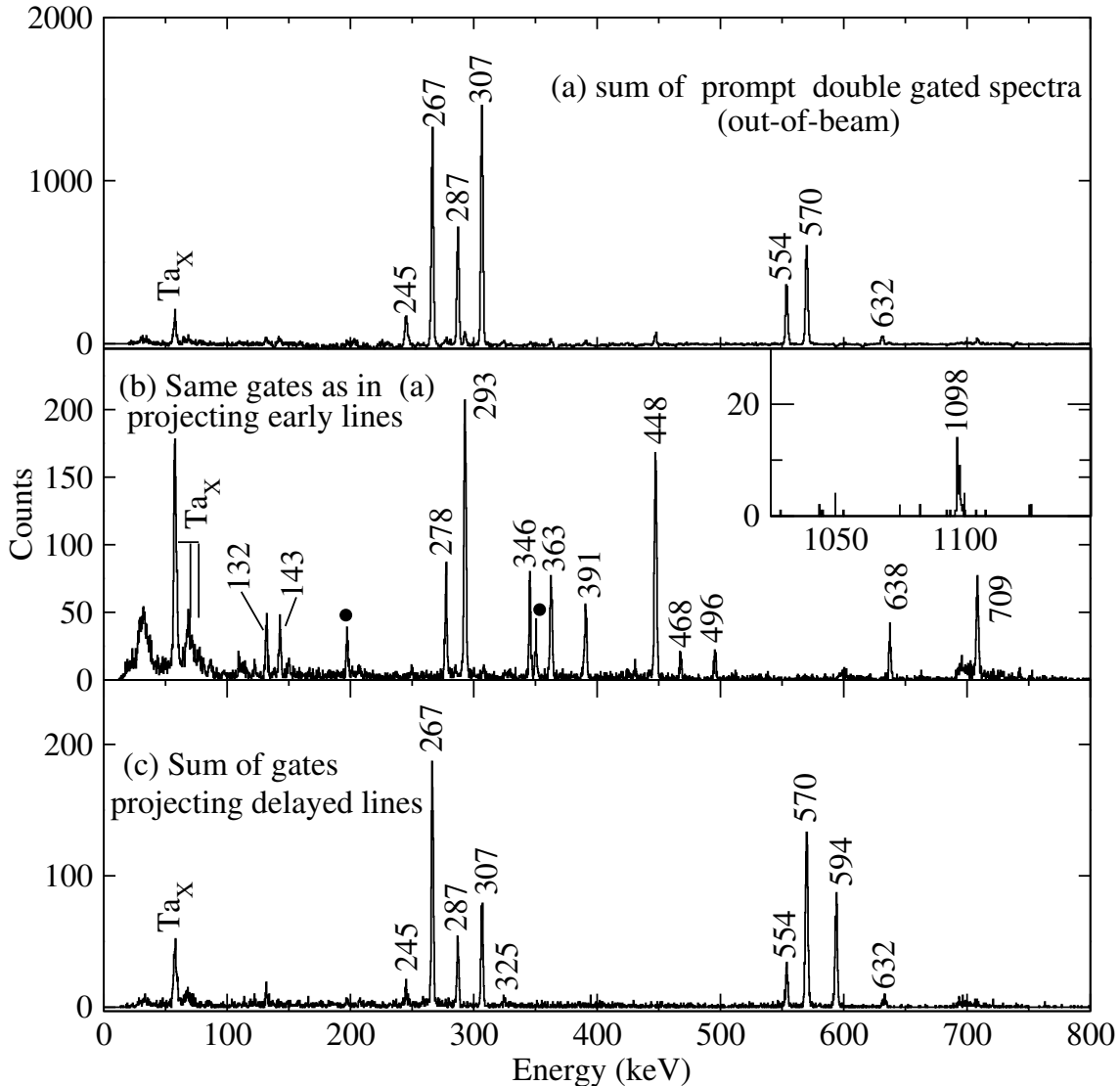


Figure 5.4: (a) Sum of double-gated spectra from the out-of-beam cube showing a new set of γ rays in coincidence with tantalum X-rays. (b) Gamma-rays 30-800 ns early with respect to transitions in (a), revealing another new set of feeding γ rays. (c) Delayed matrix projection with respect to transitions in (b) confirming the presence of a new isomer. The early/delayed time relationships imply the presence of an isomeric state between the two sets of transitions apparent in spectra (a)/(c) and spectrum (b). Filled circles indicate unknown contaminants.

307 keV gives 594 keV. These coincidence relationships and energy sums place the 267 and 287 keV parallel to 594 keV while the 287 and 307 keV are placed parallel to the 594 keV line. Figure 5.5(b) shows the spectrum from summing 245/594, 632/267 and 632/554 double-gated spectra out of beam, revealing a new transition of 325 keV together with the disappearance of the 307 and 570 keV γ rays. The summation of 245 and 325 keV is equivalent to 570 keV,

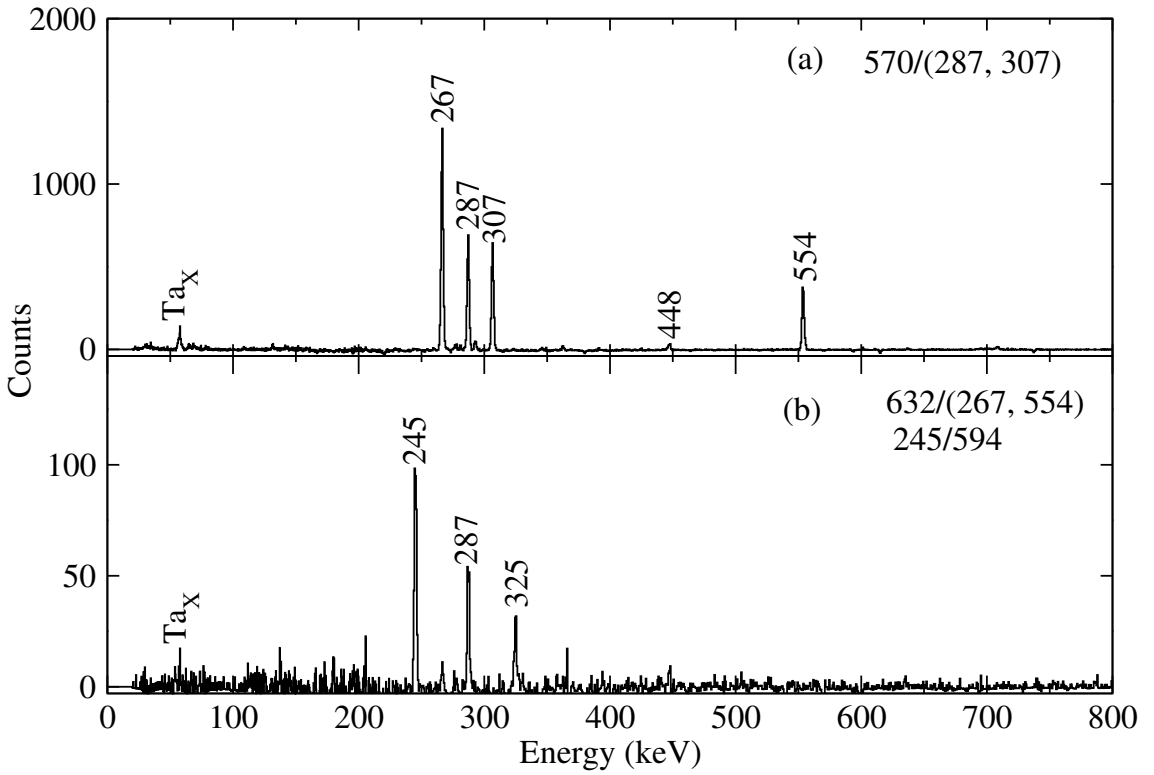


Figure 5.5: Sums of double-gated spectra from the out-of-beam cube demonstrating the coincidence relations of the new transitions. These enable the ordering of all the γ -ray transitions between the 519 and 1950 keV levels in ^{182}Ta .

while summing 325 and 307 keV gives 632 keV. These facts, together with the results from fig 5.5(a), enabled the placing of the 245 and 325 keV parallel to 570 keV, with 632 keV parallel to both 307 and 325 keV. The crossovers fully confirm the ordering of all the transitions below the 1950 keV level in the decay scheme.

Figures 5.6 (a) and (b) show double-gated spectra involving the 293, 363 and 448 keV γ rays in the out-of-beam region. The double gate 448/293 keV shows the absence of 132, 143, 278, 391, 468, 496 and 638 keV transitions, while the 448/363 keV gate shows the absence of 132, 278, 391, 468, 638 and 709 keV γ rays. These coincidence relations enabled the ordering of all the γ rays between the 1950 and 3399 keV levels as shown in the level scheme. The absence of the 132 keV γ ray in both spectra in Figure 5.6 places it parallel to all the transitions above the 1950 keV level as shown in the level scheme. The observed time differences between these γ rays are shown in section 5.2.4 below, which further confirm the ordering and establish the isomer lifetimes.

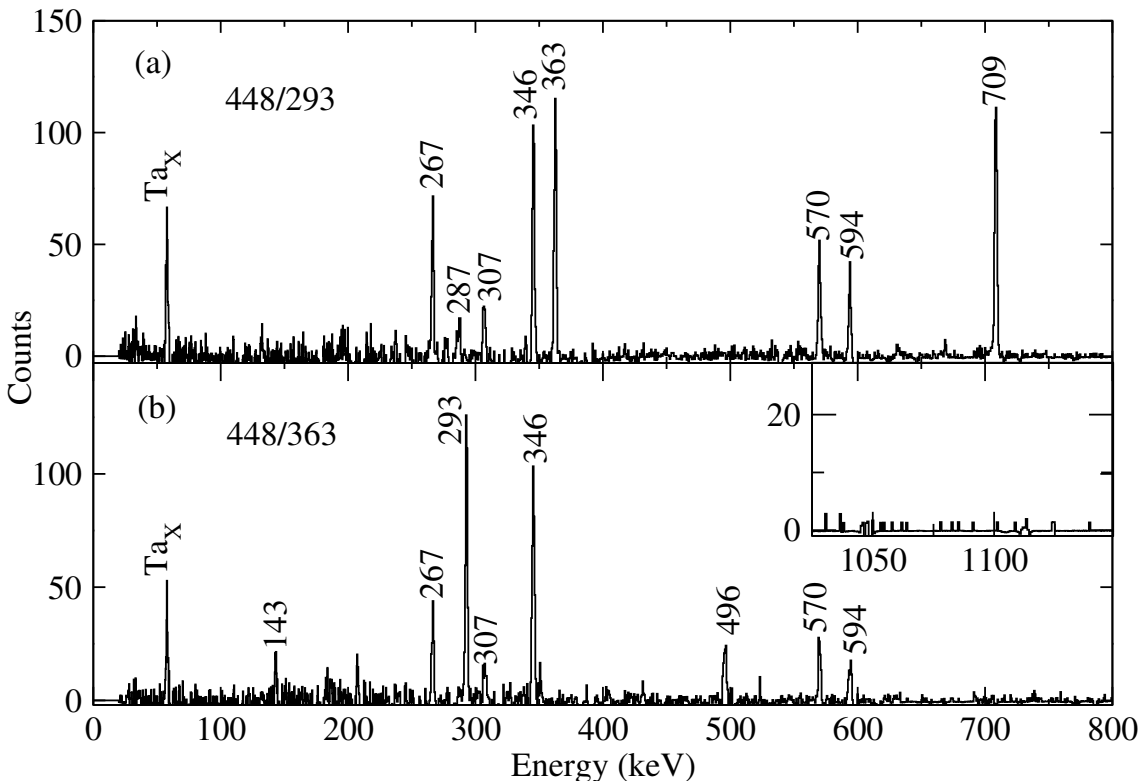


Figure 5.6: Double-gated spectra from the out-of-beam cube with gates on (a) 448/293 and (b) 448/363 keV. These coincidence relationships lead to the ordering of transitions between the 1950 keV and 3399 keV states.

5.2.2 Isotopic assignment from yields

The isotopic assignment for this new structure relies upon the comparison of the normalised intensity yield measured for this structure and other neutron-rich tantalum isotopes, obtained using targets of ^{185}Re , ^{187}Re , ^{186}W and ^{192}Os . This section is focused on the detailed information from these target yield intensity measurements.

Generally, the production cross-section of nuclei from deep-inelastic reactions changes in a systematic way depending on how close they are to the different targets used, provided that similar experimental conditions are maintained for each target [Bro06, Kró11].

For all the four targets used in this series of experiments, a ^{136}Xe beam was used, albeit with different running times and beam intensities. For the purpose of the

present analysis, a set of clean double gates in the out-of-beam cube were produced for the known isomeric decays in neutron-rich ^{181}Ta , ^{183}Ta , ^{185}Ta , together with those from the new structure. These same set of gates were applied to the cubes from each target and the measured intensity yields were then normalised to the yield of 197 and 381 keV transitions from inelastic excitation of the beam nucleus, ^{136}Xe , to account for the different total beam fluxes on each target. In order to establish the trend lines, all the intensities were further normalised to the ^{186}W target, as it has the highest yields of ^{181}Ta , ^{183}Ta and ^{185}Ta , as well as the new structure. The deduced target yields versus isotopic mass are shown in figure 5.7. (Note that the term “yield” is used for the values in Fig. 5.7, although strictly speaking they are normalised yield ratios). The yields for the unknown which appear at mass $A=182$ were first positioned at different possible mass candidates in order to see if their placement would establish any meaningful trend lines. The smoothest trends occur with the unknown structure placed at $A=182$. Further details suggesting this are listed below.

Referring to figure 5.8 and taking a ^{185}Re target as an example, the yields of neutron-rich tantalum isotopes with mass $A>182$ might be expected to decrease with increasing isotopic mass as they require additional neutrons to be transferred from the beam to the target, contrary to the equilibrium mass flow.

Considering now the yield of ^{185}Ta from the ^{185}Re target, a much lower yield (<0.1) is anticipated for any isotope of mass $A>185$ from the same target. The measured yield (> 0.1) for the unknown structure in the ^{185}Re target rules out its having $A>185$. Again, considering the yields of the unknown structure relative to that of ^{183}Ta , the possibility of the unknown to be ^{184}Ta can be ruled out too, since much lower yields would be expected compared to that of ^{183}Ta , especially from the ^{185}Re target. The well-known isomeric states in ^{183}Ta from both Shizuma *et al.* [Shi09] and the extensions in the current work (see Chapter 4), rules out an $A=183$ assignment.

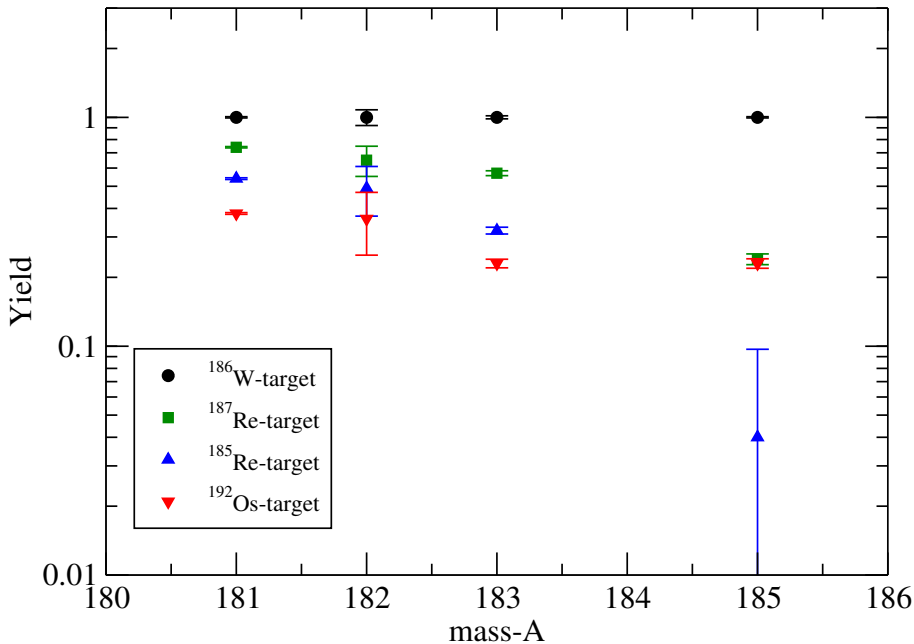


Figure 5.7: Yields of different tantalum isotopes from various targets, normalised by the target flux and plotted relative to the yield in the ^{186}W target, as described in the text. The data for the new structure appear to be consistent with it being ^{182}Ta .

^{184}Os	^{185}Os	^{186}Os	^{187}Os	^{188}Os	^{189}Os	^{190}Os	^{191}Os	^{192}Os
^{183}Re	^{184}Re	^{185}Re	^{186}Re	^{187}Re	^{188}Re	^{189}Re	^{190}Re	^{191}Re
^{182}W	^{183}W	^{184}W	^{185}W	^{186}W	^{187}W	^{188}W	^{189}W	^{190}W
^{181}Ta	^{182}Ta	^{183}Ta	^{184}Ta	^{185}Ta	^{186}Ta	^{187}Ta	^{188}Ta	^{189}Ta

Figure 5.8: Section of the nuclear chart showing the proximity of the targets, ^{185}Re , ^{187}Re , ^{186}W and ^{192}Os , to the neutron-rich tantalum isotopes. The tantalum yields are expected to vary systematically across the isotopic chain for each of the targets used.

5.2.3 Placement above the 10^- state in ^{182}Ta

The inability to project the early/feeding γ rays and correlate across the very long-lived isomeric states known in ^{181}Ta [Dra98a], ^{182}Ta [Hel71] and ^{185}Ta [Lan09], as well as the inability to project the delayed γ rays relative to the new structure using

the current data, implies that the newly observed rotational band could be feeding one of these long lived states. However, based on the conclusions in the previous section, this could be the 10^- state in ^{182}Ta . The ambiguity can be eliminated by deducing values of $(g_K - g_R)/Q_0$ for the band and making comparisons with expected values from models to deduce the configuration of the intrinsic state upon which the rotational band is built. The deduced g_K value of 0.49(6) for the band is comparable to that expected for the $K^\pi = 10^-, \tau=23.1$ min isomeric state in ^{182}Ta . Complete details on the magnetic properties will be discussed in chapter 7. Hence, despite the fact that no information is known in ^{184}Ta , both the results from the yield measurement (5.2.2) and the deduced magnetic properties of the band, favour a ^{182}Ta assignment, with the structure sitting above the known 519 keV state.

5.2.4 Lifetime measurements

The potential lifetimes of all the states between 519 and 3399 keV levels were examined using time-difference spectra between feeding and depopulating transitions. The separation of the new γ rays into two sets of early and delayed gamma-rays as shown in Fig 5.4(a) and (b) clearly implies the presence of at least two isomers above the known 519 keV level. The full analysis identified three isomeric states at 1950, 2243 and 3399 keV. Figure 5.9 shows the time difference spectrum across the 1950 keV level obtained by summing spectra that start on 293 and stop on 570 and 594 keV transitions, establishing a $\tau=356(16)$ ns lifetime.

A lifetime of 1.7(5) ns was measured for the 2243 keV state from the centroid shifts of the time difference spectra between the 293 keV transition and the feeding 709 and 1098 keV transitions. Figure 5.10 shows the corresponding time spectra where the shifts in the centroids are clearly visible.

Due to poor statistics, the lifetime for the 2082 keV state cannot be confirmed from the measured intensity variation of the depopulating transition. However, rough fitting to this data gave $\tau \sim 300$ ns. The non-observation of the transitions lying between the 519 and 2082 keV states in the chopped data implies a shorter lifetime for this state, hence the assigned limit of $\tau < 300$ ns.

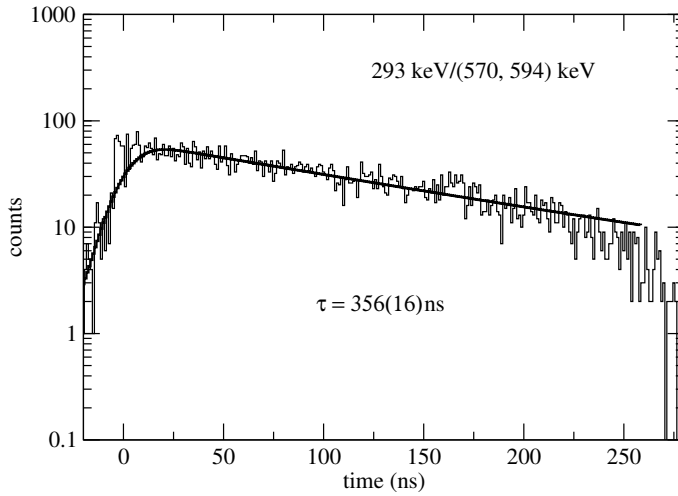


Figure 5.9: Time spectrum to illustrate the $\tau=356(16)$ ns isomer in ^{182}Ta obtained by summing two time-difference spectra, starting on the feeding 293 keV transition and stopping on the two depopulating transitions at 594 or 570 keV.

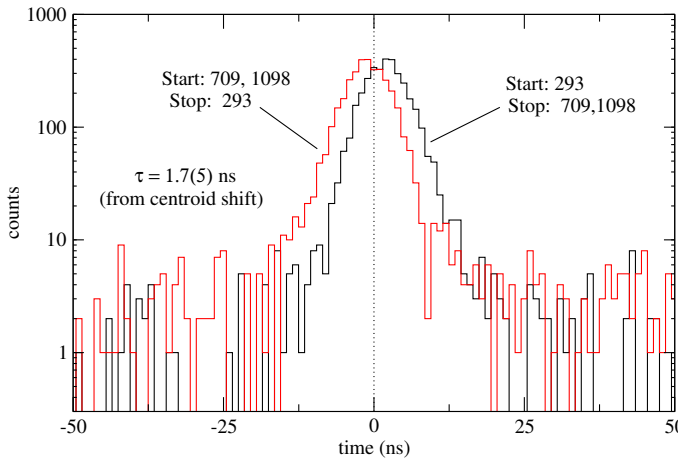


Figure 5.10: Time difference spectra between the depopulating 293 keV transition and the two feeding transitions at 709 and 1098 keV. A lifetime of $\tau=1.7(5)$ ns is established for the 2243 keV state in ^{182}Ta from the observed centroid shift when the start/stop transitions are reversed.

A lifetime of $\tau=106(4)$ ns was deduced for the uppermost state at 3399 keV using the intensity variation of the depopulating transitions across $\gamma\text{-}\gamma\text{-}\gamma$ cubes created with time gates on intervals across the beam-off region. The corresponding time curve is shown in figure 5.11. Due to contaminants, as well as low intensities of the 59, 143, 278, 391, 467, 496 and 638 keV transitions, no other state lifetimes could be measured.

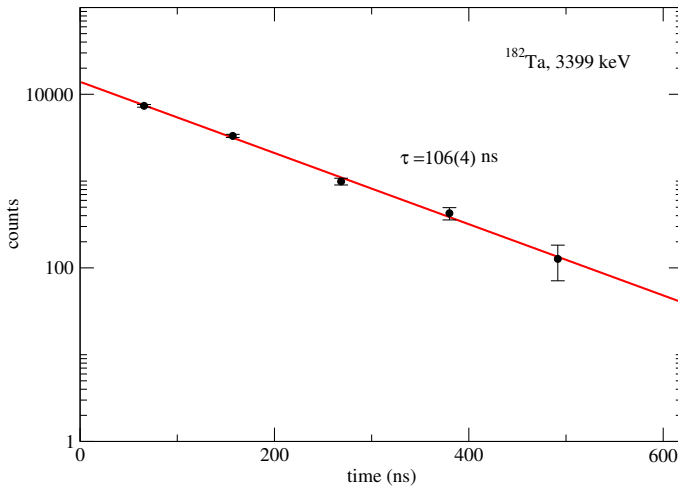


Figure 5.11: Representative decay curve for the 3399 keV isomer in ^{182}Ta , derived from the intensity variation of the depopulating transitions across five γ - γ - γ cubes in the out-of-beam region. A lifetime of $\tau=106(4)$ ns was deduced for this state.

5.2.5 Spin and parity assignments

The statistics for the ^{182}Ta structure in the present data were sufficient to obtain angular correlations. The experimental angular correlations and the corresponding mixing ratios deduced for each of the assumed spin combinations are shown in Figures 5.12 and 5.13. Where possible, intensity balances were also used to measure conversion coefficients, giving the results in Figure 5.14. This information was combined to obtain transition multipolarities and hence spin and parity assignments.

5^+ isomer at 16 keV

In almost all the previous work on ^{182}Ta , the lower energy and highly converted 16 keV γ ray transition has never been observed directly. However, its $M2$ multipolarity leading to the assigned 5^+ state was first measured by Clark *et al.* [Cla68] using relative intensities in the L X-ray pattern to deduce L-subshell conversion coefficient ratios. The configuration assignment to this state, as deduced by Helmer *et al* [Hel71], supported the 5^+ assignment.

The 16 keV transition is not observed in the present work so there is no direct evidence from the present data for the spin and parity of the 16 keV level. However,

the branching ratio of the 171 keV and 318 keV transitions (see Fig. 5.3) was used to confirm the configuration for its related band from the rotational model, hence providing indirect evidence of its spin. A value of $g_K - g_R = 0.615(28)$ was deduced for this state, giving $g_K = 0.97(8)$ for $g_R \approx 0.35(5)$. The value is in good agreement with the predicted value of $g_K = 0.986$ from the Nilsson model for a 5^+ state obtained from the $9/2^-[514]$ proton coupled to a $1/2^-[510]$ neutron, as discussed further in Sect. 7.4.

10^- isomer at 519 keV

The earlier spin and parity assignment to this state was based on the K -shell conversion coefficient measurements of the 185 and 356 keV transitions that suggested $E3$ and $M4$ character, respectively [Sun61, Biz66, Cla68]. By using the intensity balance between the in-band 171 keV transition and the inter-band 185 keV transition, as measured from the single gated spectrum in Figure 5.2(a), a conversion coefficient of $\alpha_T = 3.5(2)$ was deduced for the 185 keV transition. This is in good agreement with the expected value for an $E3$ transition (see Figure 5.14), confirming the previous assignment. The mixing ratio of $\delta = 0.244(11)$ used for the 171 keV transition in this intensity balance was derived from the branching ratio of the 171 and 319 keV transitions. Further confirmation of the 10^- assignment is obtained from the properties of the rotational band established above this isomer as discussed in Chapter 7.

14^+ isomer at 1950 keV

This isomer decays to 13^- and 14^- levels of the 10^- rotational band. Assuming a pure quadrupole (assumed $E2$) character for the 594 keV in-band transition, the 594-267 keV angular correlation in Figure 5.12 shows a mixed dipole character for the 267 keV transition, consistent with the $M1/E2$ multipolarity expected for $\Delta I=1$ cascades in rotational bands.

Again assuming the 594 keV γ ray is a pure stretched $E2$, the 594-570 correlation gives a non-zero mixing ratio were the 570 keV to be a $\Delta I=2$ transition. For a

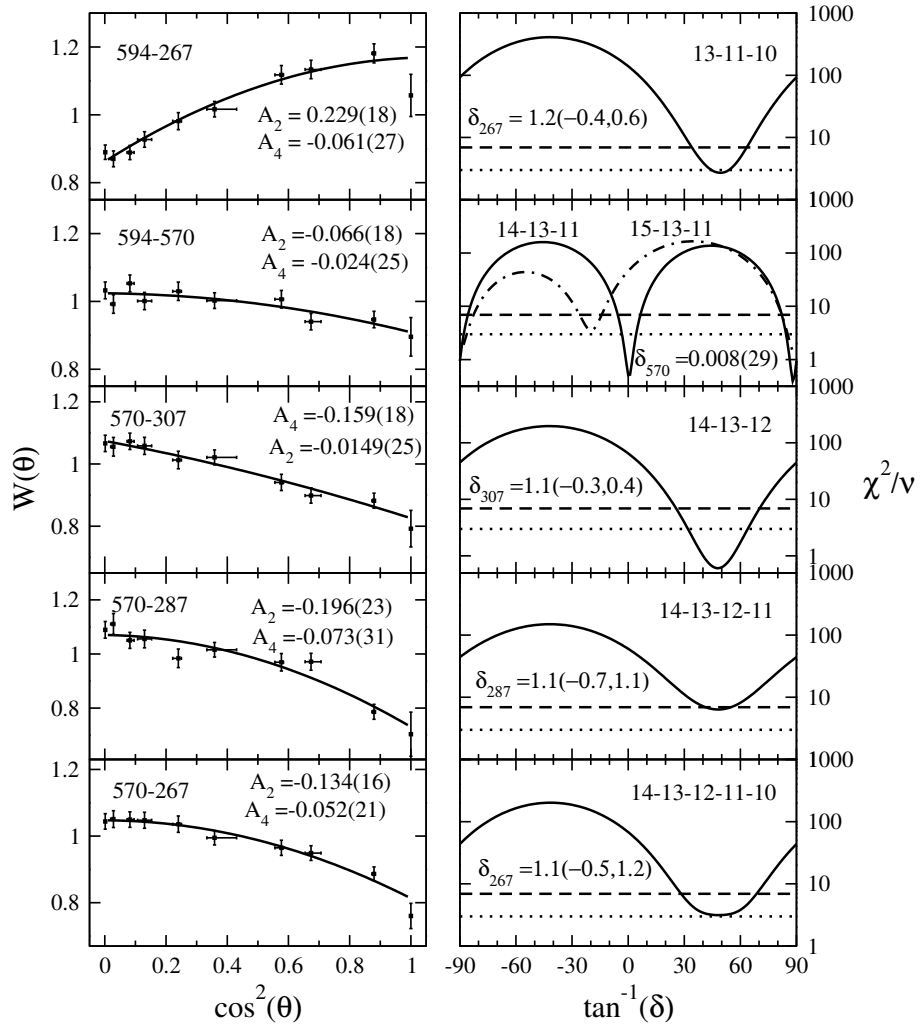


Figure 5.12: Angular correlations for selected transition pairs between the 519 and 1950 keV isomeric states in ^{182}Ta . A pure dipole character is suggested for the 570 keV transition, while the mixing ratios deduced for the 267, 287 and 307 keV $M1/E2$ in-band transitions, together with pure quadrupole character for the 594 keV transition, confirm a rotational structure built on the 10^- isomeric state.

$\Delta I=1$ assignment to the 570 keV transition, the correlations suggest pure dipole character. Both $E2/M3$ or $M2/E3$ mixtures are highly unlikely, since (a) these multipolarities would imply a much longer lifetime than 356 ns, and (b) there is a pure stretched dipole alternative. With a pure stretched dipole character being the most likely multipolarity for 570 keV, the spin and parity possibilities for the 1950 keV isomer are limited to 14^+ or 14^- . Note that with the 570 keV pure stretched dipole assignment, the 570-307, 570-287 and 570-267 keV angular correlations all give a mixed dipole character with $\delta \sim 1.1$ for the 267, 287 and

307 keV transitions, a value that is consistent with the results from the 594–267 correlation. It is also worth mentioning that the g_K value implied from this mixing ratio shows a strong agreement with the value deduced from the branching ratios within the 10^- band (see Chapter 7).

The ambiguity in the parity assignment for the isomer can be eliminated by inspection of the transition strengths of the depopulating 245 and 570 keV decays. The evaluated strengths and hindrances for these transitions are shown in table 5.1 for both possibilities. Both cases are acceptable for $E1$ and $M1$ assignments.

Table 5.1: Transition strengths and corresponding reduced hindrances for the 245 and 570 keV transitions, assuming alternative possibilities of $K^\pi = 14^+$ or $K^\pi = 14^-$ for the 356(13) ns isomeric state. Limits on the hindrances for the unobserved 877 keV transition are included to eliminate the ambiguity between the 14^+ and 14^- assignments.

I^π	E_γ (keV)	XL	I_γ	α_T	$B(XL)$ (W.u)	F_W	ν	f_ν
14^+	570.2	<i>E1</i>	98.0(47)	5.158×10^{-3}	$4.2(3) \times 10^{-9}$	$2.4(2) \times 10^8$	3	621(17); <i>29(1)</i> ^a
	245.3	<i>E1</i>	5.2(10)	3.628×10^{-2}	$2.8(6) \times 10^{-9}$	$3.6(8) \times 10^8$	3	710(50); <i>33(2)</i> ^a
	877 ^b	<i>M2</i>	<3.9 ^b	3.188×10^{-2}	$< 2.9 \times 10^{-4}$	$> 3.5 \times 10^3$	2	>59
14^-	570.2	<i>M1</i>	98.0(47)	3.709×10^{-2}	$4.2(3) \times 10^{-7}$	$2.4(2) \times 10^6$	3	134(4)
	245.3	<i>M1</i>	5.2(10)	3.489×10^{-1}	$2.8(6) \times 10^{-7}$	$3.6(8) \times 10^6$	3	153(11)
	(877) ^b	<i>E2</i>	<3.9 ^b	5.616×10^{-3}	$< 2.7 \times 10^{-6}$	$> 3.7 \times 10^5$	2	>609

a: Reduced hindrance calculations for $E1$ transitions that include a 10^4 normalisation factor are in italics.

b: Energy and intensity limit for the unobserved 877 keV transition.

For either parity, there is the possibility of a $\Delta I = 2$, 877 keV transition to the 1073 keV state. This transition is not observed in both the out-of-beam double gated spectra and the delayed spectra in Figures 5.4(a) and (c). Hence, upper intensity limits were deduced, implying reduced hindrances for the possible 877 keV transition of $f_\nu > 59$ and $f_\nu > 609$ for $M2$ and $E2$ transitions, respectively. The latter limit rules out the 14^- alternative, thus assigning $K^\pi = 14^+$ to the 1950 keV isomer.

States at 2243, 2588 and 2951 keV

Figure 5.14 shows the total conversion coefficients deduced for the 143, 293 and 346 keV transitions from intensity balances. The 293 keV transition from the 2243 keV state has a total conversion coefficient consistent with an $M1$ multipolarity (albeit with an $E2$ assignment possible only slightly beyond the uncertainty limit). Assuming the preferred $M1$ assignment gives $I^\pi = 15^+$ for the 2243 keV state. Considering the energies of the 346 and 363 keV transitions, the presence of the 709 keV crossover as well as the absence of a measured lifetime for the states at 2588 and 2951 keV, both these levels are possibly collective, implying a band built on the 15^+ state. This would suggest 16^+ and 17^+ assignments for the 2588 and 2951 keV levels, respectively. Figure 5.13 shows angular correlations for the structures above the 2243 keV level. With a pure stretched $M1$ character for the 293 keV line, the results from the 293-709 angular correlation suggest a pure quadrupole assignment for the 709 keV transition, agreeing with the likely $E2$ multipolarity were the 2588 and 2951 keV states to be part of a rotational band. From the measured conversion coefficient for the 346 keV transition, $M1$ is the preferred multipolarity over the alternative $E3$ possibility, confirming 16^+ for the 2588 keV level.

States at 2082, 2093, 2484, 2762 and 3341 keV

The statistics for decays out of these levels were insufficient to allow angular correlation measurements and hence the limited spectroscopic information only permits tentative spin and parity assignments to these levels. The measured total conversion coefficient of the 143 keV transition suggests an $M1$ multipolarity. The (14^+) assignment for the 2093 keV level agrees with this, but also rests on the configuration assignments discussed in Chapter 7. Hence 15^+ cannot be ruled out. Although the energies of the 132 and 278 keV transitions are in principle low enough to deduce conversion coefficients, their low intensities and the presence of contaminants with energies close to 278, 391 and 638 keV, makes it difficult to balance intensities across the 1950, 2484 and 2762 levels.

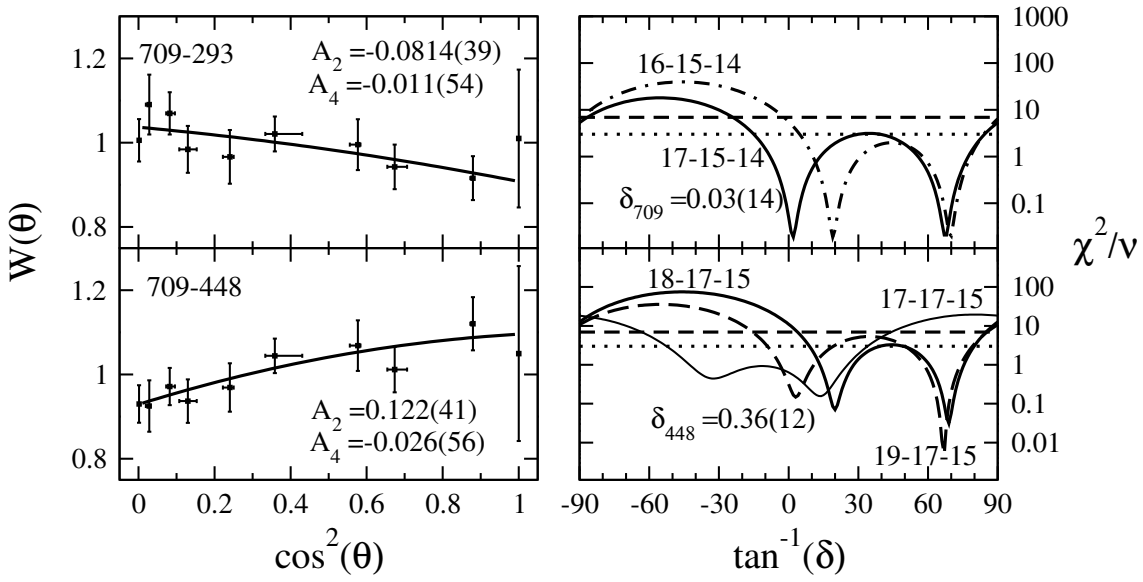


Figure 5.13: Angular correlations for selected transitions between the 1950 and 3399 keV isomeric states in ^{182}Ta . The correlations suggest pure quadrupole, most likely $E2$ character, for the 709 keV γ ray. A non-zero mixing ratio, $\delta = 0.36(12)$ is observed for the 448 keV γ ray, if it has $\Delta I=1$. Assuming the 448 keV transition has $\Delta I=2$ (19-17-15 spin sequence), results in its mixing ratio agreeing with zero.

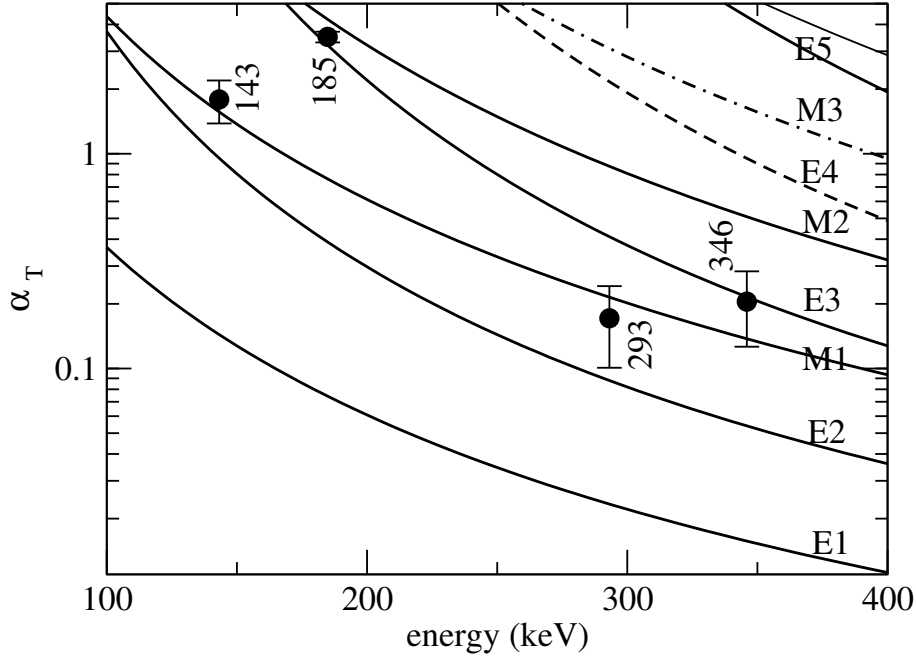


Figure 5.14: Total conversion coefficients deduced from intensity balances for transitions in ^{182}Ta . The plot compares the experimental observations (points) to theoretical expectations (curves) from Ref. [Kib08].

The spectrum gated below the 1950 keV isomer and projecting the early coincidences (Fig. 5.4(b)) shows a weak intensity for the 132 keV transition; hence the spin and parity of the 2082 keV level cannot be confirmed. Considering the suggested spin and parities for the 2951 and 2093 keV levels and the absence of a measurable lifetime for the 2951 keV state, the 391 and 468 keV decays are likely to be $\Delta I \leq 2$ transitions, implying $I^\pi = (16^\pm)$ or $I^\pi = (15^\pm)$ for the 2484 keV level. With $M2$ and $E1$ characters for these transitions highly unlikely due to the absence of lifetimes, 15^+ or 16^+ remain the only candidates for the 2484 keV state. From the predicted states in ^{182}Ta (see section 7.4.2), 16^+ is favoured although 15^+ cannot be ruled out completely. Mixing with the nearby collective 16^+ state at 2588 keV could also explain the competition of the 468 keV γ ray with the in-band decay. The energy of the highly converted 59 keV isomeric transition is close to the X-ray energies for tantalum and the target (^{186}W); this precludes an intensity balance measurement across the 3341 level. The assignment to this level and the 2762 keV state remain tentative for now and can possibly be explained after considering the assignment of the 3399 keV isomer.

(18^-) isomer at 3399 keV

With an $E2$ assignment to the 709 keV transition, the 709-448 keV angular correlation in Figure 5.13 shows a mixed dipole character ($\delta = 0.36(12)$) for the 448 keV transition, consistent with either $M1/E2$ or $E1/M2$ multipolarities. The presence of the 106 ns lifetime as well as the absence of the potential 811 keV crossover transition to the 2588 keV state, rules out the $M1/E2$ possibility. Alternatively, the 709-448 keV angular correlation gives a zero mixing ratio were the 448 keV to be a $\Delta I = 2$ transition (19-17-15 spin sequence with dotted line in Fig. 5.13). Both $E2$ and $M2$ character for the 448 keV isomeric transition could explain the lifetime, however, the lifetime seems too short for $M2$ character, especially considering that the 448 keV transition is likely to be K-hindered. Hence, while a 19^+ assignment cannot be ruled out completely, 18^- is preferred for the 3399 keV isomer.

With $K^\pi = 18^-$ for the isomer, $E1$ character is preferred over $M1$ for both the

59 and 638 keV transitions so as to explain their hindered decay, suggesting 18^+ and 17^+ for the 2762 and 3341 keV states, respectively. Additional information such as the strengths of the 59, 448 and 638 keV transition is needed for more firm multipolarity assignments and this will be discussed in Chapter 8. Also, the predictions of the multi-quasiparticle calculations described in Chapter 6 can be used to guide expectations.

The next goal is to understand the proton and neutron configurations of the single and multi-quasiparticle states observed in ^{182}Ta and ^{183}Ta . Where possible, information such as g_K values and aligned angular momenta deduced from the rotational bands built on these intrinsic states, is used to guide the configuration assignments. However, some assignments are made or supported by the predictions of multi-quasiparticle calculations, and these are presented first, in the next chapter.

Multi-quasiparticle calculations

This chapter moves towards understanding the proton and neutron configurations of the single and multi-quasiparticle states observed in ^{182}Ta and ^{183}Ta by calculating the energies of the expected multi-quasiparticle states. The first section briefly describes the known and expected intrinsic states in both odd-odd and odd-even tantalum isotopes. The second section describes the methodology of multi-quasiparticle calculations as performed for the present work, together with the results for predicted states in tantalum isotopes from $A=181$ to 185 .

6.1 Low-lying states in tantalum isotopes

6.1.1 Odd-even isotopes

An odd-mass tantalum isotope can be considered as a proton particle or proton hole coupled to the even-even hafnium or tungsten isotone, respectively. The three, single-proton configurations of $5/2^+[402]$, $7/2^+[404]$ and $9/2^-[514]$ are known to be amongst the low-lying intrinsic states close to the proton Fermi level in tantalum isotopes. Multi-quasiparticle states involving these protons have been observed in both neutron-deficient and neutron-rich cases [Car95, Das00, Kon04, Dra98a, Shi09, Lan09]. The $7/2^+[404]$ orbital is known to be the ground-state configuration in odd-mass tantalum isotopes down to $A=175$ [Kon96, Das00, Dra98a, Shi09, Lan09].

The formation of states with three or more quasiparticles in these nuclei involves breaking neutron or proton pairs in the core that then couple with one of the low-

lying protons. The neutron states most likely to be involved in the configurations can be determined by examining the low-lying spectrum of states in the nearby odd-mass tungsten or hafnium isotopes. For example, in the present case of ^{183}Ta with $N = 110$, the single neutron states close to the Fermi surface can be obtained from the neighbouring nuclei ^{183}W [Sai00] and ^{185}W [Bon05], with $N = 109$ and $N = 111$, respectively. The ground state in ^{183}W is formed from the $1/2^-[510]$ intrinsic state, with the $3/2^-[512]$ state only 209 keV higher. This situation is reversed in ^{185}W , with the $1/2^-[510]$ level at an excitation energy of only 24 keV, while the $11/2^+[615]$ state lies at 310 and 197 keV in ^{183}W and ^{185}W , respectively. The $7/2^-[503]$ comes down in energy from 453 keV in ^{183}W to 244 keV in ^{185}W , while the $9/2^+[624]$ goes up in energy from 623 keV ^{183}W to 716 keV in ^{185}W . Both the $1/2^-[521]$ and the $5/2^-[512]$ appear at energies over 800 keV and are therefore not expected to take part in the formation of low-lying two-neutron, one-proton states in the vicinity of ^{183}Ta .

Alternatively, the two-neutron states most likely to be involved in the configurations in ^{183}Ta can be determined by examining the low-lying spectrum of states in the isotope ^{184}W [Whe04, Lan15]; these states are listed in Table 6.1. The states that lie closest to the yrast line e.g. the 5^- and 7^- , are likely to contribute to the formation of the low-lying two-neutron, one-proton states in ^{183}Ta . Note that the components of these two states are the low-lying states identified in ^{183}W and ^{185}W above.

Table 6.1: Known, low-lying, two-neutron states in ^{184}W that are likely to contribute to multi-quasiparticle states observed in ^{183}Ta [Whe04, Lan15].

K^π	Configuration	E (keV)
2^+	$3/2^-[512] \otimes 1/2^-[510]$	1386
3^+	$1/2^-[510] \otimes 7/2^-[503]$	1425
5^-	$11/2^+[615] \otimes 1/2^-[510]$	1285
7^-	$11/2^+[624] \otimes 3/2^-[512]$	1502
10^+	$11/2^+[615] \otimes 9/2^+[624]$	2479

6.1.2 Odd-odd isotopes

The ground states in all even-mass tantalum isotopes are due to the coupling of the last unpaired proton and neutron. At relatively low excitation energies below the proton and neutron pair gaps, the observed intrinsic states will be dominated by two-quasiparticle configurations. The neutron states most likely to be involved are determined by examining the low-lying spectrum of excited states in the odd-tungsten or hafnium isotones, while the proton states close to the Fermi surface are similar to those in odd-mass tantalum isotopes.

6.2 Multi-quasiparticle calculations

Multi-quasiparticle calculations have been effective in predicting the possible intrinsic states in various nuclei in this mass region, see for example, Refs. [Kon97, Kon98, Dra98a, Whe00, Lan09]. The output from these calculations includes the configurations and their predicted excitation energies that are then adjusted to account for the residual interaction between the quasiparticle states. Comparison of these energies to the experimental obsevations can then aid in making configuration assignments. This section is focused on the details of the multi-quasiparticle calculations used to predict intrinsic states in ^{182}Ta and ^{183}Ta . The actual configuration assignments in ^{182}Ta and ^{183}Ta , based on the available spectroscopic information and supported by the predictions of the next sections, will be discussed in Sections 7.3 and 7.4, respectively, in the next chapter.

As a starting point to these calculations, the single-particle Nilsson orbitals in the $N = 4, 5$ and 6 oscillator shells were first evaluated for both protons and neutrons assuming deformation parameters, ε_2 and ε_4 , as predicted by Ref. [Mol95], and using the Nilsson model parameters μ and κ from Ref. [Ben85]. Table 6.2 shows the deformation parameters used in the present calculations. The value of ε_4 is comparatively large, while there is a slight decrease in ε_2 and a slight increase in ε_4 as the mass number increases. The effects of nucleon pairing on the properties of multi-quasiparticle states were also taken into account using the Lipkin-Nogami approach

(see section 2.1.4), where the effects of blocking on the magnitudes of the pair gaps are incorporated by excluding all the occupied single-particle levels from contributing to the pairing energy. Only the proton-proton and neutron-neutron pairing were considered in the present calculations. Pairing strengths of $G_\nu = 18.0/\text{A}$ MeV and $G_\pi = 20.8/\text{A}$ MeV were chosen for the neutron and proton systems, respectively. The choice of these pairing strengths was based on previous calculations for other tantalum isotopes in this region that successfully reproduced the experimental observations [Kon97, Dra98a, Lan09].

Table 6.2: Deformation parameters ε_2 and ε_4 for tantalum isotopes between $A=181\text{-}185$ as predicted in Ref. [Mol95], and used for the present multi-quasiparticle calculations.

Nucleus	ε_2	ε_4
^{181}Ta	0.242	0.093
^{182}Ta	0.233	0.100
^{183}Ta	0.233	0.107
^{184}Ta	0.225	0.107
^{185}Ta	0.225	0.113

A number of parameters can be potentially adjusted/varied during calculations to reproduce the experimental energy values. These include varying the neutron and proton pairing strengths $G_{\pi/\nu}$, the Nilsson energies of the single particles around the Fermi surface, or the deformation parameters ε_2 and ε_4 . In the present calculations, only the Nilsson energies were varied, while the pairing strengths and deformation parameters were fixed to the values mentioned above. The Nilsson energies were varied so as to reproduce the experimental energies of one/two-quasiparticle states to within 10 keV, as described immediately below.

In order to optimise the energies, adjustments were made to the Nilsson input energies so as to reproduce the known experimental one-quasiparticle energies of single-proton and single-neutron states near the Fermi surface. In some cases, the neutron Nilsson energies were further adjusted to reproduce the known two-quasi-neutron states. The neutron spectrum was relatively complex, both with changes as a function of neutron number and with some states being relatively

uncertain. In contrast, the energies of the single-proton states, $7/2^+[404]$, $9/2^-[514]$ and $5/2^+[402]$, in odd mass tantalum isotopes are well known experimentally and change smoothly from $A=175$ to 185.

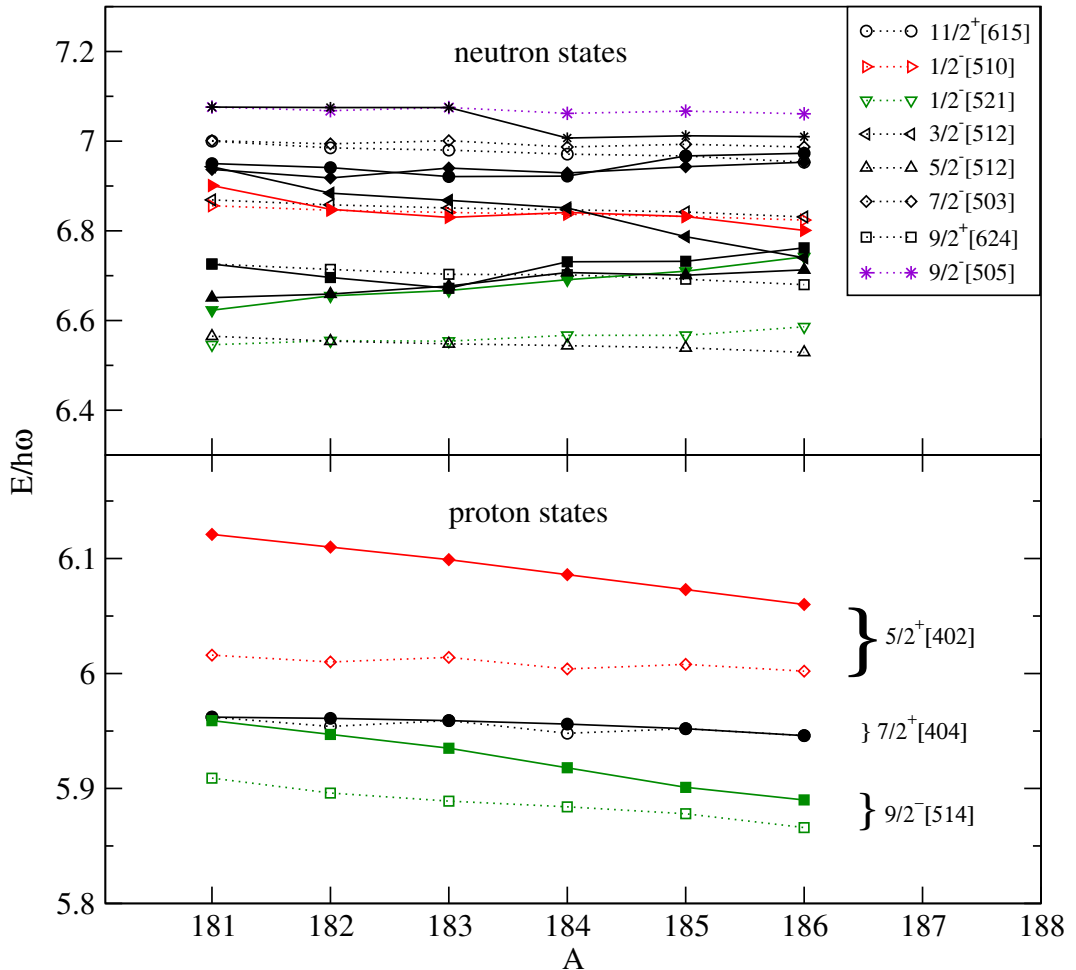


Figure 6.1: Nilsson single-particle energies (open symbols) for orbitals close to the neutron and proton Fermi surfaces in neutron-rich tantalum isotopes. The adjusted energies (filled symbols) that reproduce the experimental one and two-quasiparticle state energies are also shown.

For odd- A tantalum isotopes, the Nilsson energies of neutron states close to the neutron-Fermi surface were adjusted to reproduce approximately the experimental two-quasineutron energies in the neighbouring tungsten isotones. For example, Table 6.1 lists the low-lying, two-neutron states in ^{184}W that were reproduced for the prediction of states in ^{183}Ta . The corresponding proton states close to the Fermi surface were also adjusted to reproduce the experimental one-quasiproton

energies.

In even-A tantalum isotopes, the Nilsson proton energies were adjusted to match the average value from the two neighbouring odd-A isotopes. For example, the Nilsson energy of the $9/2^-$ [514] proton used in the calculations for ^{182}Ta is the average of the Nilsson energies of the similar proton configuration in ^{181}Ta and ^{183}Ta , after adjustments were made to reproduce experimental values in those nuclei. For the neutron states, where information is available, the Nilsson energies were adjusted to reproduce the experimental two-quasiparticle state energies in the odd-odd tantalum isotopes. Otherwise, the energies of single-neutron states were adjusted to those of neighbouring odd-mass tungsten isotopes. For example, in ^{182}Ta the $11/2^+$ [615] neutron was adjusted to reproduce the experimental energy of the $K^\pi=10^-$ state, while the rest of the single-neutron states near the Fermi surface were adjusted to match those observed to be low-lying in the ^{183}W isotope. The results for the adjusted and unadjusted proton and neutron Nilsson energies used in the present multi-quasiparticle calculations are plotted in Figure 6.1. The adjusted single-particle energies generally follow similar trends to those from the Nilsson model, and only small changes have been required.

6.2.1 Testing the results and summary of the calculations

In order to test the accuracy/credibility of the calculation prior to its application in making configuration assignments, comparisons were made between calculated and well-understood experimental configurations. For example, in odd-mass tantalum isotopes, multi-quasiparticle states up to the three-quasiparticle, $K^\pi=29/2^-$ state are known experimentally in ^{181}Ta [Dra98a, Whe99a], while a single three-quasiparticle state is known in ^{185}Ta [Lan09]. In even-A tantalum isotopes, there is limited experimental information, with only a couple of two-quasiparticle states known in ^{182}Ta , while nothing is known in ^{184}Ta . Calculations were carried out for all tantalum isotopes from ^{181}Ta to ^{185}Ta . This series of calculations can be used to investigate the expected systematic change of parameters with changing neutron

number as well as to test the reproduction of the already known states.

Predicted states in odd-even-tantalums

The energies of the predicted states (without residual interaction) for the odd-mass tantalum isotopes from $A=181\text{-}185$ are shown in figures 6.2, 6.3 and 6.4 as a function of $K(K+1)$, while results extracted for yrast and near-yrast states including the effects of residual interactions are shown in Figure 6.5. In Figure 6.2, the well known [Dra98a, Whe99a] yrast $K^\pi = 21/2^-$ and $K^\pi = 29/2^-$ states (with $K(K+1)=121$ and 225, respectively) are clearly visible and are amongst the low-lying predicted yrast states in ^{181}Ta . These two states have residual interactions of -77 and -44 keV and known configurations, $\pi\{7/2^+[404]9/2^-[514]5/2^+[402]\}$ and $\nu\{9/2^-[624]11/2^+[615]\} \otimes \pi9/2^-[514]$, respectively. The $K^\pi = 21/2^-$ state is predicted to lie ~ 100 keV above its observed value of 1483 keV, while the $K^\pi = 29/2^-$ state is predicted to be 200 keV below its measured value of 2230 keV. Dracoulis and Wheldon also performed multi-quasiparticle calculations for ^{181}Ta , but they each used slightly different approaches to the present calculations. Wheldon *et al.* [Whe99a] used BCS pairing, while Dracoulis *et al.* [Dra98a] used Lipkin-Nogami pairing and the same methodology as in the present work, except their single-neutron states were adjusted to reproduce the average of the adjusted single-neutron states in neighbouring ^{181}W and ^{179}Hf .

The known $K^\pi = 21/2^-$ state in ^{185}Ta is currently predicted 250 keV above the experimental value [Lan09, Whe99]. Note that this comparison assumes the $\nu^2\pi$ -configuration suggested by Lane *et al* [Lan09] based on comparisons with ^{186}W , and this is contrary to the π^3 assignment made in ^{181}Ta . Walker *et. al.* prefer the π^3 configuration assignment as discussed in Ref. [Wal15].

The adjustment to the single-particle energies gives, by definition, essentially perfect agreement for the single-proton levels, while a generally good agreement is also obtained between predictions and experimental observations for the few known multi-quasiparticle states in ^{181}Ta and ^{185}Ta . As discussed above, the known

three-quasiparticle states in ^{181}Ta and ^{185}Ta are predicted within 0.25 MeV of the experimental energies. Figure 6.6 shows the calculated yrast and near yrast states compared to the experimental single and multi-quasiparticle states known in ^{181}Ta [Dra98a, Whe99a], ^{183}Ta [Shi09] and ^{185}Ta [Lan09]. The strong agreement between the calculated and the experimental states in these odd-mass isotopes suggests that the other unknown states might also be well predicted and hence the results may be used to aid configuration assignments in cases where there is limited spectroscopic information.

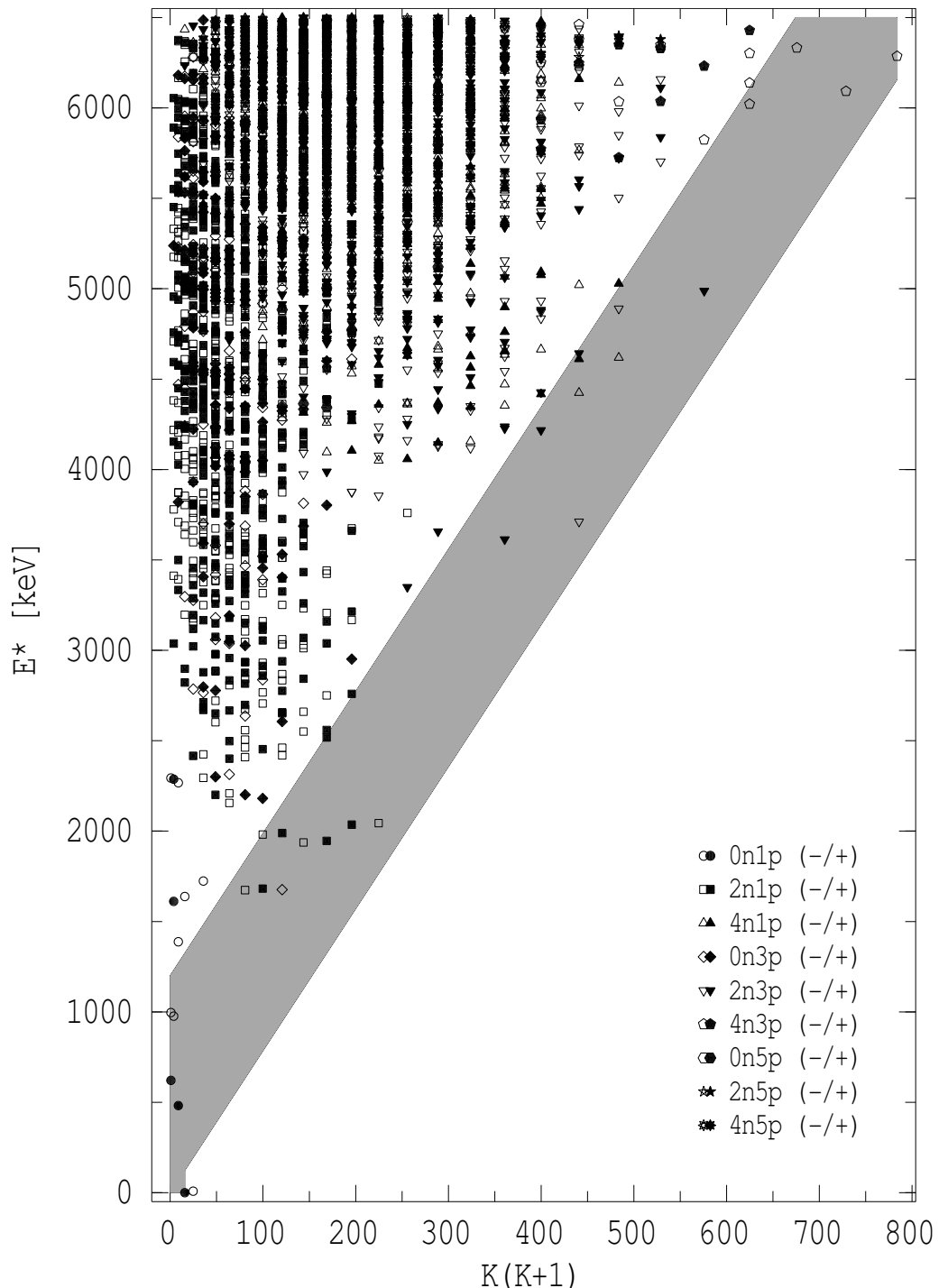


Figure 6.2: Predicted multi-quasiparticle states in ^{181}Ta , excluding the effects of residual interactions. Only configurations from parallel (high- K) couplings are plotted. The grey diagonal line denotes the approximate region of states within ~ 1.2 MeV of the yrast line.

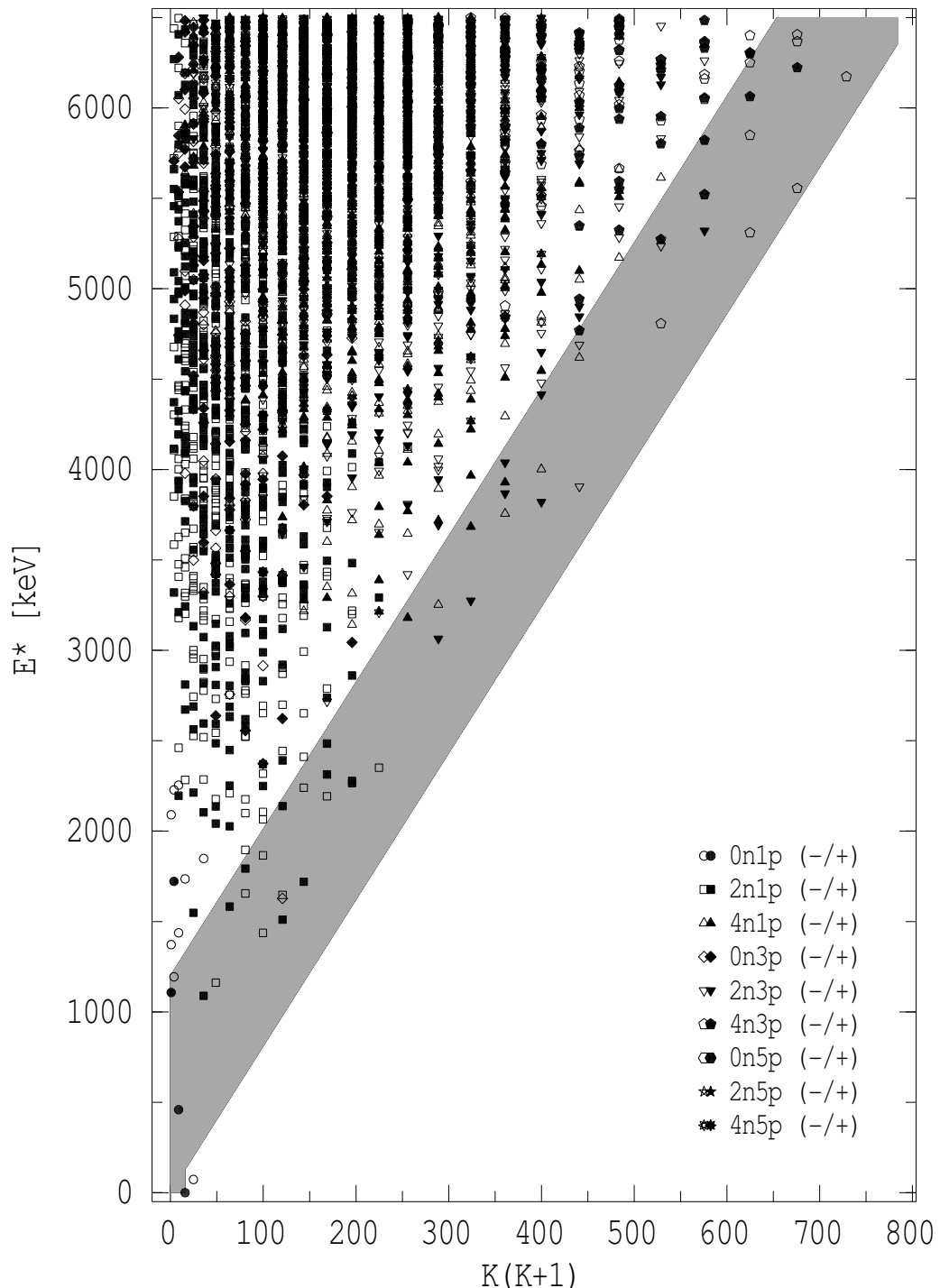


Figure 6.3: Predicted multi-quasiparticle states in ^{183}Ta , excluding the effects of residual interactions. Only configurations from parallel (high- K) couplings are plotted. The grey diagonal line denotes the approximate region of states within ~ 1.2 MeV of the yrast line.

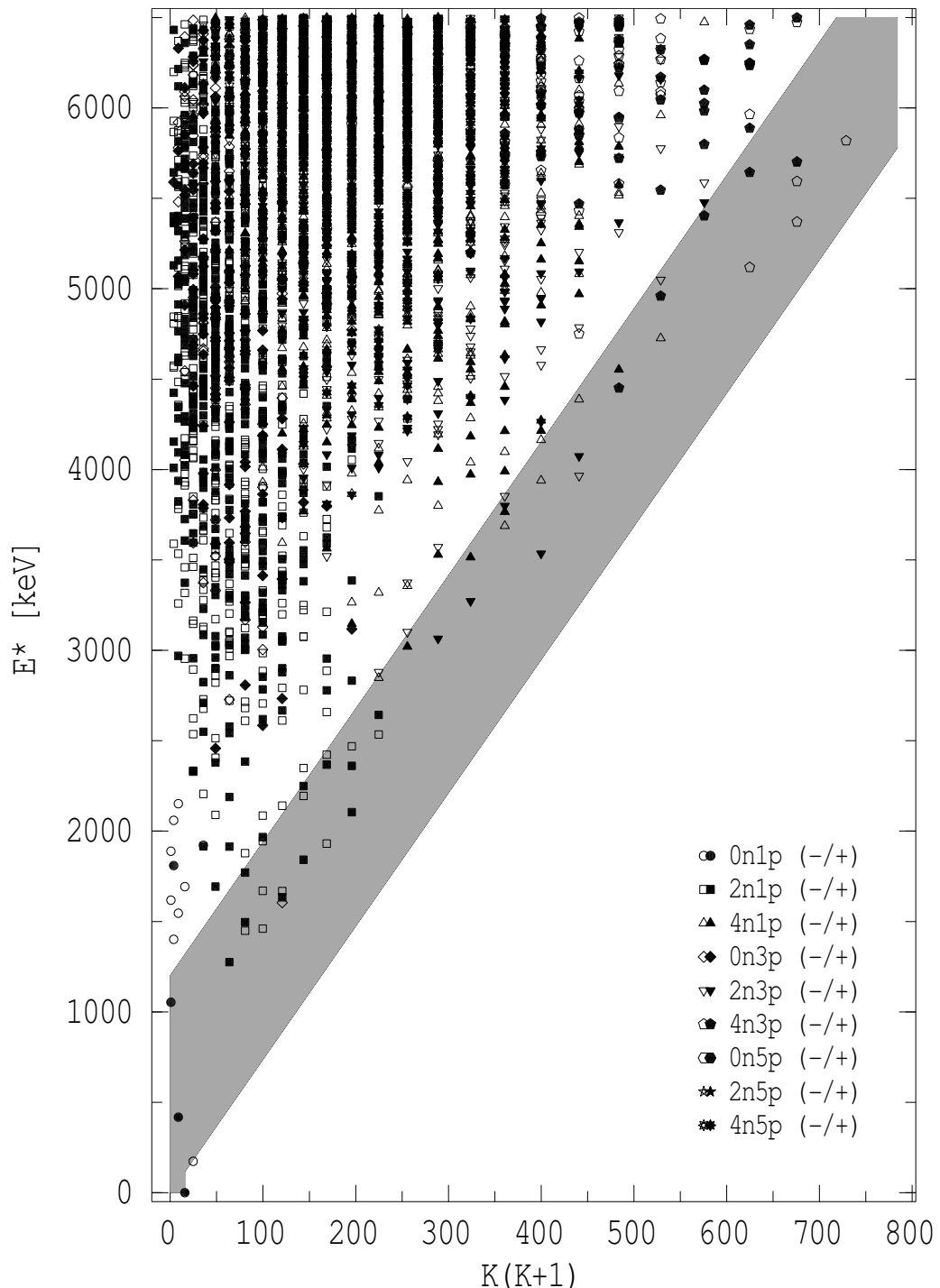


Figure 6.4: Predicted multi-quasiparticle states in ^{185}Ta , excluding the effects of residual interactions. Only configurations from parallel (high- K) couplings are plotted. The grey diagonal line denotes the approximate region of states within ~ 1.2 MeV of the yrast line.

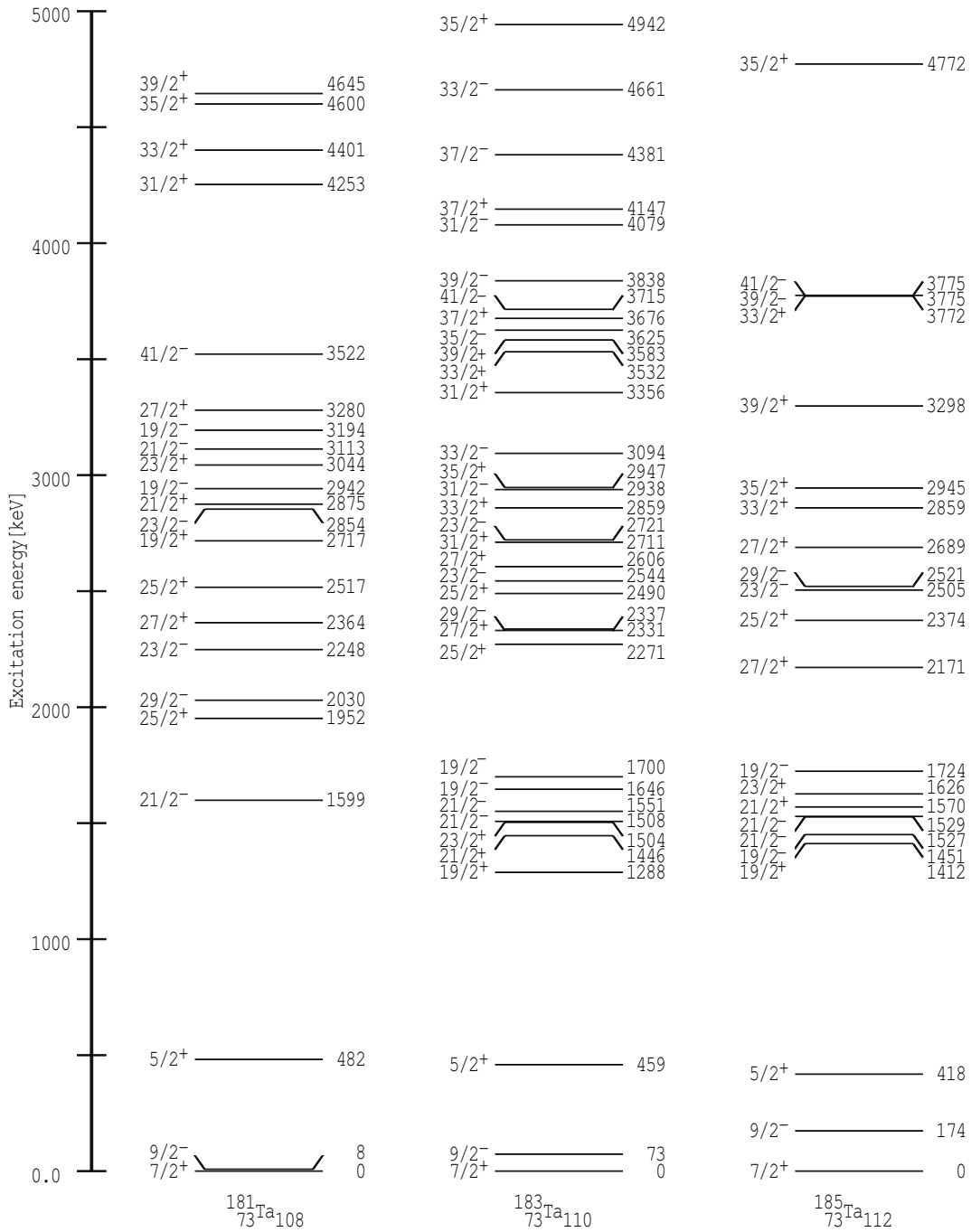


Figure 6.5: Systematics of selected yrast and near-yrast multi-quasiparticle states in odd-mass, neutron-rich tantalum isotopes as predicted by multi-quasiparticle calculations with Lipkin-Nogami pairing. The single-particle energies have been adjusted from the raw Nilsson predictions as described in the text and the effect of residual interactions has been included.

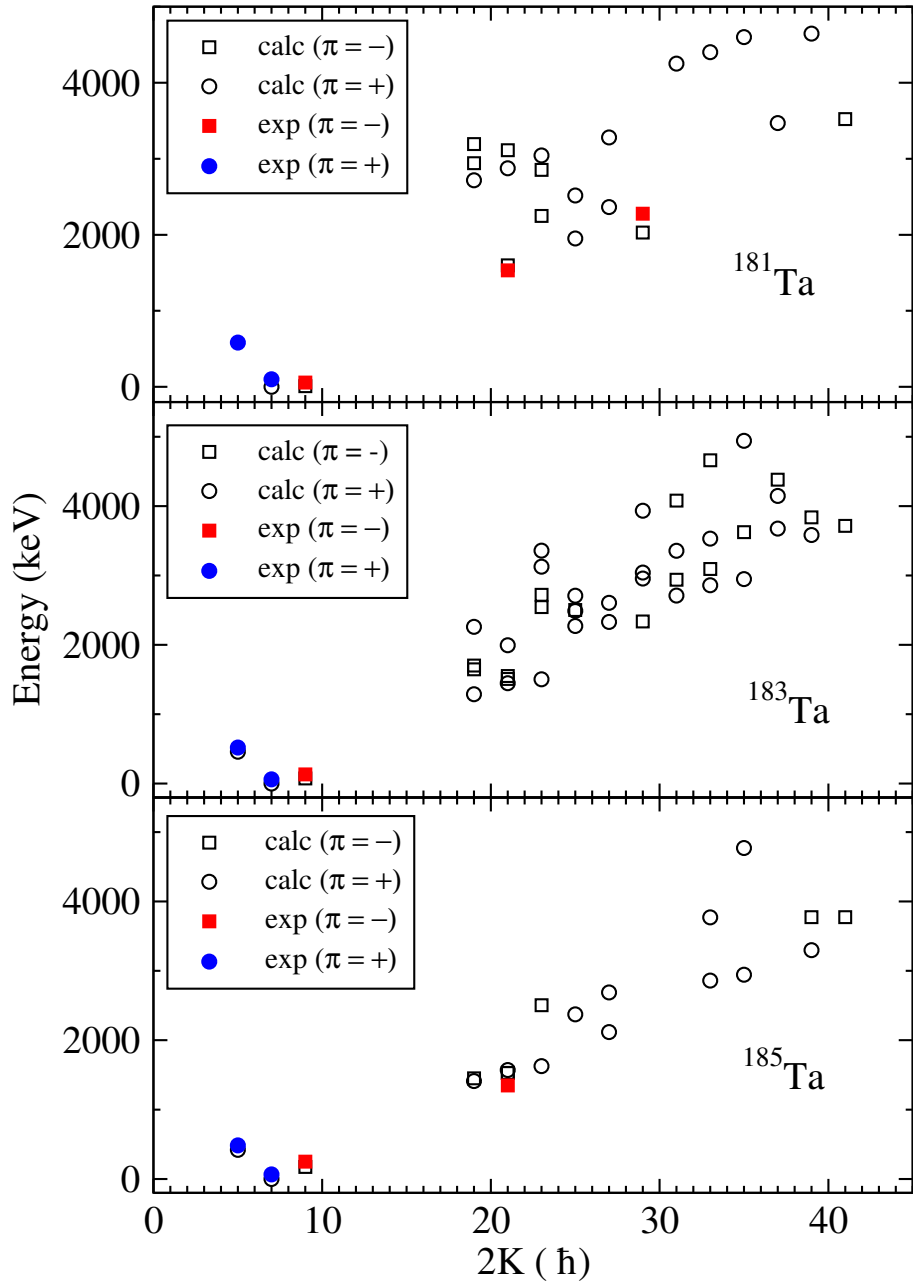


Figure 6.6: Calculated yrast and near-yrast states (open symbols) compared to the experimental single and multi-quasiparticles states (filled symbols) known in ^{181}Ta [Dra98a, Whe99a], ^{183}Ta [Shi09] and ^{185}Ta [Lan09, Shi07]. The adjustment to the single-particle energies means the single-proton levels agree perfectly, but good agreement is also obtained between predictions and experimental observations for the few known multi-quasiparticle states in ^{181}Ta and ^{185}Ta .

Predicted states in odd-odd-tantalum nuclei

The energies of the predicted states (without residual interaction) for even-mass tantalums are shown in figures 6.7 and 6.8 as a function of $K(K + 1)$. Unlike the

odd-mass cases, there is little or no experimental information that can be used to directly test the validity of the calculations in ^{182}Ta and ^{184}Ta , especially at higher spins and for configurations with more than two quasiparticles. Note that only three low-lying, two-quasiparticle states are known experimentally in ^{182}Ta [Hel71], while only the ground state is known in ^{184}Ta .

In the present calculations, the known $K^\pi = 10^-, \nu 11/2^+[615] \otimes \pi 9/2^-[514]$ state in ^{182}Ta [Hel71] is predicted to within 3 keV of the experimental value, simply because the energy of the $11/2^+[615]$ neutron state was adjusted to reproduce this exact state. For the ground state with $K^\pi = 3^-$ and a $\nu\{1/2^-[510]\} \otimes \pi 7/2^+[404]$ configuration and the $K^\pi = 5^+, \nu\{1/2^-[510]\} \otimes \pi 9/2^-[514]$ excited state at 16 keV, the energies are within 50 keV of the experimental values. The reason for this small discrepancy is due to fact that the energy of the common $1/2^-[510]$ neutron state was adjusted to reproduce the single-neutron energy in ^{183}W , unlike in the case of the $11/2^+[615]$ state that was adjusted to reproduce the energy of the 10^- in ^{182}Ta itself.

Figure 6.9 shows the calculated yrast and near yrast states plotted alongside the experimental observed states in ^{182}Ta [Hel71]. The three low-lying two quasiparticle states are well predicted. This strong agreement, although limited, suggests that four or six quasiparticle states may also be well predicted, especially considering that the single-particle states in Figure 6.1 are well-reproduced. Consistent with the odd-mass results, agreement within 0.3 MeV could be a reasonable expectation when comparing the experimental states with these predictions.

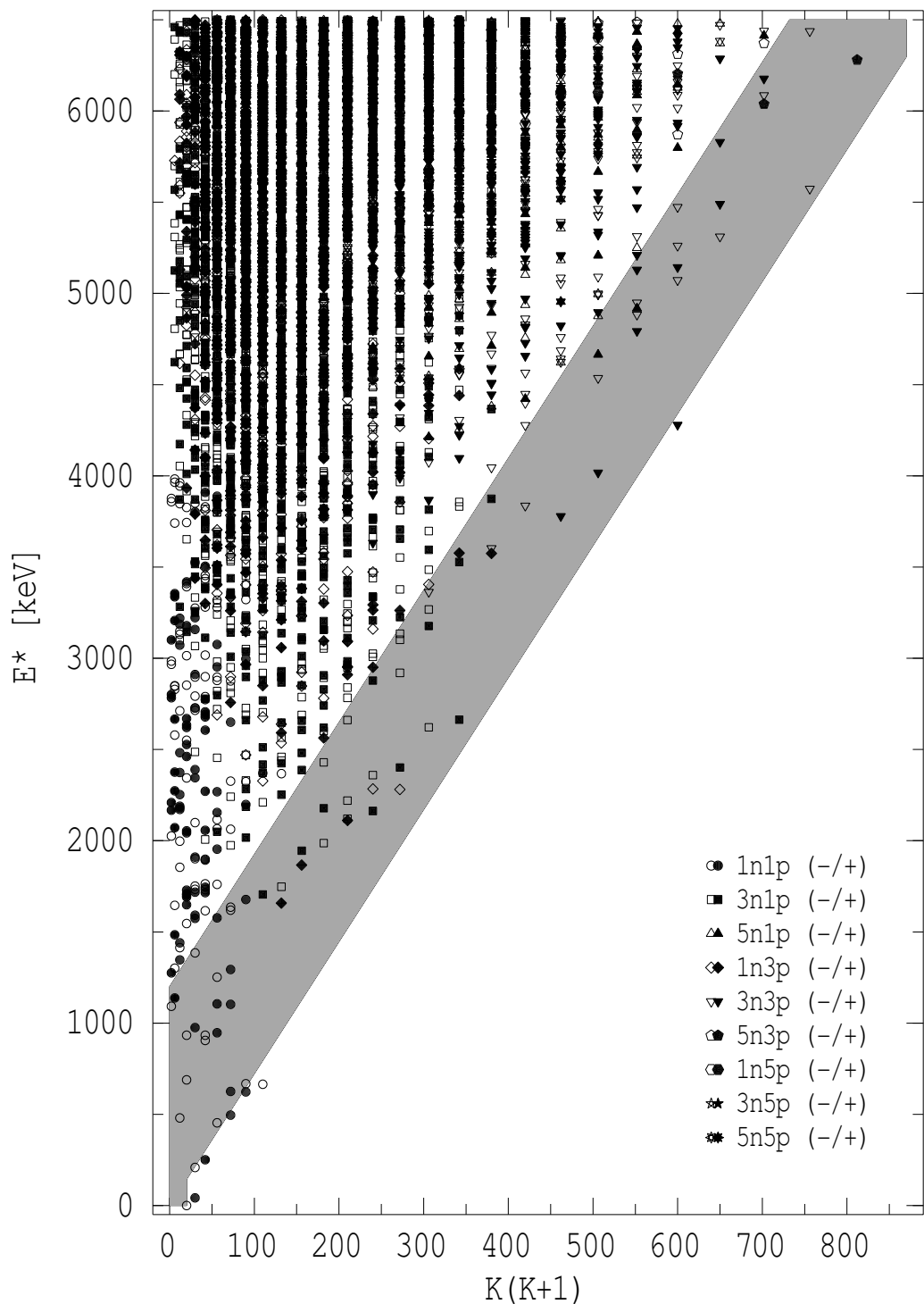


Figure 6.7: Predicted multi-quasiparticle states in ^{182}Ta , excluding the effects of residual interactions. Only configurations from parallel (high- K) coupling are plotted. The grey diagonal line denotes the approximate region of states within ~ 1.2 MeV of the yrast line.

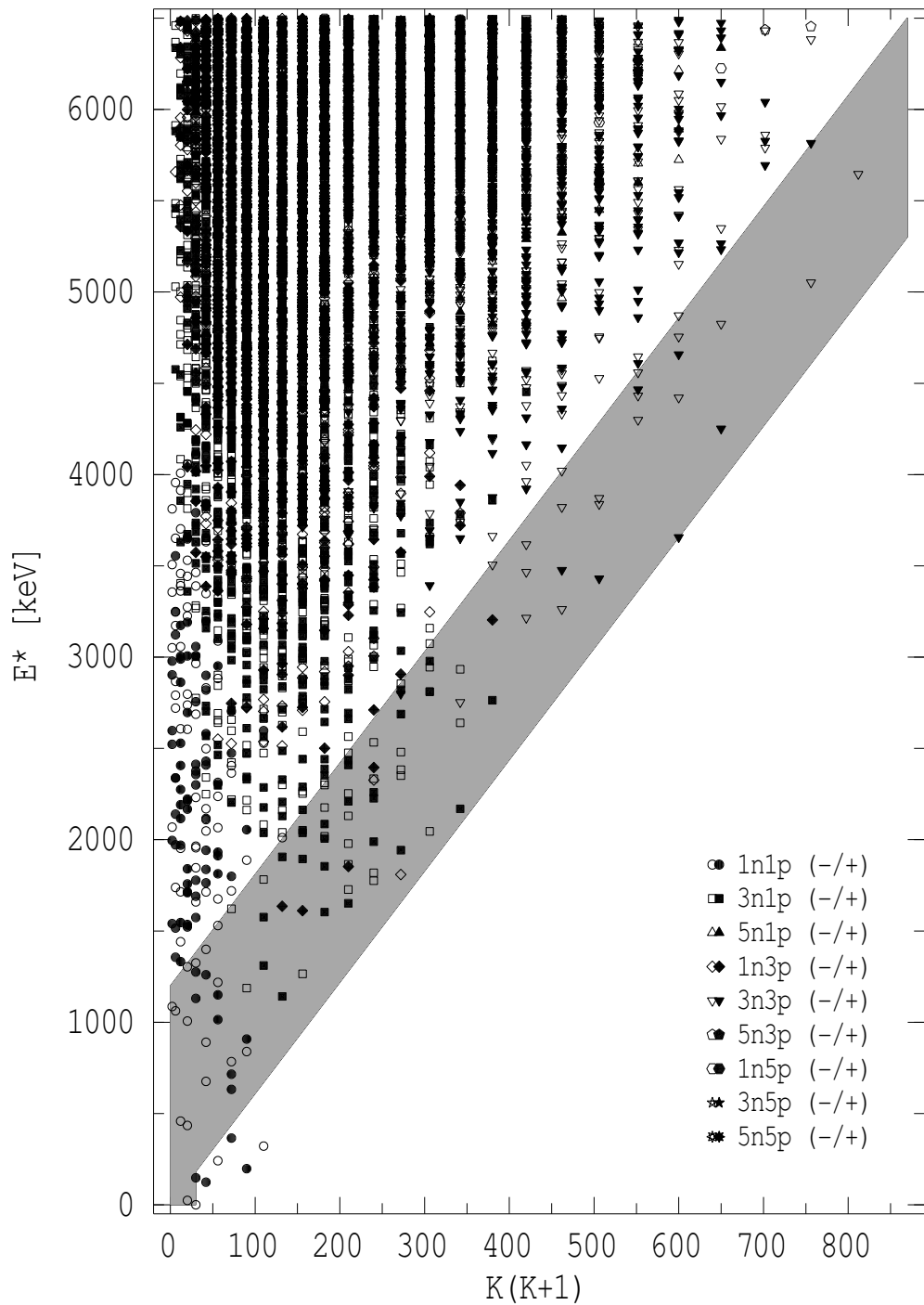


Figure 6.8: Predicted multi-quasiparticle states in ^{184}Ta , excluding the effects of residual interactions. Only configurations from parallel (high- K) coupling are plotted. The grey diagonal line denotes the approximate region of states within ~ 1.2 MeV of the yrast line.

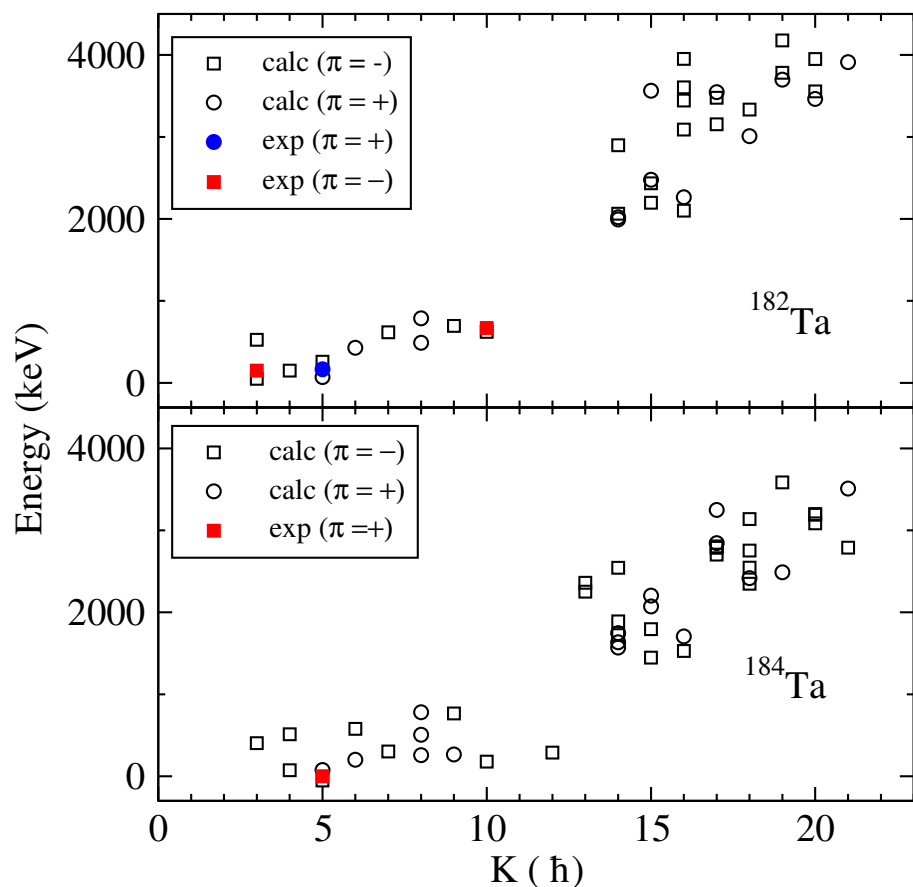


Figure 6.9: Calculated yrast and near-yrast states (open symbols) compared to the experimental states known in ^{182}Ta from Helmer *et al.* [Hel71] (top) and for ^{184}Ta (bottom), where only the ground state is known experimentally [War73]. The adjustments to the two-quasiparticle energies result in a good agreement between prediction and experimental observations for the few known multi-quasiparticle states in ^{182}Ta .

Configuration assignments

In the previous chapter, the energies of possible intrinsic states in ^{182}Ta and ^{183}Ta were predicted together with their configurations. This chapter attempts to understand the configurations of the observed states in the two isotopes using the g_K values and aligned angular momenta inferred from rotational band properties. Where there is limited spectroscopic information, assignments are made or supported by the predictions from the multi-quasiparticle calculations in the previous chapter.

The division between these two approaches is governed by the fact that, for both ^{182}Ta and ^{183}Ta , most of the observed rotational structures are built on low-energy intrinsic states, while at higher excitation energies, intrinsic states start to dominate over rotational structures. This is clearly visible in Figure 4.2 for ^{183}Ta above the 1332 keV isomeric state. This means that the evaluation of magnetic properties and alignments was only achievable for structures below ~ 2 MeV in ^{182}Ta and below ~ 1.3 MeV in ^{183}Ta . For structures above these energies, comparison with the results of multi-quasiparticle calculations (Chapter 6) are used for configuration assignments.

7.1 Magnetic properties

Well-developed rotational bands provide an opportunity to determine the multi-quasiparticle configurations from the in-band decay properties such as the γ -ray branching ratios, transition mixing ratios, and the deduced g_K values. These ex-

tracted g_K values were compared with values calculated using the Nilsson model and the additivity relation given by equation 2.51. Note that all Nilsson model values are taken from Ref. [Stu05] and assume deformations from Table 6.2. In some cases, empirical g_K values were used in preference to the Nilsson model values; these were obtained from experimental observations in the neighbouring isotopes or isotones. In deducing values for g_K , the present work has adopted the values of $g_R \sim 0.35(5)$ and $Q_o \sim 6.5$ eb, common choices in the mass-180 region, see for example Refs. [Lan09, Dra98a, Kon04, Das00].

7.2 Alignments

As discussed in section 2.4, large values of aligned angular momenta are expected for bands that have high- j and/or low- Ω orbitals amongst their configuration constituents. Hence the aligned angular momenta can be used as a guide to help assign configurations. To demonstrate this process, some known results in tantalum and tungsten nuclei around the mass-180 region will be discussed first. Analogous procedures will then be applied to the current results for ^{182}Ta and ^{183}Ta . The Harris reference parameters used for evaluating all of the aligned angular momenta are discussed in section 7.2.1 below.

Figures 7.1(a) and (b) show alignments for some of the known single-neutron bands in odd-mass ^{181}W [Lin73] and ^{183}W [Sai00]. Likewise, Figs. 7.1(c) and (d) show alignments for the three common low-lying proton bands in ^{181}Ta [Dra98a] and ^{183}Ta [Shi09].

As expected, both the high- j , $i_{13/2}$ neutron orbitals ($\Omega^\pi = 11/2^+[615]$, $\Omega^\pi = 9/2^+[624]$) and the low- Ω , $1/2^-[510]$ orbital, as shown in Figures 7.1(a) and (b), exhibit non-zero alignments of $\sim 1 \hbar$ or more. In Figures 7.1(c) and (d), the three proton bands show smaller alignments, with the $5/2^+[402]$ and $7/2^+[404]$ having $\sim 0.2 \hbar$. The $9/2^-[514]$ proton originates from a higher- j orbital ($h_{11/2}$) than the other two proton bands, which explains the slightly higher alignments that range between 0.6 and $1 \hbar$. These orbitals shown in Fig. 7.1 lie close to the

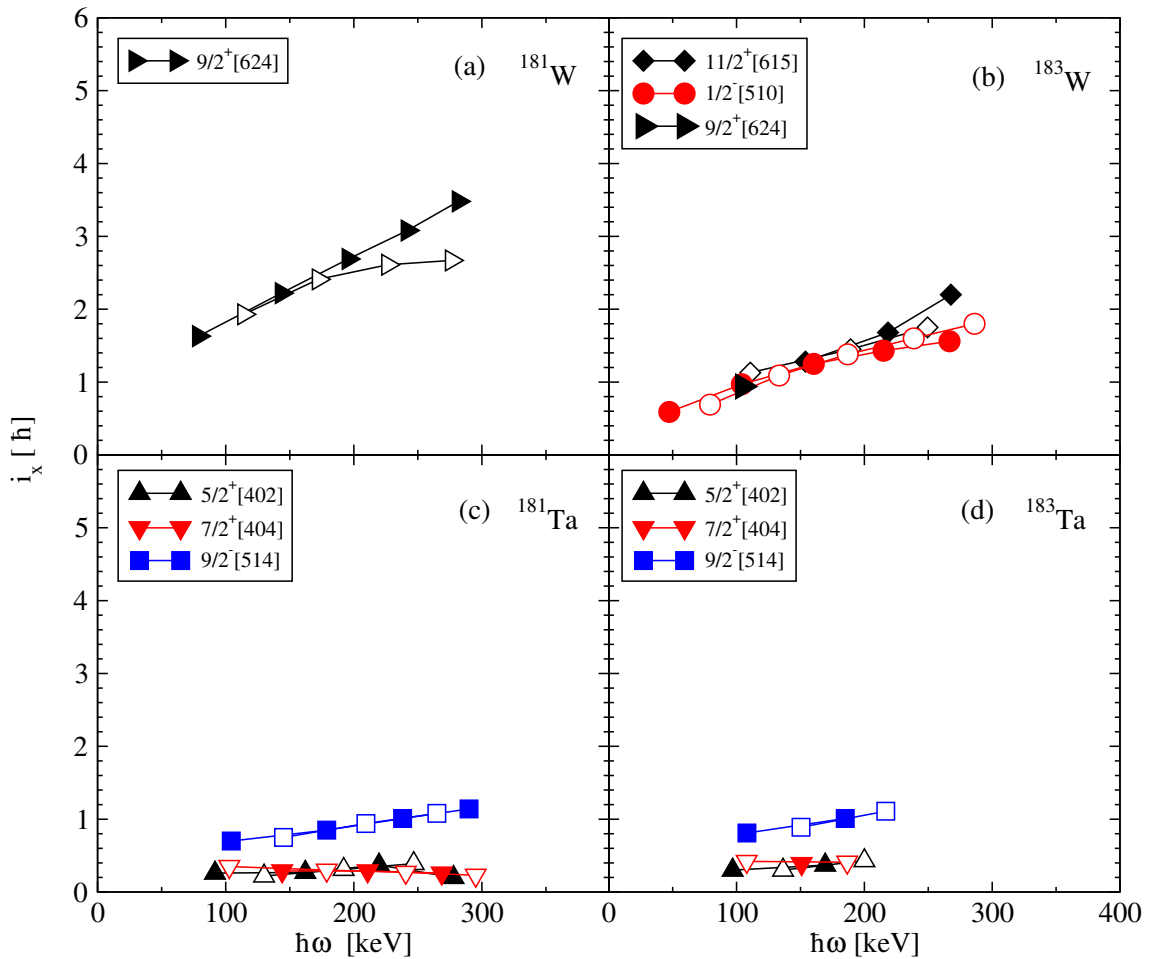


Figure 7.1: (a)-(b) Aligned angular momenta for selected single-quasineutron bands in ^{181}W [Lin73] and ^{183}W [Sai00]. (c)-(d) Aligned angular momenta for some of the three known single-quasiproton bands in ^{181}Ta [Dra98a] and ^{183}Ta [Shi09]. These values are used to illustrate the most likely alignments in single-particle states in tantalum isotopes. See table 7.1 for the reference parameters used in each nucleus. Open and filled symbols are used for the different signatures in each band.

neutron and proton Fermi surfaces in most of the tantalum isotopes around the $A=180$ region and, particularly the proton orbitals, will nearly always contribute to the configurations of the low-lying, multi-quasiparticle bands in tantalum nuclei [Kon04, Dra98a, Dra98, Lan09]. So one would expect such strong alignments to be observed also in these multi-quasiparticle configurations. To demonstrate this, the alignments of known multi-quasiparticle bands in neighbouring ^{180}Ta [Dra98] and ^{182}W [Shi95] will be examined (see Figure 7.2).

All four bands in Fig. 7.2 show relatively strong alignments $\geq 2\hbar$. In ^{180}Ta , shown

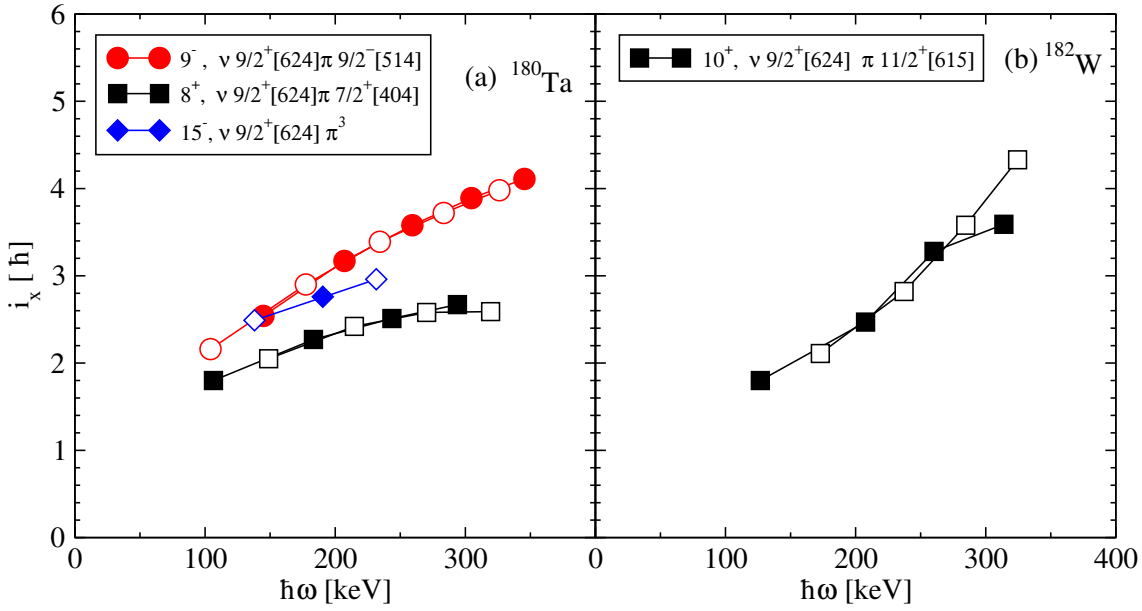


Figure 7.2: Alignments for some of the known multi-quasiparticle bands in ^{180}Ta [Dra98] and ^{182}W [Shi95] are used to illustrate the additivity of alignment in multi-quasiparticle states. See table 7.1 for the reference parameters used in each nucleus. Open and filled symbols are used for the different signatures in each band.

in Figure 7.2(a), the 8^+ band is a $9/2^+[624]$ neutron coupled to a $7/2^+[404]$ proton and has a smaller alignment than the 9^- band from the same $9/2^+[624]$ neutron now coupled to a $9/2^-[514]$ proton. The difference is analogous to the difference between the alignments of the $9/2^-[514]$ and $7/2^+[404]$ bands in both ^{181}Ta and ^{183}Ta . The 15^- band is only slightly different to the 9^- , consistent with it being the 9^- state coupled to additional $7/2^+[404]$ and $5/2^+[402]$ protons, with both of the latter carrying little alignment (see Fig. 7.1). Similarly the strong alignment of the 10^+ band in ^{182}W can be attributed to the alignments of its strongly aligned $i_{13/2}$ neutron constituents. The above scenarios demonstrate that, for a multi-quasiparticle state, the intrinsic alignments are additive. This principle will be used to test for the presence of the high- j or low- Ω neutron orbitals in the bands observed in ^{182}Ta and ^{183}Ta .

7.2.1 Harris parameters

Some comment is necessary regarding the choice of reference parameters, \mathfrak{S}_0 and \mathfrak{S}_1 , used in the present work, including in the Figures 7.1 and 7.2 above. First, the

alignments for the low-spin region of the ground-state bands in even-even hafnium and tungsten isotopes between $A=178$ and 184 are assumed to be $0 \hbar$. Hence, values for \mathfrak{S}_0 and \mathfrak{S}_1 were derived by a least-squares fit to these bands for all even-even cases in the region. The references used in the neighbouring odd-mass hafnium and tungsten isotopes, as well as the tantalum isotopes, were further derived by an averaging process. For example, the Harris parameters used in ^{181}W are an average of the references of the two neighbours, ^{180}W and ^{182}W , while that for ^{181}Hf is averaged over ^{180}Hf and ^{182}Hf . For each tantalum isotope, the reference is an average of that obtained for the two neighbouring hafnium and tungsten isotones. Table 7.1 gives a summary of the Harris parameters deduced and used in this chapter.

Table 7.1: Reference parameters \mathfrak{S}_0 and \mathfrak{S}_1 used in the present work to deduce the aligned angular momenta for rotational structures in the tantalum, tungsten and hafnium isotopes. Refer to the text for more details on how the values were deduced.

Isotope	\mathfrak{S}_0 (\hbar^2/MeV)	\mathfrak{S}_1 (\hbar^4/MeV^3)	fit or average
^{180}W	28.6	93.8	fit
^{181}W	29.2	69.6	average
^{182}W	29.8	45.5	fit
^{183}W	28.3	46.6	average
^{184}W	26.8	47.8	fit
^{180}Ta	30.5	64.3	average
^{181}Ta	30.9	41.7	average
^{182}Ta	29.8	43.9	average
^{183}Ta	28.7	46.1	average
^{178}Hf	31.7	80.1	fit
^{179}Hf	31.9	59.0	average
^{180}Hf	32.0	38.0	fit
^{181}Hf	31.3	41.2	average
^{182}Hf	30.6	44.4	fit

7.3 Configuration assignments in ^{183}Ta

7.3.1 Single-quasiparticle states

The configurations for the low-lying single proton states in ^{183}Ta had been verified by Shizuma *et al* [Shi09] from the observed spins and the g_K values deduced from the observed rotational band structures. The present work does not extend any of these bands, but the observations that were made are summarised below.

Ground state with $K^\pi = 7/2^+$

The $7/2^+[404]$ configuration for the ground state is well-established by Shizuma *et al* [Shi09] from the rotational band properties including the deduced $g_K - g_R$ value.

State at 73 keV with $K^\pi = 9/2^-$

The band built on this state was observed by Shizuma *et al.* [Shi09] up to the $19/2^-$ state and the $\pi 9/2^-[514]$ configuration was confirmed from the measured in-band decay properties. The present work observed states up to $17/2^-$ and the weighted average value of $|g_K - g_R| = 0.89(4)$ evaluated from the measured in-band branching ratios is shown in table 7.2. The implied g_K value of $1.24(6)$ (assuming $g_R = 0.35(5)$ as detailed in section 7.1) is consistent with both the previous measurement [Shi09], and the theoretical expectation of $g_K = 1.29$ for the $9/2^-[514]$ configuration [Stu05]. This band is also well known in the neighbouring ^{185}Ta isotope, with the g_K value reported as $1.21(5)$ [Lan09].

Table 7.2: Measured in-band branching ratios for the $9/2^-[514]$ band in ^{183}Ta , together with inferred gyromagnetic ratios.

K^π	J_i^π	E_γ ($I \rightarrow I-1$)	E_γ ($I \rightarrow I-2$)	λ^a	$ g_K - g_R ^b$
		(keV)	(keV)		
$9/2^-$	$13/2^-$	185.7	343.4	0.14(3)	0.83(9)
	$15/2^-$	212.2	397.6	0.25(4)	0.93(7)
	$17/2^-$	237.7	449.9	0.45(6)	0.89(6)
			weighted avg:	0.89(4)	

^a $\lambda = I_\gamma(I \rightarrow I-2)/I_\gamma(I \rightarrow I-1)$.

^b Assuming $Q_0 = 6.5 \text{ eb}$.

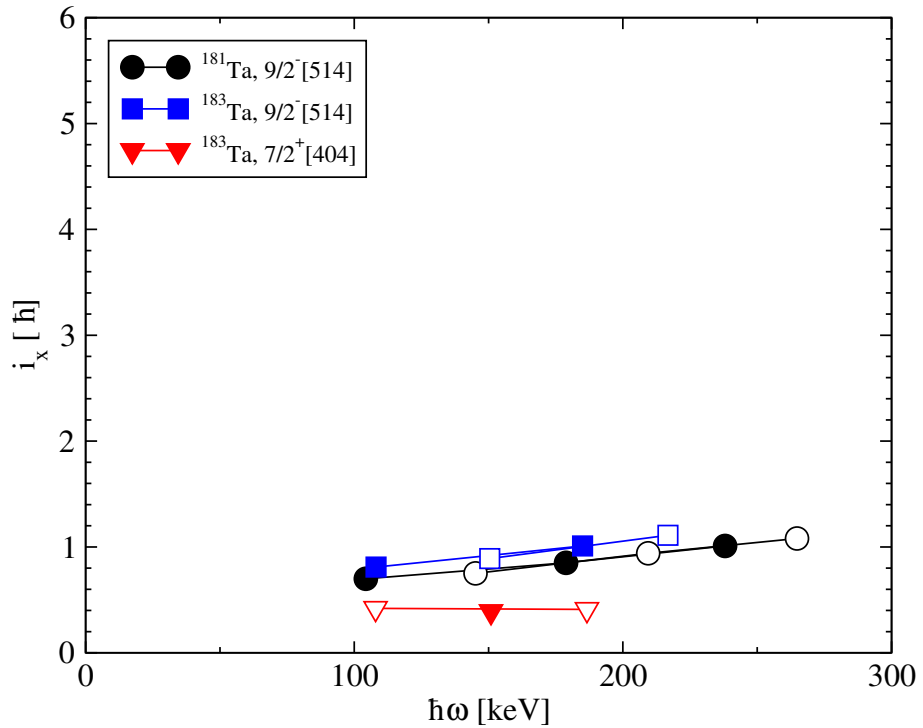


Figure 7.3: Aligned angular momenta for the $\pi 9/2^-[514]$ band in ^{183}Ta compared to the same band in ^{181}Ta [Dra98a, Sai98] and the $\pi 7/2^+[404]$ band in ^{183}Ta [Shi09]. See table 7.1 for the reference parameters used for each nucleus. Open and filled symbols are used for the different signatures in each band.

Figure 7.3 shows the aligned angular momentum of this band, compared with the $\pi 9/2^-[514]$ and $\pi 7/2^+[404]$ structures in ^{181}Ta [Sai98] and ^{183}Ta [Shi09], respectively. The band carries a small alignment, consistent with expectations for the $9/2^-[514]$ proton known in the neighbouring odd isotopes, and confirms Shizuma's prior interpretation.

7.3.2 Multi-quasiparticle states

As observed in Figure 4.2 and discussed in section 4.2.3, there was no sign of regular rotational band structures observed above the $19/2^+$, 1332 keV isomeric state. Most of the levels, except possibly the 1878 keV state, appear to be intrinsic states. Given the excitation energies of these states, configurations of three or more quasiparticles are likely. Due to the absence of collective structures, the configurations of these multi-quasiparticle states can only be presented in terms of the predicted intrinsic states from the multi-quasiparticle calculations presented in the previous chapter.

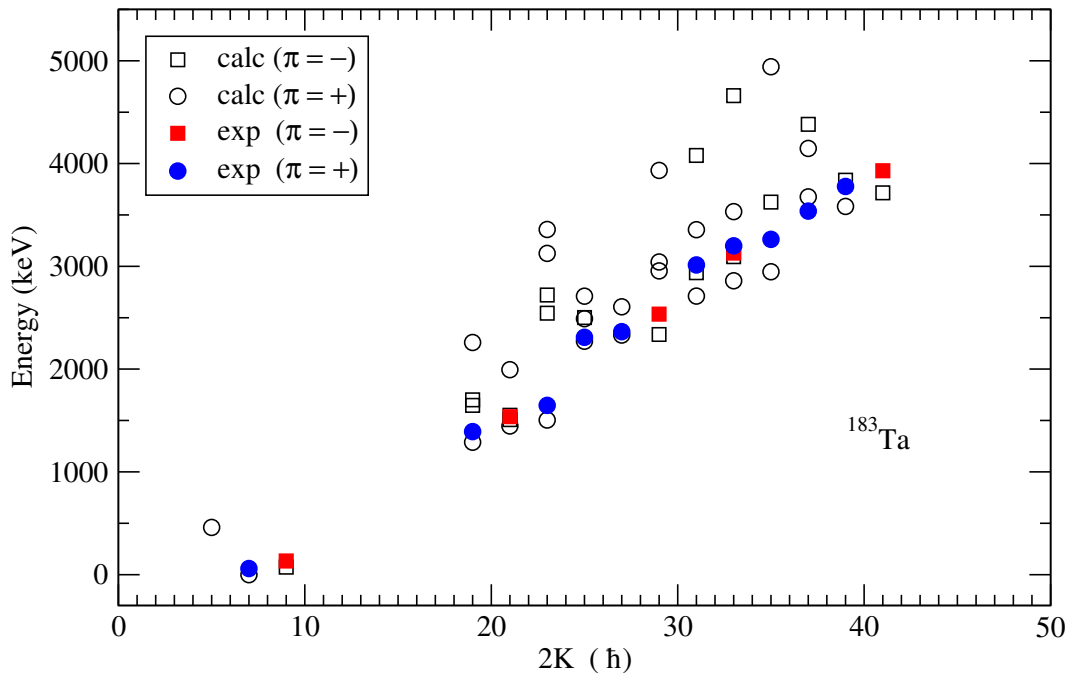


Figure 7.4: Calculated yrast and near-yrast states in ^{183}Ta , compared with experimental energies from the present work. There is good agreement between predicted values and experimental observations.

Figure 7.4 gives the energies of the predicted, near yrast states in ^{183}Ta (including residual interactions), plotted against spin and compared to the experimental states observed in the current work. The calculations predict a high density of intrinsic states above ~ 1 MeV, consistent with the observed decay scheme in Fig. 4.2. For these predicted states, there are several candidates with spins and parities that are consistent with those suggested in Figure 4.2 from the spectroscopic information. For example, the spins and parities of the isomers at 1332 keV with $I^\pi = 19/2^+$, 2475 keV with $I^\pi = 29/2^-$, and 3870 keV with $I^\pi = 41/2^-$, are well reproduced. The energies and configurations for the predicted states are shown in Table 7.3. Most of the yrast states with three or more quasiparticles are reproduced to within 300 keV of the experimental energies, consistent with the results for ^{181}Ta and ^{185}Ta used in Chapter 6 to test the calculations. The good agreement between the calculated and the experimental energies in this isotope, confirms the credibility and predictive power of the present calculations for odd-mass tantalums as discussed earlier. Hence, these results will be used for configuration assignments.

State at 906 keV, $I^\pi = 13/2^-$

Shizuma *et al.* [Shi09] suggested this state was a γ -vibration built upon the $9/2^-[514]$ state. In the present work, no state with $13/2^-$ is predicted with an energy comparable to that of the observed $13/2^-$ (refer to Fig. 7.4 and Table 7.3), suggesting a non-intrinsic state for the observed $13/2^-$ bandhead. Similarly, its energy seems too low to be a three-quasiparticle state considering the energies of 1484 keV and 1273 keV for the lowest three-quasiparticle states known in ^{181}Ta [Dra98a] and ^{185}Ta [Lan09], respectively. The many new transitions observed in the present work establish a pattern of decay for this band consisting of $J \rightarrow J$, $J \rightarrow J - 1$ and $J \rightarrow J - 2$ transitions back to the $9/2^-[514]$ band; this is consistent with other γ -bands observed in this mass region, for example, in $^{187,189}\text{Re}$ [Ree16]. It is therefore possible to assign this state as $9/2^-[514] \otimes 2_\gamma^+$, as suggested by Shizuma *et al.* [Shi09].

Three-quasiparticle states**Isomeric state at 1332 keV, $K^\pi = 19/2^+$**

The present calculations predict two $19/2^+$ states at 1288 and 2259 keV. The higher-lying $\nu\{1/2^-[510]9/2^+[624]\} \otimes \pi9/2^-[514]$ state is predicted 927 keV above the experimental value of 1332 keV, whereas the $\nu\{1/2^-[510]11/2^+[615]\} \otimes \pi9/2^-[514]$ configuration lies just 44 keV below the observed value (see Table 7.3) and is assigned to this isomer. Note that this state is a non-maximal coupling, with the $1/2^-[510]$ state contributing $\Omega = -1/2$ to the total K -value.

States at 1477, 1587, 1878, 2250 and 2304 keV

For the $21/2^-$ state at 1477 keV, two possible configurations of $\nu\{3/2^-[510]11/2^+[615]\} \otimes \pi7/2^+[404]$ and $\pi\{7/2^+[404]9/2^-[514]5/2^+[402]\}$ are predicted to lie within 80 keV of the observed value. The three-proton configuration is also known in ^{177}Ta [Das00], ^{179}Ta [Kon04] and ^{181}Ta [Whe99a]. In ^{185}Ta , Lane *et al.* [Lan09] assigned a $\nu^2\pi$ configuration to this state by comparison with the ^{186}W isotope. On the other hand, Walker *et al* [Wal15] prefer the π^3 interpretation

Table 7.3: Predicted multi-quasiparticle states in ^{183}Ta compared with experimentally observed states. Section 6.2 describes the details of the calculations and the parameters used.

K^π	Configuration	π	E_{qp}^m (keV)	E_{res} (keV)	E_{cal} (keV)	E_{exp} (keV)	ΔE (keV)
ν		π					
7/2 ⁺		7/2 ⁺	0.0	-	0.0	0.0	0
9/2 ⁻		9/2 ⁻	73.0	-	73.0	73	0
5/2 ⁺		5/2 ⁺	459	-	459		
19/2 ⁺	1/2 ⁻ , 11/2 ⁺	9/2 ⁻	1510	-222	1288	1332	-44
	9/2 ⁺ , 1/2 ⁻	9/2 ⁻	2249	+8	2259		
19/2 ⁻	1/2 ⁻ , 11/2 ⁺	7/2 ⁺	1437	+264	1701		
	3/2 ⁻ , 7/2 ⁻	9/2 ⁻	1866	-219	1647		
21/2 ⁺	1/2 ⁻ , 11/2 ⁺	9/2 ⁻	1510	-64	1446		
	9/2 ⁺ , 3/2 ⁻	9/2 ⁻	2138	-145	1994		
21/2 ⁻	3/2 ⁻ , 11/2 ⁺	7/2 ⁺	1647	-139	1508	1477	+31
		9/2 ⁻ , 7/2 ⁻ , 5/2 ⁺	1628	-77	1551		
23/2 ⁺	3/2 ⁻ , 11/2 ⁺	9/2 ⁻	1720	-216	1504	1587	-83
	9/2 ⁺ , 1/2 ⁻ , 3/2 ⁻ , 11/2 ⁺	7/2 ⁺	3180	+180	3360		
	1/2 ⁻ , 11/2 ⁺	9/2 ⁻ , 7/2 ⁺ , 5/2 ⁺	3065	+61	3126		
23/2 ⁻	9/2 ⁺ , 7/2 ⁻	7/2 ⁺	2411	+311	2721		
	5/2 ⁻ , 11/2 ⁺	7/2 ⁺	2240	+304	2544		
25/2 ⁺	9/2 ⁺ , 7/2 ⁻	9/2 ⁻	2484	+6	2490		
	5/2 ⁻ , 11/2 ⁺	9/2 ⁻	2313	-43	2271	(2250)	+21
	9/2 ⁺ , 11/2 ⁺	5/2 ⁺	2737	-28	2709		
25/2 ⁻	11/2 ⁻ , 7/2 ⁻	7/2 ⁺	2193	+310	2502		
27/2 ⁺	9/2 ⁺ , 11/2 ⁺	7/2 ⁺	2278	+328	2606		
	11/2 ⁺ , 7/2 ⁻	9/2 ⁻	2266	+66	2331	2304	+27
29/2 ⁺	9/2 ⁺ , 1/2 ⁻ , 3/2 ⁻ , 11/2 ⁺	7/2 ⁺	3180	-225	2955		
	3/2 ⁻ , 11/2 ⁺	9/2 ⁻ , 7/2 ⁻ , 5/2 ⁺	3274	-233	3042		
	11/2 ⁻ , 7/2 ⁻	9/2 ⁻ , 7/2 ⁻ , 5/2 ⁺	3820	+113	3933		
29/2 ⁻	9/2 ⁺ , 11/2 ⁺	9/2 ⁻	2351	-14	2337	2475	-138
31/2 ⁺	9/2 ⁺ , 1/2 ⁻ , 3/2 ⁻ , 11/2 ⁺	7/2 ⁺	3180	+177	3356		
	1/2 ⁻ , 11/2 ⁺	9/2 ⁻ , 7/2 ⁺ , 5/2 ⁺	3065	-354	2711	2953	-242
31/2 ⁻	9/2 ⁺ , 1/2 ⁻ , 3/2 ⁻ , 11/2 ⁻	9/2 ⁻	3253	-315	2938		
	9/2 ⁺ , 11/2 ⁺	9/2 ⁻ , 7/2 ⁺ , 5/2 ⁺	3905	+174	4079		
33/2 ⁺	9/2 ⁺ , 1/2 ⁻ , 11/2 ⁺ , 7/2 ⁻	7/2 ⁺	3274	+258	3532		
	1/2 ⁻ , 11/2 ⁺	9/2 ⁻ , 7/2 ⁻ , 5/2 ⁺	3065	-206	2859	(3139)	-280
33/2 ⁻	9/2 ⁺ , 1/2 ⁻ , 3/2 ⁻ , 11/2 ⁺	9/2 ⁻	3253	-159	3094	3068	+26
	9/2 ⁺ , 3/2 ⁻ , 11/2 ⁺ , 7/2 ⁻	9/2 ⁻	4002	+659	4661		
35/2 ⁺	3/2 ⁻ , 11/2 ⁺	9/2 ⁻ , 7/2 ⁺ , 5/2 ⁺	3274	-328	2947	3202	-255
	9/2 ⁺ , 1/2 ⁻ , 11/2 ⁺ , 7/2 ⁻	7/2 ⁺	3683	+1259	4942		
35/2 ⁻	9/2 ⁺ , 1/2 ⁻ , 11/2 ⁺ , 7/2 ⁻	9/2 ⁻	3756	-131	3625		
37/2 ⁺	9/2 ⁺ , 3/2 ⁻ , 11/2 ⁺ , 7/2 ⁻	7/2 ⁺	3929	+218	4147		
	5/2 ⁻ , 11/2 ⁺	9/2 ⁻ , 7/2 ⁺ , 5/2 ⁺	3868	-192	3676	3477	+199
37/2 ⁻	9/2 ⁺ , 1/2 ⁻ , 11/2 ⁺ , 7/2 ⁻	9/2 ⁻	3756	+626	4382		
39/2 ⁺	11/2 ⁺ , 7/2 ⁻	9/2 ⁻ , 7/2 ⁺ , 5/2 ⁺	3820	-238	3583	3717	-134
39/2 ⁻	9/2 ⁺ , 3/2 ⁻ , 11/2 ⁺ , 7/2 ⁻	9/2 ⁻	4002	-164	3838		
41/2 ⁻	9/2 ⁺ , 11/2 ⁺	9/2 ⁻ , 7/2 ⁺ , 5/2 ⁺	3905	-190	3715	3870	-155

Configurations: Neutrons: 1/2⁻: 1/2⁻[510], 3/2⁻: 3/2⁻[512], 5/2⁻: 5/2⁻[512], 7/2⁻: 7/2⁻[503], 11/2⁺: 11/2⁺[615], 9/2⁺: 9/2⁺[624]. Protons: 5/2⁺: 5/2⁺[402]; 7/2⁺: 7/2⁺[404]; 9/2⁻: 9/2⁻[514].

based on systematics of K -hindrances in this region.

Examining the systematic calculations in Fig. 6.5 of the predicted states in odd- A tantalum nuclei from ^{181}Ta to ^{185}Ta , it can be observed that the $\pi\nu^2$ state lies high in ^{181}Ta , but lowers to become competitive with the π^3 state in both ^{183}Ta and ^{185}Ta . On that basis, the $\nu\{3/2^-[510]11/2^+[615]\} \otimes \pi7/2^+[404]$ configuration is proposed for the $21/2^-$ state in ^{183}Ta , although the π^3 configuration cannot be ruled out completely.

For the proposed $23/2^+$ state at 1587 keV, the $\nu\{3/2^-[512]11/2^+[615]\} \otimes \pi9/2^-[514]$ configuration appears to be the only energy-favoured configuration among the three predicted $23/2^+$ states.

The observed energy of 1878 keV for the $25/2^+$ state appears too low to be comparable to the energies of the three predicted $25/2^+$ states in Table 7.3, with the lowest lying at 2271 keV. This suggests that the 1878 keV level may be a collective state above the $23/2^+$ bandhead. The angular correlations in Fig. 4.15 suggest a mixed $M1/E2$ character with $\delta = 0.26(5)$ for the 291 keV transition. A value of $g_K = 0.89(5)$ can be deduced from this mixing ratio (assuming $g_R = 0.35(5)$), inconsistent with the theoretical expected value of $g_K=0.437$ for the proposed $23/2^+$ configuration. Hence, the nature of the $25/2^+$ state remains somewhat unclear.

A $\nu5/2^-[512]11/2^+[615] \otimes \pi9/2^-[514]$ configuration can be proposed for the $(25/2^+)$ level at 2250 keV, despite the unconfirmed spin and parity, as well as the unknown ordering of the 54 and 663 keV transitions. This energy favoured configuration is calculated to lie at 2271 keV, 21 keV above the tentative experimental value. The other two $25/2^+$ states are predicted to lie higher at 2490 and 2709 keV.

For the $27/2^+$ state at 2304 keV, the calculations predict a low-lying $\nu\{11/2^+[615]7/2^-[503]\} \otimes \pi9/2^-[514]$ state that appears just 27 keV above the experimental value, while the other calculated $27/2^+$ configuration lies more than

300 keV above the observed energy.

Isomeric state at 2475 keV, $K^\pi = 29/2^-$

There is only one low-lying $29/2^-$ state predicted, with its energy of 2337 keV only 138 keV below the observed value. The corresponding three-quasiparticle configuration of $\nu\{9/2^-[624]11/2^+[615]\} \otimes \pi 9/2^-[514]$ has been assigned to the observed $29/2^-$ isomer. Isomers with $K^\pi = 29/2^-$ and the same configuration have been observed in the neighbouring isotope ^{181}Ta [Whe99a] and the isobar ^{183}Re [Pur00, Has98].

Five-quasiparticle states

States at 2953, 3069, 3139, 3202, 3477 and 3717 keV

From Table 7.3, the only $31/2^+$ intrinsic state calculated to lie close in energy to the experimental state at 2953 keV is a five-quasiparticle state with the $\nu\{1/2^-[510]11/2^+[615]\} \otimes \pi\{9/2^-[514]7/2^+[404]5/2^+[402]\}$ configuration. The other alternative $K^\pi = 31/2^+$ state is predicted 400 keV above the experimental value.

Only one low-lying $33/2^-$ state was predicted and this can be associated with the tentative $K^\pi=33/2^-$ experimental state at 3069 keV. The $\nu\{9/2^+[624]1/2^-[510]11/2^+[615]3/2^-[512]\} \otimes \pi 9/2^-[514]$ configuration is calculated to lie just 25 keV below the experimental value.

The spin and parity for the $(33/2^+)$ state at 3139 keV is tentative, as is the ordering of the 64 and 186 keV transitions. Nevertheless, the calculations predict two $K^\pi = 33/2^+$ states, with the $\nu\{1/2^-[510]11/2^+[615]\} \otimes \pi\{9/2^-[514]7/2^+[404]5/2^+[402]\}$ lying at 2859 keV, 280 keV below the experimental value. The other alternative $K^\pi = 33/2^+$ state with a $\nu^4\pi$ configuration is predicted 390 keV above the experimental value.

Of the two $35/2^+$ states predicted, the only energy favoured state corresponds to the $\nu\{3/2^-[512]11/2^+[615]\} \otimes \pi\{9/2^-[514]7/2^+[404]5/2^+[402]\}$ configuration,

appearing 255 keV below the observed value of 3202 keV.

For the $37/2^+$ state at 3477 keV, the calculations predict a low-lying state with the $\nu\{5/2^-[512]11/2^+[615]\} \otimes \pi\{9/2^-[514]7/2^+[404]5/2^+[402]\}$ configuration that appears 200 keV above the experimental energy value, while the other calculated $37/2^+$ configuration lies over 600 keV above the observed energy.

Only one low-lying $39/2^+$ state is predicted. This state with a $\nu\{7/2^-[503]11/2^+[615]\} \otimes \pi\{9/2^-[514]7/2^+[404]5/2^+[402]\}$ configuration is predicted 134 keV above the experimental value of 3717 keV.

Isomeric state at 3870 keV, $K^\pi = 41/2^-$

Only one low-lying $41/2^-$ state is predicted and this state can be associated with the 3870 keV isomer. This $\nu\{9/2^+[624]11/2^+[615]\} \otimes \pi\{9/2^-[514]7/2^+[404]5/2^+[402]\}$ configuration is calculated 155 keV below the experimental value.

7.4 Configuration assignments in ^{182}Ta

7.4.1 Two-quasiparticle states

Ground state at 3^-

The ground state rotational band remains unobserved, so no information is available concerning its g_K value. Bizzarri *et al.* [Biz66] and Helmer *et al.* [Hel71] assigned the $\nu1/2^-[510] \otimes \pi7/2^+[404]$ configuration to this state based on model calculations. In the present calculation this configuration is predicted to be the ground state while the other 3^- state appears higher in energy (see Table 7.5).

$K^\pi = 5^+$ state at 16 keV

The band built on this state was observed in previous work [Biz66, Hel71] and both groups assigned it to the $\nu1/2^-[510] \otimes \pi9/2^-[914]$ configuration. In the present

work, a value of $|g_K - g_R|$ was evaluated from the measured in-band branching ratio of the 172 and 318 keV transitions as shown in table 7.4. The deduced value of $g_K = 0.97(8)$ compares well with the predicted value of $g_K = 0.987$ for the $\nu 1/2^-[510] \otimes \pi 9/2^-[914]$ configuration [Stu05].

Table 7.4: Measured in-band branching ratios for the 5^+ , 10^- and 15^+ bands in ^{182}Ta , together with inferred gyromagnetic ratios.

K^π	J_i^π	E_γ ($I \rightarrow I - 1$)	E_γ ($I \rightarrow I - 2$)	λ^a	$ g_K - g_R ^b$
		(keV)	(keV)		
5^+	7^+	171.8	318.4	0.16(1)	0.615(28)
10^-	12^-	287.3	553.9	0.82(6)	0.141(11)
	13^-	306.8	594.1	1.4(2)	0.165(19)
	14^-	324.8	631.7	3.6(4)	0.098(18)
				weighted avg:	0.14(1)
15^+	17^+	362.9	708.6	1.02(3)	0.028(10)

^a $\lambda = I_\gamma(I \rightarrow I - 2)/I_\gamma(I \rightarrow I - 1)$.

^b Assuming $Q_0=6.5$ eb.

Figure 7.5(b) shows the deduced alignments for different bands observed in ^{182}Ta in the present work. The aligned angular momentum of the 5^+ band is $\sim 1.2 \hbar$, consistent with contributions from both the $1/2^-[510]$ neutron and the $9/2^-[514]$ proton (c.f. Fig. 7.5(a)). The present calculations predict only one low-lying 5^+ state. It has the expected $\nu 1/2^-[510] \otimes \pi 9/2^-[914]$ configuration and an energy within 45 keV of the experimental value.

$K^\pi = 10^-$ state at 519 keV

The rotational band built on this state is observed for the first time in the present work. Helmer *et al.* [Hel71] and Bizzarri *et al.* [Biz66] proposed a $\nu 11/2^+[615] \otimes \pi 9/2^-[514]$ configuration for this isomer based on its measured an-

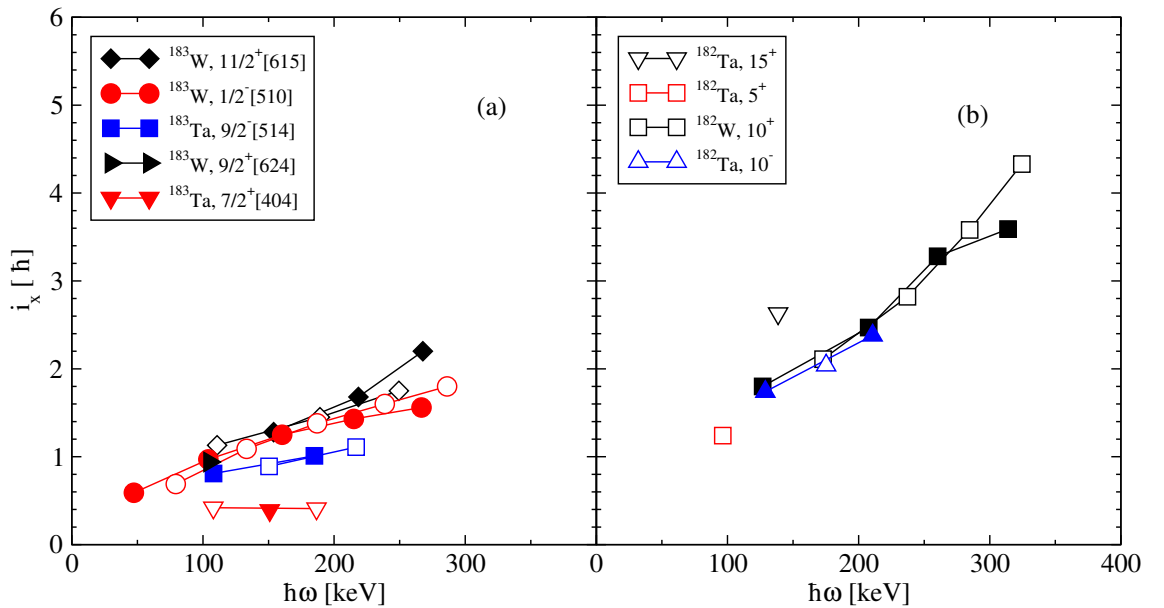


Figure 7.5: Aligned angular momenta for the 5^+ , 10^- and 15^+ bands in ^{182}Ta compared to single-particle rotational bands in the nearby odd-mass nucleus ^{183}W [Sai00] and the 10^+ band in ^{182}W [Shi95].

gular momentum and comparison with the predicted energies for two-quasiparticle states. In the present work, the measured $|g_K - g_R|$ value of 0.14(1) as shown in Table 7.4 corresponds to $g_K=0.49(6)$. This value is in good agreement with the predicted value of $g_K=0.46$ for the $\nu 11/2^+[615] \otimes \pi 9/2^-[514]$ configuration from the Nilsson model. From the calculations, only this configuration is calculated to lie low in energy. Note, however, that the $11/2^+[615]$ neutron energy was adjusted to give this good agreement. Nevertheless, the alignment for this band in Fig. 7.5(b) is seen to increase from 1.8 to 2.4 \hbar and this can be attributed to the intrinsic alignment of the $i_{13/2}$ neutron and $9/2^-[514]$ proton components, providing further evidence that the configuration assignment is correct.

7.4.2 Four and six-quasiparticle states

Amongst the states above 1.9 MeV in ^{182}Ta (see Fig. 5.3), there are almost no signs of rotational band structures except for two states built above the 15^+ state. Hence, configurations proposed for these states are based mostly on the predicted multi-quasiparticle states described in Chapter 6.

Figure 7.6 shows the calculated yrast and near yrast states in ^{182}Ta compared with

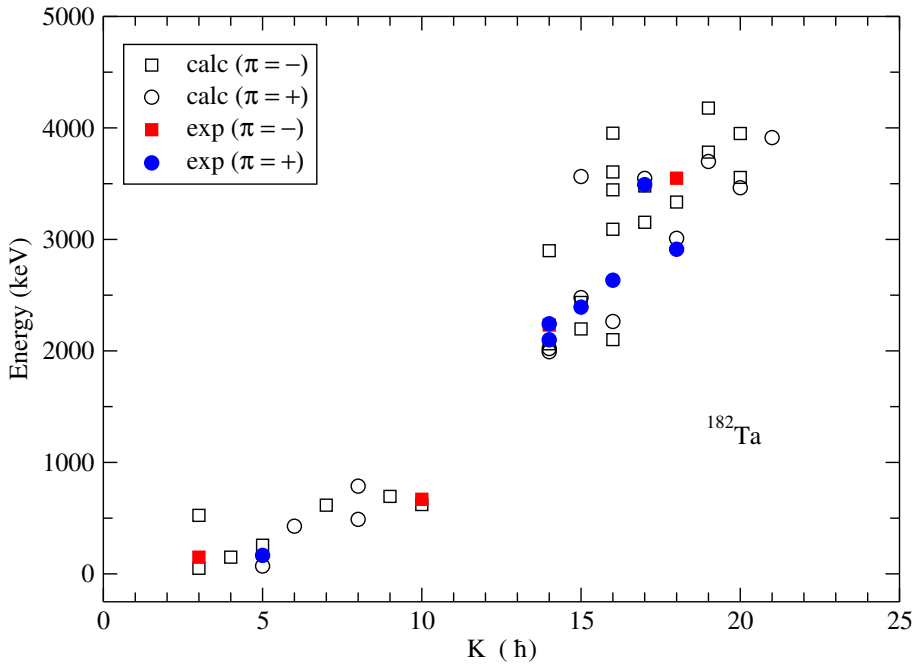


Figure 7.6: Calculated yrast and near-yrast states in ^{182}Ta , compared with experimental energies from the present work. There is good agreement between the predicted values and experimental observations, except for the yrast 15^- and 16^- states discussed in section 8.4.2.

the experimental states observed. The calculations predict a high density of intrinsic states above 1.9 MeV, consistent with the level scheme in Figure 5.3. Also, there are several predicted low-lying states with spin and parities comparable to those suggested from the experiment. Table 7.5 shows a summary of the predicted low-lying states in ^{182}Ta together with their configurations.

$K^\pi = 14^+$ states at 1950 and 2093 keV

From table 7.5, two possible 14^+ configurations are low-lying, these being the $\nu 7/2^-[503] \otimes \pi 9/2^-[514] 7/2^+[404] 5/2^+[402]$ and $\nu 9/2^+[624] 1/2^-[510] 11/2^+[615] \otimes \pi 9/2^-[514]$ states calculated at 1893 and 1921 keV, respectively. With the closeness of the predicted 14^+ alternatives, either candidate is possible for the two 14^+ states observed experimentally, although a $\nu^3\pi$ configuration for the 14^+ , 1950 keV isomer is more likely, as will be discussed below.

Table 7.5: Predicted multi-quasiparticle states in ^{182}Ta compared with experimentally observed states. Section 6.2 describes the details of the calculations and the parameters used.

K^π	Configurations		E_{qp}^m (keV)	E_{res} (keV)	E_{cal} (keV)	E_{exp} (keV)	ΔE
	ν	π					
3 ⁻	1/2 ⁻	7/2 ⁺	0.0	-50	-50	0	-50
	1/2 ⁻	5/2 ⁺	480	-55	425		
4 ⁻	1/2 ⁻	7/2 ⁺	0.0	+50	50		
5 ⁺	1/2 ⁻	9/2 ⁻	42.1	-71.5	-29.5	16	-45
5 ⁻	3/2 ⁻	7/2 ⁺	208	-52	157		
6 ⁺	3/2 ⁻	9/2 ⁻	251	+77	328		
7 ⁻	7/2 ⁻	7/2 ⁺	454	+62	516		
8 ⁺	7/2 ⁻	9/2 ⁻	496	-107	389		
	9/2 ⁺	7/2 ⁺	626	+64	690		
9 ⁺	11/2 ⁺	7/2 ⁺	623	+64	687		
9 ⁻	9/2 ⁺	9/2 ⁻	668	-73	595		
10 ⁻	11/2 ⁺	9/2 ⁻	665	-143	522	519	+3
14 ⁺	7/2 ⁻	9/2 ⁻ , 7/2 ⁺ , 5/2 ⁺	2111	-218	1893	2093	-200
	9/2 ⁺ , 1/2 ⁻ , 11/2 ⁺	9/2 ⁻	2163	-242	1921	1950	-29
14 ⁻	9/2 ⁺ , 1/2 ⁻ , 11/2 ⁺	7/2 ⁺	2121	+679	2800		
	9/2 ⁺ , 3/2 ⁻ , 7/2 ⁻	9/2 ⁻	2220	-256	1964	2082	-118
15 ⁺	9/2 ⁺ , 1/2 ⁻ , 11/2 ⁺	9/2 ⁻	2163	+215	2378	2243	+135
	5/2 ⁻ , 11/2 ⁺ , 7/2 ⁻	7/2 ⁺	2878	+587	3465		
15 ⁻	9/2 ⁺	9/2 ⁻ , 7/2 ⁺ , 5/2 ⁺	2283	-187	2096		
	9/2 ⁺ , 3/2 ⁻ , 11/2 ⁺	7/2 ⁺	2359	-24	2335		
16 ⁺	9/2 ⁺ , 3/2 ⁻ , 11/2 ⁺	9/2 ⁻	2401	-237	2164	2484	-320
	11/2 ⁺	9/2 ⁻ , 7/2 ⁺ , 5/2 ⁺	2281	-280	2001		
16 ⁻	5/2 ⁻ , 11/2 ⁺ , 7/2 ⁻	9/2 ⁻	2920	+72	2992		
	5/2 ⁻ , 9/2 ⁺ , 11/2 ⁺	9/2 ⁻	3177	+271	3448	3341	+107
17 ⁻	9/2 ⁺ , 11/2 ⁺ , 7/2 ⁻	7/2 ⁺	2621	+758	3379		
18 ⁺	9/2 ⁺ , 11/2 ⁺ , 7/2 ⁻	9/2 ⁻	2663	+248	2911	2762/3122	+149/211
18 ⁻	9/2 ⁺ , 1/2 ⁻ , 7/2 ⁻	9/2 ⁻ , 7/2 ⁺ , 5/2 ⁺	3603	-368	3235	3399	-164
19 ⁺	9/2 ⁺ , 11/2 ⁺ , 9/2 ⁻	9/2 ⁻	3874	-275	3599		
19 ⁻	5/2 ⁻ , 1/2 ⁻ , 11/2 ⁺	9/2 ⁻ , 7/2 ⁺ , 5/2 ⁺	4045	+33	4078		
	9/2 ⁺ , 1/2 ⁻ , 7/2 ⁻	9/2 ⁻ , 7/2 ⁺ , 5/2 ⁺	3603	+80	3683		
20 ⁺	9/2 ⁺ , 1/2 ⁻ , 11/2 ⁺	9/2 ⁻ , 7/2 ⁺ , 5/2 ⁺	3779	-415	3364		
	9/2 ⁺ , 3/2 ⁻ , 7/2 ⁻	9/2 ⁻ , 7/2 ⁺ , 5/2 ⁺	3836	-380	3456		
20 ⁻	5/2 ⁺ , 3/2 ⁻ , 11/2 ⁺	9/2 ⁻ , 7/2 ⁺ , 5/2 ⁺	4277	-427	3850		
	9/2 ⁺ , 1/2 ⁻ , 11/2 ⁺	9/2 ⁻ , 7/2 ⁺ , 5/2 ⁺	3779	+34	3813		

Configurations: Neutrons: 1/2⁻: 1/2⁻[510], 3/2⁻: 3/2⁻[512], 5/2⁻: 5/2⁻[512], 7/2⁻: 7/2⁻[503], 11/2⁺: 11/2⁺[615], 9/2⁺: 9/2⁺[624]. Protons: 5/2⁺: 5/2⁺[402]; 7/2⁺: 7/2⁺[404]; 9/2⁻: 9/2⁻[514].

$K^\pi = 15^+$ state at 2243 keV

From Figure 7.5(b), it can be seen that the 15^+ band carries a degree of rotational alignment greater than the alignment of the 10^+ band in ^{182}W [Shi95] that is known to contain both the $9/2^+[624]$ and the $11/2^+[615]$ $i_{13/2}$ neutrons. This implies the presence of these high- j orbitals in the configuration of the 15^+ state, consistent with the predicted low-lying $\nu 9/2^+[624]1/2^-[510]11/2^+[615] \otimes \pi 9/2^-[514]$ configuration that is calculated just 135 keV above the experimental value.

A $|g_K - g_R|$ value of 0.028(10) was deduced from the branching ratio of the 363 and 709 keV transitions. Taking the two possible signs, this gives $g_K = +0.38(6)$ or $g_K = -0.32(6)$, with the former being slightly above the predicted value of $g_K = 0.23$ for the above configuration. Note that the empirical g_K -value of the 10^+ band in ^{182}W [Shi95] was used for the $9/2^+[624]11/2^+[615]$ part of the configuration. This choice, and the approximations used for Q_o and g_R (see section 7.1), could explain the small discrepancy.

State at 2082 keV, $K^\pi = (14^-)$

Although the spin and parity for this state cannot be confirmed, the calculations predicted a low-lying 14^- state at 1964 keV. The proximity of its energy to the observed 2082 keV state suggests a $\nu 9/2^+[624]3/2^-[512]7/2^-[503] \otimes \pi 9/2^-[514]$ configuration. Note that there are other possibilities of low-lying 15^- and 16^- states predicted at 2096 and 2001 keV, respectively, however they are unlikely as will be discussed further in section 8.4.2.

State at 2484 keV, $K^\pi = (16^+)$

The only 16^+ candidate predicted at low energy has the $\nu\{9/2^+[624]3/2^-[512]11/2^+[615]\} \otimes \pi 9/2^-[514]$ configuration and appears at 2164 keV, 320 keV below the $K^\pi = (16^+)$ state at 2484 keV. The other 16^+ state lies even higher at 2588 keV, consistent with this state being a collective band member, as discussed in section 5.2.5.

States at 2951 and 3341 keV with $I^\pi = (17^+)$

The calculations predict only one low-lying 17^+ state at 3448 keV with configuration $\nu\{5/2^-[512]9/2^+[624]11/2^+[615]\} \otimes \pi9/2^-[514]$, while there are two 17^+ states observed at 2951 and 3341 keV. The 17^+ level observed at 2951 keV appears 500 keV below the prediction, consistent with it being part of the 15^+ band as discussed in earlier sections. The other (17^+) state observed at 3341 keV is 107 keV below the predicted state and hence is associated with this configuration.

State at 2762 keV with $I^\pi = (18^+)$

Only one low-lying 18^+ state was predicted and this can be associated with the $K^\pi = (18^+)$ at 2762 keV. This state with a $\nu\{9/2^+[624]11/2^+[615]7/2^-[503]\} \otimes \pi\{9/2^-[514]\}$ configuration is calculated 149 keV above the experimental value.

Isomer at 3399 keV with $K^\pi = (18^-)$

The (18^-) state predicted at 3235 keV with a $\nu\{9/2^+[624]1/2^-[510]7/2^-[503]\} \otimes \pi\{9/2^-[514]7/2^+[404]5/2^+[402]\}$ configuration is energy-favoured, appears 164 keV below the (18^-) isomer, and is the suggested assignment for the 106 ns isomer.

Discussion

In this chapter, the structure of ^{182}Ta and ^{183}Ta is investigated by comparing transition strengths with similar transitions in the mass region. Possible explanations for some of the anomalous transition strengths will be discussed alongside other features such as expected states that are not observed and structural changes across the nearby nuclei.

8.1 Transition strengths in ^{183}Ta

Table 8.1 shows the measured transition strengths and hindrances for decays in ^{183}Ta observed in the present work. For states with no measured lifetimes only limits ($\tau < 5$ ns) were evaluated.

8.1.1 $9/2^-$, 157 ns isomer

The value of $B(E1) = 2.7(1) \times 10^{-6}$ W.u for the 73 keV, $E1$ decay between the $9/2^-$ [514] and $7/2^+$ [404] intrinsic states is consistent with the previous measurement [Fir92]. It also agrees well with equivalent transitions known in ^{179}Ta [Löb65], ^{181}Ta [Hau61, Löb65] and ^{185}Ta [Lan09], as can be seen in table 8.2.

8.1.2 $19/2^+$, 1200 ns isomer

The 465 and 23 keV decay branches from the $K^\pi = 19/2^+$ isomer are both stretched $E1$ transitions that decay to the $17/2^-$ members of the $9/2^-$ [514] and $9/2^-$ [514] $\otimes 2_\gamma^+$ -bands, respectively. Since $E1$ transitions are intrinsically hindered, the reduced hindrance values in italics in Table 8.1 transitions include a 10^4 intrinsic hindrance. The 465 keV transition with $f_\nu = 34$ falls in the range for K -forbidden transitions.

The low-value of $f_\nu = 5$ for the 23 keV transition is likely due to K -mixing that occurs in the $9/2^- \otimes 2\gamma^+$ -band from the γ -vibration, hence the daughter state is not pure $K = 13/2$.

8.1.3 $29/2^-$, 40 ns isomer

The 171 keV decay branch from this isomer is a stretched $E1$ transition to a $27/2^+$ intrinsic state. Its strength of $B(E1) = 1.4(1) \times 10^{-6}$ W.u compares well with those for K -allowed $E1$ transitions in other tantalum isotopes [Löb65, Lan09] and is consistent with that for the 73 keV, $E1$ transition discussed above in section 8.1.1.

8.1.4 $41/2^-$, 70 ns isomer

Similar to 8.1.1 and 8.1.3 above, the value of $B(E1) = 1.1(1) \times 10^{-6}$ W.u for the 153 keV, $E1$ decay is consistent with other $B(E1)$ values for K -allowed decays in the region.

8.1.5 Transitions from states with lifetime limits of $\tau < 5$ ns

Most decays from the non-isomeric states between the $19/2^+$ and $41/2^-$ isomers are K -allowed transitions between intrinsic states, except perhaps the 291 keV transition that might be due to the possible first rotational excitation above the $23/2^+$ bandhead, and, if it is, the 426 keV transition may have forbiddenness, $\nu = 1$.

The deduced limits on the strengths of all these decays are summarised in Table 8.1 for each multipolarity proposed. Essentially, all values are plausible except for the $E1$ transitions at 110 and 145 keV that both show relatively larger strengths, $> 10^{-5}$ W.u, an order of magnitude higher than the $E1$ strengths observed for the 73, 153 and 171 keV transitions. This is discussed further below.

Table 8.1: Transition strengths observed in ^{183}Ta . For cases where no lifetime has been given, an assumed limit of $\tau < 5$ ns has been used to evaluate transition strengths.

K_i^π	E_γ (keV)	I_L	I_γ^*	α_T	$B(XL)$ (W.u)	F_W	ν	f_ν
73 keV; $\tau = 157(4)$ ns								
$9/2^-$	73.2	$E1$	100	0.8141	$2.7(1) \times 10^{-6}$	$3.7(1) \times 10^5$	0	
1332 keV; $\tau = 1200(140)$ ns								
$19/2^+$	22.7^b	$E1$	$27.01(178)^b$	3.95	3.5×10^{-6}	$2.44(37) \times 10^5$	2	$494(37); 5.0(4)^a$
		$E1$	$4.14(83)$	7.99×10^{-3}	$7.3(18) \times 10^{-11}$	$1.4(3) \times 10^{10}$	4	$342(21); 34(2)^a$
465.4		$M2$	< 0.93	1.98	$< 1.4 \times 10^{-2}$	> 71	1	> 71
230^b		$M2$	< 1.56	5.92×10^{-2}	$< 8.4 \times 10^{-5}$	$> 1.2 \times 10^4$	3	> 22
703^b								
$21/2^-$	144.6	$E1$	36.7	0.1404	$> 1.8 \times 10^{-5}$	$< 5.6 \times 10^4$	0	
23/2⁺								
110.3	$E1$	$49.1(42)$	0.2843	$> 2.5 \times 10^{-5}$	$< 4.0 \times 10^4$	0		
254.9	$E2$	$15.1(15)$	0.1353	$> 4.0 \times 10^{-1}$	< 2.5	0		
25/2⁺								
663.2	$M1$	7.1	2.519×10^{-2}	$> 2.1 \times 10^{-5}$	$< 4.8 \times 10^4$	0		
27/2⁺								
53.9^b	$M1$	$1.3(0.3)^b$	4.467	$> 1.1 \times 10^{-3}$	$< 9.1 \times 10^2$	0		
425.7	$M1$	$23.1(21)$	7.937×10^{-2}	$> 4.3 \times 10^{-5}$	$< 2.3 \times 10^4$	1		
717.1	$E2$	$6.5(21)$	8.642×10^{-3}	$> 1.5 \times 10^{-3}$	$< 6.7 \times 10^2$	0		
2475 keV; $\tau = 41(4)$ ns								
$29/2^-$	171.1	$E1$	36.4	9.076×10^{-2}	$1.4(1) \times 10^{-6}$	$7.1(5) \times 10^5$	0	

(*): relative γ -ray intensities.

(a): Values in italics are reduced hindrances with a 10^4 normalisation factor included for hindered $E1$ transitions.

(b): Energies and intensities of unobserved transitions, either transitions implied from coincidence relationships with real intensities or limits based on non-observation of γ rays.

Table 8.1 continued

K_i^π	E_γ	X_L	I_γ	α_T	$B(XL)$ (W.u)	F_W	ν	f_ν
$31/2^+$								
	477.7	$E1$	$10.6(16)$	7.545×10^{-3}	$> 2.0 \times 10^{-7}$	$< 5.0 \times 10^6$	0	
	648.8	$E2$	$13.6(20)$	1.082×10^{-2}	$> 1.1 \times 10^{-2}$	$< 9.1 \times 10^1$	0	
$33/2^-$								
	593.5	$E2$	2.6	1.329×10^{-2}	$> 3.5 \times 10^{-2}$	$< 2.8 \times 10^1$	0	
$33/2^+$								
	185.5	$M1$	5.7	7.559×10^{-1}	$> 5.7 \times 10^{-4}$	$< 1.8 \times 10^3$	0	
$35/2^+$								
	63.6 ^b	$M1$	$2.7(5)^b$	2.751	$> 1.3 \times 10^{-3}$	$< 7.7 \times 10^3$	0	
	133.1	$E1$	$12.5(17)$	1.743×10^{-1}	$> 6.3 \times 10^{-6}$	$< 1.6 \times 10^5$	0	
	249.1	$E2$	$15.8(16)$	1.455×10^{-1}	$> 9.0 \times 10^{-1}$	$< 1.1 \times 10^{-1}$	0	
$37/2^+$								
	274.9	$M1$	20.9	2.557×10^{-1}	$> 2.4 \times 10^{-4}$	$< 4.2 \times 10^3$	0	
$39/2^+$								
	240.0	$M1$	18.5	3.705×10^{-1}	$> 3.4 \times 10^{-4}$	$< 2.9 \times 10^3$	0	
3870 keV; $\tau = 70(5)$ ns								
$41/2^-$	153.0	$E1$	25.7	1.213×10^{-1}	$1.1(1) \times 10^{-6}$	$9.1(8) \times 10^5$	0	

(b): Energies and intensities of unobserved transitions, either transitions implied from coincidence relationships with real intensities or limits based on non-observation of γ rays.

Table 8.2: Known transition strengths for $9/2^- \rightarrow 7/2^+$, $E1$ decays in $^{179,181,183,185}\text{Ta}$. The table is adapted from Lane *et al.* [Lan09] to also include the present results.

Nucleus	τ	E_γ (keV)	I_γ	$\sigma\lambda$	α_T	$B(\sigma\lambda)$ (W.u.)	ν	f_ν
$^{185}\text{Ta};$	17(3) ns	175.5	100(7)	$E1$	0.085	$2.8(6) \times 10^{-6}$	0	—
		(22.6)	1.52(12)	$E1$	4.00	$2.0(4) \times 10^{-5}$	0	—
$^{183}\text{Ta} ;$	154(16) ns	73.2	100	$E1$	0.815	$2.76(28) \times 10^{-6}$	0	—
$^{181}\text{Ta} ;$	8.73(17) μs	6.24	100	$E1$	30.1	$4.63(9) \times 10^{-6}$	0	—
$^{179}\text{Ta} ;$	2.05(12) μs	30.7	100	$E1$	1.731	$1.90(11) \times 10^{-6}$	0	—

8.2 Transition strengths in ^{182}Ta

Table 8.3 shows the transition strengths and reduced hindrances evaluated for the decays in ^{182}Ta .

8.2.1 10^- , 1380 s isomer

Only the 185 keV, $E3$ transition from the $K^\pi = 10^-$ isomer was observed in the present work, while for the unobserved 356 keV, $M4$ transition, an upper intensity limit was deduced. The observed branching ratio limit of $\lambda < 0.04$ (from $I_\gamma(\Delta I = 4; 356)/I_\gamma(\Delta I = 3; 185)$), is consistent with the previous measurement of 0.01 from Refs. [Biz66, Hel71]. Using the present intensities and prior lifetime, these two transitions have reduced hindrances of 225(26) and > 1 (see Table 8.3), both of which are consistent with the $f_\nu \sim 30 - 300$ range expected for axially symmetric nuclei with a well defined K -quantum number.

8.2.2 14^+ , 356 ns isomer

The two $E1$ decay transitions of 245 and 570 keV out of this state have reduced hindrances of 29(1) and 33(2), respectively, after allowing for a factor of 10^4 intrinsic hindrance, consistent with K -conservation, albeit at the low end of the range.

8.2.3 (18^-) , 106 ns isomer

From angular correlation measurements discussed in section 5.2.5, the 448 keV transition was identified as a mixed dipole, implying either an $M1/E2$ or $E1/M2$ multipolarity. A tentative (18^-) assignment was suggested in section 5.2.5 for the 106 ns isomer, assuming the 448 keV transition was likely to have mixed $E1/M2$ character. In this section, both of the $M1/E2$ and $E1/M2$ possibilities, with implied (18^+) or (18^-) assignments, will be investigated.

Evaluated strengths for the three depopulating transitions of 59, 448 and 638 keV are shown in Table 8.3. Note that the dipole and the quadrupole components of

the 448 keV branch are extracted and evaluated separately, in both cases.

For the 448 keV, $M1/E2$ transition, very large reduced hindrances are observed for the $M1$ and $E2$ components. Similar results are obtained for the limit on the reduced hindrance of the potential 811 keV crossover transition to the 2588 level deduced from the intensity limit on this unobserved transition. These unphysical values rule out the 18^+ assignment.

For the (18^-) assignment, the $E1$ and $M2$ components of the 448 keV transition have reasonable reduced hindrances that are within the usual range for K -forbiddenness. Similarly, the limit on the potential 811 keV, $M2$ transition is plausible. The competing K -allowed, $E1$ transition at 58 keV has $B(E1)=1.4(2)\times 10^{-6}$ W.u, a value consistent with normal $B(E1)$ values already observed in the neighbouring tantalum isotopes and in ^{183}Ta in the present work (see section 8.1). In contrast, the strength of the K -allowed 638 keV transition is much lower, at only 1.6×10^{-9} W.u. This will be discussed in detail below.

8.2.4 Transitions from states with lifetime limits $\tau < 5$ ns

A similar analysis to that performed for ^{183}Ta in section 8.1.5 is given in Table 8.3. For the K -allowed transitions from states with no observed lifetime, the limits on the strengths all have plausible values.

Table 8.3: Transition strengths observed in ^{182}Ta . For cases where no lifetime has been given, an assumed limit of $\tau < 5$ ns has been used to evaluate transition strengths.

I^π	E_γ (keV)	XL	I_γ	α_T	$B(XL)$ (W.u)	F_W	ν	f_ν
519 keV; $\tau = 1380(300)$ s								
10^-	184.9	$E3$	$68.2(35)$	3.200	$2.0(5) \times 10^{-5}$	$5.0(2) \times 10^4$	2	225(26)
	356.4^b	$M4$	< 2.36	4.768	$< 7.0 \times 10^{-1}$	> 1.4	1	> 1.4
1950 keV; $\tau = 356(16)$ ns								
14^+	570.2	$E1$	$98.0(47)$	5.158×10^{-3}	$4.2(3) \times 10^{-9}$	$2.4(2) \times 10^8$	3	$621(17); 29(1)^a$
	245.3	$E1$	$5.2(10)$	3.628×10^{-2}	$2.8(6) \times 10^{-9}$	$3.6(8) \times 10^8$	3	$710(50); 33(2)^a$
	877^b	$M2$	$< 3.9^b$	3.188×10^{-2}	$< 2.9 \times 10^{-4}$	$> 3.5 \times 10^3$	2	> 59
14^+	143.2	$M1$	19.9	1.565	$> 8.4 \times 10^{-4}$	$< 1.2 \times 10^3$	0	
2243 keV; $\tau = 1.7(5)$ ns								
15^+	293.1	$M1$	94.1	2.149×10^{-1}	$6.1(18) \times 10^{-4}$	$1.64(48) \times 10^3$	0	
16^+	391.0	$E2$	28.4	3.838×10^{-2}	$> 2.8 \times 10^{-1}$	< 3.6	0	
17^+	1097.7	$E2$	1.5	3.564×10^{-3}	$> 1.7 \times 10^{-3}$	$< 5.9 \times 10^2$	0	
18^+	277.8	$E2$	30.4	1.036×10^{-1}	> 1.5	< 0.67	0	

(a): Italic values indicate reduced hindrances with a 10^4 normalisation factor included for hindered $E1$ transitions.

(b): Intensity limit for the known 356 keV transitions that was not observed in the current work.

Table 8.3 continued

I^π	E_γ (keV)	XL	I_γ	α_T	$B(XL)$ (W.u)	F_W	ν	f_ν
3399 keV; $\tau = 106(4)$ ns^c								
18 ⁺	58.7	<i>M1</i>	0.33(04)	3.478	$4.3(6) \times 10^{-5}$	$2.3(3) \times 10^4$	0	
	447.6	<i>M1</i>	6.32(39)	6.957×10^{-2}	$1.8(2) \times 10^{-6}$	$5.6(6) \times 10^5$	2	737(35)
	447.6	<i>E2</i>	0.82(46)	2.674×10^{-2}	$5.0(28) \times 10^{-4}$	$2.0(11) \times 10^3$	1	$2.0(11) \times 10^3$
	637.5	<i>M1</i>	1.63(15)	2.786×10^{-2}	$1.6(2) \times 10^{-7}$	6.3×10^6	0	
	811 ^b	<i>E2</i>	< 0.71	6.620×10^{-3}	< 2.4×10^{-5}	$> 4.2 \times 10^4$	1	$> 4.2 \times 10^4$
3399 keV; $\tau = 106(4)$ ns^c								
18 ⁻	58.7	<i>E1</i>	1.15(14)	2.899×10^{-1}	$1.4(2) \times 10^{-6}$	$7.1(10) \times 10^5$	0	
	447.6	<i>E1</i>	6.32(39)	8.713×10^{-3}	$1.8(2) \times 10^{-8}$	$5.6(6) \times 10^7$	2	$7.5(4) \times 10^3$; 75(4) ^a
	447.6	<i>M2</i>	0.82(46)	2.259×10^{-1}	$5.3(30) \times 10^{-2}$	$1.9(11) \times 10^1$	1	19(11)
	637.5	<i>E1</i>	1.63(15)	4.093×10^{-3}	$1.6(2) \times 10^{-9}$	$6.3(8) \times 10^8$	0	
	811 ^b	<i>M2</i>	< 0.97	3.958×10^{-2}	< 3.4×10^{-3}	$> 2.94 \times 10^2$	1	> 294

(a): Italic values indicate reduced hindrances with a 10^4 normalisation factor included for hindered $E1$ transitions.

(b): Implied energy and intensity limit for the unobserved 811 keV transition.

(c): Both 18⁻ and 18⁺ assignments are evaluated for the 3399 keV isomer (see text).

8.3 Comments on transition strengths

This section highlights and suggests possible explanations for some of the inconsistencies observed regarding some of the $B(E1)$ values observed in ^{182}Ta and ^{183}Ta . The fact that 468 and 496 keV inter-band transitions compete with in-band collective decays in ^{182}Ta will also be discussed.

8.3.1 Enhanced $E1$ strengths for the 110 and 145 keV transitions in ^{183}Ta

Considering the strengths observed for K -allowed, $E1$ decays in the mass-180 region (see e.g. Table 8.2) and including those from the $9/2^-$, $29/2^-$ and the $41/2^-$ states in ^{183}Ta , one would have anticipated measurable lifetimes for both the 1477 and 1587 keV levels. Instead, the < 5 ns lifetime limits imply that the 110 and 145 keV, $E1$ transitions have $B(E1) > 10^{-5}$ W.u. Best evidence suggests they are $E1$, but there must be some doubt, especially given that a low-lying $21/2^+$ state is predicted at 1446 keV that could be the origin of the 1477 keV, $21/2^-$ state. A change in parity of this state would make both transitions $M1$ and no lifetime would be expected. At present these anomalies cannot be explained and this will be worth investigating in the future.

8.3.2 $B(E1) \sim 10^{-9}$ W.u for the 638 keV transition in ^{182}Ta

The large hindrance for the 638 keV transition can possibly be explained in terms of the large configuration change that takes place between the 3399 keV isomer and the 2767 keV state. The proposed configurations for these two states are $\nu\{9/2^+[624]1/2^-[510]7/2^-[503]\} \otimes \pi\{9/2^-[514]7/2^+[404]5/2^+[402]\}$ and $\nu\{9/2^+[624]11/2^+[615]7/2^-[503]\} \otimes \pi\{9/2^-[514]\}$, respectively (see Table 7.5), so that the decay between them would require a change from three protons to one proton as well as a change of one of the neutron orbitals from $1/2^-[510]$ to $11/2^+[615]$. This large change could possibly suppress the strength of the 638 keV transition.

8.3.3 468 and 496 keV transitions competing with in-band decays in ^{182}Ta

Transitions between related collective states in a rotational band are enhanced and would usually be expected to dominate over competing interband transitions to unrelated intrinsic states. For the proposed (15^+) band in ^{182}Ta , one would naively expect the 363, 346 keV and 709 keV in-band transitions to take all the intensity from the 2588 and 2951 keV states. However, 468 and 496 keV transitions compete with the in-band decays and feed what are assigned as intrinsic states at 2484 and 2093 keV, respectively.

The enhancement of these transitions might be explained in terms of a K -mixing between the $K^\pi = (16^+)$, 2484 keV intrinsic state and the collective 16^+ state at 2588 keV. The enhancement of the 468 keV could be due to an admixture of the wavefunction for the 16^+ collective state into the nearby 16^+ , 2484 keV wavefunction so that the 468 keV transition has an in-band component. Similarly, the 496 keV transition may result from an admixture of the $K^\pi = (16^+)$ intrinsic state wavefunction into the collective (16^+) wavefunction. Thus the 496 keV transition may compete as it has an intrinsic state to intrinsic state component.

8.4 Comments on overall state configurations and changes between them.

This section highlights some of the key features of the predicted states and the assigned configurations in ^{182}Ta and ^{183}Ta .

8.4.1 Commonality of base configurations in ^{183}Ta

For most states from $19/2^+$ up to the $29/2^-$ isomer, (except the $21/2^-$), there is a common $\nu^2\pi$ base configuration involving the lowest lying two-neutron states known in the neighbouring ^{184}W nucleus, for example the 10^+ , 7^- and 5^- coupled to the $9/2^-$ [514] proton. This is not unexpected, and in some ways reflects initial

assumptions made in the multi-quasiparticle calculation when adjusting the Nilsson single-particle energies to reproduce the experimental energy values of the low-lying two neutron states in the ^{184}W core (see section 6.2).

Above the $29/2^-$ isomer, the majority of the suggested five-quasiparticle configurations are from the similar low-lying two-neutron states, but now coupled to a $21/2^-$ state from the three-proton coupling. Note that this $\pi^3, 21/2^-$ building block is known in the odd-mass isotopes of ^{181}Ta [Whe99a] and ^{179}Ta [Kon97].

The 10^+ , two-neutron component common to the $29/2^-$ and $41/2^-$ isomers results from the coupling of the $i_{13/2}$ -neutron orbitals, $9/2^+[624]$ and $11/2^+[615]$. This 10^+ state is also an isomer in ^{182}W [Shi95] and would be in ^{184}W were it not for an accidental degeneracy with the 10^+ member of the γ -band [Lan15]. This 10^+ state is also known to be a part of the $29/2^-$ isomers in ^{181}Ta and ^{183}Re [Whe99a, Pur00, Has98]. The present calculations suggest that the, as yet unobserved, $41/2^-$ state in ^{181}Ta will have the same 10^+ and $21/2^-$, neutron and proton components.

The above observations are reasonable since the 10^+ state is among the known yrast two-neutron states in the neighbouring even-even tungsten isotopes (see Table A.3) and generates the highest value of K that is possible from combining two low-lying neutron states. Furthermore, at high excitation energy and spin, it makes sense that all of the three low-lying proton states may start to take part in the many-particle configuration.

8.4.2 Missing 15^- and 16^- states in ^{182}Ta

The evidence for the agreement between the predicted states and the observed state in ^{183}Ta has already been discussed in Chapters 6 and 7. Most of the yrast states predicted in the calculations have already been assigned to the observed states. However, the calculated yrast states at 15^- and 16^- (see Figure 7.6) are low-lying and one would expect to observe them, but they are not seen. A number

of possibilities are explored below to try and understand this.

Although the spin and parity of the 2082 keV state cannot be confirmed, its lifetime appears to be $\tau < 300$ ns as described in section 5.2.4. Note that in the chopped-beam data no transitions are observed that could correspond to the depopulation of this state or any longer lived state; only states fed by the 10^- isomer are observed at greater than few micro seconds out-of-beam. The $\tau < 300$ ns limit would appear to rule out $M2$ character for the 132 keV transition and a 16^- assignment for the 2082 keV level. The tentative $K^\pi = (14^-)$ assignment for this level is then based on the three possible predicted states, further implying that both the 15^- and the 16^- are possibly just above the 2082 keV state. If this is true, they would be expected to feed the $14^-, 2082$ keV state via low energy transitions.

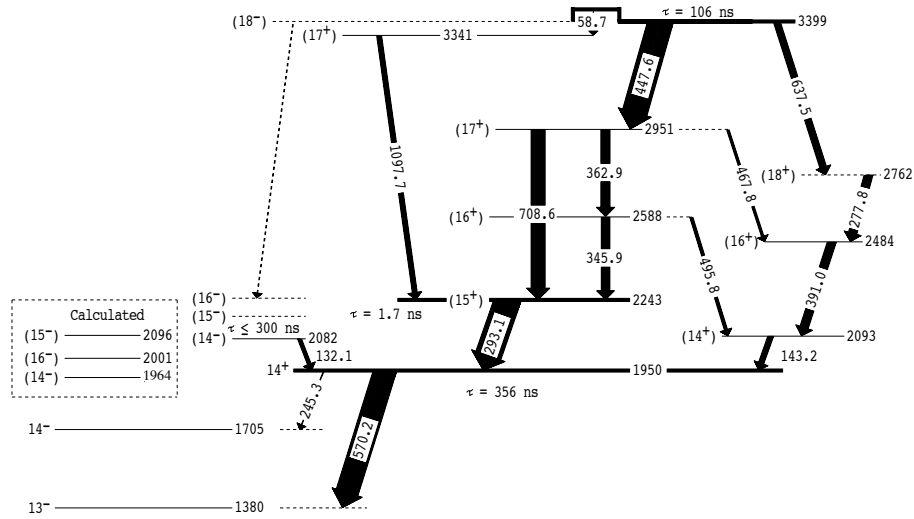


Figure 8.1: Partial level scheme of ^{182}Ta above the 356 ns isomer as deduced in the present work. The two predicted yrast states of 15^- and 16^- are unobserved in the present work. The reasons they might have been missed are described in the text.

With this arrangement, there is a potential high energy $E2$ transition from the 3399 keV, $K^\pi = (18^-)$ isomer, to the predicted $K^\pi = 16^-$ state as shown in figure 8.1. If the present configuration assignments are correct, this K -allowed transition would involve a change from the $\nu\{9/2^+[624]1/2^+[510]7/2^-[503]\} \otimes \pi9/2^-[514]7/2^+[404]5/2^+[402]$ configuration to $\nu\{11/2^+[615]\} \otimes \pi9/2^-[514]7/2^+[404]5/2^+[402]$. While the same protons are in-

volved, the three neutrons $9/2^+[624]$, $1/2^+[510]$ and $7/2^-[503]$ change to a fourth (different) neutron $11/2^+[615]$. So there might be a very small wavefunction overlap. This large configuration change could potentially suppress the K -allowed $E2$ transition, so there is only a weak branch from the 18^- state. One would still expect strong feeding of the 16^- state, as it is yrast, but this feeding would be prompt (in-beam) and hard to see. Note that the present experiment was mainly focused on the study of isomers, with only limited prompt spectroscopic information.

8.4.3 Missing $21/2^+$ state in ^{183}Ta

For ^{183}Ta there is also a missing $21/2^+$ state expected to lie near the observed $21/2^-$. A possible explanation is that this state could be fed in-beam and would be hard to observe since the present experiment was optimised to study isomers, however, there is no evidence to support this. There is also a possibility that the 1477 keV state assigned as $21/2^-$ could in fact be $21/2^+$. However, then, the absence of the $21/2^-$ state would remain unexplained.

8.4.4 Structural changes and systematics

Figure 8.2 shows the partial level scheme for ^{176}Ta and ^{177}Ta from Dasgupta *et. al.* [Das94]. Despite the occurrence of isomers, there are still well developed rotational sequences, even at high-spin. This is “normal” behaviour in this region.

A similar sudden increase in the level density of intrinsic states (but with no rotational structures exposed) at higher excitation energies is also visible in the high-spin part of the level scheme for the isotope ^{184}W , just above the $K^\pi = 10^+$ state at 2480 keV [Whe04, Lan12, Lan15].

Figure 8.3 shows the predicted intrinsic state energies in ^{184}W from multi-quasiparticle calculations performed by Lane *et al.* [Lan08]. The experimental ground state and γ -bands are shown for comparison. Above $I = 14$, the theoretical yrast line consists of a sequence of intrinsic states mostly separated by $\Delta I = 1$.

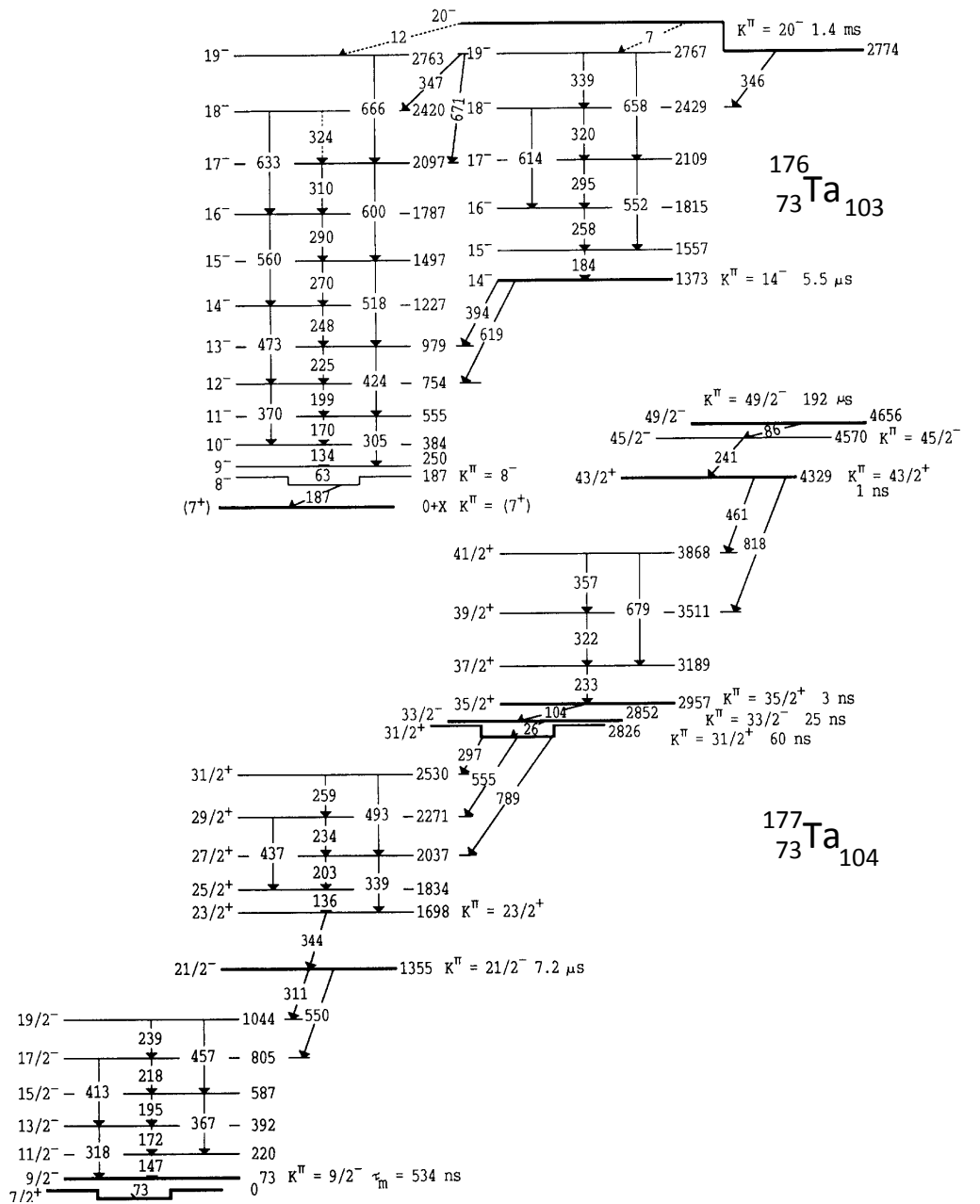


Figure 8.2: Known level scheme for $^{176,177}\text{Ta}$ showing many intrinsic states with some favoured such that they expose rotational structures in their decay. This is in contrast with results for ^{184}W , ^{182}Ta and ^{183}Ta where more intrinsic states are yrast but with K -allowed decays being favoured. Figure taken from Ref. [Das94].

This is in agreement with the experimental level scheme [Whe04, Lan15] and lies in stark contrast to ^{176}Ta and ^{177}Ta .

Figure 8.4 shows a similar comparison for ^{183}Ta . Solid lines illustrate the collective $7/2^+$, $9/2^- \otimes \gamma$ and $9/2^-$ bands known experimentally. The dotted line shows

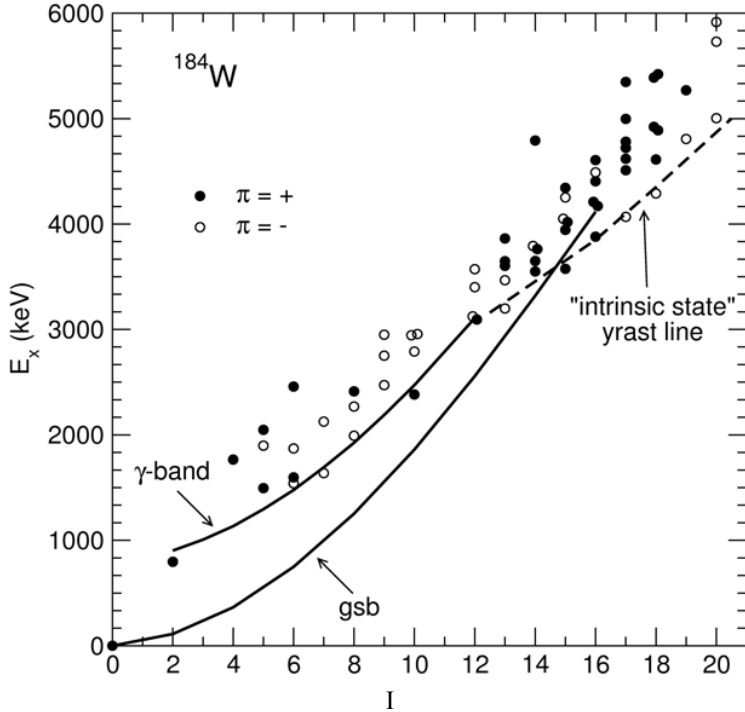


Figure 8.3: Intrinsic state energies for ^{184}W from multi-quasiparticle calculations performed by Lane *et al.* [Lan08], compared to the solid lines that illustrate the collective bands known experimentally. Above $I = 14$, an yrast sequence of intrinsic states separated by $\Delta I = 1$ is predicted as indicated by the dotted line. Figure taken from Ref. [Lan08].

the intrinsic state yrast line that would form at high spins, similar to ^{184}W . Both calculations show a similar pattern and both are consistent with experimental observations. The new level scheme for ^{183}Ta deduced in the present work and presented in Fig 4.2 shows both intrinsic and collective structures up the $19/2^+$, 1332 keV isomer. Above this level, only a sequence of intrinsic states is observed up to the highest state at $41/2^-$. A somewhat similar behaviour is also observed in ^{182}Ta , as illustrated in Figs. 5.3 and 6.6.

From the above experimental observations in ^{176}Ta , ^{177}Ta , ^{184}W , ^{182}Ta and ^{183}Ta , together with the results from the present multi-quasiparticle calculations in Fig. 6.6 and 6.9, it is evident that as we approach the more neutron-rich side along the tantalum isotopic chain, high-energy intrinsic states come down in energy and become yrast, changing the nature of the high-spin level schemes. Hence, there is a more uniform distribution of energy states with no especially favoured states that expose rotational band structure.

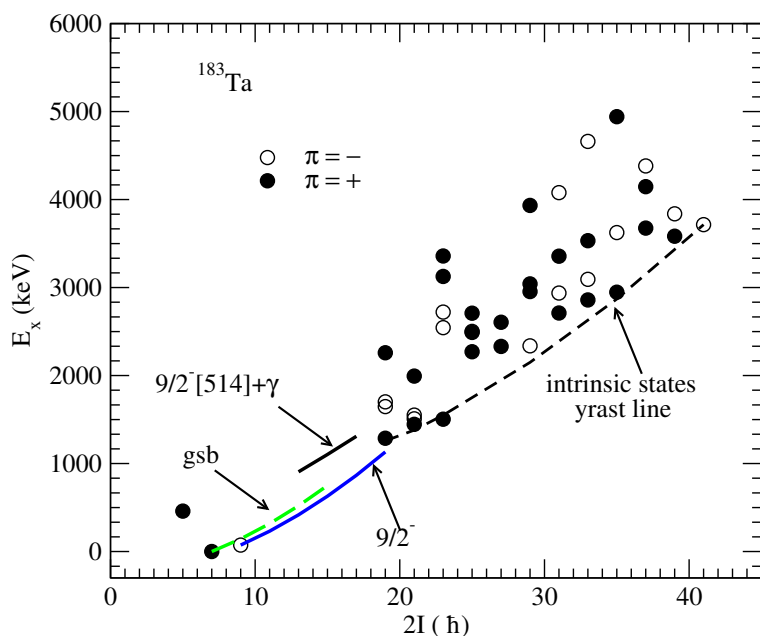


Figure 8.4: Intrinsic state energies for ^{183}Ta from multi-quasiparticle calculations performed in the present work, compared to the solid lines that illustrate the collective bands known experimentally. Above $I = 19/2$, an yrast sequence of intrinsic states is predicted as indicated by the dotted line.

Conclusions

This chapter summarises the new findings in the present work, followed by discussion of future plans.

9.1 New findings

The present combination of deep inelastic reactions and time correlated γ -ray coincidence techniques, has allowed the establishment of new level schemes for neutron-rich ^{182}Ta and ^{183}Ta , beyond the line of stability. Spins and parities were established from angular correlations, internal conversion coefficients deduced from intensity balances, and consideration of transition strengths. The structure and configuration assignments have been established from the measured magnetic properties and alignments of the observed rotational bands, as well as comparison with multi-quasiparticle calculations.

Self-consistent calculations using adjusted Nilsson energies and Lipkin-Nogami pairing were carried out to predict the possible configurations for multi-quasiparticle states in neutron-rich tantalums nuclei from ^{181}Ta to ^{185}Ta . The predicted energies showed a good agreement with observed states, typically within 300 keV.

Structures associated with the decay of two new isomeric states have been identified above the previously known 1300 ns isomer in ^{183}Ta [Shi09]. The 1300 ns isomer was remeasured to be $\tau=1200(140)$ ns and the state has been assigned $K^\pi = 19/2^+$. The decay of two new higher-lying isomers with $K^\pi = 29/2^-$ and $41/2^-$ has been fully characterised, allowing identification of ten new intrinsic states, however no

well-developed rotational structures have been observed.

Configurations for levels above the $19/2^+$ state up to the $41/2^-$ state have been established from the measured spins and parities and comparison with predicted multi-quasiparticle states and configurations. A $\nu\{1/2^-[510]11/2^+[615]\} \otimes \pi9/2^-[514]$ configuration was proposed for the $19/2^+$ isomer, while $\nu\{9/2^-[624]11/2^+[615]\} \otimes \pi9/2^-[514]$ and $\nu\{9/2^+[624]11/2^+[615]\} \otimes \pi\{9/2^-[514]7/2^+[404]5/2^+[402]\}$ configurations were established for the $K^\pi = 29/2^-$ and $41/2^-$ isomers, respectively.

In the case of ^{182}Ta , three new isomeric states have been identified to feed towards the known [Hel71] $K^\pi = 10^-$ isomer. A rotational band built on the 10^- isomer has now been observed and is fed by a new 14^+ , 356 ns isomer at 1950 keV with several intrinsic states above this isomer also identified. Firm spins and parities have been established up to the 14^+ isomeric state, however, above this level, no firm spin and parity assignments were made. Two alternative configurations for the 14^+ state are predicted to lie close in energy to the observed state at 1950 keV, while configuration assignments above this level remain tentative.

9.2 Physics summary

Most of the transition strengths measured in ^{182}Ta and ^{183}Ta are in good agreement with expectations in the region, except for a few cases of $E1$ decays, in particular two enhanced $E1$ decays in ^{183}Ta . Both the calculations and experimental results suggest a high density of intrinsic states occurs along the yrast line at high excitation energy in both nuclei. This pattern seems to emerge in the more neutron-rich tantalum isotopes resulting in a more complex level scheme that is difficult to interpret. There are a few cases where the predicted yrast states are not observed experimentally in both ^{182}Ta and ^{183}Ta .

9.3 Future work

Some of the key questions and challenges that have arisen from the current results are listed below.

- So far, it has not been possible to identify ^{184}Ta in the current data, despite observation of both of its neighbours.
- A number of higher-lying states still have unconfirmed spin and parities, and have only tentative configuration assignments, mostly due to limited spectroscopic information.
- A number of favoured yrast states are predicted at high excitation energies that are beyond the reach of the current experiment.
- Some of the measured transition strengths are anomalous.
- There are cases where low-lying states are predicted, but are unobserved in the data.

The above observations clearly suggest that there is considerable scope for future experiments and studies to improve the results.

Developments regarding future experiments are already in place. Previous experiments by our research group including the current work, focused mainly on the study of isomers, limiting the possibilities for prompt spectroscopy. A new experiment is approved to run with GAMMASPHERE at the Argonne National Laboratory and is tentatively scheduled to take place in the first half of 2016. One of the main objectives is to improve the quality of the prompt data. This will be addressed using unchopped beams and the digital data acquisition for GAMMASPHERE to minimise the in-beam random rate, handle higher data rates, and hence optimise the in-beam statistics.

It is planned to use deep inelastic reactions with ^{181}Ta as a target as part of the upcoming experiment. With $^{182,183,184}\text{Ta}$ being just a few neutrons away from the

^{181}Ta target, the production cross-sections are expected to be higher for $^{181,182,183}\text{Ta}$ compared to the present results, although it is not clear whether the yield of ^{184}Ta will improve compared to the ^{186}W target. Nevertheless, it is hoped that some of the present problems may be resolved with the new data.

As a final note, the results of the present calculations predict favoured states at high excitation energies that are beyond the present experimental reach. These predictions remain to be tested by future experiments.

Appendices

Appendix A

A.1 Properties of all γ rays in ^{183}Ta and ^{182}Ta .

Tables A.1 and A.2 in this appendix summarise the properties of all the transitions in ^{182}Ta and ^{183}Ta observed in the present work. These include the γ -ray energies, relative intensities, initial and final level energies and spins/parities, together with the proposed multipolarities. The intensities are measured out-of-beam and normalised relatives to the 73 and 448 keV γ -rays intensities in ^{183}Ta and ^{182}Ta , respectively.

A.2 Single and two-quasiparticle states in tungsten isotopes.

The low-lying, two neutron states known in even-even tungsten isotopes [Shi95, Whe04, Whe98, Whe99a, Lan12, Lan15] between $A=182$ and $A=186$ are given in Table A.3. These states are likely to contribute to the multi-quasiparticle states in ^{181}Ta , ^{183}Ta and ^{185}Ta . Single-neutron states known in odd-tungsten isotopes that are likely to contribute to the multi-quasiparticle states in odd-odd tantalum isotopes between $A = 180$ and $A = 186$ [Lin73, Sai00, Bon05, Shi08] are summarised in Table A.4.

Table A.1: Properties of transitions in ^{183}Ta . The intensities are measured out-of-beam relative to the 73.3 keV γ ray.

E_γ (keV)	I_γ	E_i (keV)	E_i (keV)	K_i^π	J_i^π	K_f^π	J_f^π	Multipolarity
22.7(2) ^a	27.0(18) ^b	1332	1309	$\frac{19}{2}^+$	$\frac{19}{2}^+$	$\frac{13}{2}^-$	$\frac{17}{2}^-$	$E1$
53.9(2) ^a	1.3(3) ^b	2304	2250	$\frac{27}{2}^+$	$\frac{27}{2}^+$	$(\frac{25}{2}^+)(\frac{25}{2}^+)$		$(M1)$
63.6(2) ^a	2.7(5) ^b	3202	3139	$\frac{35}{2}^+$	$\frac{35}{2}^+$	$(\frac{33}{2}^+)(\frac{33}{2}^+)$		$(M1)$
73.3(1)	100.0(8)	73	0	$\frac{9}{2}^-$	$\frac{9}{2}^-$	$\frac{7}{2}^+$	$\frac{7}{2}^+$	$E1$
110.3(2)	49.1(42)	1587	1477	$\frac{23}{2}^+$	$\frac{23}{2}^+$	$\frac{21}{2}^-$	$\frac{21}{2}^-$	$E1$
133.1(1)	12.4(17)	3202	3069	$\frac{35}{2}^+$	$\frac{35}{2}^+$	$\frac{33}{2}^-$	$\frac{33}{2}^-$	$E1$
144.6(2)	36.7(30)	1477	1332	$\frac{21}{2}^-$	$\frac{21}{2}^-$	$\frac{19}{2}^+$	$\frac{19}{2}^+$	$E1$
153.0(2)	25.7(23)	3870	3717	$\frac{41}{2}^-$	$\frac{41}{2}^-$	$\frac{39}{2}^+$	$\frac{39}{2}^+$	$E1$
158.2(2)	34.7(27)	232	73	$\frac{9}{2}^-$	$\frac{11}{2}^-$	$\frac{9}{2}^-$	$\frac{9}{2}^-$	$M1/E2$
171.1(2)	36.4(28)	2475	2304	$\frac{29}{2}^-$	$\frac{29}{2}^-$	$\frac{27}{2}^+$	$\frac{27}{2}^+$	$E1$
185.5(1)	5.7(11)	3139	2953	$(\frac{33}{2}^+)(\frac{33}{2}^+)$		$\frac{31}{2}^+$	$\frac{31}{2}^+$	$(M1)$
185.7(2)	29.5(23)	417	231	$\frac{9}{2}^-$	$\frac{13}{2}^-$	$\frac{9}{2}^-$	$\frac{11}{2}^-$	$M1/E2$
196.7(2)	18.6(16)	1102	906	$\frac{13}{2}^-$	$\frac{15}{2}^-$	$\frac{13}{2}^-$	$\frac{13}{2}^-$	$M1/E2$
207.7(2)	50.4(35)	1309	1102	$\frac{13}{2}^-$	$\frac{17}{2}^-$		$\frac{15}{2}^-$	$M1/E2$
212.2(1)	10.2(11)	629	417	$\frac{9}{2}^-$	$\frac{15}{2}^-$	$\frac{9}{2}^-$	$\frac{13}{2}^-$	$M1/E2$
237.7(1)	2.5(6)	867	629	$\frac{9}{2}^-$	$\frac{17}{2}^-$	$\frac{9}{2}^-$	$\frac{15}{2}^-$	$M1/E2$
240.0(2)	18.5(18)	3717	3477	$\frac{39}{2}^+$	$\frac{39}{2}^+$	$\frac{37}{2}^+$	$\frac{37}{2}^+$	$M1$
249.1(2)	15.8(16)	3202	2953	$\frac{35}{2}^+$	$\frac{35}{2}^+$	$\frac{31}{2}^+$	$\frac{31}{2}^+$	$E2$
254.9(1)	15.1(15)	1587	1332	$\frac{23}{2}^+$	$\frac{23}{2}^+$	$\frac{19}{2}^+$	$\frac{19}{2}^+$	$E3$
274.9(2)	20.9(19)	3477	3202	$\frac{37}{2}^+$	$\frac{37}{2}^+$	$\frac{35}{2}^+$	$\frac{35}{2}^+$	$M1$
291.3(2)	23.0(20)	1878	1587	$\frac{23}{2}^+$	$\frac{25}{2}^+$	$\frac{23}{2}^+$	$\frac{23}{2}^+$	$M1/E2$
319.1(2)		2794	2475	$(\frac{31}{2}^+)(\frac{31}{2}^+)$		$\frac{29}{2}^-$	$\frac{29}{2}^-$	$(M1)$
337.0(1)		2641	2304	$(\frac{29}{2}^-)(\frac{29}{2}^-)$		$\frac{27}{2}^+$	$\frac{27}{2}^+$	$(M1)$
343.4(1)	3.7(7)	417	73	$\frac{9}{2}^-$	$\frac{13}{2}^-$	$\frac{9}{2}^-$	$\frac{9}{2}^-$	$E2$
382.9(2)		4882	4499	$(\frac{43}{2}^+)(\frac{45}{2}^+)$		$(\frac{43}{2}^+)(\frac{43}{2}^+)$		$(M1)$
395.1(2)		5277	4882	$(\frac{43}{2}^+)$	$\frac{47}{2}^+$	$(\frac{43}{2}^+)(\frac{45}{2}^+)$		$(M1)$
397.6(3)	2.1(7)	629	231	$\frac{9}{2}^-$	$\frac{15}{2}^-$	$\frac{9}{2}^-$	$\frac{11}{2}^-$	$E2$
403.9(1)	10.0(12)	1309	906		$\frac{17}{2}^-$		$\frac{13}{2}^-$	$E2$
425.7(1)	23.1(21)	2304	1878	$\frac{27}{2}^+$	$\frac{27}{2}^+$	$\frac{23}{2}^+$	$\frac{25}{2}^+$	$M1$
442.5(3)	1.4(6)	1309	867		$\frac{17}{2}^-$	$\frac{9}{2}^-$	$\frac{17}{2}^-$	$M1$
449.9(1)	0.95(61)	867	417	$\frac{9}{2}^-$	$\frac{17}{2}^-$	$\frac{9}{2}^-$	$\frac{13}{2}^-$	$E2$

- (a) Energy of unobserved transition inferred from coincidence relationships.
- (b) Intensity inferred from intensity balances.

Table A.1 continued

E_γ	I_γ	E_i	E_i	K_i^π, J_i^π	K_f^π, J_f^π	Multipolarity
(keV)		(keV)	(keV)			
465.4(3)	4.1(8)	1332	867	$\frac{19}{2}^+$ $\frac{19}{2}^+$	$\frac{9}{2}^-$ $\frac{17}{2}^-$	$E1$
473.1(1)	1.4(12)	1102	629	$\frac{15}{2}^-$	$\frac{9}{2}^-$ $\frac{15}{2}^-$	$M1$
477.7(1)	10.6(16)	2953	2475	$\frac{31}{2}^+ \quad \frac{31}{2}^+$	$\frac{29}{2}^- \quad \frac{29}{2}^-$	$E1$
488.0(3)	2.4(7)	906	417	$\frac{13}{2}^-$	$\frac{9}{2}^-$ $\frac{13}{2}^-$	$M1$
593.5(1)	2.6(12)	3069	2475	$\frac{33}{2}^- \quad \frac{33}{2}^-$	$\frac{29}{2}^-$ $\frac{29}{2}^-$	$E2$
629.2(2)		4499	3870	$(\frac{43}{2}^+) (\frac{43}{2}^-)$	$\frac{41}{2}^-$ $\frac{41}{2}^-$	$(M1)$
648.8(1)	13.6(20)	2953	2304	$\frac{31}{2}^+ \quad \frac{31}{2}^+$	$\frac{27}{2}^+ \quad \frac{27}{2}^+$	$E2$
663.2(2)	7.1(17)	2250	1587	$(\frac{25}{2}^+) (\frac{25}{2}^+)$	$\frac{23}{2}^+ \quad \frac{23}{2}^+$	$M1$
674.1(1)	5.1(12)	906	231	$\frac{13}{2}^-$	$\frac{9}{2}^-$ $\frac{11}{2}^-$	$M1$
680.0(2)	15.0(22)	1309	629	$\frac{17}{2}^-$	$\frac{9}{2}^-$ $\frac{15}{2}^-$	$M1$
685.0(2)	8.7(18)	1102	417	$\frac{15}{2}^-$	$\frac{9}{2}^-$ $\frac{13}{2}^-$	$M1$
717.1(3)	6.5(16)	2304	1587	$\frac{27}{2}^+ \quad \frac{27}{2}^+$	$\frac{23}{2}^+ \quad \frac{23}{2}^-$	$E2$
832.2(1)	32.1(29)	906	73	$\frac{13}{2}^-$	$\frac{9}{2}^-$ $\frac{9}{2}^-$	$E2$
870.5(1)	30.7(28)	1102	231	$\frac{15}{2}^-$	$\frac{9}{2}^-$ $\frac{11}{2}^-$	$E2$
892.7(1)	28.0(26)	1309	417	$\frac{17}{2}^-$	$\frac{9}{2}^-$ $\frac{13}{2}^-$	$E2$

Table A.2: Properties of transitions in ^{182}Ta . The intensities are measured out-of-beam relative to the 447.6 keV γ ray.

E_γ (keV)	I_γ	E_i (keV)	E_f (keV)	K_i^π	J_i^π	K_f^π	J_f^π	Multipolarity
58.7(1) ^a	16(2) ^b	3399	3341	(18 $^-$)	(18 $^-$)	(17 $^+$)	(17 $^+$)	(E1)
132.1(1)	34(23)	2082	1950	(14 $^-$)	(14 $^-$)	14 $^+$	14 $^+$	(E1)
143.2(1)	19.9(18)	2093	1950	(14 $^+$)	(14 $^+$)	14 $^+$	14 $^+$	M1
146.8(1)	78.3(38)	163	16	5 $^+$	6 $^+$	5 $^+$	5 $^+$	M1/E2
171.8(1)	96.7(42)	334	163	5 $^+$	7 $^+$	5 $^+$	6 $^+$	M1/E2
184.9(1)	68.2(35)	519	334	10 $^-$	10 $^-$	5 $^+$	7 $^+$	E3
245.3(1)	5.2(10)	1950	1705	14 $^+$	14 $^+$	10 $^-$	(14 $^-$)	E1
266.7(1)	75.0(35)	786	519	10 $^-$	11 $^-$	10 $^-$	10 $^-$	M1/E2
277.8(1)	30.4(20)	2762	2484	(18 $^+$)	(18 $^+$)	(16 $^+$)	(16 $^+$)	(E2)
287.3(1)	20.9(17)	1073	786	10 $^-$	12 $^-$	10 $^-$	11 $^-$	M1/E2
293.1(1)	94.1(41)	2243	1950	15 $^+$	15 $^+$	14 $^+$	14 $^+$	M1
306.8(1)	35.8(22)	1380	1073	10 $^-$	13 $^-$	10 $^-$	12 $^-$	M1/E2
318.4(1)	16.0(14)	334	16	5 $^+$	7 $^+$	5 $^+$	5 $^+$	E2
324.8(1)	2.4(9)	1705	1380	10 $^-$	14 $^-$	10 $^-$	13 $^-$	M1/E2
345.9(1)	31.1(21)	2588	2243	15 $^+$	(16 $^+$)	15 $^+$	(15 $^+$)	M1/E2
356.4(1)	< 2.4	519	163	10 $^-$	10 $^-$	5 $^+$	6 $^+$	M4
362.9(1)	37.5(23)	2951	2588	15 $^+$	(17 $^+$)	15 $^+$	(16 $^+$)	M1/E2
391.0(1)	28.4(20)	2484	2093	(16 $^+$)	(16 $^+$)	(14 $^+$)	(14 $^+$)	(E2)
447.6(1)	100.0(46)	3399	2951	(18 $^-$)	(18 $^-$)	15 $^+$	(17 $^+$)	(E1/M2)
467.8(1)	9.2(14)	2951	2484	15 $^+$	(17 $^+$)	(16 $^+$)	(16 $^+$)	(M1)
495.8(1)	11.4(16)	2588	2093	15 $^+$	(16 $^+$)	(14 $^+$)	(14 $^+$)	(M1)
553.9(1)	19.0(19)	1073	519	10 $^-$	12 $^-$	10 $^-$	10 $^-$	E2
570.2(1)	98.0(47)	1950	1380	14 $^+$	14 $^+$	10 $^-$	13 $^-$	E1
594.1(1)	56.7(33)	1380	786	10 $^-$	13 $^-$	10 $^-$	11 $^-$	E2
631.7(1)	5.8(14)	1705	1073	10 $^-$	14 $^-$	10 $^-$	12 $^-$	E2
637.5(1)	22.9(22)	3399	2762	(18 $^-$)	(18 $^-$)	(18 $^+$)	(18 $^+$)	(E1)
708.6(1)	56.0(35)	2951	2243	15 $^+$	17 $^+$	15 $^+$	15 $^+$	E2
1097.7(1)	20.7(26)	3341	2243	(17 $^+$)	(17 $^+$)	15 $^+$	15 $^+$	(E2)

(a) Energy of unobserved transition inferred from coincidence relationships.

(b) Intensity inferred from intensity balances.

Table A.3: Low-lying, two-neutron states known in ^{182}W [Shi95], ^{184}W [Whe04, Lan12, Lan15] and ^{186}W [Whe98, Whe99a, Lan12]. These states are likely to contribute to the multi-quasiparticle states in ^{181}Ta , ^{183}Ta and ^{185}Ta , respectively.

Nucleus	K^π	Configuration	E_{exp} (keV)
^{182}W	4^-	$9/2^+[624]\otimes1/2^-[510]$	1553
	5^-	$9/2^+[624]\otimes1/2^-[510]$	1810
	6^-	$9/2^+[624]\otimes3/2^-[512]$	1830
	8^-	$9/2^+[624]\otimes7/2^-[503]$	2120
	10^+	$9/2^+[624]\otimes11/2^+[615]$	2230
^{184}W	2^+	$3/2^-[512]\otimes1/2^-[510]$	1386
	3^+	$1/2^-[510]\otimes7/2^-[503]$	1425
	5^-	$11/2^+[614]\otimes1/2^-[510]$	1285
	7^-	$11/2^+[614]\otimes3/2^-[512]$	1502
	10^+	$11/2^+[614]\otimes9/2^+[624]$	2479
^{186}W	7^-	$11/2^+[614]\otimes3/2^-[512]$	1517
	9^-	$11/2^+[614]\otimes7/2^-[503]$	2118
	10^-	$11/2^+[614]\otimes9/2^-[505]$	2286

Table A.4: Single-neutron states known in odd-tungsten isotopes that are likely to contribute to the multi-quasiparticle states in odd-odd tantalum isotopes between $A = 180$ and $A = 186$ [Lin73, Sai00, Bon05, Shi08].

Isotope	^{181}W	^{183}W	^{185}W	^{187}W
Ω^π	(keV)	(keV)	(keV)	(keV)
$1/2^-[510]$	458	0	24	146
$3/2^-[512]$	726	209	0	0
$7/2^-[503]$	661	453	244	350
$9/2^+[624]$	0	623	716	798
$11/2^+[615]$	-	310	197	410
$9/2^-[505]$	-	-	785	364
$5/2^+[512]$	366	905	889	-
$1/2^-[521]$	385	935	1006	-

Appendix B

B.1 Published results on ^{183}Ta

This appendix present a published paper (conference proceedings) on some of the preliminary results for ^{183}Ta [Pal12]. The results were presented at the annual Heavy Ion Accelerator Sympsium (HIAS) held in April 2012 at the Australian National University. The results have been published in EPJ web of conferences.

Decay of a three-quasiparticle isomer in the neutron-rich nucleus ^{183}Ta

N. Palalami^{1,a}, G.J. Lane¹, G.D. Dracoulis¹, F.G. Kondev², A.P. Byrne¹, M.P. Carpenter², C.J. Chiara², P. Chowdhury³, R.O. Hughes¹, R.V.F. Janssens², T. Lauritsen², C.J. Lister², E.A. McCutchan², D. Seweryniak², I. Stefanescu², H. Watanabe¹, and S. Zhu²

¹ Department of Nuclear Physics, The Australian National University, ACT 0200, Australia.

² Argonne National Laboratory, Argonne, Illinois 60439, USA

³ University of Massachusetts Lowell, Lowell, Massachusetts 01854, USA

Abstract. Excited states in neutron-rich tantalum isotopes have been studied with deep-inelastic reactions using ^{136}Xe ions incident on a ^{186}W target. New transitions observed below the $\tau=1.3\ \mu\text{s}$ isomer in ^{183}Ta have enabled the establishment of its energy and put limits on the spin and parity. On the basis of the reduced hindrances for the depopulating transitions, a 3-quasiparticle configuration of $\nu 1/2^- [510] 11/2^+ [615] \otimes \pi 9/2^- [514]$ is suggested.

1 Introduction

Nuclei in regions far from closed shells are known to have non-spherical equilibrium shapes which are either oblate, or, more usually, prolate. The single particle energy levels in these nuclei depend on the component of the nucleon angular momentum (denoted by $j_z = Q$) along the symmetry axis. These components can be summed over the valence nucleons to give a quantum number $K = \sum_i Q_i$ that is nominally conserved. Nuclei around mass-180 exhibit metastable states known as K-isomers [1, 2], that form when states with high K values can only decay via transitions whose multipole order λ is less than the change in K, thus violating the K-selection rule, $\Delta K \leq \lambda$. Such transitions are, in principle, forbidden, with the forbiddenness characterised by $\nu = \Delta K - \lambda$.

Experimental access to K-isomers that are expected to occur in the neutron-rich region has been limited by the lack of stable beams and targets that can populate them using conventional fusion-evaporation reactions. Recently, K isomers in the neutron-rich hafnium, lutetium and tungsten isotopes [3–8] have been studied using more exotic techniques such as deep-inelastic reactions [9] and relativistic fragmentation [10]. The present report focusses on the tantalum isotopes and, in particular, on ^{183}Ta .

The heaviest stable tantalum nucleus is ^{181}Ta and little is known concerning high spin states in isotopes heavier than ^{183}Ta , except for the decay of the $K^\pi=21/2^-$ isomer in ^{185}Ta [11, 12]. Recently, Shizuma et al [13] investigated ^{183}Ta using the $^{181}\text{Ta}(^{18}\text{O}, ^{16}\text{O})^{183}\text{Ta}$ transfer reaction and reported the decay from a new isomeric state with a $1.3\ \mu\text{s}$ lifetime. The tentative spin, parity and configuration assignments were based on the assumption that an unobserved transition depopulated the isomer. At present no information on high spin states is available for ^{184}Ta . The current work aims to extend the level schemes for these neutron-rich tantalum nuclei to high-spin using deep-inelastic reactions. This forms part of an ongoing program to explore the structures of well deformed

neutron-rich nuclei (see, for example, [4, 6, 7, 14, 15] and references therein). In the current work, additional transitions below the $1.3\ \mu\text{s}$ isomer in ^{183}Ta have been identified, so that the energy and likely multipolarity of the unobserved transition, and hence the energy and the configuration for the isomer, have been obtained. While states above the isomer have also been observed, including two new isomers, and γ -rays possibly associated with ^{184}Ta have been identified, the analysis of these is still in progress and will not be discussed in the present report.

2 Experimental Methods

The current results are from data collected at Argonne National Laboratory using Gammasphere with 99 Compton-suppressed HPGe detectors in operation. A beam of 840 MeV ^{136}Xe ions from the ATLAS accelerator was incident on a 99% enriched ^{186}W target with a gold backing. This reaction is expected to populate tantalum nuclei from $A \approx 182$ to $A \approx 187$. The experimental measurements involved a variety of macroscopic beam pulsing conditions, ranging from microseconds to seconds, to enable identification of isomers with a range of lifetimes. The data were gain-matched offline for each individual detector and sorted into a Blue database [16] for time correlated coincidence analysis.

3 Experimental Results

3.1 ^{183}Ta level scheme

Several gate combinations were set in the out-of-beam time region on γ -rays below the isomer in ^{183}Ta . All the known γ -rays from Ref. [13] were observed, together with new $J \rightarrow J$ transitions at 488, 473 and 442 keV that decay from the $13/2^-$ band to the $9/2^-$ band. The new transitions extend the decay pattern expected for the $13/2^-$ band if it were to be the $9/2^-$ configuration coupled to the γ -vibration, as already suggested by Shizuma et al [13]. In

^a e-mail: nyalandzi.p@gmail.com

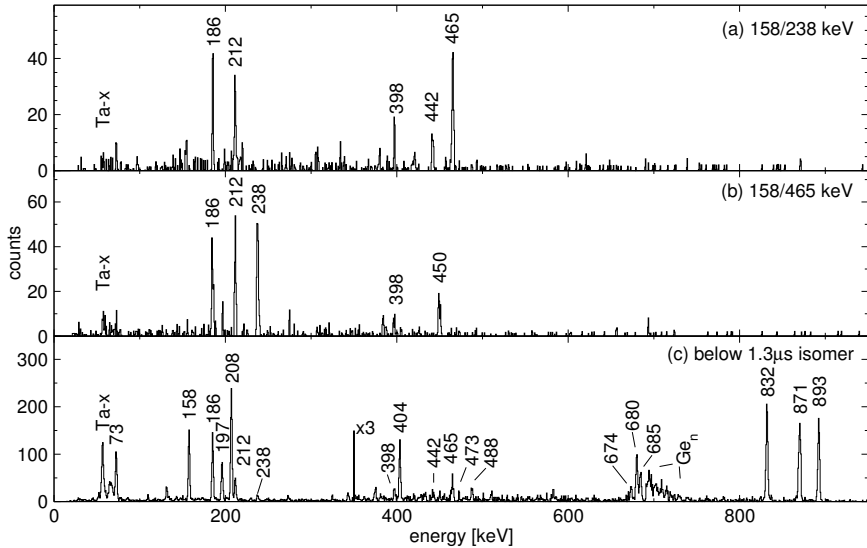


Fig. 1. (a) and (b) Coincidence spectra projected from the out-of-beam $\gamma - \gamma - \gamma$ coincidence cube double gated on 158/238 and 158/465 keV transitions, respectively. Spectrum (c) shows the new 442 and 465 keV transitions, while spectrum (b) demonstrates that they arise from parallel decay paths. (c) Delayed γ -ray spectrum showing the transitions that follow the decay of the 1.3 μs isomer (see text for details). Contaminants due to inelastic neutron excitation in ^{72}Ge are labelled.

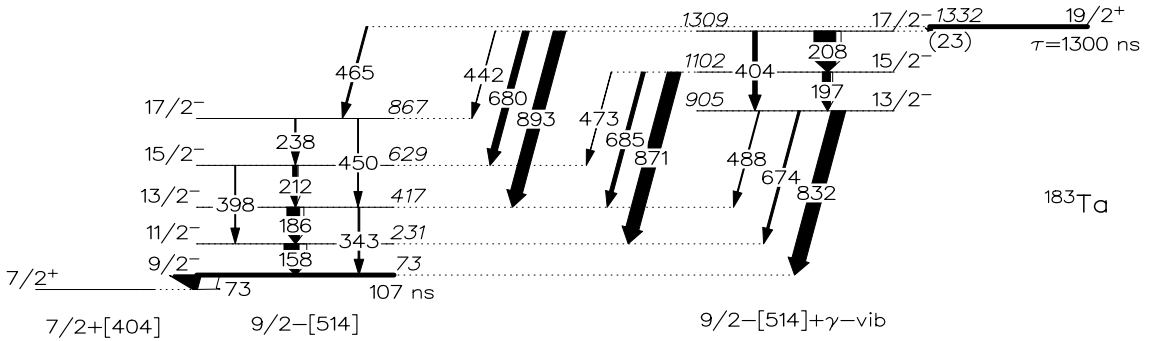


Fig. 2. Level scheme for ^{183}Ta including new transitions that establish the energy of the unobserved 23 keV transition.

addition, a 465 keV direct decay from the isomer was identified. A representative double-gated spectrum comprising gates on known transitions in the 9/2⁻[514] band (158 and 238 keV) is shown in Figure 1.

The level scheme for ^{183}Ta below the 1.3 μs isomer as deduced from the coincidence information is illustrated in Figure 2. The structure below the isomeric state reported by Shizuma et al [13] is confirmed, and new transitions included. The spectrum in Figure 1(b) demonstrates that two of the new transitions are parallel and implies that the 465 keV transition directly depopulates the isomer. From this information, the energy of the unobserved transition previously proposed in Ref. [13] is deduced to be 23 keV.

By double-gating on transitions below the isomer and projecting the γ -rays that precede it in time, a new set of feeding γ -rays was identified. While these γ -rays are not presented here, they were used to isolate the delayed γ -rays emitted below the 1332 keV state. The 200 to 800 ns delayed spectrum in Figure 1(c) was used to deduce the γ -ray intensities for decay branches out of the isomer.

4 Discussion

The ground state band is known to be formed from the 7/2⁺[404] orbital, while the first excited band is built on

the 9/2⁻[514] intrinsic state. The 13/2⁻ bandhead is suggested in Ref [13] to be a γ -vibration coupled to the 9/2⁻[514] state. Therefore, the following discussion is focused on the establishment of the spin, parity and single-particle configuration for the 1332 keV isomer.

4.1 Spin assignment for the 1332 keV state

To determine the multipolarity of the 23 keV transition, several possible spins and parities for the 1332 keV state were assumed. For each case, the implied multipolarities of the 23 and 465 keV transitions were deduced, and γ -ray intensities were determined based on measured γ -ray intensities, intensity balances and internal conversion coefficients. The transition strengths and reduced hindrances for the 465 and 23 keV transitions thus obtained are shown in Table 1. Since E1 transitions are already hindered by large factors, the reduced hindrances for E1 transitions were calculated both with (italic) and without an additional factor of 10^4 in the nominal single particle hindrance. In the absence of competing mechanisms for enhanced decays, extreme values of the reduced hindrances can be used to rule out the assumed spin and parity.

At first glance, reasonable values for the reduced hindrances (expected range 30-300) are only obtained for a 19/2⁻ assignment to the isomeric state. However, for

Table 1. Transition strengths and corresponding reduced hindrances for the 465 and 23 keV transitions, assuming alternative spins and parities for the $1.3\ \mu\text{s}$ isomeric state.

I^π	λ	E_γ (keV)	I_γ	α_T	B_γ (W.u)	ν	f_ν
$19/2^-$	<i>M1</i>	$(22.7)^a$	$(74.3)^b$	5.771×10^1	3.46×10^{-5}	2	170
	<i>M1</i>	465.4	100	6.282×10^{-2}	5.42×10^{-9}	4	117
$19/2^+$	<i>E1</i>	$(22.7)^a$	$(884.1)^b$	0.3932×10^1	3.92×10^{-6}	2	$505 / (5.1)^c$
	<i>E1</i>	465.4	100	7.991×10^{-3}	5.17×10^{-11}	4	$373 / (37)^c$
$21/2^+$	<i>M2</i>	$(22.7)^a$	$(0.494)^b$	8.834×10^3	1.94×10^1	2	0.23
	<i>M2</i>	465.4	100	2.004×10^{-1}	1.09×10^{-3}	4	5.5
$21/2^-$	<i>E2</i>	$(22.7)^a$	$(1.16)^b$	3.758×10^3	4.35×10^{-1}	2	1.5
	<i>E2</i>	465.4	100	2.417×10^{-2}	1.04×10^{-5}	4	18

^a Energy of unobserved transition.

^b Intensity of unobserved transition inferred from intensity balance and implied conversion coefficients.

^c Entries in italics include a normalisation factor of 10^4 (see text for details).

$J^\pi=19/2^-$ there are potential E2 transitions of 703 and 230 keV that should directly depopulate the isomer and feed the 629 and 1102 keV states, respectively. Such transitions were not observed in any of the (various) out-of-beam, double-gated spectra or in the delayed spectrum in Figure 1(c). Hence, upper intensity limits were deduced, giving limits on the reduced hindrances for the possible 703 and 230 keV transitions of $f_\nu > 103$ and $f_\nu > 6900$ respectively. The latter limit effectively rules out the $19/2^-$ assignment. The $21/2^+$ possibility can be ruled out on the basis of the very low values of the reduced hindrances for both the 465 and 23 keV transitions that fall outside the expected range mentioned above.

For the $21/2^-$ alternative, both notional E2 decays of 23 and 465 keV are fast, however, they could have been enhanced by mixing between the isomer and the $21/2^-$ state in the $9/2^-$ band, resulting in the low reduced hindrance. If the entire strength of the 465 keV transition were due to a collective admixture of the $K^\pi = 9/2^-$ wavefunction into the isomeric state wavefunction, a mixing matrix element of 23 eV would be implied, as deduced using the method described in [7], a reasonable value. However, in this scenario, there should also be a 203 keV M1/E2 transition from the isomer to the known $19/2^-$ band member at 1131 keV [13], with a branching ratio relative to the 465 keV transition that is consistent with the collective properties expected (and observed) in the $9/2^-[514]$ band.

Table 2 presents the corresponding magnetic moment properties deduced from the measured crossover/cascade intensity ratios within this band. The values deduced for $|g_K - g_R|$ are consistent with the previous measurement [13], theoretical expectations ($g_K = 1.29$ for the $9/2^-[514]$ configuration and $g_R \sim 0.35$) and with branching ratios in the same band in the neighbouring nucleus, ^{185}Ta [11, 12]. For the decays from the isomer to reproduce the average $|g_K - g_R|$ for the inband decays, the intensity ratio $\lambda = I_\gamma(\Delta I = 2; 465)/I_\gamma(\Delta I = 1; 203)$ would have to be 1.07(13). The observed limit is $\lambda > 2.57$. While this tends to discount the $21/2^-$ possibility, it still cannot be ruled out.

The remaining possibility for the spin assignment is $19/2^+$. Given the known variability in $E1$ strengths, the measured reduced hindrances for the 23 and the 465 keV transitions are within acceptable limits, as are the limits for the possible 703 and 230 keV $M2$ transitions of $f_\nu > 22$ and $f_\nu > 67$, respectively. Based on the above discussions,

it can be concluded that $19/2^+$ or $21/2^-$ are the likely assignments for the $1.3\ \mu\text{s}$ isomer.

4.2 Configuration assignment

Given the excitation energy of the isomer, a 3-quasiparticle configuration is probable. In the light odd mass tantalum isotopes, $21/2^-$ isomers are observed systematically across the isotopic chain. Their nature is discussed in detail by Kondev et al [17] for isotopes with $A \leq 179$, while the isomer persists into ^{181}Ta [18, 19]. Although mixing of specific configurations is likely, particularly for the $A=179$ case [17], a three-proton configuration is a possible candidate for the isomer configuration in ^{183}Ta . Note that in ^{185}Ta , the 17 ms, $21/2^-$ isomer has been assigned as the $\pi 7/2^+[404] \otimes \nu 3/2^-[512] 11/2^+[615]$ configuration in [11], however, the three proton configuration has also been suggested as an alternative [21] based on the transition strength systematics. In ^{183}Ta , all possibilities must be considered, including the fact that $19/2^+$ appears to be the more likely spin and parity assignment.

The neutron states most likely to be involved in the configuration can be determined by examining the low-lying spectrum of excited states in the nearby odd-mass tungsten isotopes, especially ^{183}W [20] and ^{185}W [22]. The ground state in ^{183}W is formed from the $1/2^-[510]$ intrinsic state, with the $3/2^-[512]$ state only 209 keV higher. This situation is reversed in ^{185}W , with the $1/2^-[510]$ level at an excitation energy of only 24 keV, while the $11/2^+[615]$ state lies at 310 and 197 keV in ^{183}W and ^{185}W , respectively. The $7/2^-[503]$ and $9/2^+[624]$ levels are higher in energy and therefore are not expected to

Table 2. Measured in-band branching ratios for the $9/2^-[514]$ band in ^{183}Ta , together with inferred gyromagnetic ratios.

J_i^π	E_γ ($I \rightarrow I-1$) (keV)	E_γ ($I \rightarrow I-2$) (keV)	λ^a	$ g_K - g_R ^b$
$13/2^-$	186	343	0.14(3)	0.83(9)
$15/2^-$	212	397	0.25(4)	0.93(7)
$17/2^-$	238	450	0.45(6)	0.89(6)
weighted avg:				0.89(4)

^a $\lambda = I_\gamma(I \rightarrow I-2)/I_\gamma(I \rightarrow I-1)$.

^b Calculations assume a value of $Q_0=6.5$ eb.

Table 3. Expected low-lying 3-quasiparticle configurations.

K^π	Configurations ^a	E_{qp} (keV)	E_{res} (keV)	E_{cal} (keV)
19/2 ⁻	$\nu 1/2^- 11/2^+ \pi 7/2^+$	1930	+263	2193
17/2 ⁻	$\nu(1/2^-) 11/2^+ \pi 7/2^+$		-137	1793
21/2 ⁺	$\nu 1/2^- 11/2^+ \pi 9/2^-$	2097	-64	2033
19/2 ⁺	$\nu(1/2^-) 11/2^+ \pi 9/2^-$		-222	1875
21/2 ⁻	$\nu 3/2^- 11/2^+ \pi 7/2^+$	1984	-138	1846
23/2 ⁺	$\nu 3/2^- 11/2^+ \pi 9/2^-$	2151	-216	1935
21/2 ⁻	$\pi 5/2^+ 7/2^+ 9/2^-$	1406	-77	1329

^a Neutrons: 1/2⁻: 1/2⁻[510]; 3/2⁻: 3/2⁻[512]; 11/2⁺: 11/2⁺[615]. Protons: 5/2⁺: 5/2⁺[402]; 7/2⁺: 7/2⁺[404]; 9/2⁻: 9/2⁻[514]. An orbital in brackets, e.g. (1/2⁻), refers to an anti-parallel coupling.

take part in the formation of low-lying two-neutron one-proton states in odd-mass tantalum nuclei. As discussed above, the $\pi 5/2^+[402]7/2^+[404]9/2^-[514]$ configuration will also be competitive in energy.

To quantify the situation, preliminary multi-quasiparticle calculations were performed for ^{183}Ta , as well as for ^{181}Ta and ^{185}Ta to investigate the isotopic dependence. The results are illustrated in figure 3, and the detailed energies for ^{183}Ta are given in table 3. The calculated energy dependence for the $\pi 5/2^+[402]7/2^+[404]9/2^-[514]$, 21/2⁻ state is flat (labelled F in figure 3). The 21/2⁻ state from the $\nu 3/2^-[512]11/2^+[615] \otimes \pi 7/2^+[404]$ configuration (labelled G) comes down in energy with increasing mass number, becoming more competitive in ^{185}Ta . If the state in ^{183}Ta were to be 21/2⁻, it would have the $\pi 5/2^+[402]7/2^+[404]9/2^-[514]$ configuration. However, the energy of the the 19/2⁺ state in ^{183}Ta (1875 keV in table 3) is clearly over-estimated in the calculation given that the 5⁻ two neutron component of the configuration is observed in the N=110 isotope, ^{184}W , at 1285 keV [23]. If the state in ^{183}Ta were to be 19/2⁺, this would imply that $\nu 1/2^-[510] 11/2^+[615] \otimes \pi 9/2^-[514]$ is the likely configuration.

To distinguish between these possibilities requires either better spectroscopic information for the 465 keV direct decay, or observation of the characteristic band structure above the isomer. However, preliminary analysis of the states above the isomer does not result in a well developed band structure. This is perhaps not unexpected given the high density of intrinsic states predicted to occur in the vicinity of the isomer, as shown in figure 3.

5 Conclusion

Excited states in neutron-rich tantalum isotopes have been studied using deep-inelastic reactions between a ^{136}Xe beam and a ^{186}W target. The energy of the isomeric state in ^{183}Ta previously reported by Shizuma et al [13] has now been established on the basis of a γ -ray transition that directly depopulates it. The measured reduced hindrances for the depopulating transitions support either a 19/2⁺ or 21/2⁻ assignment. The 19/2⁺ possibility is currently favoured, in which case a 3-quasiparticle $\pi 9/2^-[514] \otimes \nu 1/2^-[510] 11/2^+[615]$ configuration is suggested.

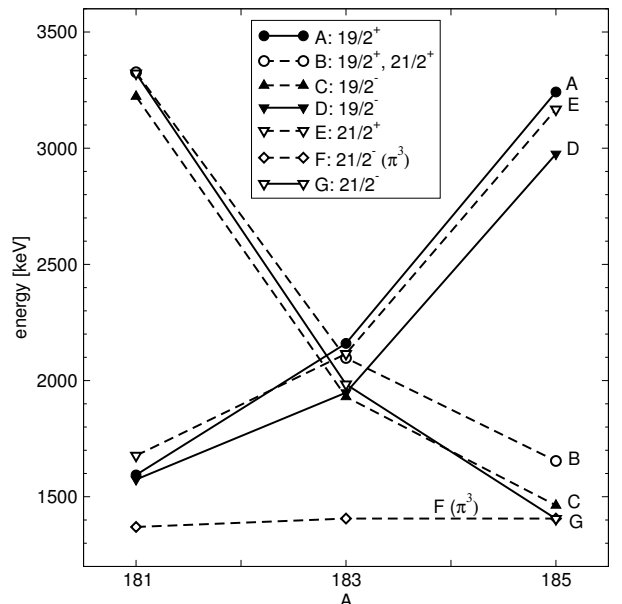


Fig. 3. Systematic behaviour between $A=181$ and $A=185$ for the lowest intrinsic states calculated in ^{183}Ta . (preliminary calculations)

References

- P. M Walker and G.D. Dracoulis, Nature **399** (1999) 35.
- P. M Walker and G.D. Dracoulis, Hyperfine Interactions **135** (2001) 83.
- R. D'Alarcao et al, Phys. Rev. C **59** (1999) R1227.
- G. J. Lane et al, Phys. Rev. C **82** (2010) 052304(R).
- G. F. Farrelly et al., Acta Phys. Pol. B **40** (2009) 885.
- G. D. Dracoulis et al, Phys. Lett. B **584** (2004) 22.
- G. D. Dracoulis et al, Phys. Rev. Lett. **97** (2006) 122501.
- C. Wheldon et al J. Phys. G: Nucl. Part. Phys. **27** (2001) L13.
- R. Broda, J. Phys. G: Nucl. Part. Phys. **32** (2006) R151.
- M. Pfutzner et al Phys. Lett. B **444**, (1998) 32.
- G. J. Lane et al, Phys. Rev. C **80**, (2009) 024321.
- C. Wheldon et al, Eur. Phys. J. A **5**, (1999) 353-355.
- T. Shizuma et. al, Eur. Phy. J. A **39**, (2009) 263.
- G. D. Dracoulis et al, Phys. Lett. B **709** (2012) 59.
- F. G. Kondev et al, Phys. Rev. C **80** (2009) 014304
- M. Cromaz et al, Nucl. Instrum. Methods A **462**, (2001) 519.
- F. G. Kondev et al, Nucl. Phys. A **617** (1997) 91.
- C. Wheldon et al, Phys. Lett. B **425** (1998) 239.
- G. D. Dracoulis et al Phys. Rev. C **58** (1998) 1837.
- T. R. Saitoh et al, Nucl Phys A **669** (2000) 381.
- P. M Walker et al, Phys. Rev. C **81** (2010) 041304(R).
- V. Bondarenko et al, Nucl. Phys. A **762** (2005) 167.
- C. Wheldon et al, Eur Phys. J. A **20** (2004) 365.

Bibliography

- [Åbe78] S. Åberg *et al.*, Nucl. Phys. A **306**, 89 (1978).
- [Ada97] J. Adam *et al.*, Nucl. Instr. Meth. A **385**, 492 (1997).
- [Ahm95] I. Ahmad and W. R. Philips, Rep. Prog. Phys. **58**, 1415 (1995).
- [Akk12] S. Akkoyun *et al.*, Nucl. Instr. Meth. Phys. Res. A **668** 26 (2012).
- [Bar57] J. Bardeen, L.N Cooper and J.R. Schrieffer, Phys. Rev. **108**, 1175 (1957).
- [Baz04] D. Bazzacco, Nucl. Phys. A **746** 248c (2004).
- [Bel59] S. T. Belyaev and K. Dan. Vidensek. Selsk. Mat. Fys. Medd. **31**, 11 (1959).
- [Bea96] C. W. Beausang and J. Simpson, J. Phys. G: Nucl. Part. Phys. **22**, 527 (1996).
- [Ben79] R. Bengtsson and S. Frauendorf, Nucl. Phys. A **327**, 139 (1979).
- [Ben85] T. Bengtsson and I. Ragnarsson, Nucl. Phys. A **436**, 14 (1985).
- [Ben86] R. Bengtsson *et al.*, At. Data. Nucl. Data. Tab.,**35**, 15 (1986).
- [Biz66] B. Bizzarri *et al.*, Nuovo Cim. **46**, 13 (1966).
- [Bon05] V. Bonderenko *et al.*, Nucl. Phys. A **762**, 167 (2005).
- [Boh58] A. Bohr, B. R. Mottelson and D. Pines, Phys. Rev. **110**, 936 (1958).
- [Boh75] A. Bohr and B Mottelson, Nuclear Structure, Vol. II (Benjamin, New York, 1975)
- [Bos66] L. Bostrom, B. Olsen, W. Schneider and E. Matthias, Nucl. Instrum. Methods in Phys. Res. **44**, 61 (1966).
- [Bro06] R. Broda, J. Phys. G: Nucl. Part. Phys. **32**, R151 (2006).

- [Bur96] O. Burglin and N. Rowley, Nucl. Phys. A **602**, 21 (1996).
- [Car95] H. Carlsson *et al.*, Nucl. Phys. A **592**, 89 (1995).
- [Cas00] R.F. Casten, Nuclear structure from a simple perspective, Second Edition, (Oxford University Press Inc., New York, 2000)
- [Coc99] J. F. C. Cocks *et al.*, Nucl. Phys. A **645**, 61 (1999).
- [Cro01] M. Cromaz *et al.*, Nucl. Inst. Methods A **462**, 519 (2001).
- [Cro95] B. Crowell *et al.*, Nucl. Instr. Meth. A **355**, 575 (1995).
- [Cum85] J.B. Cumming and D.E Alburger, Phys. Rev. C **31**, 1494 (1985).
- [Cla68] D. D. Clark and W. F. Stabenau, Phys. Rev. Lett. **21**, 925 (1968).
- [D'Al99] R. D'Alarcao *et al.*, Phys. Rev. C **59**, R1227 (1999).
- [Das94] M. Dasgupta *et al.*, Phys. Lett. B **328**, 16 (1994).
- [Das00] M. Dasgupta *et al.*, Phys. Rev. C **61**, 044321 (2000).
- [Das94] C. H. Dasso, G. Pollaro and A. Winther, Phys.Rev.Lett. **73**, 1907 (1994).
- [Del99] M. A. Deleplanque *et al.*, Nucl. Instr. Meth Phys. Res. A **430**, 292 (1999).
- [de V83] M. J. A. de Voigt, J. Dudek, J. and Z. Szymanski, Rev. Mod. Phys. **55**, 949 (1983).
- [Don87] F. Dönau, Nucl. Phys. A **471**, 469 (1987).
- [Dra96] G.D. Dracoulis *et al.*, Phys. Rev. C **53**, 1205 (1996).
- [Dra97] G.D. Dracoulis *et al.*, J. Phys. G **23**, 1191 (1997).
- [Dra98] G. D. Dracoulis *et al.*, Phys. Rev. C **58**, 1444 (1998).
- [Dra98a] G. D. Dracoulis *et al.*, Phys. Rev. C **58**, 1837 (1998).
- [Dra98b] G. D. Dracoulis, F. G. Kondev and P. M. Walker, Phys. Lett. B **419**, 7 (1998).

- [Dra04] G. D. Dracoulis *et al.*, Phys. Lett. B **584**, 22 (2004).
- [Dra05] G. D. Dracoulis *et al.*, Phys. Rev. C **71**, 044326 (2005).
- [Dra05a] G. D. Dracoulis, Nucl. Phys. A **752**, 213c (2005).
- [Dra06] G. D. Dracoulis *et al.*, Phys. Rev. Lett. **97**, 122501 (2006).
- [Dra06a] G. D. Dracoulis *et al.*, Phys. Lett. B **635**, 200 (2006).
- [Dra09] G. D. Dracoulis *et al.*, Phys. Rev. C **79**, 061303(R) (2009).
- [Dra10] G. D. Dracoulis *et al.*, Phys. Rev. C **81**, 054313 (2010).
- [Dra10a] G. D. Dracoulis *et al.*, Phys. Rev. C **82**, 034317(R) (2010).
- [Dra10b] G. D. Dracoulis *et al.*, Phys. Rev. C **81**, 011301(R) (2010).
- [Dra12] G. D. Dracoulis *et al.*, Phys. Lett. B **709**, 59 (2012).
- [Dra13] G. D. Dracoulis, Phys. Scr. T **152**, 014015 (2013).
- [Ebe08] J. Eberth and J. Simpson, Prog. in Part. and Nucl. Phys. **60**, 283 (2008).
- [Eji89] H. Ejiri and M.J.A. de Voigt, Gamma-Ray and Electron Spectroscopy in Nuclear Physics, (Clarendon Press, Oxford, 1989).
- [Ers64] J. R. Erskine and W. W. Buechner, Phys. Rev. **133**, B370 (1964).
- [Eks92] L. P. Ekström and A. Nordlund, Nucl. Instrum. Meth. Phys. Res. **A313**, 421 (1992).
- [Eks84] L. P. Ekström, Comp. Phys. Comm. **32**, 399 (1984).
- [Fra81] S. Frauendorf, Phys. Scr. **24**, 349 (1981).
- [Fén02] T. Fényes, Structure of Atomic Nuclei, (Akadémiai Kiadó, Budapest, Hungary, June 2002).
- [Fir92] R. B. Firestone, Nucl. Data Sheets **65**, 589 (1992).

- [Fir99] R. B. Firestone, Table of Isotopes, 8th edition (John Wiley and Sons, New York, 1999 update).
- [Gre96] W. Greiner and J. A. Maruhn, Nuclear Models (Springer, New York, 1996).
- [Gal58] C. J. Gallagher and S. A. Moszkowski, Phys. Rev. **111**, 1282 (1958).
- [Ham40] D. R. Hamilton, Phys. Rev. **58**, 122 (1940).
- [Har65] S. M. Harris, Phys. Rev. **138**, B509 (1965).
- [Has98] N. Hashimoto *et al.*, Eur. Phys. J. A **2**, 327 (1998).
- [Hax49] O. Haxel *et al.*, Phys. Rev. **75**, 1766 (1949).
- [Hau61] U. Hauser, Nucl. Phys. **24**, 488 (1961).
- [Hel71] R. G. Helmer, R. C. Greenwood and C. W. Reich, Nucl. Phys. A **168**, 449 (1971).
- [Hel68] R. G. Helmer and C. W. Reich, Nucl. Phys. A **114**, 649 (1968).
- [Hug12] R. O. Hughes *et al.*, Phys. Rev. C **86**, 054314 (2012).
- [Jai94] K. Jain *et al.*, Phys. Lett. B **322**, 27 (1994).
- [Jai95] K. Jain *et al.*, Nucl. Phys. A **591**, 61 (1995).
- [Jan96] R.V.F. Janssens and F.S. Stephens, Nucl. Phys. News **6**, 9 (1996).
- [Kib08] T. Kibédi *et al.*, Nucl. Instr. Meth. in Phys. Res. A **589**, 202 (2008).
- [Kon96] F. G. Kondev, Interplay between intrinsic and collective motion in tantalum nuclei, The Australian National University, PhD thesis, (1996), unpublished.
- [Kon97] F. G. Kondev *et al.*, Nucl. Phys. A **617**, 91 (1997).
- [Kon98] F. G. Kondev *et al.*, Nucl. Phys A **632**, 473 (1998).
- [Kon99] F. G. Kondev *et al.*, Phys. Rev. C **59**, R575 (1999).
- [Kon04] F. G. Kondev *et al.*, Eur. Phys. J A **22**, 23 (2004).

- [Kon09] F. G. Kondev *et al.*, Phys. Rev. C **80**, 014304 (2009).
- [Kno89] G.F. Knoll, Radiation Detection and Measurement (Wiley, Singapore, 1989).
- [Kra73] K. S. Krane, R. M. Steffen and R. M. Wheeler, At. Nucl. Data Tables A **11**, 351 (1973).
- [Kra88] K. S Krane, Introductory Nuclear Physics, (John Wiley sons New York, 1988).
- [Kró11] W. Królas, Acta Phys. Pol. B **42**, 689 (2011).
- [Lan08] G. J. Lane *et al.*, Limits of K-isomerism and astrophysical processes in neutron-rich tungsten, rhenium and osmium nuclei, ATLAS experimental proposal, unpublished (2008).
- [Lan09] G. J. Lane *et al.*, Phys. Rev. C **80**, 024321 (2009).
- [Lan10] G. J. Lane *et al.*, Phys. Rev. C **82**, 052304(R) (2010).
- [Lan12] G. J. Lane *et al.*, Nuclear structure 2012 conference, unpublished. Talk is available via, <http://ns12.anl.gov/program.shtml>
- [Lan15] G. J. Lane, Werner *et al.*, private communication, to be published.
- [Lee90] I.Y. Lee, Nucl. Phys. A**520**, 641c (1990).
- [Lee99] I. Y. Lee, Nucl. Instr. Meth.Phys. Res. A **422** 195 (1999).
- [Lee06] A. B. F. Lee, High-spin States and K-isomers of ^{185}Re , Honours thesis, The Australian National University, (2006).
- [Lin73] Th. Lindblad *et al.*, Nucl. Phys. A **210**, 253 (1973).
- [Lil01] J. S. Lilley, Nuclear Physics (Principles and applications), (John Wiley and Sons,Ltd, 2001).
- [Lip60] H. Lipkin, Ann. Phys. **9**, 272 (1960).

- [Löb65] K.E.G. Löbner, Phys. Lett. **12**, 33 (1965).
- [Löb68] K.E.G. Löbner, Phys. Lett. B **26**, 369 (1968).
- [Löb75] The Electromagnetic interactions in Nuclear Spectroscopy, (edited by W.D. Hamilton, North Holland, New York, 1975, pg 173-231).
- [Măr10] N. Mărginean *et al.*, Eur. Phys. J. A **46**, 329 (2010).
- [Mac89] H. Mach, R. L. Gill and M. Moszynski, Nucl. Instrum. Meth. A**280**, 49 (1989).
- [May50a] M. G. Mayer, Phys. Rev. **78**, 16 (1950).
- [May50b] M. G. Mayer, Phys. Rev. **78**, 22 (1950).
- [McG00] T. R. McGoram *et al.*, Phys. Rev. C **62**, 031303(R), (2000).
- [Mol95] P. Möller, J. R. Nix, W. D. Myers and W. J. Swiatecki, At. Nucl. Data. Tab. **59**, 185 (1995).
- [Mot60] B. R. Mottelson and J. G. Vatalin, Phys. Rev. Lett. **5**, 511 (1960).
- [Mut84] U. Mutz, P. Ring and J. Phys. G: Nucl. Phys. **10**, L39 (1984).
- [Mul97] S. M. Mullins *et al.*, Phys. Lett. B **393**, 279 (1997).
- [New62] N. D. Newby, Phys. Rev. **125** 1525 (1962).
- [Nil55] S. G. Nilsson, Dan. Mat. Fys. Medd. **29**, 16 (1955).
- [Nil69] S. G. Nilsson, Nucl. Phys. A **131**, 1 (1969).
- [Nil95] S. G. Nilsson and I. Ragnarsson: Shapes and Shells in Nuclear Structure (Cambridge University Press, UK, Cambridge, 1995).
- [Nom11] K. Nomura *et al.*, Phys. Rev. C **84**, 054316 (2011).
- [Nog64] Y. Nogami, Phys. Rev. **134**, 313 (1964).
- [Nog65] Y. Nogami, Phys. Lett. **15**, 4 (1965).

- [Nol94] P. J. Nolan, F.A Beck and D.B. Fossan, Ann. Rev. Nucl. Part. Sci. **45**, 561 (1994).
- [Ols66] B. Olsen and L. Bostrom, Nucl. Instr. Meth. **44**, 65 (1966).
- [Pal12] N. Palalani *et al.*, EPJ Web of Conferences **35**, 06004 (2012).
- [Pal85] G. Palameta and J. C. Waddington, Nucl. Instr. Meth. A **234**, 476 (1985).
- [Pau75] H.C. Paul, K. Alder, and R.M Steffen, Chapter in The Electromagnetic interactions in Nuclear Spectroscopy, (edited. W.D. Hamilton, North Holland, New York, 1975).
- [Pau95] E. S. Paul, Angular correlations analysis with EUROGRAM II, Oliver Lodge Laboratory, University of Liverpool, (September 1995), internal report, unpublished.
- [Pfüt98] M. Pfützner *et al.*, Phys. Lett. B **444**, 32 (1998).
- [Pra73] H. C. Pradhan, Y. Nogami and J. Law, Nucl. Phys. A **201**, 357 (1973).
- [Pur00] C. S. Purry *et al.*, Nucl. Phys. A **672**, 54 (2000).
- [Rad95] D. C. Radford, Nucl. Instr. Meth. A **361**, 297 (1995).
- [Rad95a] D. C. Radford, Nucl. Instr. Meth. A **361**, 306 (1995).
- [Rad00] D. C. Radford, Online information on RadWare (2000).
<http://radware.phy.ornl.gov/info.html#intro>
- [Ree10] M. W. Reed *et al.*, Phys. Rev. Lett **105**, 172501 (2010).
- [Ree16] M. W. Reed *et al.*, Phys. Lett B **752**, 311 (2016)
- [Rég09] J. M Régis *et al.*, Nucl. Instr. Meth. Phys. Res. **A606**, 466 (2010).
- [Rin80] P. Ring and P. Schuck, The Nuclear Many - Body Problem, (Springer Verlag, Heidelberg, 1980).
- [Rob09] L.M. Robledo *et al.*, J. Phys. G. Nucl. Part. Phys. **36**, 115104 (2009).

- [Ros53] M. E. Rose, Angular correlation of nuclear radiations, Oak Ridge National Laboratory, Oak Ridge, Tennessee, (November 1953)
- [Rot59] M. Rotenberg, R. Bivins, N. Metropolis, and J. Wooten, The 3-j and 6-j symbols (The Technology Press, Cambridge, Mass, 1959).
- [Sai98] T. R. Saitoh *et al.*, Eur. Phys. J. A **3**, 197 (1998).
- [Sai00] T. R. Saitoh *et al.*, Nucl. Phys. A **669**, 381 (2000).
- [Sha88] J. F. Sharpey-Schafer and J. Simpson, Prog. Part. Nucl. Phys. **21**, 293 (1988).
- [Shi89] Y. R. Shimizu, J. D. Garrett, R. A. Broglia, M. Gallardo and E. Vigezzi, Rev. Mod. Phys. **61**, 131 (1989).
- [Shi09] T. Shizuma *et al.*, Eur. Phys. J. A **39**, 263 (2009).
- [Shi07] T. Shizuma *et al.*, Eur. Phys. J. A **34**, 1 (2007).
- [Shi08] T. Shizuma *et al.*, Phys. Rev. C **77**, 1 (2008).
- [Shi95] T. Shizuma *et al.*, Nucl. Phys. A **593**, 247 (1995).
- [Sie55] K. Siegbahn, Beta- and gamma-ray spectroscopy, (North-Holland publishing company Amsterdam, 1955).
- [Sie66] K. Siegbahn, Alpha-Beta- And Gamma-ray spectroscopy, Vol 2 (North Holland, 1966, pg 863)
- [Sie87] P. Siemens and A. Jensen, Elements of Nuclei, (Addison-Wesley, 1987).
- [Sol61] V.G. Soloviev, Soviet Physics-Doklady **5**, 778 (1961).
- [Ste11] S. J. Steer *et al.* Phys. Rev. C **84**, 044313 (2011).
- [Ste75] F. S. Stephens, Rev. Mod. Phys. **47**, 43 (1975).
- [Ste05] P. D. Stevenson *et al.*, Phys. Rev. C **72**, 047303 (2005).

- [Stu05] A. E. Stuchbery, *Nilsson wavefunctions with s_3 and g_K values for nuclei with $50 < Z < 82$ and $82 < N < 126$* , ANU Internal Report (2005), *unpublished*.
- [Sun61] A. W. Sunyar and P. Axel, Phys. Rev. **121**, 1354 (1961).
- [Twin84] P. J. Twin *et al.*, Nuovo Cim. A **81**, 219 (1984).
- [Van80] J. Van Klinken *et al.*, Nucl. Phys. A **339**, 189 (1980).
- [Wan09] H. Wanatabe *et al.* Phys. Rev. C **79**, 064311 (2009).
- [Wap77] A. H. Wapstra and K. Bos., At. Nucl. Data Tables **19**, 215 (1977).
- [Wal91] P. M Walker *et al.*, Phys. Rev. Lett **67**, 433 (1991).
- [Wal94] P. M Walker *et al.*, Nucl. Phys. A **568**, 397 (1994).
- [Wal97] P. M Walker *et al.*, Phys. Lett. B **408**, 42 (1997).
- [Wal99] P. M Walker and G.D. Dracoulis, Nature **399**, 35 (1999).
- [Wal01] P. M Walker and G.D. Dracoulis, Hyperfine Interactions **135**, 83 (2001).
- [Wal15] P. M Walker *et al.*, *unpublished*.
- [War73] T. E. Ward *et al.*, Phys. Rev. C **8**, 340 (1973).
- [Wei51] V.F. Weisskopf, Phys. Rev. **83**, 1073 (1951).
- [Whe98] C. Wheldon *et al.*, Phys. Lett. B **425**, 239 (1998).
- [Whe99] C. Wheldon *et al.*, Eur. Phys. J. A **5**, 353 (1999).
- [Whe99a] C. Wheldon, *K-isomerism at high spin beyond the fusion limit*, University of Surrey, PhD thesis, (1999), unpublished.
- [Whe00] C. Wheldon *et al.*, Phys. Rev. C **62**, 057301 (2000).
- [Whe01] C. Wheldon *et al.*, J. Phys. G: Nucl. Part. Phys. **27**, L13 (2001).
- [Whe04] C. Wheldon *et al.*, Eur. Phys. J. A **20**, 365 (2004).
- [Woo54] R. Woods and D. S. Saxon, Phys. Rev. **95**, 577 (1954).

[Www1] Designing gammasphere, Florida state university. Figure available via
<http://nucalf.physics.fsu.edu/~riley/gamma/gamma3.html>

[Zen83] J. Y. Zeng and T. S. Cheng, Nucl. Phys. A **405**, 1 (1983).